SISSA
Scuola
Internazionale
Superiore di
Studi Avanzati

Physics Area - PhD course in
Statistical Physics

# Stochastic processes in biological, active and quantum systems

Candidate:
Gennaro TUCCI

Advisors:
Prof. Andrea GAMBASSI
Prof. Édgar ROLDÁN

Academic Year 2020-21



# Contents

**Introduction** **vii**

**1 Brownian motion with resetting from an interval** **1**
1.1 Introduction . . . 1
1.2 Brownian motion with Poissonian resetting . . . 2
1.2.1 Brownian motion with non-Poissonian resetting . . . 5
1.2.2 Statistic of the first-passage time to an absorbing point . . . 6
1.2.3 Spatially inhomogeneous resetting . . . 7
1.3 Controlling diffusion . . . 9
1.3.1 Brownian tunnelling ($\sigma_c = 0$) . . . 10
1.3.2 Minimal diffusivity for a resetting interval ($\sigma_c = 1$) . . . 11
1.4 Resetting gauge invariance on a ring . . . 13
1.4.1 Resetting current . . . 16
1.4.2 Minimal path protocol . . . 19
1.4.3 Constant rate protocol . . . 22
1.5 Application to the RNA polymerase . . . 24
1.6 Conclusions . . . 29

**2 An experimental protocol for run-and-tumble particles with resetting** **31**
2.1 Introduction . . . 31
2.2 Run-and-tumble dynamics . . . 33
2.2.1 First-passage time statistics . . . 35
2.2.2 RTPs in a confining potential . . . 37
2.3 Effect of the initial position distribution $\rho(x)$ . . . 38
2.4 RTPs with stochastic resetting . . . 41
2.4.1 Brownian motion . . . 45
2.4.2 Run-and-tumble particles . . . 46
2.5 Periodic resetting and experimental protocol . . . 47
2.6 Conclusions . . . 48

**3 Modelling active non-Markovian oscillations** **51**
3.1 Introduction . . . 51
3.2 Active non-Markovian oscillator . . . 52

3.3 Dynamics . . . 54
3.3.1 Switching probability density $G_S(x, \sigma, t|x_0, \sigma_0)$ . . . 54
3.3.2 Probability density $G(x, \sigma, t|x_0, \sigma_0)$ . . . 57
3.3.3 Fokker-Planck description . . . 59
3.4 Power spectrum . . . 63
3.5 Energetics . . . 66
3.5.1 First moment . . . 67
3.5.2 Second moment . . . 68
3.5.3 Work Fano factor for symmetric waiting-time distributions . . . 69
3.5.4 Energy and heat moments . . . 72
3.6 Experimental application: spontaneous oscillations of the bullfrog hair bundles . . . 73
3.7 Conclusions . . . 74

**4 Stochastic representation of a quantum anharmonic oscillator 79**
4.1 Introduction . . . 79
4.2 Stochastic representation of the quantum quartic oscillator . . . 81
4.3 Physical observables . . . 84
4.3.1 Dynamics of a Gaussian wave packet . . . 84
4.3.2 Exactly solvable cases . . . 87
4.4 Stochastic interpretation and numerical benchmark . . . 88
4.5 Perturbative Expansion . . . 91
4.6 Semiclassical approximation . . . 93
4.6.1 Propagator . . . 93
4.6.2 Partition function . . . 96
4.7 Conclusions . . . 98

**Appendices 98**

**A Langevin equation and stochastic thermodynamics 99**
A.1 Wiener process . . . 99
A.2 Stochastic differential equations . . . 100
A.2.1 Itô's Lemma . . . 101
A.3 Euler method . . . 101
A.4 Brownian motion and Langevin equation . . . 102
A.5 First law of thermodynamics at the mesoscopic scale . . . 103
A.6 Second law of Thermodynamics at the Mesoscopic scale . . . 104

**B Calculations of Chapter 1 107**
B.1 General expressions for $\tilde{P}_{\rm nc}(x, s|x_0)$ and $\tilde{P}(x, s|x_0)$ . . . 107
B.2 Open boundary conditions . . . 108
B.2.1 Case with $x_0 < -a$ . . . 108
B.2.2 Case with $|x_0| < a$ . . . 110
B.3 Periodic boundary conditions . . . 111
B.3.1 Case with $-L < x_0 < -a$ . . . 112

B.3.2 Case with $x_0 \in (-a, a)$ . . . 114

**C Calculations of Chapter 3** **117**
C.1 Moments of $G_S(x, \sigma, t|x_0, \sigma_0)$ . . . 117
C.1.1 First moment . . . 117
C.1.2 Second moment . . . 120
C.2 Moments of $G(x, \sigma, t|x_0, \sigma_0)$ . . . 122
C.2.1 First moment . . . 122
C.3 Statistics of $c(t)$ . . . 125
C.3.1 General probability distribution with asymmetric waiting times . . . 127
C.4 Simulation-based inference . . . 131

**D Calculations of Chapter 4** **133**
D.1 Gaussian integral . . . 133
D.2 Time-dependent quartic Hamiltonian . . . 134
D.3 Action of $\exp(w\, \hat{S}^{\pm,z})$ on a Gaussian wave packet . . . 135
D.4 Time evolution of a Gaussian wave packet . . . 139
D.5 Derivations of the Dyson series . . . 140
D.6 Evaluation of $G_{\mathrm{HO}}(0, t|0, 0)$ . . . 143
D.7 Semiclassical limit . . . 145
D.8 Crank-Nicholson algorithm . . . 146
D.8.1 Space discretization: Numerov approximation . . . 147

# Introduction

In 1827, the Scottish scientist Robert Brown, pioneer in the use of the microscope in botany, discovered the "swarming" motion of pollen particles suspended in water. Driven by his intuition, he analysed the motion of inorganic particles, encountering the same type of behaviour. These observations led him to the conclusion that this phenomenon is not life-related, and to the discovery of the so-called *Brownian motion* [31]. The first theoretical description of the Brownian motion was proposed to the physics community in 1905 by Albert Einstein [65, 64], and a year later, independently, by Marian Smoluchowski [200, 201]. Finally, in 1908 Jean Baptiste Perrin provided experimental evidence of Einstein's theory [161], for which he was awarded with Nobel Prize in 1926. These developments were fundamental to close the long-standing debate about the existence of atoms and molecules, and to set a solid ground for modern statistical mechanics. Since then, stochastic processes have been applied to describe several systems in various fields of knowledge: physics, biology, mathematics, chemistry, economics, to mention a few.

In physics, whenever the time evolution of a system depends on of a large number of degrees of freedom, but at a macroscopic scale one observes well-defined averaged macroscopic features obeying simple laws, a stochastic description naturally emerges. For example, we may consider a system consisting of a large number of particles in a box with reflecting boundaries. The force that these particles exert on one another varies extremely quickly and unpredictably, and it can be interpreted as stochastic. This stochastic description depends crucially on the space-time scale at which one observes the system. However, when averaging over all the stochastic degrees of freedom one always recovers the same macroscopic average. Namely, stochastic description fixes a *mesoscopic* scale that carries more information on the fluctuations than the macroscopic measurements. The stochastic equation describing the time evolution of these mesoscopic degrees of freedom goes under the name of its discoverer, the French physicist Paul Langevin [117]. The study of the Langevin equation has inspired beautiful lines of research. From a mathematical point of view, it has led to the development of a rigorous framework to treat stochastic differential equation, known as *stochastic calculus*. On the physics side, it has made possible to construct a *stochastic thermodynamic* theory at the mesoscopic scale based on the Langevin equation, which enables one to extend standard concepts of thermodynamics to the mesoscopic scale. Another fundamental tool to the study of (Markovian) continuous stochastic processes is the Fokker-Planck equation [78, 165]. This approach relies on the statistical mechanical concept of *ensemble* of realizations of the same stochastic process. In particular, the Fokker-Planck equation expresses the time evolution of the probability density of the possible configurations of the system. Notably, given a Langevin equation, it is possible to construct the relative Fokker-Planck description. In addition, the Fokker-Planck equation associated with the overdamped motion of particles in confining potential is formally equivalent the a Schrödinger

equation in imaginary time. This analogy is not only formal, but also practical, since it allows one to employ tools from quantum mechanics and apply them to study stochastic processes.

In this thesis, the concepts mentioned above are applied to and developed in a wide class of physical systems, all described by stochastic processes, sharing important common features.

Most of the physical systems that we will consider here can be modelled via stochastic processes displaying externally driven *sudden events*. This is a very wide class of multi-layered stochastic processes. They are constituted by a main underlying process, and one (or more) extra stochastic mechanism which modifies the evolution of the system by abruptly changing in time one of the state variables. The first example that we consider is *stochastic resetting* [70, 74] in this case the controlling mechanism randomly resets the position of the particle to some prescribed position, that may also be drawn from some probability distribution. A prototypical model of stochastic resetting is given by Brownian particle resetting its position with constant rate in space and time to the origin of the motion. Since this seminal work, the rich phenomenology and the vast range of potential applications of these processes has attracted great attention and a massive amount of work has been done and it is still done on the topic. In the first two Chapters of the thesis, we connect to this recent line of research and we provide explicit examples of how stochastic resetting can be interesting per se, and how it can be used to model properties of real biological systems.

In particular, in **Chapter 1**, we analyse how space-inhomogeneous resetting and topological constraints modify the statistics of the Brownian motion. Namely, we study minimal stochastic models of diffusing particles evaporating or resetting from a finite one-dimensional region with either open, periodic and/or absorbing boundary conditions. As a first case, we consider the *tunnelling* of Brownian particles across an interval with a constant evaporation rate. The solution of such a *Brownian tunnelling* model allows us to tackle the problem with resetting [179]. In the case of resetting with open boundary conditions, we highlight the appearance of *Brownian yet non-Gaussian* diffusion at large times [48, 42, 204, 136], meaning that although the distribution of the particle position is non-Gaussian, its mean-squared displacement grows linearly in time at leading order.

Our key findings concern the transport properties of diffusion processes with resetting and periodic boundary conditions. For these systems, a stationary state exists and we can define a probability current with a non-vanishing stationary value. Contrarily to what happens for the probability density of particles, we reveal that the actual value of this current depends genuinely on the local *direction* of resetting. Accordingly, we show that currents provide useful and insightful information about the underlying non-equilibrium resetting process, in addition to that conveyed by the probability distribution. Drawing an analogy with field theory, we dub this result "resetting gauge invariance": a whole class of dynamics, all with very different behaviour of the current, results in the same distribution, both in stationary and non-stationary regimes. Eventually, we use our results to model the fluctuating motion of RNA polymerase during transcriptional pauses, allowing us to analytically predict relevant statistical properties which have been measured experimentally [118, 180].

Stochastic resetting naturally emerges in the context of search processes and their optimization. Imagine one wants the process to represent some randomly agent moving and looking for a target located in a point or region of space. Then, the time that the particle takes to reach the target, which is called *first-passage time*, is also a random variable [172]. In this spirit, it is possible to characterize the search process in terms of the first-passage time statistics, and investigating the

average first-passage time becomes relevant, in the optics to try to optimize it by acting on the resetting parameters. For example, in the case of the one-dimensional Brownian motion, whose mean first-passage time diverges, the introduction of a resetting mechanism not only allows the system to hit the target (on average) in a finite amount of time, but gives also the possibility to optimize its mean first-passage time. With this in mind, in **Chapter 2**, we derive new analytical predictions concerning the first-passage statistics of several models belonging to the class of *run-and-tumble* particles [210, 149, 66, 203, 39]. These systems, sometimes referred to as *persistent* Brownian motion, consist of self-propelled particles moving ballistically (run phase) with random changes of direction (tumble phase). Run-and-tumble motion has been observed in several species of bacteria and it is a representative model of the class of *active* matter [53, 56, 170, 77]. In these systems, the motion of the particles is sustained by energy consumption and is characterized by entropy production, with resulting breaking of time-reversal symmetry and fluctuation-dissipation theorem [52]. As anticipated, we employ the run-and-tumble particle as a model of a random searcher. In particular, by extending previous works on the Brownian motion [23, 22], we investigate the effect on the statistics of the first-passage time of having a (random) location of the initial position of the particle, and of resetting. Finally, in the same spirit as in Ref. [22], we collect all these ingredients to discuss an experimentally relevant protocol that allows one to reproduce resetting by means of optical lasers traps.

In **Chapter 3**, we continue investigation of among active stochastic systems characterized by externally driven sudden events. Also in this case, we introduce a multi-layered process based on an underlying dynamics, identified with the Brownian motion of a particle, and on an external stochastic driving, due to a harmonic potential with equilibrium position coinciding with a time-dependent dichotomous stochastic process. Hence, the dynamics of the particle consists in the alternate relaxation towards the two minima of the stochastic potential. In this sense, the system represents a minimal model for non-Markovian linear *active oscillators*, an important subclass of active matter whose main degrees of freedom display an oscillatory dynamics [5, 17, 18, 24, 35, 44, 45, 76, 102, 129, 130, 132]. Contrarily to previous existing models introduced to design and describe these active systems, based on Van der Pol and Duffing oscillators, our system is linear, enabling us to determine exact expressions for dynamical variables, such as statistics and power spectrum for the particle position, and thermodynamic observables, such as the work moments and power dissipation. In addition, this model generalizes, in some proper limit, those introduced in Chapters 1 and 2. Among the variety of beautiful examples of active oscillators appearing in nature, we apply our finding to describe and fit the spontaneous oscillations of the hair bundles in the ear of the bullfrog, for which experimental measurements are available [102, 132, 130]. Then, we use the values of the fitted parameters in order to predict quantitatively the stationary dissipated power, a quantity which cannot be accessed experimentally.

In **Chapter 4**, instead of looking at systems that can be described effectively by stochastic processes, we show how these processes may naturally arise from the analysis of non-equilibrium dynamics of *quantum* systems. Recent works in the field of quantum spin chains have revealed an exact mapping between the quantum evolution of these systems and a set of stochastic differential equations [98, 81, 175, 184]. Following a similar path, we show how this procedure can be extended to the case of a zero-dimensional bosonic system. In particular, we consider the quantum anharmonic oscillator with quartic potential, which represents the simplest anharmonic extension of the quantum harmonic oscillator. Then, via a sequence of exact transformations, we parametrize the dynamics

of the time evolution operator of the quantum quartic oscillator in terms of stochastic differential equations: for this particular quantum model, quantum fluctuations can be mapped into classical stochastic ones. Accordingly, expectation value of observables in this stochastic approach translates into an average over the ensemble of trajectories generated by these stochastic processes. This leads to an intuitive implementation of the numerical analysis of these observables. In general, this approach allows one to use all the analytical and numerical tools of stochastic processes and classical field theories to analyse the dynamics of an anharmonic quantum system. Indeed, we expect that this approach can be extended to higher spatial dimensions, and eventually to many-body bosonic systems with quartic couplings.

The content of this thesis is reported in the following writings:

(i) **Gennaro Tucci**, Andrea Gambassi, Shamik Gupta, and Édgar Roldán
*Controlling particle currents with evaporation and resetting from an interval*
Phys. Rev. Research 2, 043138 – Published 27 October 2020

(ii) **Gennaro Tucci**, Satya N. Majumdar, Andrea Gambassi, and Grégory Schehr
*First-passage time of run-and-tumble particles: an experimental protocol*
(To appear)

(iii) **Gennaro Tucci**, Édgar Roldán, Andrea Gambassi, Roman Belousov, and A. James Hudspeth's laboratory
*Modelling Active Non-Markovian Oscillators*
arXiv:2201.12171 – February 2022

(iv) **Gennaro Tucci**, Stefano De Nicola, Sascha Wald, and Andrea Gambassi
*Stochastic Representation of the Quantum Anharmonic Oscillator*
(To appear)

# Chapter 1

# Brownian motion with resetting from an interval

## 1.1 Introduction

Stochastic processes whereby incremental changes are interspersed with sudden and large changes occurring at unpredictable times are common in nature [155, 106, 33, 160, 70, 113, 88, 63, 92, 97, 118, 140, 22, 211]. Examples range from epidemics (e.g., Covid-19), to financial market (e.g., the 2008 crisis) and biology (e.g., the catastrophic events of sudden shrinkage during the polymerization of a microtubule [155, 33, 160], the flashing ratchet mechanism of molecular motors [106], etc.). Recent developments of the theoretical framework of "stochastic resetting" aims to describe features of this kind of stochastic processes.

A paradigmatic model of these phenomena is provided by a Brownian particle diffusing and resetting instantaneously its position to a fixed value at exponentially-distributed random times [70]. The concept of stochastic resetting has been invoked in many different fields such as first-passage properties [113, 158], continuous-time random walk [134], foraging [88, 27, 25, 171], reaction-diffusion models [63], fluctuating interfaces [92, 93], exclusion processes [14], phase transitions [97], large deviations [50], RNA transcription [118, 180], quantum dynamics [143], cellular sensing [140], population dynamics [82], stochastic thermodynamics [79], and active matter [125]; see, e.g., Ref. [74] for a recent review.

One of the main physical consequences of resetting is the possibility to induce a stationary state in systems that otherwise would not admit it. A paradigmatic example is the Brownian motion, where the addition of spatially homogeneous resetting, in any spatial dimensionality $d$ [70, 71], ensures a stationary state even in the absence of confining boundary conditions and/or potentials. Moreover, because of resetting, the Brownian motion displays a finite first-passage time to a given target, inspiring new search algorithms [120, 205]. In the recent past, a variety of situations have been studied within this framework, e.g., Brownian particles resetting under the action of an external potential to a generic spatial distribution [179], and for various choices of the resetting time probability distribution [147]. Most of these studies consider resetting phenomena with occurring in the presence of open boundary conditions. However, excepting for few studies such as Refs. [40, 47], not much is known about systems that experience stochastic resetting in a closed

geometry. In particular, an important question to address is how topological constraints in one dimension (e.g., boundary conditions) affect the stationary and dynamical properties of diffusion in the presence of stochastic resetting. Below we will address, inter alia, this issue.

In particular, we answer these questions by analysing several prototypical stochastic models, using as building blocks exact results that we derive by extending the path-integral formalism for resetting [179]. We introduce models of diffusion with resetting or evaporation occurring with a fixed rate only within a small spatial region. First, we study the effect of open boundary conditions. In the case of evaporation, we investigate the *tunnelling* probability of Brownian particles crossing a spatial window with constant evaporate rate. These results allow us to study the equivalent problem with resetting. In this case, we show that the system displays *Brownian yet non-Gaussian* diffusion: the probability density of the particle position is non-Gaussian but its variance grows linearly at large times. Then, we consider the presence of periodic boundary conditions. In this ring geometry, at a reset event, particles can ambiguously reset counterclockwise or clockwise, reflecting the existence of infinity possible currents. However, as a consequence of the fact that resetting is instantaneous, these currents are all compatible with an unique probability density. We refer to this phenomenon as *gauge invariance* of the probability density of the position of the particles with respect to the *protocol* that fixes their direction at a reset. We also show that our analysis, besides being of interest for physics, applies usefully to a stochastic model of the motion of a biological system, i.e., RNA polymerases during transcriptional pauses, shedding light on available experimental results [118, 180].

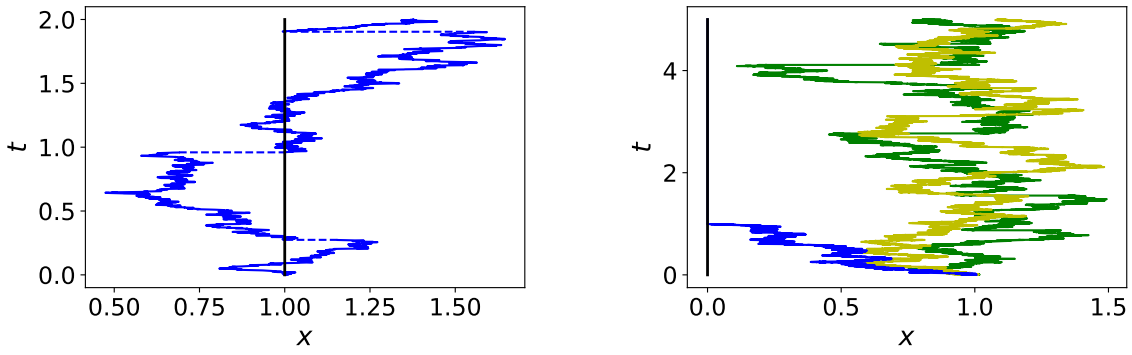
The Chapter is organized as follows. In Sec. 1.2 we briefly recall essential theoretical results concerning Brownian particles resetting with constant rate in time and space to some prescribed position. In Sec. 1.3, we address the problem of the Brownian particle in one spatial dimension in the case of space-inhomogeneous evaporation or resetting in the presence of open boundary conditions. In Sec. 1.4, we discuss particle currents due to diffusion and resetting in one-dimensional systems with periodic boundary conditions. In Sec. 1.5, we apply our results to the biological system mentioned above. We conclude the Chapter with a discussion in Sec. 1.6. We provide the exact analytical calculations and further numerical results in Appendix B.

## 1.2 Brownian motion with Poissonian resetting

In this Section we summarize some theoretical results concerning the motion of a one-dimensional Brownian particle with initial position $x_0$, resetting with constant rate $r$ to the resetting point $x_r$ [70, 74]. Accordingly, the dynamics of the particle position $x(t)$ is given by the following stochastic rule: within an infinitesimal time interval $\mathrm{d}t$, the updated position $x(t+\mathrm{d}t)$ is given by

$$\begin{aligned} x(t+\mathrm{d}t) &= x(t) + \xi(t)(\mathrm{d}t)^{1/2} \quad \text{with probability} \quad 1-r\mathrm{d}t, \\ &= x_r \qquad\qquad\qquad\quad \text{with probability} \quad r\mathrm{d}t, \end{aligned} \tag{1.1}$$

where $\xi(t)$ is a Gaussian white noise with zero average $\langle \xi(t) \rangle = 0$, and two-time correlator $\langle \xi(t')\xi(t) \rangle = 2D\delta(t-t')$, with $D$ being the diffusion constant. Due to the fact that $r$ is constant, the number of resets within a time interval of duration $t$ is distributed according to a Poisson with mean $rt$. It follows that the probability density $\psi(\tau)$ of the waiting time between two consecutive resetting events is exponentially distributed, i.e., $\psi(\tau) = r\, e^{-r\tau}$, and that the process $x(t)$ is Markovian [222].




(a) (b)

Figure 1.1: **Brownian motion with resetting.** Panel **(a)** shows typical trajectories of Brownian particle originating and resetting to $x_0$ (black vertical line). Whenever particles reset they are teleported from their current location to the resetting point: the resetting events are marked by with an horizontal blue line. The parameters of the trajectory are: $D = 0.1$, $r = 1$, and $x_0 = x_r = 1$. Panel **(b)** shows trajectories of Brownian motion with Poissonian resetting in the presence of an absorbing boundary (black vertical line) located at the origin. Each trajectory is identified with a different color, and the parameters of their dynamics are: $D = 0.1$, $r = 2$, and $x_0 = x_r = 1$.

Figure 1.1a shows a typical realization of the process: at a reset (dashed horizontal line) the particle is teleported to its initial position (black vertical line) with constant rate.

We denote by $P(x, t|x_0, t_0; x_r)$, the probability density for the particle to be in $x$ at time $t$, given the initial position $x_0$ at time $t_0$. Whenever no ambiguity arises, we omit the dependence of $P$ on $x_r$, and on $t_0$ if $t_0 = 0$. One can express the infinitesimal time evolution equation for $P(x, t|x_0)$ as:

$$P(x, t + \mathrm{d}t|x_0) = r\mathrm{d}t\, \delta(x - x_r) + (1 - r\mathrm{d}t)\langle P(x - \xi(t)(\mathrm{d}t)^{1/2}, t|x_0)\rangle, \tag{1.2}$$

where $\langle \cdots \rangle$ represents the average with respect to the Gaussian noise $\xi(t)$. The first term on the right hand side considers contribution from particles resetting at time $t$, whereas the second to those that simply diffuse. By applying Itô's Lemma (see Appendix A) on can Taylor-expand Eq. (1.2) in the limit $\mathrm{d}t \to 0$, one gets

$$\begin{aligned} P(x,t + \mathrm{d}t|x_0) &= r\mathrm{d}t\, \delta(x - x_r) + (1 - r\mathrm{d}t) \\ &\times \left[P(x, t|x_0) + (\mathrm{d}t)^{1/2}\langle\xi(t)\rangle\frac{\partial P(x, t|x_0)}{\partial x} + \mathrm{d}t\, D\frac{\partial^2 P(x, t|x_0)}{\partial x^2} + O\left((\mathrm{d}t)^{3/2}\right)\right], \end{aligned} \tag{1.3}$$

which, together with the Brownian motion relations $\langle\xi(t)\rangle = 0$, reduces to the Fokker-Planck equation

$$\frac{\partial P(x, t|x_0)}{\partial t} = D\frac{\partial^2 P(x, t|x_0)}{\partial x^2} - rP(x, t|x_0) + r\delta(x - x_r), \tag{1.4}$$

with initial condition $P(x,0|x_0) = \delta(x - x_0)$. The first term on the right hand side of Eq. (1.4) expresses the diffusive contribution to the dynamics. While the contribution of resetting is described by the second and third term. The second accounts for the probability loss due to resetting, while the third to the resulting gain of probability at the resetting point $x_r$.

Alternatively, it is possible to write an integral equation for $P(x,t|x_0)$ equivalent to Eq. (1.4) by means of a renewal approach. In the absence of resetting, i.e., for $r = 0$, the system reduces to a Brownian particle with Gaussian probability density $P_{\rm BM}(x,t|x_0,0)$ of mean $x_0$, and variance $\sqrt{2Dt}$. In presence of resetting, one can classify the trajectories of the particle in two categories: those corresponding to particles that never reset in the interval $(0,t)$, and those who reset at least once. Keeping this in mind, one can write a renewal equation for $P(x,t|x_0)$:

$$P(x,t|x_0) = e^{-rt} P_{\rm BM}(x,t|x_0,0) + r \int_0^t {\rm d}\tau \, e^{-r\tau} P_{\rm BM}(x,\tau|x_r,0). \tag{1.5}$$

The first term on the right hand side of Eq.(1.5) coincides with the contribution to $P(x,t|x_0)$ due to particles that never reset in the time interval $(0,t)$: it consists of the product of the probability of having no reset in $(0,t)$, i.e., $e^{-rt} = \int_t^\infty {\rm d}\tau \, \psi(\tau)$, and the probability density $P_{\rm BM}(x,t|x_0,0)$ of the dynamics with no resetting. The second term can be understood by conditioning on the last reset at the intermediate time $t - \tau$. For Poissonian resetting, the probability to have a reset between $(t-\tau, t-\tau+{\rm d}\tau)$ is $r{\rm d}\tau$. The condition of last reset at $t-\tau$ is obtained by imposing that no other resetting event occurs in $(\tau,t)$, contributing with probability $e^{-r\tau} P_{\rm BM}(x,\tau|x_r,0)$.

Similarly, one can derive a renewal equation for $P(x,t|x_0)$ by conditioning with respect to the first resetting event:

$$P(x,t|x_0) = e^{-rt} P_{\rm BM}(x,t|x_0,0) + r \int_0^t {\rm d}\tau \, e^{-r\tau} P(x,t-\tau|x_r,0). \tag{1.6}$$

The probability of having a first reset at $\tau$ is $\psi(\tau){\rm d}\tau$, while the probability to reach $x$ at $t$ from the the resetting point $x_r$ at the intermediate time $\tau$ is equal to $P(x,t-\tau|x_r,0)$. The equivalence of Eqs. (1.5) and (1.6) is easily proved by taking their Laplace transform. Given a function $f(t)$, its Laplace transform is denoted by $\tilde{f}(s) = \mathcal{L}[f(t)](s) = \int_0^\infty {\rm d}t \, e^{-st} f(t)$ [188]. By taking the Laplace transform of Eq. (1.5) one finds

$$\tilde{P}(x,t|x_0,0) = \tilde{P}_{\rm BM}(x,s+r|x_0,0) + \frac{r}{s} \tilde{P}_{\rm BM}(x,s+r|x_r,0). \tag{1.7}$$

This equality follows from applying the convolution theorem of the Laplace transform, the properties of the Laplace transform $\mathcal{L}[f(t)e^{-rt}] = \tilde{f}(s+r)$, and $\mathcal{L}[\int_0^t {\rm d}\tau \, f(\tau)] = \tilde{f}(s)/s$. Moreover, Eq. (1.7) allows one to find the stationary distribution $P_{\rm st}(x)$ via the final value theorem of the Laplace transform:

$$P_{\rm st}(x) = \lim_{t\to\infty} P(x,t|x_0) = \lim_{s\to 0} s\, \tilde{P}(x,t|x_0) = r \tilde{P}_{\rm BM}(x,r|x_r). \tag{1.8}$$

By substituting the Laplace transform transform of the Gaussian distribution, see, e.g., Ref. [188],

$$\tilde{P}_{\rm BM}(x,s|x_0) = \frac{\exp\left(-\frac{|x-x_0|}{\mu(s)}\right)}{D\mu(s)}, \tag{1.9}$$

where we define the auxiliary quantity

$$\mu(s) \equiv \sqrt{\frac{s}{D}}, \tag{1.10}$$

in Eq. (1.8), one gets

$$P_{\rm st}(x) = \mu(r)\, \exp\left(-\frac{|x-x_r|}{\mu(r)}\right). \tag{1.11}$$

The stationary distribution $P_{\rm st}(x)$ reflects the existence of a non-equilibrium stationary state [70, 74]. This is one of the main effect of resetting on the Brownian motion. Moreover, the appearance of a cusp at $x_r$ in $P_{\rm st}(x)$ is also a consequence of resetting: it results from the probability flux towards $x_r$ at all times.

### 1.2.1 Brownian motion with non-Poissonian resetting

For later convenience, we report how one can extend the above analysis to the case where resetting is no longer homogeneous in time [74]. Equivalently, the waiting-time probability density $\psi(\tau)$ is no longer an exponential, the number of reset events is generically not distributed according to a Poissonian and, as a consequence, the process is *non-Markovian*. Then, one can express the probability $\Psi(t)$ that no reset has occurred in the time interval $(0,t)$ as

$$\Psi(t) = \int_t^\infty {\rm d}\tau\, \psi(\tau) = 1 - \int_0^t {\rm d}\tau\, \psi(\tau). \tag{1.12}$$

Also in the case of time-dependent resetting rate, it is possible to write down a renewal equation for the probability density $P(x,t|x_0)$. To do so, one has to classify the possible trajectories of the system in terms of the number of resets that occur in a given time interval $(0,t)$. In the case of no resetting events, the contribution to the total probability density reads $\Psi(t)P_{\rm BM}(x,t|x_0)$. For one resetting event, instead, one gets

$$\int_0^t {\rm d}\tau_1\, \psi(\tau_1)\Psi(t-\tau)P_{\rm BM}(x,t-\tau|x_r), \tag{1.13}$$

expressing the fact that after the reset at the intermediate time $\tau$, happening with probability $\psi(\tau){\rm d}\tau$, the particle shows only Brownian dynamics starting from $x_r$ at $\tau$ until $t$, contributing with weight $\Psi(t)P_{\rm BM}(x,t|x_r)$. This reasoning can be generalized to a generic number $n$ of resets, leading to

$$\begin{aligned} P(x,t|x_0) &= \Psi(t)P_{\rm BM}(x,t|x_0) \\ &+ \sum_{n=1}^\infty \int_0^t {\rm d}\tau_1\, \psi(\tau_1) \cdots \int_0^{t-\sum_{k=1}^{n-1}\tau_k} {\rm d}\tau_n\, \psi(\tau_n)\Psi\left(t-\sum_{k=1}^n \tau_k\right) P_{\rm BM}\left(x, t-\sum_{k=1}^{n-1}\tau_k \middle| x_r\right). \end{aligned} \tag{1.14}$$

Equation (1.14) is significantly simplified after a Laplace transform:

$$\begin{aligned}\tilde{P}(x,s|x_0) &= \mathcal{L}\left\{\Psi(t)P_{\rm BM}(x,t|x_0)\right\}(s) + \sum_{n=1}^{\infty}(\tilde{\psi}(s))^n \mathcal{L}\left\{\Psi(t)P_{\rm BM}(x,t|x_r)\right\}(s) \\ &= \mathcal{L}\left\{\Psi(t)P_{\rm BM}(x,t|x_0)\right\}(s) + \frac{\tilde{\psi}(s)}{1-\tilde{\psi}(s)}\mathcal{L}\left\{\Psi(t)P_{\rm BM}(x,t|x_r)\right\}(s),\end{aligned} \tag{1.15}$$

where the first line follows from multiple application of the Laplace convolution theorem [188], and the second from the geometric sum, which converges due to the fact that $|\tilde{\psi}(s)| < 1$ for $\mathrm{Re}(s) > 0$.

### 1.2.2 Statistic of the first-passage time to an absorbing point

Stochastic resetting arises naturally in the context of *search process*, i.e., systems where the a stochastic process is used to track the location of a given target in the space. In these models, it turns out that resetting allows one to optimize the search process. Examples of these systems appear in several different areas of both human and natural sciences: intermittent search strategies [67, 70, 73, 114, 25, 158, 41, 115, 157, 29], search algorithms [120, 205], optimization [139, 183, 16, 54, 55], foraging [88, 27, 25, 171] to mention a few.

We can use as a simple example to illustrate how resetting influences search processes the Brownian motion with stochastic resetting. More precisely, we consider the effect of stochastic resetting on the statistics of the first-passage time to an absorbing point located at the origin, see Fig. 1.1; we refer to Refs. [70, 74] for more details. For this purpose, one introduces the survival probability $S_r(x_0,t|x_r)$, i.e., the fraction of particles that has not hit the origin up to time $t$, given the initial point $x_0 > 0$ and resetting point $x_r > 0$; in what follows, we omit the dependence on $x_r$ of the various quantities. Similarly to what it has been done for $P(x,t|x_0)$ in the previous Section, it is possible to write a renewal equation for $S_r(x_0,t)$:

$$S_r(x_0,t) = e^{-rt}S_{\rm BM}(x_0,t) + r\int_0^t \mathrm{d}\tau\, e^{-r\tau}S_{\rm BM}(x_r,\tau)S_r(x_0,t-\tau), \tag{1.16}$$

where $S_{\rm BM}(x_0,t)$ is the survival probability in the absence of resetting. The first contribution to $S_r(x_0,t)$ comes for particles that evolve without resetting. The second term accounts for particles that reset for the last time at $t-\tau$. Moreover, the knowledge of $S_r(x_0,t)$ allows one to calculate the first-passage time probability density $F_r(t|x_0)$ as the rate of particle loss due to absorption at time $t$: $F_r(t|x_0) = -\partial_t S_r(x_0,t)$.

By taking the Laplace transform of Eq. (1.16) and applying the Laplace convolution theorem, one finds

$$\tilde{S}_r(x_0,s) = \tilde{S}_{\rm BM}(x_0,s+r) + r\,\tilde{S}_r(x_0,s)\tilde{S}_{\rm BM}(x_r,s+r), \tag{1.17}$$

where $\tilde{S}(x_0,s) = \int_0^\infty \mathrm{d}t\, e^{-st}S(x_0,t)$ denotes the Laplace transform of the survival probabilities. The equation above allows one to determine the Laplace transform of $S_r(x_0,t)$ in terms of $\tilde{S}_{\rm BM}(x_0,s)$:

$$\tilde{S}_r(x_0,s) = \frac{\tilde{S}_{\rm BM}(x_0,s+r)}{1-r\tilde{S}_{\rm BM}(x_r,s+r)}. \tag{1.18}$$

Finally, one can calculate the Laplace transform of the first-passage probability density as $\tilde{F}_r(s|x_0) = 1 - s\tilde{S}_r(x_0, s)$, following from the formula for the Laplace transform of the derivative.

One can show that the Laplace transform of the survival probability of Brownian motion [74] is given by

$$\tilde{S}_{\rm BM}(x_0, s) = \frac{1 - e^{-\mu(s)x_0}}{s}, \tag{1.19}$$

which can be inverted easily [172] as

$$S_{\rm BM}(x_0, t) = \mathrm{erf}\left(\frac{x_0}{\sqrt{4Dt}}\right), \quad \text{and} \quad F_{\rm BM}(t|x_0) = \frac{x_0}{\sqrt{4\pi D t^3}} \exp\left(-\frac{x_0^2}{4Dt}\right), \tag{1.20}$$

where erf($\bullet$) denotes the error function. The long-time behaviour of the first-passage probability $F_{\rm BM}(t|x_0) \sim t^{-3/2}$ for the Brownian motion implies the divergence of its first moment, as a consequence of the fact that Brownian particles have non-vanishing probability to diffuse away from the origin.

Then the mean first-passage time $\langle t_f \rangle(x_0, r) \equiv \int_0^\infty \mathrm{d}t\, t\, F_r(t|x_0)$ in the presence of the absorbing boundary reads

$$\begin{aligned} \langle t_f \rangle(x_0, r) &= -\int_0^\infty \mathrm{d}t\, t\, \frac{\partial S_r(x_0, t)}{\partial t} = \int_0^\infty \mathrm{d}t\, S_r(x_0, t) \\ &= \tilde{S}_r(x_0, 0) = \frac{\tilde{S}_{\rm BM}(x_0, r)}{1 - r\tilde{S}_{\rm BM}(x_r, r)}; \end{aligned} \tag{1.21}$$

the first line follows from an integration by parts, whereas the second one by substituting Eq. (1.18). To fix the ideas, one may consider that the resetting point $x_r$ coincides with the initial position $x_0$, i.e., $x_r = x_0$, implying that $\langle t_f \rangle$ can be expressed explicitly as

$$\langle t_f \rangle(x_r, r) = \frac{e^{\mu(r)x_r} - 1}{r}. \tag{1.22}$$

Upon increasing resetting rate $r$, particles are localised more and more close to $x_r$, leading to an exponential growth of $\langle t_f \rangle(x_0, r)$. Similarly, for $r \to 0$ the mean-first passage time $\langle t_f \rangle(x_0, r)$ diverges as $r^{-1/2}$ in agreement with the Brownian limit. Between these two divergent limits a minimum appears for the mean first-passage time at the optimal rate $r^*$, such that $\mu(r^*)\, x_r \simeq 1.59$ . To summarize, not only resetting allows the system to reach the target in a finite time, but also to optimize its search. These concepts will be analysed in more details for another stochastic process in Chapter 2.

### 1.2.3 Spatially inhomogeneous resetting

In this Section, by following the strategy of Ref. [179], spatially uniform resetting is extended to the case of a space-dependent resetting rate $r_c(x)$. The probability density $P(x, t|x_0)$ satisfies the Fokker-Planck equation

$$\frac{\partial P(x, t|x_0)}{\partial t} = D\frac{\partial^2 P(x, t|x_0)}{\partial x^2} - r_c(x)P(x, t|x_0) + R(t|x_0)\delta(x - x_r), \tag{1.23}$$

where the gain term is now proportional to

$$R(t|x_0) \equiv \int \mathrm{d}x\, r_c(x) P(x,t|x_0), \tag{1.24}$$

the fraction of particles that are reset at time $t$. In this setting, it is useful to introduce $P_{\rm nc}(x,t|x_0)$, the probability density to reach $x$ at time $t$ from the initial position $x_0$, given that no resetting event has occurred. Accordingly, the probability $P_{\rm nc}(x,t|x_0)$ satisfies Eq. (1.23) without the gain term:

$$\frac{\partial P_{\rm nc}(x,t|x_0)}{\partial t} = D\frac{\partial^2 P_{\rm nc}(x,t|x_0)}{\partial x^2} - r_c(x) P_{\rm nc}(x,t|x_0), \tag{1.25}$$

with initial condition $P_{\rm nc}(x,0|x_0) = \delta(x-x_0)$. As it is reported below, the knowledge of $P_{\rm nc}(x,t|x_0)$ allows one to construct all the statistics of the process.

By means of $P_{\rm nc}(x,t|x_0)$, one can express $P_{\rm res}(t|x_0)$, the probability the first reset event happens at time $t$ given the initial position $x_0$, as

$$P_{\rm res}(t|x_0) = \int_{-\infty}^{+\infty} \mathrm{d}y\, r_c(y)\, P_{\rm nc}(y,t|x_0), \tag{1.26}$$

which corresponds to trajectories with no resetting event until time $t$, when particles reset from their position $y$ with rate $r_c(y)$. By integrating Eq. (1.25) with respect to $x$, one finds an equivalent representation of $P_{\rm res}(t|x_0)$:

$$P_{\rm res}(t|x_0) = -\frac{\partial S_{\rm nc}(t|x_0)}{\partial t}, \tag{1.27}$$

where $S_{\rm nc}(t|x_0) \equiv \int \mathrm{d}x\, P_{\rm nc}(x,t|x_0)$ denotes the fraction of particles that has not reset at time $t$. Indeed, in Eq. (1.27) the probability of first reset $P_{\rm res}(t|x_0)$ is represented as the time variation of particles that have experienced resetting, i.e., $1 - P_{\rm nc}(x,t|x_0)$. Moreover, Eqs. (1.27) and (1.25) allow one to easily check the validity of the normalisation condition $\int_0^\infty \mathrm{d}t\, P_{\rm res}(t|x_0) = 1$.

Once $P_{\rm nc}(x,t|x_0)$ and $P_{\rm res}(t|x_0)$ are known, one can construct the probability density $P(x,t|x_0,x_r)$ by means of renewal theory [179]:

$$\begin{aligned} P(x,t|x_0,x_r) &= P_{\rm nc}(x,t|x_0) + \int_0^t \mathrm{d}\tau \int_{-\infty}^{+\infty} \mathrm{d}y\, r_c(y) P(y,t-\tau|x_0) P_{\rm nc}(x,\tau|x_r) \\ &= P_{\rm nc}(x,t|x_0) + \int_0^t \mathrm{d}\tau R(t-\tau|x_0) P_{\rm nc}(x,\tau|x_r). \end{aligned} \tag{1.28}$$

The first term on the right hand side of Eq. (1.28) corresponds to particles that never reset. The second term accounts for trajectories along which particles reset for the last time in any position $y$ at any intermediate time $t-\tau$ and then restart from $x_r$, subsequently diffusing to $x$ without undergoing resetting within the time interval $(t-\tau, t)$. Operatively, the appearance of time convolution for $P(x,t|x_0,x_r)$ on the right hand side of Eq. (1.28) makes natural to look for its solution in the Laplace transform domain:

$$\tilde{P}(x,s|x_0) = \tilde{P}_{\rm nc}(x,s|x_0) + \tilde{R}(s|x_0)\tilde{P}_{\rm nc}(x,s|x_r), \tag{1.29}$$

where $\tilde{P}_{\rm nc}(x,s|\bullet)$ appears both conditioned to the initial point $x_0$ and the resetting point $x_r$. Equation (1.29) states that the knowledge of $\tilde{R}(s|x_0)$ readily allows one to express $\tilde{P}(x,s|x_0)$. Accordingly, by multiplying Eq. (1.28) by $r_c(x)$ and integrating over $x$, one gets

$$R(t|x_0) = P_{\rm res}(t|x_0) + \int_0^t {\rm d}\tau\, R(t-\tau|x_0) P_{\rm res}(\tau|x_r), \tag{1.30}$$

whose Laplace transform can be expressed in a closed form as

$$\tilde{R}(s|x_0) = \frac{\tilde{P}_{\rm res}(s|x_0)}{1-\tilde{P}_{\rm res}(s|x_r)}. \tag{1.31}$$

Finally, the expression of the Laplace transform of the desired probability density $P(x,t|x_0)$ is obtained by substituting into Eq. (1.29) the expression of $R(\tilde{s}|x_0)$ in Eq. (1.31):

$$\tilde{P}(x,s|x_0) = \tilde{P}_{\rm nc}(x,s|x_0) + \frac{\tilde{P}_{\rm res}(s|x_0)}{1-\tilde{P}_{\rm res}(s|x_r)} \tilde{P}_{\rm nc}(x,s|x_r). \tag{1.32}$$

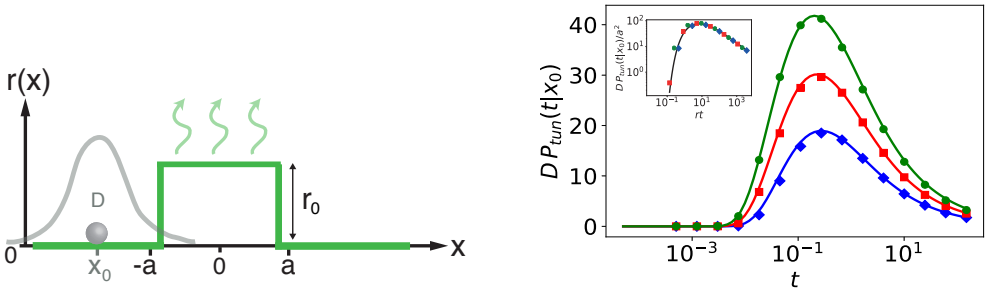
One can check the normalization condition $\int_{-\infty}^{+\infty} {\rm d}x\, \tilde{P}(x,s|x_0) = 1/s$ by considering the Laplace transform of Eq. (1.27), i.e., $\tilde{S}_{\rm nc}(s|x_0) = \left[1-\tilde{P}_{\rm res}(s|x_0)\right]/s$. Summarizing, the knowledge of $\tilde{P}_{\rm res}(x,s|x_0)$ allows one to compute the first reset probability $\tilde{P}_{\rm res}(s|x_0) = 1 - s\tilde{S}(s|x_0)$, and finally $\tilde{P}(x,s|x_0)$ from Eq. (1.32). In the next Section, we apply the analytic procedure presented here for a significant choice of $r_c(x)$.

## 1.3 Controlling diffusion

Now that we have recalled some well-known results on diffusion with stochastic resetting and the necessary analytical tools to study the generic case of space-inhomogeneous resetting rate, we have all the ingredients to propose and to investigate our model. We consider a single one-dimensional Brownian particle, with diffusion coefficient $D$ and initial position $x(t=0) = x_0$. Within the time interval $[t, t+{\rm d}t]$ with $t \geq 0$, the particle at position $x(t)$ can either diffuse, or, be controlled by an external agent with a probability $r_c(x(t)){\rm d}t$ that depends on its current $x(t)$ position. We consider two types of control mechanisms, labelled by the parameter $\sigma_c$: (i) no control or evaporation ($\sigma_c = 0$), which annihilates the particle; and (ii) resetting ($\sigma_c = 1$), which moves instantaneously the particle to a prescribed position $x_r$ that may be different from $x_0$. The conditional probability density $P(x,t|x_0)$ of the particle position $x$ at time $t$ obeys the Fokker-Planck in Eq. (1.4) with source term parametrized by $\sigma_c$:

$$\frac{\partial P(x,t|x_0)}{\partial t} = D\frac{\partial^2 P(x,t|x_0)}{\partial x^2} - r_c(x)P(x,t|x_0) + \sigma_c R(t|x_0)\delta(x-x_r). \tag{1.33}$$

Indeed, in the case of resetting $\sigma_c = 1$, Eq. (1.33) coincides with Eq. (1.23) of Subsec. 1.2.3. For $\sigma_c = 0$ where no control is exerted on the system, particles evaporate with rate $r_c(x)$. In this case, Eq. (1.33) reduces to Eq. (1.25), meaning that the probability density of a Brownian particle evaporating with rate $r_c(x)$ coincides with the probability density $P_{\rm nc}(x,t|x_0)$ of no resetting with




(a) (b)

Figure 1.2: **Diffusion with evaporation within a finite region (Brownian tunnelling). (a)** Sketch of the model: a Brownian particle (gray sphere) moves in one spatial dimension from an initial position $x_0$, with diffusion coefficient $D$. The particle evaporates (light green arrows) with rate $r$ only from a spatial window $[-a, a]$, i.e., with the evaporation rate $r(x)$ in Eq. (1.34) (green line). **(b)** Fraction of "tunnelled" particles $P_{\rm tun}(t|x_0)$ (multiplied by $D$) at time $t$ that survived evaporation by reaching the region $x \geq a$: results from numerical simulations (thick lines) and analytical calculations (solid lines). Here $x_0 = -3.2$, $r = 25$, $D = 200$ (green), 150 (red), 100 (blue) and $a = 0.05 \times \sqrt{D}$ respectively. Simulations were done using the Euler integration scheme (see Appendix A) with time step $\Delta t = 5 \times 10^{-4}$, and $N = 10^4$ runs. The inset shows the collapse of the three curves in dimensionless units.

same rate $r_c(x)$. In particular, we consider a control exerted on the particle at a rate $r$ only when the particle is located within the interval $[-a, a]$, i.e.,

$$r_c(x) = r\,\theta(a - |x|), \tag{1.34}$$

where $\theta$ is the Heaviside step function. This choice of the resetting profile turns out to be more realistic for experimental realizations [211, 22] with respect to the ideal, spatially homogeneous case, which can be retrieved for $a \to \infty$. We will discuss in the following sections a collection of transport phenomena described by Eqs. (1.33) and (1.34), together with appropriate boundary conditions introduced below. The general procedure to solve Eq. (1.33) is reported in Appendix B.1.

### 1.3.1 Brownian tunnelling ($\sigma_c = 0$)

We first consider a minimal model – which we call "Brownian tunnelling" – given by a Brownian particle moving in one dimension and subject to the evaporation rate in Eq. (1.34), see Fig. 1.2a. Its Fokker-Planck, i.e., Eq. (1.33) with $\sigma_c = 0$, corresponds to a Schrödinger equation $i\hbar\partial_\tau \Psi_\tau(x) = -(\hbar^2/2m)\partial_x^2 \Psi_\tau(x) + V(x)\Psi_\tau(x)$, in imaginary time $\tau = -it$, with effective mass $m = \hbar/2D$ and effective quantum barrier potential $V(x) = \hbar\, r_c(x)$ [179]. We derive and report the Laplace transform of the solution $P_{\rm nc}(x, t|x_0)$ of Eq. (1.33) in Appendix B.2. Building on the analogy with tunnelling through a quantum barrier, we compute the probability $P_{\rm tun}(t|x_0) \equiv \int_a^\infty {\rm d}x\, P_{\rm nc}(x, t|x_0)$ for a particle starting at $x_0 < -a$ to be found at any point $x > a$ at time $t$, i.e., the probability for a Brownian particle to "tunnel" through the evaporation window. In particular, we derive the

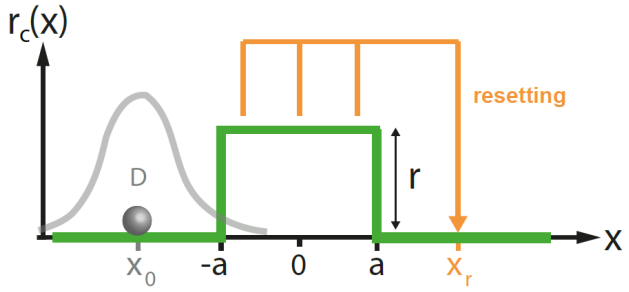



Figure 1.3: **Diffusion with stochastic resetting from an interval**. A Brownian particle (gray sphere) diffuses with diffusion coefficient $D$ from its initial position $x_0$, and it undergoes resetting at rate $r$ from the interval $[-a, a]$ to a resetting destination $x_r$.

analytical expression for the Laplace transform $\tilde{P}_{\rm tun}(s|x_0)$ of the Brownian tunnelling probability:

$$\tilde{P}_{\rm tun}(s|x_0) = \frac{(\nu/D\mu)\exp\left[(a+x_0)\mu\right]}{2\mu\nu\cosh\left(2a\nu\right) + (\mu^2+\nu^2)\sinh\left(2a\nu\right)}, \tag{1.35}$$

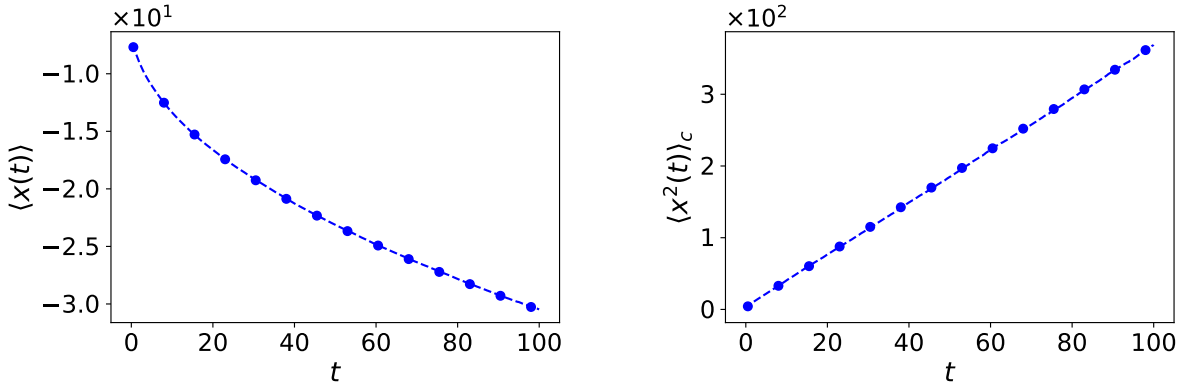
with $\mu$ introduced in Eq. (1.10), and $\nu \equiv \sqrt{(s+r)/D}$. Equation (1.35) suggests a natural set of dimensionless quantities:

$$y \equiv \frac{x}{a}, \quad y_r \equiv \frac{x_r}{a}, \quad \tau_r \equiv rt, \quad \text{and} \quad \rho \equiv a\sqrt{\frac{r}{D}}. \tag{1.36}$$

In Fig. 1.2b we show the comparison between numerical simulations for $P_{\rm tun}(t|x_0)$ and the numerical inverse Laplace transform of Eq. (1.35). Upon rescaling variables, the rescaled tunnelling probability $P_{\rm tun}(t|x_0) \times D/a^2$ depends only on one parameter $\rho$ and the variables $\tau_r$ and $y_r$ (Fig. 1.2b inset). Furthermore, Eq. (1.35) provides information on the long-time limit and moments of $P_{\rm tun}(t|x_0)$ by considering the series expansion of $\tilde{P}_{\rm tun}(s|x_0)$ for small $s$, for which we obtain $\tilde{P}_{\rm tun}(s|x_0) = [\sqrt{s\,r}\sinh(2\rho)]^{-1} + O(s^0)$. The presence of half-integer powers implies that the integer moments of the tunnelling probability diverge, due to the existence of many trajectories that never cross the resetting region [172]. In fact, for large times and arbitrary $x_0$, $P_{\rm tun}(t|x_0) \sim t^{-1/2}$, which coincides with the long-time behaviour of the first-passage time survival probability of a one-dimensional Brownian particle in Eq. (1.20).

### 1.3.2 Minimal diffusivity for a resetting interval ($\sigma_c = 1$)

We now consider an extension of the preceding problem, where the particle undergoing evaporation, discussed in Sec. 1.3.1, is actually instantaneously reset to a given position $x_r$, see Fig. 1.3 for an illustration. The dynamics of the probability density $P(x,t|x_0)$ of the particle position is described by Eqs. (1.33) and (1.34) with $\sigma_c = 1$, for which we derive an analytical solution in the Laplace domain (see Appendix B.2). We point out two main features of the resulting distribution: the existence of a cusp at $x_r$ [70, 71] at all times, and the absence of a stationary state due to the long-time prevalence of diffusion over resetting. Motivated by this observation, we investigate the




(a) (b)

Figure 1.4: **Brownian tunnelling with resetting.** Comparison between numerical simulation (dashed line) and inverse Laplace transform of the analytical prediction (symbols) of the time evolution of the average $\langle x(t)\rangle$ (panel **(a)**) and variance $\langle x^2(t)\rangle_c$ (panel **(b)**) of the particle position with parameters $D = 5$, $a = 5$, $r = 2.5$ and $x_0 = x_r = -7.5$. Simulations are performed with a time step $\Delta t = 0.01$, for $N = 10^5$ trajectories. Error bars, given by the standard deviation over the ensemble average, are not visible on the plot scale.

long-time behaviour of the particle distribution moments. In particular, we quantify the drift and the amplitude of fluctuations via the mean position $\langle x(t)\rangle$ and the variance $\langle x^2(t)\rangle_c \equiv \langle x^2(t)\rangle - \langle x(t)\rangle^2$. We calculate the Laplace transform of $\langle x(t)\rangle$, and of $\langle x^2(t)\rangle_c$ from the probability density $\tilde{P}(x,t|x_0)$ in Appendix B.2. Their expressions are too long and not very particularly instructive to be reported here; for this reason we discuss only their long-time behaviour, derived by considering the leading contribution of their Laplace transform for $s \to 0$. In Fig. 1.4, we represent the time evolution of $\langle x(t)\rangle$ and $\langle x^2(t)\rangle_c$ at short and long times.

At short times, until resetting kicks in, $\langle x(t)\rangle$ is constant as in Brownian diffusion. At longer times, $\langle x(t)\rangle$ grows $\propto \sqrt{t}$ as

$$\langle x(t)\rangle = \mathrm{sign}(y_r)\sqrt{\frac{4Dt}{\pi}}\,\phi(y_r,\rho) + O(t^0), \tag{1.37}$$

where

$$\phi(y_r,\rho) \equiv \begin{cases} \tanh(\rho)\,\frac{\tanh(\rho)+\rho(|y_r|-1)}{\rho\tanh(\rho)(|y_r|-1)+1} & \text{for } |y_r|>1, \\ \tanh(\rho)\tanh(|y_r|\rho) & \text{for } |y_r|<1, \end{cases} \tag{1.38}$$

with $y_r$ and $\rho$ given by Eq. (1.36).

Notably, a similar behaviour emerges also without resetting by introducing a reflecting boundary (RB) at $x = 0$. The probability distribution of a Brownian particle with a reflecting boundary at $x = 0$ reads [105]

$$P_{\mathrm{RB}}(x,t|x_0) = \frac{\exp\left[-\frac{(x-x_0)^2}{4Dt}\right]}{\sqrt{Dt\pi}\left(1+\mathrm{erf}\left(\frac{|x_0|}{2\sqrt{Dt}}\right)\right)}. \tag{1.39}$$

The long-time limit of the first moment $P_{\rm RB}(x,t|x_0)$ is given by

$$\langle x_{\rm RB}(t)\rangle = 2\,\mathrm{sign}(x_0)\sqrt{\frac{Dt}{\pi}} + O(t^0), \tag{1.40}$$

while its variance

$$\langle x^2_{\rm RB}(t)\rangle_c = 2Dt\left(1-\frac{2}{\pi}\right) + O(\sqrt{t}), \tag{1.41}$$

where the initial position $x_0$ of the particle plays formally the role of $x_r$ in Eq. (1.37).

Because $|\phi(y_r,\rho)|<1$, resetting acts as a weaker reflecting boundary, whose efficiency depends on the dimensionless variables $\rho$ and $y_r$. Due to the recurrence property of one-dimensional Brownian motion, even for $|y_r|\gg 1$, a fraction of particles eventually reach the resetting region and is pushed back to $x_r$: the larger $x_r$ is, the longer the time is the particles spend in the half plane containing $x_r$. Accordingly, the maximum value $\phi(y_r,\rho)=1$, corresponding to a reflecting boundary limit, is attained for $|y_r|\to\infty$.

The analytical expression for the variance turns out to have a diffusive long-time behaviour $\langle x^2(t)\rangle_c \propto t$. In fact, these particles diffuse without displaying a Gaussian distribution, a phenomenon that has recently attracted considerable attention in statistical physics and which is known as *Brownian yet non-Gaussian* diffusion [48, 42, 204, 136], see Fig. 1.5a. At long times, we may define an effective diffusion coefficient $D_{\rm eff} \equiv \lim_{t\to\infty}\langle x^2(t)\rangle_c/2t$, which generically differs from the diffusion coefficient $D$ [174, 162]. For this model, we have

$$\frac{D_{\rm eff}}{D} = 1-\frac{2}{\pi}\phi^2(y_r,\rho), \tag{1.42}$$

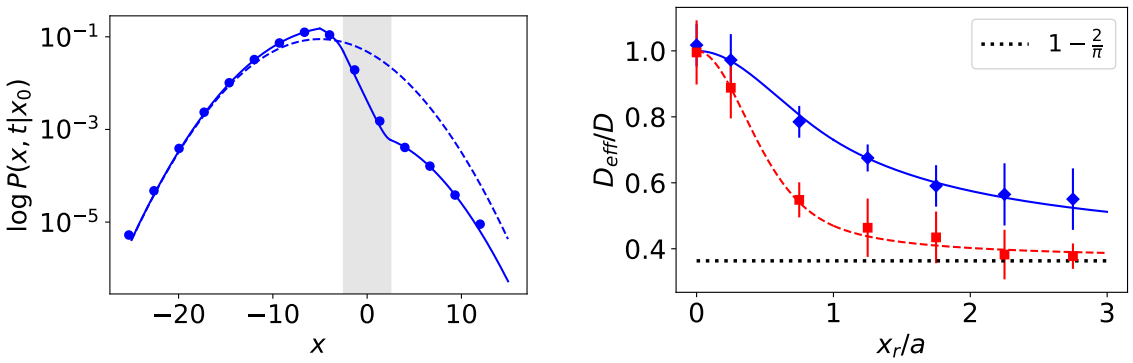
which depends only on the dimensionless variables $y_r$ and $\rho$ in Eq. (1.36), encoding the actual dependence on the width $a$ and the ratio $r/D$. An interesting feature of $D_{\rm eff}$ is that it is bounded from above by its maximum value $D_{\rm eff}^{\rm max}=D$, which is obtained under symmetric resetting $y_r=0$, while its minimum value is attained for large $|y_r|$:

$$1-\frac{2}{\pi} < \frac{D_{\rm eff}}{D} \le 1. \tag{1.43}$$

Resetting prevents the particles from diffusing freely, implying $D_{\rm eff}\le D$. On the other hand, Eq. (1.43) reveals the existence of a lower bound $D_{\rm eff}^{\rm min} = D(1-2/\pi)$ for the effective diffusion coefficient, coinciding with the value for a Brownian particle diffusing in the presence of a reflecting wall in Eq. (1.41). Figure 1.5b confirms the lower bound in Eq. (1.43) with numerical simulations of the present model, for various values of the involved parameters. In addition, we have checked numerically that the same qualitative behaviour, i.e., a *Brownian yet non-Gaussian* diffusion, occurs even when the resetting profile is made by the union of disjoint intervals of various lengths (data not shown). Moreover, one can recover the correct analytical predictions for the delta-like resetting rate $r_c(x)=r_0\delta(x)$ by setting $r=r_0/2a$ in Eqs. (1.33) and (1.34) and by taking the limit $a\to 0$.

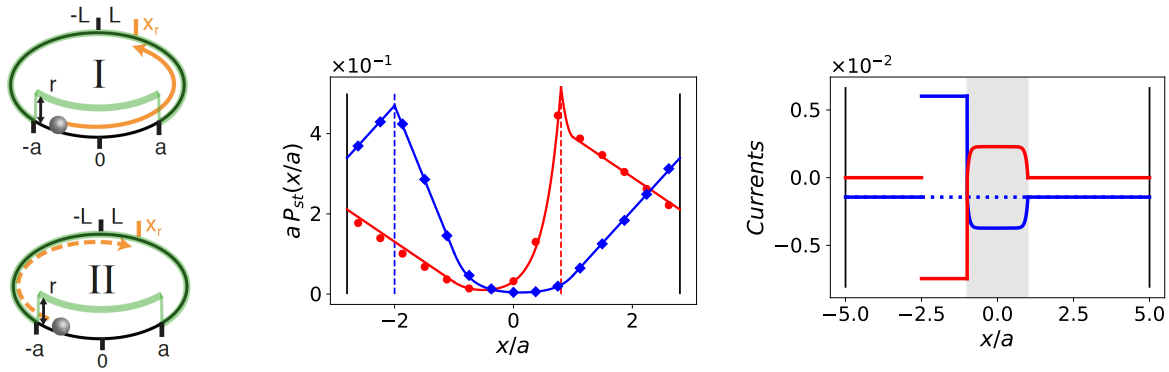
## 1.4 Resetting gauge invariance on a ring

Let us now consider the Brownian particle diffusing on the segment $(-L,L)$ with periodic boundary conditions (e.g., on a ring of perimeter $2L$) which, with a constant rate $r$, experiences resetting




(a) (b)

Figure 1.5: **Brownian yet non-Gaussian diffusion induced by resetting.** **(a)** Probability density $P(x,t|x_0)$ for a Brownian particle to be at position $x$ at time $t = 10$ with $D = 1$, $r = 1.0$, $a = 2.5$, $x_0 = x_r = -5$, for the model in Fig. 1.3: numerical simulations (symbols), numerical inverse Laplace transform of Eq. (B.8) (solid line), and exact (Gaussian) distribution in the absence of resetting, i.e., $r = 0$ (dashed line). The grey shaded area highlights the interval where resetting occurs. The numerical simulations were done using the Euler numerical integration scheme with time step $\Delta t = 0.05$, and $N = 10^5$ runs. **(b)** Effective diffusion coefficient $D_{\rm eff} = \lim_{t\to\infty}\langle x^2(t)\rangle_c/2t$, with $\langle x^2(t)\rangle_c$ the variance of the position, in units of the "bare" diffusion coefficient $D$, as a function of the normalized resetting point $y_r = x_r/a$. The simulations (symbols) and the analytical expression in Eq. (1.42) (solid lines) correspond to $\rho \simeq 1.12$ realized with $r = 2.5$, $a = 5$, $D = 50$ (blue diamonds and solid line) and $\rho \simeq 1.89$ realized with $r = 5$, $a = 5$, $D = 35$ (red squares and dashed line). The horizontal dotted line indicates the theoretical lower bound predicted by Eq. (1.43). The simulations were done using Euler's numerical integration scheme with time step $\Delta t = 5 \times 10^{-2}$, time duration $t = 10^3$ and $N = 10^5$ runs.




(a) (b) (c)

Figure 1.6: **Diffusion with stochastic resetting on a ring** according to different protocols (resetting "gauge invariance"). **(a)** Sketch of two resetting protocols: the particles are reset to a fixed destination $x_r > 0$ at a rate $r$ only when located in the window $[-a, a]$. Top (model I): resetting moves the particle along the path that does not cross the endpoints $\pm L$. Bottom (model II): resetting occurs via the path of minimal distance between the positions before and after resetting. **(b)** Numerical results for the stationary spatial distribution for $y_r = x_r/a = -2$ (blue diamonds) and $y_r = 0.8$ (red circles), compared with the corresponding analytical predictions (solid lines, see Appendix B.3) with $D = 50$, $r = 1$, $a = 25$, $L = 70$. **(c)** Space-dependent decomposition of the total stationary current $J(x) = J_{\rm diff}(x) + J_{\rm res}(x)$ (dotted line) as a function of the normalized position $y = x/a$ for the model II: diffusive current $J_{\rm diff}(x)$ (blue line) and resetting current $J_{\rm res}(x)$ (red line). With $\rho = 15.0$, $y_r = -2.5$ and $l = L/a = 5$. A discontinuous jump of both $J_{\rm diff}(x)$ and $J_{\rm res}(x)$ occurs at $x = x_r$. In all the panels, numerical results are obtained from $N = 10^5$ simulations with time step $\Delta t = 0.1$ while the gray area corresponds to the resetting region.

to a point $x_r$ when its position is within the interval $(-a, a)$ with $a < L$, see Fig. 1.6a for an illustration. Periodic boundary conditions ensure the existence of a non-equilibrium stationary state, which induces a stationary probability distribution for the particle position. This distribution displays a cusp, (global maximum) at $x_r$ [70, 71], and it is shown in Fig. 1.6b, where we compare analytical (see Appendix B.3) and numerical results for $P(x, t|x_0)$ for various values of the relevant parameters. Importantly, in order to characterize resetting on the ring, one needs to specify the physical direction of the particle flux arising from it. In this framework, it is often assumed that particles, once reset, reach $x_r$ instantaneously, i.e., in a teleporting fashion, without specifying *how* this actually occurs. For example, on a ring, particles may reset by moving always clockwise, always counterclockwise or in both directions. The one-time statistics of the particle position is a physical observable quantity whose distribution $P(x, t|x_0)$ is actually independent of how resetting occurs, as long as it is instantaneous. On the other hand, local and conserved particle currents arise in ring-like geometries and their values depend on the specific resetting rule. In this spirit, it is natural to define a *resetting current* $J_{\rm res}(x, t)$ by integrating the right-hand side of Eq. (1.33):

$$J_{\rm res}(x,t) - J_{\rm res}(-L,t) = \int_{-L}^{x} {\rm d}y\, r_c(y) P(y,t|x_0) - \theta(x - x_r) R(t|x_0). \tag{1.44}$$

The space-dependent current $J_{\rm res}(x, t)$ is defined up to the spatial constant $J_{\rm res}(-L, t)$, which stems from the gauge freedom in the choice of the specific protocol according to which resetting actually occurs. Thus, the total probability current

$$J(x,t) \equiv J_{\rm res}(x,t) + J_{\rm diff}(x,t), \tag{1.45}$$

with $J_{\rm diff}(x, t) = -D\partial_x P(x, t|x_0)$, obeys the continuity (Fokker-Planck) Eq. (1.33), which can be cast in the form $\partial_t P(x, t|x_0) = -\partial_x J(x, t)$. Note that as long as resetting is instantaneous, the particle diffusive dynamics is insensitive to how resetting occurs. Consistently, $P(x, t|x_0)$ — and hence $J_{\rm diff}(x, t)$ — does not depend on the details of the resetting protocol, while $J_{\rm res}$ — and hence $J(x, t)$ — does depend by an overall possibly time-dependent spatial constant. In the stationary state, the total current $J(x, t)$ either vanishes, as it happens in infinite systems, or becomes space-independent, while $J_{\rm res}$ and $J_{\rm diff}$ are generically space-dependent, as shown in Fig. 1.6c (see Appendix B.3). Thus, we have gauge invariance in both stationary and non-stationary regimes: many different currents, corresponding to the different reset protocols, refer to the same spatial probability distribution.

### 1.4.1 Resetting current

We now show how to interpret the resetting current $J_{\rm res}$ in Eq. (1.44) in terms of *physical* fluxes of resetting particle. The resetting current $J_{\rm res}$ depends on the region of space where particles are reset. In this spirit, we introduce $R_a(x_1, x_2; t)$, the fraction of particles that reset in a generic interval $x_1 < x < x_2$ at time $t$, i.e.,

$$R_a(x_1, x_2; t) \equiv \int_{x_1}^{x_2} {\rm d}y\, r_c(y) P(y, t|x_0); \tag{1.46}$$

in what follows we omit the $t$-dependence. It is then natural to split $R_a$ in two contributions: $R_a^l$ the fraction of particles resetting clockwise (leftward), and $R_a^r$ those resetting counterclockwise

(rightward), such that

$$R_a(x_1, x_2) = R_a^l(x_1, x_2) + R_a^r(x_1, x_2). \tag{1.47}$$

Note that, while $R_a(x_1, x_2)$ is independent of the choice of the resetting protocol, its decomposition in $R_a^{r,\,l}(x_1, x_2)$ is. Indeed, fixing the resetting protocol is equivalent to prescribe the amount of particles that contribute to rightward and leftward $R_a^{r,l}$ to $J_{\rm res}$. Thereafter, provided a specific protocol, we address the problem of expressing the current $J_{\rm res}$ in terms of $R_a^{r,\,l}$.

First, we investigate the case in which $x_r \in (-L, -a)$. In order to determine the expression of the current $J_{\rm res}$ one has to consider contributions from the different regions of space:

(i) The current of reset particles through a generic point $x$ within the region $(-L, x_r)$ is only due to right-moving particles crossing the boundary point $L$ and, due to periodic boundary condition, come back from $-L$ to $x_r$. Instead, left-moving particles stops at $x_r$ without crossing any point in $(-L, x_r)$. We refer to Fig. 1.7a for a pictorial representation of the current contributions. It follows that the current $J_{\rm res}$ will be positive (right-moving) and equal to

$$J_{\rm res}(x, t) = R_a^r(-a, a). \tag{1.48}$$

(ii) Analogously, the current through the region $(x_r, -a)$ is only due to left-moving particles. Right-moving particles cross the boundary $L$ and come back from $-L$ to $x_r$ without reaching the region $(x_r, -a)$. This scenario is sketched in Fig. 1.7b: the current is negative (left-moving) and given by

$$J_{\rm res}(x, t) = -R_a^l(-a, a). \tag{1.49}$$

(iii) In the region $(-a, a)$, refer to Fig. 1.7c, left-moving and right-moving particles contribute to the flux, whose magnitude depends on the position at which the current is gauged: the left contribution to $J_{\rm res}$ come from the fraction particles $R_a^l$ resetting in $(x, a)$ while the right one $R_a^r$ from the region $(-a, x)$, yielding

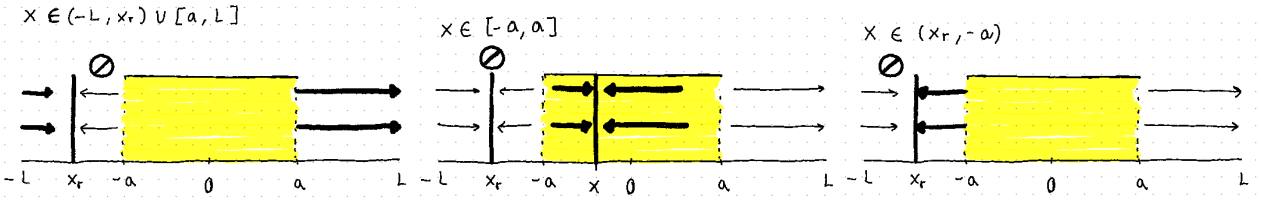
$$J_{\rm res}(x, t) = R_a^r(-a, x) - R_a^l(x, a). \tag{1.50}$$

(iv) In the region $(a, L)$ the current is the same as in $(-L, x_r)$ because of periodic boundary conditions.

Finally, collecting Eqs. (1.48), (1.49) and (1.50), if the resetting point $x_r$ belongs to the interval $x_r \in (-L, -a)$, the current $J_{\rm res}(x, t)$ across the point $x$ at time $t$ is given by

$$J_{\rm res}(x, t) = \begin{cases} R_a^r(-a, a) & \text{for } x \in [-L, x_r) \cup [a, L], \\ -R_a^l(-a, a) & \text{for } x \in (x_r, -a], \\ R_a^r(-a, x) - R_a^l(x, a) & \text{for } x \in (-a, a). \end{cases} \tag{1.51}$$

Note that the resetting current $J_{\rm res}(x)$ as a function of $x$ is discontinuous in $x_r$ at all times. This is due to the fact that once resetting particles reach $x_r$ they stop. This discontinuity explains




(a) (b) (c)

Figure 1.7: **Resetting current.** Pictorial representation of the contribution to the resetting current $J_{\rm res}(x)$ in the case of $x_r < -a$. The yellow area corresponds to the resetting region in which the resetting current $J_{\rm res}$ originates. Horizontal arrows correspond to particles moving towards the resetting point $x_r$ in the two possible directions (left-moving and right-moving): thick arrows represent particle currents that contribute to $J_{\rm res}$ while thin ones to the particles that reach $x_r$ without crossing ("stop" sign) the region in which we compute the current.

the presence of a cusp in the probability density at $x_r$ [70, 71]. Moreover, one can easily check that Eq. (1.51) is equivalent to Eq. (1.44) by identifying $J_{\rm res}(-L,t) = R^r_a(-a,a)$. Therefore, choosing a resetting protocol is equivalent to fixing the value of the current at a given point in space. In practice, one may compute once for all $J_{\rm res}(x) - J_{\rm res}(-L)$ which depends only on $P(x,t|x_0)$ and then determine explicitly the value $J_{\rm res}(-L)$ for the resetting protocol adopted in that specific case.

Analogously, it is easy to check that the current $J_{\rm res}$ , in the case $x_r \in (-a,a)$, coincides with

$$J_{\rm res}(x,t) = \begin{cases} R^r_a(x_r,a) - R^l_a(-a,x_r) & \text{for } |x| \in [a,L], \\ R^r_a(x_r,x) + R^r_a(x_r,a) - R^l_a(x,x_r) & \text{for } x \in (-a,x_r), \\ R^r_a(x_r,x) - R^l_a(x,a) - R^l_a(-a,x_r) & \text{for } x \in (x_r,a), \end{cases} \tag{1.52}$$

with $J_{\rm res}(-L,t) = R^r_a(x_r,a) - R^l_a(-a,x_r)$.

The current $J_{\rm res}$ for $x_r > a$ can be obtained from the value of $J_{\rm res}$ for $x_r < -a$ by making the following change of variables: $x \leftrightarrow -x$, $x_r \leftrightarrow -x_r$ and $l \leftrightarrow r$.

In the stationary state, the total current $J$ in Eq. (1.45) is independent of time and space, hence, the expression

$$J - J_{\rm res}(-L) = J_{\rm diff}(x) + [J_{\rm res}(x) - J_{\rm res}(-L)], \tag{1.53}$$

is constant and independent of the resetting protocol. We can therefore reconstruct the value of the total current $J$ by computing $J - J_{\rm res}(-L)$ according to Eq. (1.45) and Eq. (1.44) and then add $J_{\rm res}(-L)$ for the specific protocol. Note that in the stationary state $J_{\rm diff}(x) + J_{\rm res}(x)$ is also independent of $x$. The expression of $J - J_{\rm res}(-L)$, computed by plugging Eqs. (B.18) and (B.22) in Eqs. (1.45) and (1.44), as a function of the resetting point is

$$\frac{J - J_{\rm res}(-L)}{r} = \begin{cases} \frac{\sinh\rho \sinh(y_r\rho)}{2[(\ell-1)\rho\cosh(y_r\rho)+\sinh\rho][(\ell-1)\rho\cosh\rho+\sinh\rho]} & \text{for } |y_r| \le 1, \\ \frac{\mathrm{sign}(y_r)\sinh\rho[\sinh\rho-\rho(1-|y_r|)\cosh\rho]}{[(\ell-1)\rho\cosh\rho+\sinh\rho][2(\ell-1)\rho\cosh\rho+(2+\rho^2(1-2\ell+|y_r|)(1-|y_r|))\sinh\rho]} & \text{for } |y_r| > 1, \end{cases} \tag{1.54}$$

where $y_r = x_r/a$ and $\ell \equiv L/a$. Equation (1.54) can also be seen as the stationary current corresponding to $J_{\rm res}(\pm L) = 0$, i.e., the resetting protocol which assumes particles to reset without

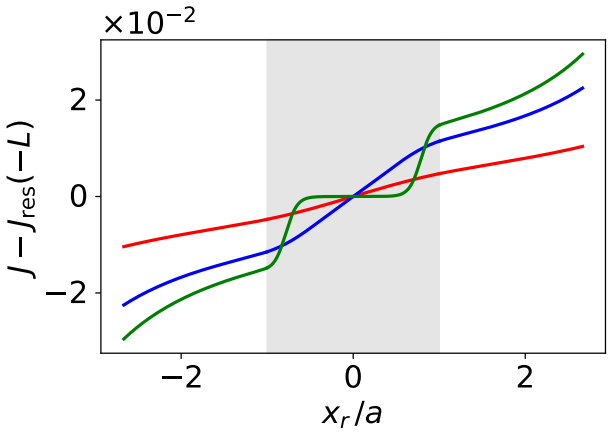



Figure 1.8: $J_{\rm res}(L) = 0$ **protocol.** Stationary current $J - J_{\rm res}$ in Eq. (1.54) as a function of the normalized position of the resetting point $x_r/a$ and for various values of $r = 0.1$ (red), 1.0 (blue), 20 (green) and with $D = 5$, $a = 7.5$ and $L = 20$. The grey area corresponds to the resetting region.

crossing the points $x = \pm L$, see Model I in Fig. 1.6a. The latter displays robust qualitative features in its dependence on the resetting destination $x_r$, see Fig. 1.8: with $x_r$ outside (inside) the resetting region compared to the typical values outside it, i.e., $|x_r| > a$ ($|x_r| < a$), $J$ increases (decreases) upon increasing (decreasing) the resetting rate $r$, because resetting induces particles to be concentrated in a region with low (high) local resetting rate. As a result, the current is exponentially suppressed upon increasing $r$ inside the resetting region, inducing a discontinuity at $x = \pm a$ for $r \to \infty$.

In the following Sections, we make two examples of specific protocol choice for which we explicitly compute $J_{\rm res}(-L)$ in order to compute the total stationary current $J$ through Eqs. (1.53) and (1.54).

### 1.4.2 Minimal path protocol

As first example, we consider the *minimal path* protocol: upon resetting, the particle $x_r$ along the trajectory that minimizes the distance between its current location $x$ and $x_r$, i.e., the path of length $\min(|x - x_r|, 2L - |x - x_r|)$. The visual representation of the protocol is shown in Model II of Fig. 1.6a . Let us indicate by $l_1$ the path of length $|x_r - x|$ and $l_2$ the path of length $2L - |x - x_r|$. Our aim is to evaluate the value of the current $J_{\rm res}(-L)$, which fixes the value of $J_{\rm res}(x, t)$. This resetting protocol naturally distinguishes two regions that can contribute to the resetting current:

(i) First, we consider contribution to $J_{\rm res}(-L)$ which come from particles resetting from position $x \in (x_r, L)$, keeping in mind that resetting is possible only for $|x| < a$. Under this hypothesis, $l_1$ satisfies the minimal path condition if the resetting particles come from the region $x \in (x_r, L + x_r)$, while $l_2$ does for those coming from $x \in (L + x_r, L)$ ($x_r$ can be negative). In order to understand how particles reset to the left or the right it is necessary to study the problem by distinguishing the possible choices of $x_r$.

If $x_r \in (-L, -a)$, see Fig.1.9a, the contribution to the current in $\pm L$ is given by particles

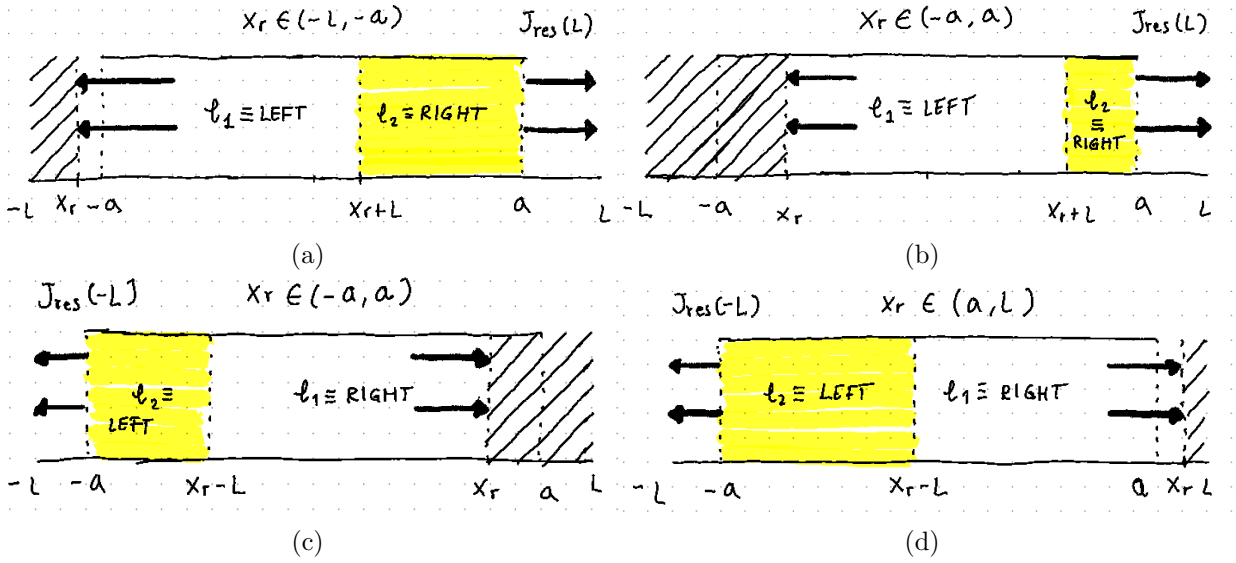


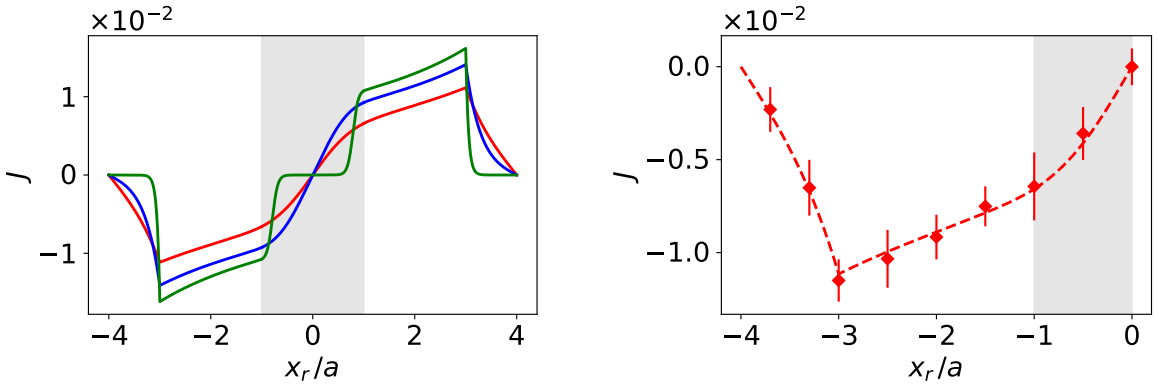

Figure 1.9: **(a) and (b): Minimal path protocol for $x \in (x_r, L)$.** Schematic representation of the contribution to the current $J_{\rm res}(-L)$ from particles resetting in the region $(x_r, L)$ according to the minimal path protocol, the forbidden complementary region $(-L, x_r)$ is denoted by oblique lines. In both cases $x_r \in (-L, -a)$, panel **(a)**, and $x_r \in (-a, a)$, panel **(b)**, the protocol identifies two distinct regions: the yellow shaded region $(x_r + L, a)$ refers to the particles resetting following $l_2$ (right-moving) and the white region $(-a, x_r + L)$ following $l_1$ (left-moving). The resetting particles, horizontal arrows, that contribute to the current $J_{\rm res}(-L)$ are only those following $l_2$. **(c) and (d): Minimal path protocol for $x \in (-L, x_r)$.** Schematic representation of the contribution to the current $J_{\rm res}(-L)$ from particles resetting in the region $(-L, x_r)$ according to the minimal path protocol, the forbidden complementary region $(x_r, L)$ is denoted by oblique lines. In both cases $x_r \in (-a, a)$, panel **(c)**, and $x_r \in (a, L)$, panel **(d)**, the protocol identifies two distinct regions: the yellow shaded region $(-a, x_r - L)$ refers to the particles resetting following $l_2$ (left-moving) and the white region $(x_r - L, a)$ following $l_1$ (right-moving). The resetting particles, horizontal arrows, that contribute to the current $J_{\rm res}(-L)$ are only those following $l_2$.

resetting to the right, since all those resetting leftward stop at $x_r$ before reaching $\pm L$. For this specific case, particles that follow $l_1$ are left-moving while those following $l_2$ are right-moving. Therefore, we identify the current $J_{\rm res}(-L)$ with the flux of particles resetting rightward. Accordingly, the value of the current $J_{\rm res}(-L) = R_a(x_r + L, a)$ is associated to $l_2$. Note that Eq. (1.46) implies that $J_{\rm res}(-L)$ vanishes for $x_r + L \geq a$.

Also for $x_r \in (-a, a)$, see Fig.1.9b, particles that move to the left are those that reset along $l_1$ and do not contribute to the current. The right-moving resetting particles, associated to $l_2$, contribute by a term $R_a(x_r, L)$.

If $x_r > a$ there is no contribution to the resetting current, due to the initial hypothesis $x > x_r$.

(ii) If we consider the contribution to $J_{\rm res}(-L)$ of particles resetting from $x \in (-L, x_r)$, the path $l_1$ satisfies the minimal path condition if resetting takes place within the interval $x \in (x_r - L, x_r)$




(a) (b)

Figure 1.10: **Minimal path protocol. (a)** Total stationary current $J = J_{\rm diff} + J_{\rm res}$ as a function of $x_r/a$ and for various of $r = 0.5$ (red), 2.5 (blue), 75 (green) and with $D = 5$, $a = 5$ and $L = 20$ according the minimal path protocol. **(b)** Comparison between the analytic prediction for $J$ (red curve in panel (a)) and the numerical simulations (red symbols with error bars). The grey shaded area corresponds to the resetting region. Simulations were done using the Euler numerical integration scheme with time step $\Delta t = 0.5$, and they were repeated $N = 10^5$ times.

while $l_2$ within $x \in (-L, x_r - L)$. If $x_r \in (-L, -a)$ there is no contribution to the resetting current: $x$ is outside of the resetting region. If $x_r \in (-a, a)$, see Fig. 1.9c, we are interested in left-moving particles through $l_2$ resetting in the region $x \in (-a, x_r - L)$, contributing to the current with $-R_a(-a, x_r - L)$. Analogously, if $x_r \in (a, L)$, see Fig. 1.9d, the contribution to the resetting current is given by $-R_a(-a, x_r - L)$.

Finally, taking into account all the contributions discussed above, the value of the resetting current at $\pm L$ reads

$$J_{\rm res}(-L,t) = \begin{cases} R_a(x_r + L, a) & \text{for } x_r \in (-L, -a), \\ R_a(x_r + L, a) - R_a(-a, x_r - L) & \text{for } x_r \in [-a, a], \\ -R_a(-a, x_r - L) & \text{for } x_r \in (a, L). \end{cases} \tag{1.55}$$

All the information of the minimal path protocol are contained in Eq. (1.55). Indeed, we recover the total current $J(x,t)$ by substituting the expression of $J_{\rm res}(\pm L)$ in Eq. (1.53).

For completeness, we report the stationary values of the various $R_a$ contributions appearing in Eq. (1.55) as a function of $x_r$; they are calculated integrating $P_{\rm st}(x)$ in Eqs. (B.18) and (B.22). To lighten the notation, we introduce the dimensionless flux $r_a(y_1, y_2) \equiv R_a(x_1 \equiv a y_1, x_2 \equiv a y_2)$, as a function of the dimensionless parameters $y_r$, $\rho$, and $\ell$. The dimensionless version of the fluxes $R_a(x_r + L, a)$ and $R_a(-a, x_r - L)$ appearing in Eq. (1.55) can be cast in a compact way by introducing $\sigma_r = \text{sign}(-x_r)$ and by exploiting the property $R(x_1, x_2) = -R(x_2, x_1)$:

(i) Case $|y_r| > 1$:

$$r_a(\sigma_r(\ell-|y_r|),\sigma_r) =$$
$$\begin{cases} 0 & \text{for } \ell-|y_r|>1, \\ \frac{[\sinh\rho-\sinh(\rho(\ell-|y_r|))][\sinh\rho+\rho(\ell-1)\cosh\rho]-\rho\sinh\rho(\ell-|y_r|)[\cosh\rho-\cosh(\rho(\ell-|y_r|))]}{[(\ell-1)\rho\cosh\rho+\sinh\rho][2(\ell-1)\rho\cosh\rho+(2+\rho^2(1-2\ell+|y_r|)(1-|y_r|))\sinh\rho]} & \text{for } |\ell-|y_r||\leq 1, \\ \frac{2\sinh\rho}{2(\ell-1)\rho\cosh\rho+(2+\rho^2(1-2\ell+|y_r|)(1-|y_r|))\sinh\rho} & \text{for } \ell-|y_r|<-1; \end{cases} \tag{1.56}$$

(ii) Case $|y_r|<1$:

$$r_a(\sigma_r(\ell-|y_r|),\sigma_r) =$$
$$\sigma_r \begin{cases} 0 & \text{for } \ell-|y_r|>1, \\ \frac{\rho(\ell-1)\cosh(\rho(1-|y_r|))\sinh(\rho(1-\ell+|y_r|))+\sinh\rho[\sinh(|y_r|\rho)-\sinh(\rho(\ell-1))]}{2[(\ell-1)\rho\cosh(y_r\rho)+\sinh\rho][(\ell-1)\rho\cosh\rho+\sinh\rho]} & \text{for } \ell-|y_r|\leq 1. \end{cases} \tag{1.57}$$

Figure 1.10 shows the comparison between the analytical calculations and the numerical simulations for the total stationary current $J$ as a function of the resetting point $x_r$ and various values of $r$. The cusps in $|x_r|=L-a$ are due to the vanishing of $J_{\rm res}(-L)$ in Eq. (1.55) for $a<|x_r|<L-a$, i.e., no particle resets along $l_2$ and the total stationary current $J$ is only given by Eq. (1.54); for $L-a<|x_r|<L$, Eq. (1.55) contributes and causes the cusp. We conclude that, given that $J-J_{\rm res}(-L)$ in Eq. (1.54) increases monotonically with increasing $x_r$, and that adding $J_{\rm res}(-L)$ reduces the magnitude of $J$ in $|x_r|=L-a$, these cusp points are also global maxima or minima for $J$.

### 1.4.3 Constant rate protocol

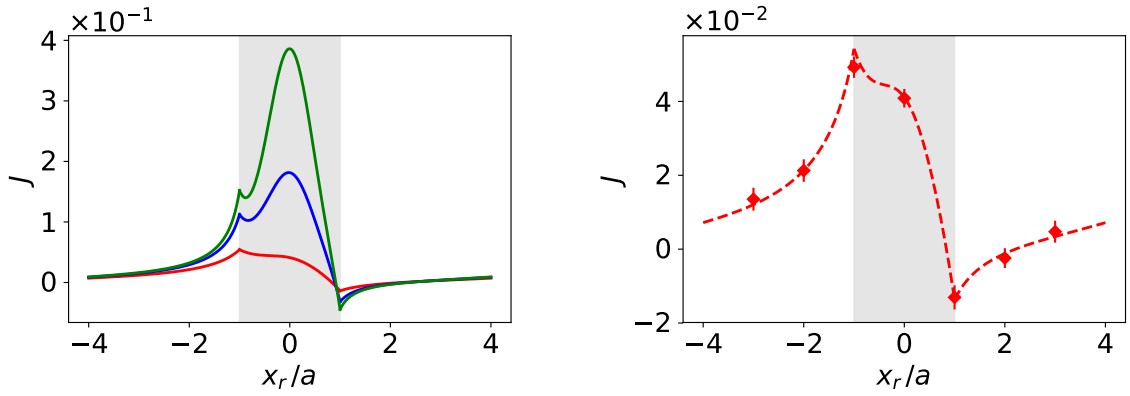
As a second example, we consider the case in which particles reset with probability $0<\lambda\leq 1$ along the rightward direction, or with probability $1-\lambda$ along the leftward one. According to this protocol, the left-moving and right-moving fluxes are simply given by

$$\begin{aligned} R_a^r(x_1,x_2) &= \lambda R_a(x_1,x_2), \\ R_a^l(x_1,x_2) &= (1-\lambda)R_a(x_1,x_2). \end{aligned} \tag{1.58}$$

The resetting current is calculated by determining the value of $J_{\rm res}(-L)$, whose expression is given by

$$J_{\rm res}(-L,t) = \begin{cases} \lambda R_a(-a,a) & \text{for } -L<x_r<-a, \\ \lambda R_a(x_r,a)-(1-\lambda)R_a(-a,x_r) & \text{for } |x_r|<a, \\ -(1-\lambda)R_a(-a,a) & \text{for } a<x_r<L. \end{cases} \tag{1.59}$$

In the stationary limit, from Eq. (B.18), we find:




(a) (b)

Figure 1.11: **Constant rate protocol. (a)** Total stationary current $J = J_{\rm diff} + J_{\rm res}$ as a function of $x_r/a$ and various values of $r = 0.5$ (red), 1.5 (blue), 2.5 (green) and with $D = 5$, $a = 5$, $L = 20$ and $\lambda = 0.75$ fixed. **(b)** Comparison between the analytic prediction for $J$ (red curve in panel (a)) and the numerical simulations (red symbols with error bars). The grey shaded area corresponds to the resetting region. Simulations were done using the Euler numerical integration scheme with time step $\Delta t = 0.2$, and they were repeated $N = 10^5$ times.

(i) Case $|y_r| > 1$:

$$r_a(-1,1) = \frac{2\sinh\rho}{2(\ell-1)\rho\cosh\rho + [2+\rho^2(1-2\ell+|y_r|)(1-|y_r|)]\sinh\rho}, \tag{1.60}$$

(ii) Case $|y_r| < 1$: From Eq. (B.22) one has

$$\begin{aligned} r_a(-1,\,y_r) &= \frac{\rho(\ell-1)\cosh(\rho(1-y_r))\sinh(\rho(1+y_r)) + \sinh\rho[\sinh(\rho) + \sinh(y_r\rho)]}{2\,[(\ell-1)\rho\cosh(y_r\rho) + \sinh\rho]\,[(\ell-1)\rho\cosh\rho + \sinh\rho]}, \\ r_a(y_r,1) &= \frac{\rho(\ell-1)\cosh(\rho(1+y_r))\sinh(\rho(1-y_r)) - \sinh\rho[\sinh(y_r\rho) - \sinh(\rho)]}{2\,[(\ell-1)\rho\cosh(y_r\rho) + \sinh\rho]\,[(\ell-1)\rho\cosh\rho + \sinh\rho]}. \end{aligned} \tag{1.61}$$

In Fig. 1.11 the total stationary current $J$ is plotted as a function of the resetting point $x_r$. For the specific choice of $\lambda = 0.75 > 1/2$ particles reset mostly to the right, making the current positive for almost all values of $x_r$. The current $J$ within the region $|x_r| > a$ increases monotonically as a function of $x_r$ as $J - J_{\rm res}(-L)$ in Eq. (1.54), while $J_{\rm res}(-L)$ is constant. Inside the resetting region (grey area) the current $J$ grows upon increasing $r$ and, for sufficiently large $r$, it attains its maximum at $x_r = 0$. Being $J - J_{\rm res}(-L)$ a decreasing function of $r$ inside the resetting region, we conclude that the increase in amplitude of $J$ coincides with the one of $J_{\rm res}$; note that the sign of $J$ is $\mathrm{sign}(\lambda - 1/2)$. As $r$ increases, the flux of resetting particles towards $\pm L$ grows and it is maximal at $x_r = 0$, the point where the ratio of the fluxes between the right-moving and left-moving resetting particles is maximal. It is easy to check from Eq. (1.61), that the fraction $R_a(-a,a)$ of resetting particles increases upon increasing $r$, and that the two regions $(-a,0)$, and $(0,a)$ contribute equally, i.e.,

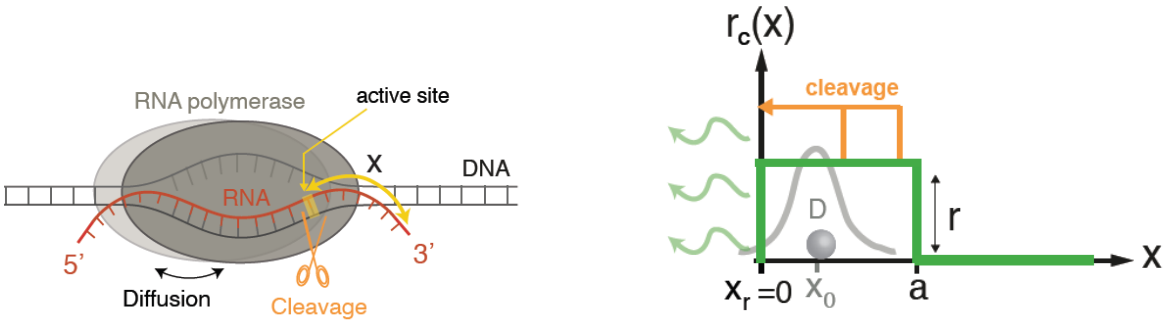



Figure 1.12: **Modelling backtrack recovery of RNA polymerase**. **(a)** Illustration of an RNA polymerase (grey area) diffusing along a DNA template (black ladder). During a transcriptional pause, the polymerase cannot resume RNA polymerization because its active site (yellow box) — where new nucleotides are added — is blocked by backtracked RNA (red line). Polymerases "recover" from the backtracking state when the distance $x \geq 0$ ("backtrack depth", yellow arrows) between the active site and the 3'-end of the RNA vanishes. Recovery from backtracking is due to Brownian diffusion of the polymerase with diffusion coefficient $D$ (arrows) or to the action of active processes that allow cleavage (orange scissors) of backtracked RNA of length up to a finite length $a \geq 0$ and at random times with constant rate $r$ [118]. **(b)** Model for the evolution of the backtrack depth $x$ from an initial value $x_0$. Polymerases recover by reaching the absorbing state $x = 0$ either by diffusion or by resetting, representing RNA cleavage [118, 180].

$R_a(-a, a) = 2R_a(0, a)$. Accordingly, the total current equals $J = J_{\rm res}(-L) = (\lambda - 1/2)R_a(-a, a)$: its magnitude is maximal when $|\lambda - 1/2| = 1/2$ (completely asymmetric resetting) and minimal at $\lambda = 1/2$ (completely symmetric).

## 1.5 Application to the RNA polymerase

We now apply the analytical findings reported and discussed in Sec. 1.3 to a biophysical model describing the fluctuating motion of RNA polymerases along a DNA template during transcriptional pauses, introduced in Ref. [118].

Figure 1.12a sketches two recovery mechanisms that can be employed by an RNA polymerase enzyme to recover from the inactive state ("backtracking"): (i) Brownian diffusion due to thermal fluctuations, and (ii) active cleavage of the backtracked RNA induced by chemical reactions. This dynamics can be modelled as shown in Fig. 1.12b, as confirmed by *in vitro* single-molecule experimental data obtained for yeast *S. Cerevisiae* [118]. The model describes the evolution of the *backtrack depth* $x \geq 0$, i.e., the spatial distance between the active site of the polymerase and the 3′-end[1] of the backtracked RNA. The dynamics consists of one-dimensional diffusion starting from

[1] A single RNA strand is constituted of a series of nucleotides. Each of these nucleotides contains a pentose-sugar-ring, with carbons numbered from the 1' to 5'. A base is attached to the 1' carbon, i.e., adenine (A), cytosine (C), guanine (G), or uracil (U). A phosphate group is attached to the 3' position of one ribose and the 5' position of the next. Thanks to this structure it is possible to identify a *directionality* for the RNA: the 5'-end (pronounced "five

the initial value $x_0 > 0$ with an absorbing boundary in $x_a = 0$ corresponding to the return to the RNA polymerization state. Cleavage of backtracked RNA is modelled by a sudden jump (i.e., resetting) of the backtrack depth $x \to x_r = 0$ at a rate $r$ from the region $(0, a)$; note that resetting is equivalent here to evaporation. The choice of a finite interval for resetting is motivated by previous experimental observations which suggested that polymerases can only cleave RNA transcripts of a finite length [111, 68], and has been tested in recent single-molecule experiments [118].

The presence of the absorbing boundary implies that $P_a(x, t|x_0)$, the probability density of the particle position $x$ at time $t$ starting at $x_0$, vanishes at the absorption boundary $x_a = 0$. The linearity of Eq. (1.33) allows us to obtain $P_a(x, t|x_0)$ from $P(x, t|x_0)$, the probability density in the absence of the absorbing boundary, by means of the method of image charges, e.g., see Ref. [172]. This is accomplished by positioning "negatively charged" source of particles originating from $-x_0$ which reset in $(-a, 0)$ to the same $x_r = 0$, with distribution $P(x, t| - x_0)$, yielding

$$P_a(x, t|x_0) = P(x, t|x_0) - P(x, t| - x_0). \tag{1.62}$$

The Laplace transform of this expression is readily computed by considering the expression of $\tilde{P}(x, s|x_0)$ in Eq. (1.32) in terms of the Laplace transform of the probability density $P_{\rm nc}(x, t|x_0)$, the probability density for the particles not to reset in the time interval $(0, t)$ moving from $x_0$ to $x$, and $P_{\rm res}(t|x_0)$, the probability distribution of the first resetting time (see Appendix B.1):

$$\begin{aligned}
\tilde{P}_a(x, s|x_0) =& \tilde{P}(x, s|x_0) - \tilde{P}(x, s| - x_0) \\
=& \tilde{P}_{\rm nc}(x, s|x_0) + \frac{\tilde{P}_{\rm res}(s|x_0)}{1 - \tilde{P}_{\rm res}(s|x_r)} \tilde{P}_{\rm nc}(x, s|x_r) \\
& - \tilde{P}_{\rm nc}(x, s| - x_0) - \frac{\tilde{P}_{\rm res}(s| - x_0)}{1 - \tilde{P}_{\rm res}(s|x_r)} \tilde{P}_{\rm nc}(x, s|x_r) \\
=& \tilde{P}_{\rm nc}(x, s|x_0) - \tilde{P}_{\rm nc}(x, s| - x_0),
\end{aligned} \tag{1.63}$$

where we exploit $P_{\rm res}(s|x_0) = P_{\rm res}(s| - x_0)$, which follows from Eqs. (B.6) and (B.10). As expected, $P_a(x, t|x_0)$ depends only on $P_{\rm nc}(x, t|x_0)$, the probability of no resetting or, equivalently, the probability density in the presence of evaporation $r$ in the region $(0, a)$. Its Laplace transform is calculated by substituting Eq. (B.9) in Eq. (1.63).

Because of absorption at $x_r = 0$ the density of particles $P_a(x, t|x_0)$ is not conserved. Then, it is interesting to calculate the fraction of non-absorbed particles, which is given by the survival probability $S_a(t|x_0) = \int_0^\infty {\rm d}x\, P_a(x, t|x_0)$. We calculate its Laplace transform by integrating Eq. (1.63):

$$\tilde{S}_a(s|x_0) = \begin{cases} \frac{1}{D\nu^2} \left[ 1 - \frac{\nu \cosh(\nu(a - x_0)) + \mu \sinh(\nu(a - x_0)) - r \sinh(x_0\nu)/D\mu}{\mu \sinh(a\nu) + \nu \cosh(a\nu)} \right] & \text{for } 0 < x_0 < a, \\ \frac{1}{D\mu^2} \left[ 1 - \frac{e^{\mu(a - x_0)}(r \cosh(a\nu) + s)}{D\nu(\mu \sinh(a\nu) + \nu \cosh(a\nu))} \right] & \text{for } x_0 > a. \end{cases} \tag{1.64}$$

prime end") designates the end of the RNA strand that has the fifth carbon in the sugar-ring of the deoxyribose or ribose at its terminus. The 3'-end (pronounced "three prime end") of a strand is so named due to it terminating at the hydroxyl group of the third carbon in the sugar-ring, and is known as the tail end. During transcription, the RNA polymerase slides along the template of the DNA strand in the 3' to 5' direction, synthesizing a complementary RNA molecule oriented in the 5' to 3' direction [119].

In our model, Eq. (1.64) represents the probability that a RNA strand has not been backtracked yet. As a consequence of the recurrency of the one-dimensional Brownian motion, all particles are absorbed in the long-time limit, i.e., $\lim_{t\to\infty} S_a(t|x_0) = 0$: eventually, RNA exits the backtracking phase. It can be easily checked that, in the case $r = 0$ corresponding to the presence of the sole absorption at the boundary $x_a = 0$, we recover $\tilde{S}_{\rm BM}(s|x_0)$ in Eq. (1.19).

Figure 1.13 shows $1 - S_a(t|x_0)$, i.e., the probability that RNA has backtracked from initial position $x_0$ at time $t$: we compare the experimental measurements in Fig. 1.13a-b, with its numerical prediction via simulation (dashed line) with the numerical inverse Laplace transform of Eq. (1.64) (symbols) in Fig. 1.13c. All these predictions display a good quantitative agreement: the model accurately describes all the relevant features of the biological system. In spite the RNA polymerase moves on a discrete template, the continuous description provides is valid: this is due to the fact that the typical elongation $l_c \equiv \sqrt{2D/r}$ of the backtracked RNA for the three species of polymerase considered here (see Table 1.1) before a cleavage is much larger than the size of a nucleotide [180].

We now derive two statistical properties of the RNA polymerase backtracking for which no analytical results have been reported so far. First, we focus on the distribution of the length of cleaved RNAs. In the model, this quantity corresponds to the probability density $Q_{\rm res}(x,t|x_0)$ of particles, with initial point $x_0$, that are absorbed in the time interval $(0,t)$ from the position $x$ through resetting only. We can express $Q_{\rm res}(x,t|x_0)$ as

$$Q_{\rm res}(x,t|x_0) = r_c(x) \int_0^t {\rm d}\tau \, P_a(x,\tau|x_0). \tag{1.65}$$

Note that $Q_{\rm res}(x,t|x_0)$ vanishes outside of the support $r_c(x)$, where resetting is not possible. Once again, we can easily express the Laplace transform $\tilde{Q}_{\rm res}(x,s|x_0)$ in terms of $\tilde{P}_a(x,s|x_0)$ in Eq. (1.63):

$$\begin{aligned}\tilde{Q}_{\rm res}(x,s|x_0) &= r_c(x)\,\frac{\tilde{P}_a(x,s|x_0)}{s} \\ &= \begin{cases} \frac{r\sinh(x_<\nu)}{s\,D\nu}\,\frac{\nu\cosh((a-x_>)\nu)+\mu\sinh((a-x_>)\nu)}{\mu\sinh(a\nu)+\nu\cosh(a\nu)} & \text{for } 0<x_0<a, \\ \frac{r\,e^{\mu(x_0-x)}}{D\,s}\,\frac{\sinh(x\nu)}{\mu\sinh(a\nu)+\nu\cosh(a\nu)} & \text{for } x_0>a, \end{cases}\end{aligned} \tag{1.66}$$

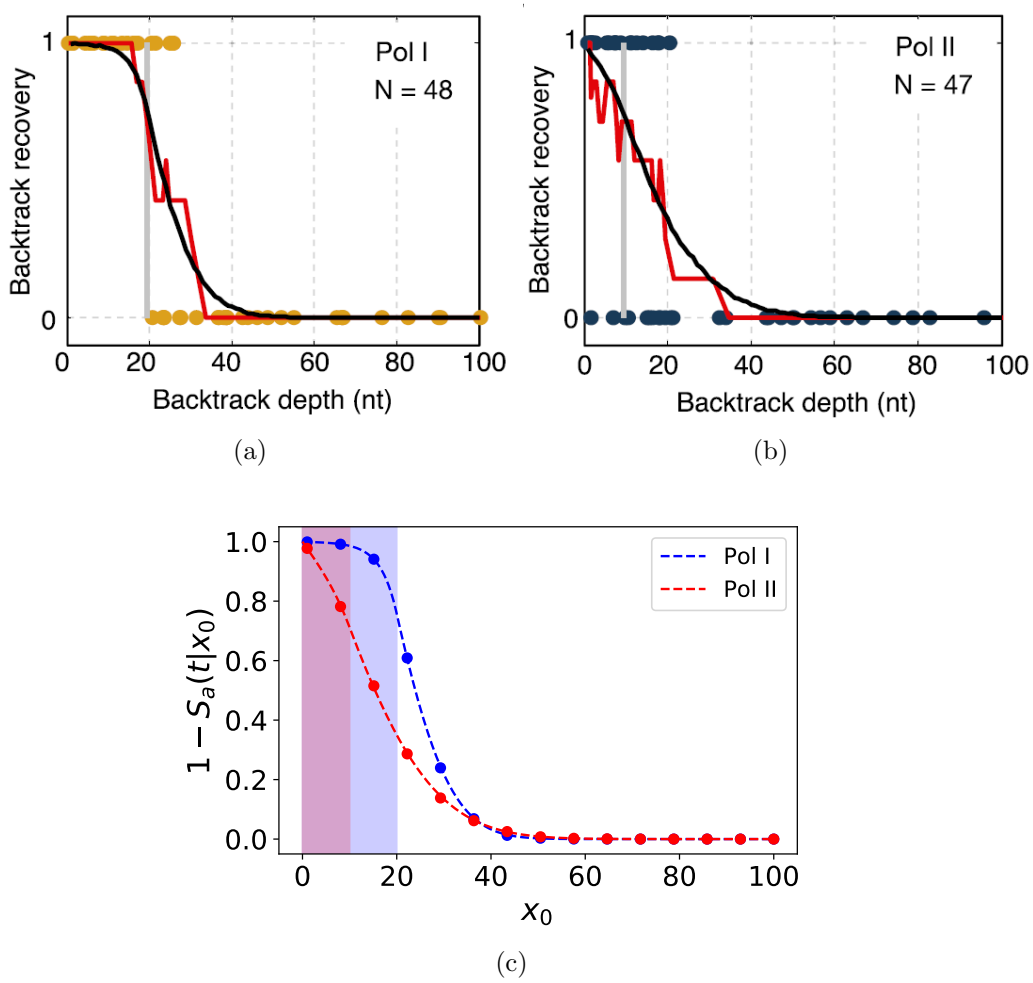
with $x \in (0,a)$, $x_> = \max(x,x_0)$ and $x_< = \min(x,x_0)$.

Notably, $Q_{\rm res}(x,t|x_0)$ does have a well defined stationary limit, following from the fact that we consider trajectories of resetting particles. We calculate the stationary limit of $Q_{\rm res}(x,t|x_0)$, by applying the the final value theorem of the Laplace transform to Eq. (1.66), i.e., $Q_{\rm res}(x|x_0) = \lim_{s\to 0} s\,\tilde{Q}(x,s|x_0)$. In terms of the dimensionless quantities in Eq. (1.36), we cast $q_{\rm res}(y|y_0) \equiv a\,Q_{\rm res}(x|x_0)$ as

$$q_{\rm res}(y|y_0) = \frac{\rho\sinh(y_<\rho)}{\cosh\rho}\left\{1-\theta(1-y_0)\left[1-\cosh\left((1-y_>)\rho\right)\right]\right\}, \tag{1.67}$$

with $y_> \equiv \max(y,y_0)$, $y_< \equiv \min(y,y_0)$, and $y \in (0,1)$.

Furthermore, we quantify the overall efficiency of cleavage in recovery by defining the "resetting efficiency" $\eta_{\rm res}(y_0) \le 1$ as the fraction of polymerases that recover from any $x \le a$ and at any time $t > 0$ due to RNA cleavage (resetting). The efficiency $\eta_{\rm res}(y_0)$ is related to $Q_{\rm res}(x|x_0)$ in Eq.(1.67),




(a) (b)

(c)

Figure 1.13: **Backtrack probability.** Panels **(a)** and **(b)**, taken from Ref. [118] with permission of the authors, represent the experimental determination of the backtrack probability as a function of backtrack depth for Pol I and Pol II as a function of the initial backtrack depth in units of nucleotides (1 nt=0.3 nm), whose parameters are reported in Table 1.1. In the experiment, the enzymes are declared unrecovered if they do not resume elongation within $t = 5$ min. In panel **(c)**, we report the theoretical prediction of the backtrack probability $1 - S_a(t|x_0)$ in Eq. (1.64) (dashed line), compared with the numerical simulations (symbols), for both Pol I and Pol II at $t = 300$ s. Our findings show quantitative agreement with the experimental measurements. The blue and the red area denote the region where cleavage is possible for the two enzymes. Simulations are performed with time step $\Delta t = 0.05$ and number of simulations $N = 1.5 \times 10^4$.

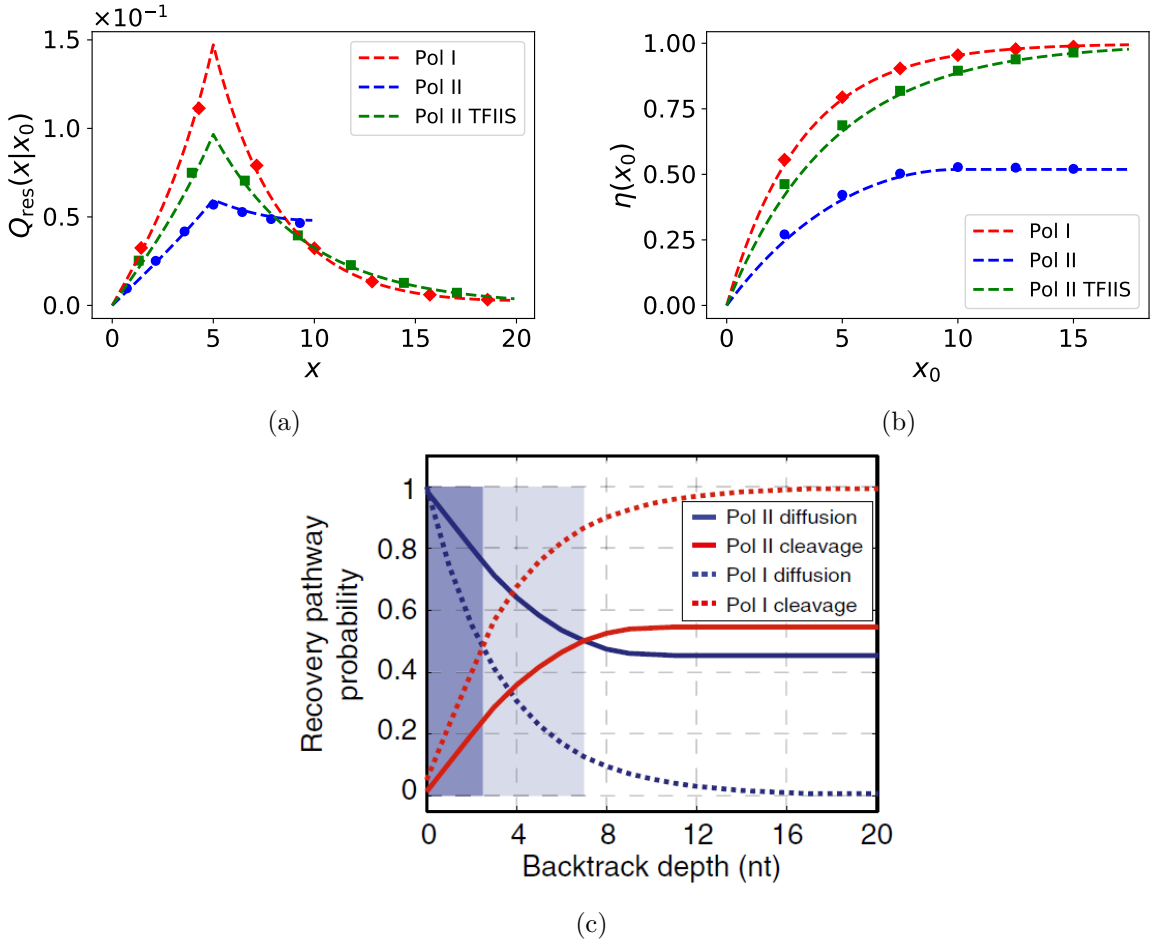



Figure 1.14: **Cleavage statistics**. **(a)** Distribution of the length of cleaved RNA for Pol I, Pol II, and Pol II TFIIS with initial backtrack depth $x_0 = 5$ (nucleotides). We recall that the support of $Q_{\rm res}(x|x_0)$ is given by $(0, a)$: this explains why in the plot the lines stop, see, e.g., the case of Pol II (blue curve) with $a = 10$nt. **(b)** Cleavage (resetting) efficiency as a function of the initial backtrack depth. The numerical prediction for $\eta_{\rm res}(y_0) \equiv \eta(x_0 = a\, y_0)$ has been already reported in Ref. [118]. In both panels (a) and (b) , the symbols are obtained from numerical simulations and the dashed lines are theoretical predictions given by Eq. (1.67) in panel (a) and Eq. (1.68) in panel (b). Values of the parameters $D$, $r$ and $a$ are reported in Table 1.1. Simulations were done with time step $\Delta t = 0.01$ with number of simulations $N = 1.5 \times 10^5$. Our theoretical prediction quantitatively agree with panel **(c)**, where, from Ref. [118], we report the experimental measurements of cleavage efficiency $\eta(x_0)$ (red curves), and the diffusive efficiency $1 - \eta(x_0)$ (blue curves).

| Type | $a$ (nt) | $r$ (1/s) | $D$ (nt$^2$/s) |
|---|---|---|---|
| Pol I | 20 | 0.02 | 0.21 |
| Pol II | 10 | 0.01 | 0.54 |
| Pol II TFIIS | $\infty$ | 0.076 | 1.6 |

Table 1.1: **Values of the parameters** associated with the various species of polymerase, see Ref. [118], corresponding to Fig. 1.14 a-b. The length unit is a nucleotide, 1 nt =0.3 nm.

as

$$\begin{aligned}\eta_{\rm res}(y_0) &= \int_0^\infty {\rm d}x\, Q_{\rm res}(x|x_0) \\ &= 1 - \frac{\cosh\left((1-y_0)\rho\right) + \theta(y_0-1)\left[1-\cosh\left((1-y_0)\rho\right)\right]}{\cosh\rho}.\end{aligned} \tag{1.68}$$

Both the distribution in Eq. (1.67) of cleaved RNA length and the efficiency (1.68) of RNA cleavage obey universal scaling laws in terms of the parameter $\rho$ and $y_0$ in Eq. (1.36). We demonstrate these results in Fig. 1.14 with numerical simulations using values of the parameters which were measured for the enzymes Pol I, Pol II and Pol II complemented with TFIIS from yeast *S. Cerevisiae* [118]. Interestingly enough, the distributions of the length of the cleaved RNA in Fig. 1.14a display a cusp at the initial position and exponential tails. $Q_{\rm res}(x|x_0)$ is positive on a broader range of positions for Pol I and Pol II-TFIIS, because these enzymes can cleave RNA of lengths $a$ larger than Pol II. On the other hand, the cleavage efficiency, $\eta_{\rm res}(y_0) \equiv \eta(x_0 = a\, y_0)$ in Fig. 1.14b, increases monotonically upon increasing the initial backtrack depth $x_0$ for all the enzymes. Notably, Pol II maximum cleavage efficiency attained for deep backtracks is $\simeq$50% for Pol II and twice larger and almost $\simeq$100% for both Pol I and Pol II-TFIIS. The similarities in the cleavage efficiency of Pol I and Pol II-TFIIS may stimulate further research on evolutionary-conserved performance between different types of transcription enzymes. Once again, we point out the quantitative agreement of $\eta(x_0)$ between the analytical prediction of Eq. (1.68) in Fig. 1.14b and the experimental measurements in Fig. 1.14c.

## 1.6 Conclusions

In this Chapter we provided analytical and numerical insight into the particle currents emerging in the presence of control mechanisms (evaporation and/or resetting) on an otherwise unbiased Brownian diffusion, for various boundary conditions. In Section 1.3, for open boundary conditions, we have shown that resetting the particle position at stochastic times to a prescribed location leads to Brownian yet non-Gaussian diffusion. On the other hand, periodic boundary conditions induce stationary particle current that can be decomposed as the sum of diffusive and resetting fluxes. In Section 1.4, for ring-like geometries, we have proved a resetting gauge invariance of the distribution with respect to the resetting protocol (direction), resulting into different particle currents. Finally, in Section 1.5, we have applied our findings to a biophysical model, deriving analytical predictions concerning the efficiency of RNA polymerase backtracking. Our work indicates new avenues for

understanding the non-equilibrium features of resetting, e.g., in the study of optimization of resetting pathways for efficient particle transport. Furthermore, we expect that our formalism could be extended to shed light on various biophysical problems described by one-dimensional diffusions with suitable boundary and/or resetting conditions, such as microtubule dynamics [150, 167], molecular motors [106, 108, 90], single-file diffusion of water in carbon nanorings [142], or polymer translocation through nanopores [2, 1]. Moreover, from a theoretical point of view, it would be worth to investigate how these models can be extended to more than one spatial dimension. In particular, it would be interesting to investigate how the loss of the recurrence property of the one-dimensional Brownian motion could affect the features of the system in higher dimensions, and how to implement simple and relevant topological constrains.

# Chapter 2

# An experimental protocol for run-and-tumble particles with resetting

## 2.1 Introduction

In the previous Chapter we have seen that resetting of stochastic processes turns out to have two rather generic major consequences: (i) it typically drives the system into a non-trivial stationary state and (ii) in many cases, an optimal resetting rate emerges which minimises the mean first-passage time of the reset process to a given fixed target. Both aspects have motivated a lot of theoretical work during the last few years (see Ref. [74] for a recent review). It is only recently that resetting protocols were realized experimentally [211, 22, 23]. These experimental works revealed two important facts: (i) physical resetting is often non-instantaneous and (ii) it is rather unrealistic to reset the particle exactly at a fixed position $x_r$. In particular, in Refs. [22, 23], the experiments are conducted on colloidal particles diffusing in the presence of a trap, which is realized via optical tweezers and it is well approximated by a harmonic potential $V(x) = \kappa\, x^2/2$. This experimental protocol consists of two distinct phases which alternate periodically in time. First, we have an *equilibration* phase of fixed duration $T_{\rm eq}$: the harmonic trap is switched on and the dynamics of the particle reaches thermal equilibrium at inverse temperature $\beta$ (see red shaded area of Fig. 2.1). Accordingly, the position $x$ of the particle is distributed according to the Boltzmann weight $\rho(x) \propto e^{-\beta V(x)}$, i.e., a Gaussian distribution centred in the origin with variance $\sigma \propto \beta^{-1/2}$. Equilibrium is attained if the relaxation time scale $\tau_{\rm rel} \equiv \kappa^{-1}$ of the particle in the trap, is much smaller than the duration of the equilibration phase $T_{\rm eq}$. At the end of the equilibration phase, the particle enters the *"search"* phase: the trap is switched off for a period $T$ and the particle diffuses freely (see blue shaded area of Fig. 2.1). Then, these two phases repeat cyclically.

If one keeps track of what happens to the particle only during the search phases, it is observed that the system behaves effectively as a Brownian particle resetting periodically to the stationary distribution $\rho(x)$. A simple generalization of this protocol consists in considering $T$ to be a random variable, allowing one to reproduce stochastic resetting. One of the main focus of Ref. [22] was on the first-passage time distribution to a target located at a distance $L$ from the center of the optical

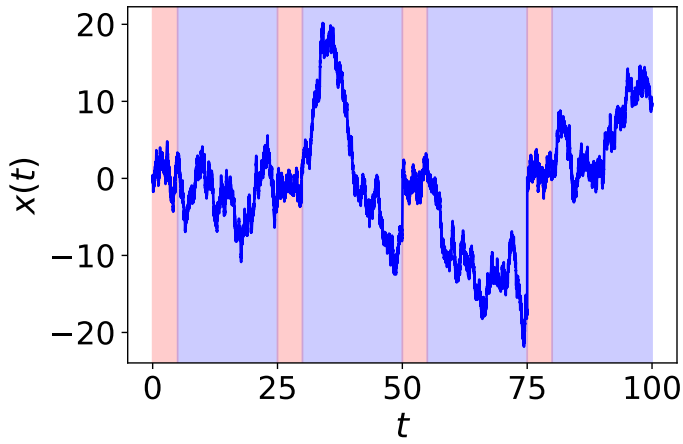



Figure 2.1: **Experimental protocol for Brownian particles.** We represent a typical trajectory of a Brownian particle evolving according the experimental protocol proposed in Ref. [22]. During the *equilibration* phase (red shaded areas) the Brownian particle relaxes in a harmonic trap for a time $T_{\rm eq}$. At the end of this phase, the particle diffuses freely (blue shaded area) for a period $T$. For this particular realization of the process we have chosen $T_{\rm eq} = 10\tau_{\rm rel}$ and $T = 40\tau_{\rm rel}$, where $\tau_{\rm rel}$ denotes the relaxation time scale of the particle in the trap.

trap: as anticipated, measurements are performed only during the search phase.

A first question, which naturally raises from this experimental protocol, is what happens to the first-passage time distribution to a fixed target located at $L$ after *averaging* over the initial position, which is distributed according a certain probability density $\rho(x)$ which is the stationary distribution corresponding to the external potential $V(x)$ (i.e., in the limit $T \to \infty$). In the case of Brownian motion, where $\rho(x)$ is a Gaussian of zero mean and variance $\sigma \propto \sqrt{1/\beta}$, it was shown that the averaged first-passage time exhibits a very rich behaviour, including a dynamical phase transition in the appearances between a two-peak to a single-peak shape as the ration $L/\sigma$ is varied [23]. This transition was not only predicted theoretically but also observed in experiments [23]. Given the relevance of first-passage time for a variety of applications in physics and beyond [28], it is then natural to extend these studies to other stochastic processes, beyond the simple Brownian motion.

In this Chapter, we consider the case of the persistent random walk, also known as the run-and-tumble particle (RTP) in one spatial dimension. The dynamics of this model consists of running phases during which the particle moves ballistically with velocity $v$, and of tumbling events where the particle changes its direction of motion and which happen randomly in time with a constant rate $\gamma$. This simple model has been used to describe the motion of some species of bacteria, e.g., *Escherichia Coli* [21, 210]. In these cases, the bacteria propel by consuming energy, which is absorbed by the surrounding environment. In this sense, RTPs have been widely used to model the dynamics of active particles [210, 149, 66, 203, 39]. The effect of *instantaneous* resetting towards a fixed location $x_r$ was studied in Refs. [72, 133, 29, 187]. There it was shown that resetting of a RTP induces a non-trivial stationary state, which is different from the one found for Brownian motion

with resetting, but which also allows to optimize the mean first-passage time to a given target. Here, motivated by the recent experimental realizations of resetting of a Brownian particle, and in view of possible implementations of the resetting dynamics of active particles, we characterize the main features of a non-instantaneous resetting of the RTP. In particular, we consider the aforementioned protocol that was proposed and realised for the case of a Brownian particle [22, 23]. The crucial difference compared to the Brownian motion is that the RTP reaches a stationary state $\rho(x)$ which differs significantly from the Boltzmann weight [58]. In fact, $\rho(x)$ has a *finite support* and exhibits a transition from a bell-shaped to a U-shaped distribution as the stiffness $\kappa$ (of the trap) is varied [58].

In this Chapter, we show that this different probability density $\rho(x)$ modifies qualitatively the first-passage time statistics of the RTP when subject to such a non-instantaneous resetting protocol. In order to build up a protocol that mimics non-instantaneous resetting, we first investigate the first-passage time distribution for RTPs at a position drawn from the probability density $\rho(x)$ corresponding to their stationary state in a harmonic trap. As a result, the first-passage time distribution may display some singularities, which are reminiscent of those of $\rho(x)$ near the boundaries of its support. Then, as in Chapter 1, we add stochastic resetting to the distribution $\rho(x)$ to the dynamics of RTPs: this leads to a finite mean first-passage time, which can be now optimized. These optimal values of the mean first-passage time depend on the location of the target, and the behaviour of $\rho(x)$ in proximity of the edges of its support. Eventually, we let RTPs reset periodically to $\rho(x)$, mimicking the experimental protocol presented above.

This Chapter is organised as follows. In Section 2.2, we summarize some results on the first-passage statistics of RTPs starting from a given initial position and in the absence of resetting. In Section 2.3, we let the initial position of RTPs to be drawn from the initial distribution $\rho(x)$. We choose $\rho(x)$ to be the stationary probability density of a RTP in an harmonic trap. We then study the effect of this choice on the first-passage time probability density. In Section 2.4, we study how the introduction of stochastic resetting to a distribution with finite support affects the mean first-passage time for the RTPs. Finally, in Section 2.5, we provide theoretical predictions about experimental setup realized in Ref. [22] but for the case of RTPs.

## 2.2 Run-and-tumble dynamics

In this Section we recall some essential facts about RTPs in one dimension; we mainly refer to Refs. [126, 218]. The position $x(t)$ of a one-dimensional RTP evolves according to the following Langevin equation

$$\dot{x}(t) = v\,\sigma(t). \tag{2.1}$$

The velocity $\dot{x(t)}$ of the particle consists of two contributions: its modulus $v > 0$, and its sign, determined by the telegraphic noise $\sigma(t)$, that is a dichotomous process, whose value switches in time between the two states $\pm 1$ with constant rate $\gamma$ [107]. The sign of the initial velocity is positive or negative with equal probability. Figure 2.2a show typical RTP trajectories. By integrating Eq. (2.1) over time, one has that $|x - x_0| = v|\int_0^t \mathrm{d}t\,\sigma(t)| \leq vt$: the bound corresponds to the purely ballistic dynamics $x = x_0 \pm vt$ (dashed lines in Fig. 2.2a). Accordingly, the state of the particle is fully identified by the pair of variables $(x(t), \sigma(t))$, that is, its position at time $t$ and its orientation $\sigma$. It is then natural to address the study of $\rho_\sigma(x, t|x_0)$, the probability density to be in the state $(x, \sigma)$

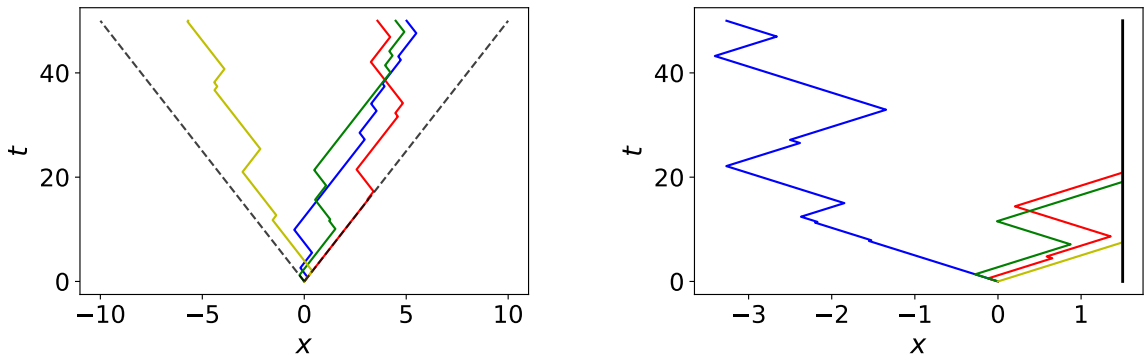



Figure 2.2: **Run-and-tumble particles (RTP) .** Panel **(a)** shows typical trajectories of RTPs originating at $x = 0$ at time $t = 0$. The dashed grey lines identify the lower and upper bounds of the distance travelled by the particles given by the purely ballistic motion $\pm vt$. Panel **(b)** shows trajectories of RTPs in the presence of an absorbing target (black vertical line) located at $L = 1.5$. The parameters of the dynamics are $\gamma = 0.15$, and $v = 0.2$.

at time $t$, given the initial position $x_0$; with a small abuse of notation, we identify the subscript $\sigma \in \{\pm\}$ with the sign of the telegraphic noise. The infinitesimal time evolution of $\rho_\sigma(x, t|x_0)$ can be expressed as

$$\rho_\sigma(x, t + \mathrm{d}t) = (1 - \gamma \mathrm{d}t)\, \rho_\sigma(x - \sigma v\, \mathrm{d}t, t) + \gamma \mathrm{d}t\, \rho_{-\sigma}(x\, \mathrm{d}t, t). \tag{2.2}$$

The first contribution on the right hand side of Eq. (2.2) is due to particles in the state $(x', \sigma)$ at time $t$, not tumbling in the interval $[t, t + \mathrm{d}t]$, and reaching the position $x = x' + \sigma v\, \mathrm{d}t$. The second contribution accounts for particles that tumble at $t$. Then, by Taylor-expanding Eq. (2.2) for $\mathrm{d}t \to 0$, one finds that the probability density $\rho_\sigma(x, t|x_0)$ satisfies the Fokker-Planck equation

$$\frac{\partial \rho_\sigma(x, t|x_0)}{\partial t} = -\sigma v \frac{\partial \rho_\sigma(x, t|x_0)}{\partial x} + \gamma \rho_{-\sigma}(x, t|x_0) - \gamma \rho_\sigma(x, t|x_0), \tag{2.3}$$

with initial condition $\rho_\sigma(x, 0|x_0) = \delta(x - x_0)/2$, where the $1/2$ factor comes from the randomization of the initial velocity. Equation (2.3) expresses the time evolution of $\rho_\sigma(x, t|x_0)$ as the net probability flux of particles tumbling in or out the state $(x, \sigma)$ at time $t$, plus the current of RTPs drifting with constant velocity $\sigma v$. Then, the knowledge of $\rho_\sigma(x, t|x_0)$ allows one to calculate the total probability density

$$\rho(x, t|x_0) = \rho_+(x, t|x_0) + \rho_-(x, t|x_0). \tag{2.4}$$

The dynamics of this process can be characterized in terms of the dimensionless variables

$$\tau \equiv \frac{t}{\tau_\gamma} \quad \text{and} \quad y \equiv \frac{x}{l_\gamma}, \tag{2.5}$$

where $\tau_\gamma \equiv \gamma^{-1}$ is the average time between two consecutive tumblings, and $l_\gamma \equiv v/\gamma$ is the typical distance that the RTP covers in $\tau_\gamma$. Accordingly, the total density $\rho_d(y,\tau) = \rho(x,t|0)$, solution of Eq. (2.3), is written in Eq. (10) of Ref. [126] as

$$\rho_d(y,\tau) = \frac{e^{-\tau}}{2}\left\{\delta\left(\tau-|y|\right) + \theta\left(\tau-|y|\right)\left[I_0\left(\sqrt{\tau^2-y^2}\right) + \frac{\tau}{\sqrt{\tau^2-y^2}}\, I_1\left(\sqrt{\tau^2-y^2}\right)\right]\right\}, \tag{2.6}$$

where $I_n$ is the $n$-th order modified Bessel function of the first kind, and $\theta$ is the Heaviside step function. The delta contribution to Eq. (2.6) accounts for RTPs that never tumble, while the contribution proportional to the Heaviside function for particles that undergo at least one tumble. In the time-space region $\tau \gg 1 \gg |y|$, the probability density $\rho_d(y,\tau)$ in Eq. (2.6) is well approximated by a Gaussian with zero mean and variance $\langle y^2(t)\rangle_c \simeq \tau$; which follows from the central limit theorem and explicitly the asymptotic expansion of the Bessel function $I_n(\tau) \simeq (2\pi\tau)^{-1}e^{\tau}[1+O(\tau^{-1})]$ for $\tau \to \infty$ [3]. Indeed, whenever the time $t$ is much larger that the tumbling time scale $\tau_\gamma$, the time coarse-grained dynamics of the RTP is analogous to that of a Brownian particle with $D = v^2/(2\gamma)$. In general, one can show that the Brownian motion can be retrieved from the RTP by taking the joint limit $\gamma \to \infty$, $v \to \infty$, with constant $D = v^2/(2\gamma)$.

### 2.2.1 First-passage time statistics

The brief summary on the free RTP dynamics is concluded here by considering the effect of having an absorbing target located at the position $L$. Accordingly, the time that RTPs take to be absorbed coincides with the first-passage time to the target, and we are interested in studying its statistics. We refer to Fig. 2.2b to visualize typical trajectories of the system. Let $S_\sigma(x,t)$ denote the fraction of non-absorbed particles at time $t$ with initial velocity $\sigma\, v$ and initial position $x$; for the time being we omit the $L$ dependence. Following the steps of Ref. [126], we show how to write a backward Fokker-Planck equation for $S_\sigma(x,t)$. One considers the evolution of the system in the interval $[0, t+\mathrm{d}t]$ and breaks it in the two sub-intervals $[0,\mathrm{d}t]$ and $[\mathrm{d}t, t+\mathrm{d}t]$. In the first sub-interval the particle position is updated according to Eq. (2.1) to $x' = x + \sigma(0) v\, \mathrm{d}t$ with probability $1-\gamma\,\mathrm{d}t$ (no tumble), while to $x' = x$ with probability $\gamma\,\mathrm{d}t$ (tumble). Then, the position $x'$ coincides with the new initial position in $[\mathrm{d}t, t+\mathrm{d}t]$. Hence, one can write the infinitesimal time evolution of $S_\sigma(x,t)$ as

$$S_\sigma(x, t+\mathrm{d}t) = (1-\gamma \mathrm{d}t) S_\sigma(x + \sigma(0) v\, \mathrm{d}t, t) + \gamma \mathrm{d}t\, S_{-\sigma}(x,t). \tag{2.7}$$

By Taylor-expanding $S_\sigma(x+\sigma v\,\mathrm{d}t, t)$ for $\mathrm{d}t \to 0$, one retrieves the backward Fokker-Planck equation

$$\frac{\partial S_\sigma(x,t)}{\partial t} = \sigma v\, \frac{\partial S_\sigma(x,t)}{\partial x} + \gamma S_{-\sigma}(x,t) - \gamma S_\sigma(x,t). \tag{2.8}$$

At $t = 0$ no particles are absorbed, hence the initial condition of the survival probability is given by $S_\sigma(x,0) = 1$ for any $x \neq L$. Moreover, the survival probability vanishes at $L$, implying the boundary condition $S_{-\sigma_0}(L,t) = 0$, with $\sigma_0 = \mathrm{sign}(L)$. As shown in Ref. [126], it is convenient to consider the LT of Eq. (2.8), i.e.,

$$\sigma v \frac{\partial \tilde{S}_\sigma(x,s)}{\partial x} + \gamma \tilde{S}_{-\sigma}(x,s) - (s+\gamma)\tilde{S}_\sigma(x,s) = -1, \tag{2.9}$$

whose is solution is found to be

$$\tilde{S}_{\sigma_0}(x,s) = \frac{1}{2s}\left[1 - \frac{\gamma\, e^{-\lambda(s) d_L(x)}}{v\lambda(s) + \gamma + s}\right] \quad \text{and} \quad \tilde{S}_{-\sigma_0}(x,s) = \frac{1}{2s}\left[1 - e^{-\lambda(s) d_L(x)}\right], \tag{2.10}$$

where one defines the distance $d_L(x) \equiv |x - L|$ from the target, and $\lambda(s) \equiv \sqrt{s^2 + 2s\gamma}/v$.

The LT of the total survival probability is then given by

$$\begin{aligned} \tilde{S}_0(s|d_L(x)) &\equiv \tilde{S}_+(x,s) + \tilde{S}_-(x,s) \\ &= \frac{1}{s}\left[1 - \frac{s + 2\gamma - v\lambda(s)}{2\gamma}\, e^{-\lambda(s) d_L(x)}\right]. \end{aligned} \tag{2.11}$$

The first-passage time probability $F_\sigma(x,t)$ is related to the survival probability $S_\sigma(x,t)$ according to $F_\sigma(x,t) = -\partial_t S_\sigma(x,t)$, or, equivalently, $\tilde{F}_\sigma(x,s) = 1 - s\tilde{S}_\sigma(x,s)$ in Laplace transform. Then, we denote the total first-passage probability as

$$F_0(t|d_L(x)) \equiv F_+(x,t) + F_-(x,t). \tag{2.12}$$

We report the dimensionless expression of the first-passage probability $f_0(\tau|y) \equiv F_0(t|d_L(x))/\gamma$, in terms of the dimensionless variables $\tau$ in Eq. (2.5) and $y \equiv d_L(x)/l_\gamma$:

$$f_0(\tau|y) = \frac{e^{-\tau}}{2}\left[\delta(\tau - y) + \theta(\tau - y) g_0(\tau|y)\right], \tag{2.13}$$

which follows from the fact that it is possible to compute exactly the inverse LT of $\tilde{F}_\sigma(x,s)$. In the above formula we have introduced the auxiliary function

$$g_0(\tau|y) \equiv \frac{y}{y+\tau} I_0\left(\sqrt{\tau^2 - y^2}\right) + \left[\frac{\sqrt{\tau - y}}{(\tau + y)^{3/2}} + \frac{y}{\sqrt{\tau^2 - y^2}}\right] I_1\left(\sqrt{\tau^2 - y^2}\right). \tag{2.14}$$

The first term in Eq. (2.13), proportional to $\delta(\tau - y)$, accounts for trajectories that reach the target $L$ without tumbles, while the second for trajectories with at least one tumble. The function $\theta(\tau - y)$ in the second contribution expresses the fact that particles need a minimal time $\tau_0 = y$ to reach the target at $L$. On the other hand, on time scales much larger than the tumbling rate, i.e., for $\tau \gg 1$, the first-passage time probability density is given by

$$f_0(\tau|y) \simeq \left(y + \frac{1}{2}\right)(2\pi\tau^3)^{-1/2}. \tag{2.15}$$

The long-time decay $\propto \tau^{-3/2}$ is characteristic of the Brownian motion. Namely, one can show that the first-passage probability density of the Brownian motion $F_{\rm BM}(t|d_L(x))$ in Eq. (1.20) is retrieved by fixing $D = v^2/(2\gamma)$ while taking the limit $v, \gamma \to \infty$.

### 2.2.2 RTPs in a confining potential

For later convenience, we also recall some results concerning the effect of a confining potential $V(x)$ on the dynamics of RTPs, see Ref. [58] for more details. In this case, the motion of the RTP obeys the equation

$$\dot{x}(t) = -V'(x) + v\,\sigma(t), \tag{2.16}$$

with $x(0) = x_0$, and $\sigma(0)$ takes the value $\pm 1$ with equal probability $1/2$. To fix the ideas, let $V(x)$ be the potential corresponding to a harmonic trap with stiffness $\kappa$, i.e.,

$$V(x) = \frac{\kappa}{2}x^2. \tag{2.17}$$

The effect of $V(x)$ on the probability density $\rho(x, t|x_0)$ is twofold. First, it allows the existence of a non-equilibrium stationary state, and of a stationary probability density, that for simplicity we indicate as $\rho(x)$. Second, it confines particles in a finite region $(-c, c)$, whose edges $\pm c$ coincide with the zero-velocity condition for Eq. (2.16), i.e.,

$$V'(x) = v\,\sigma(t), \tag{2.18}$$

yielding $c = v/\kappa$. Figure 2.3a shows the time-evolution of RTPs trajectories in a harmonic potential: between two successive tumbling events, the position of the RTPs with velocity $\pm v$ relaxes exponentially towards the edge $\pm c$. Namely, the dynamics results from the competition between two time $\tau_\gamma$ scales: the average time between two tumbles , and the typical relaxation time $\tau_{\rm rel} \equiv \kappa^{-1}$ in the harmonic trap.

The expression of $\rho(x)$, see Eq. (21) in Ref. [58], is given by

$$\rho(x) = \frac{1}{c}\rho_0\left(\frac{x}{c}\right), \tag{2.19}$$

where we introduce the rescaled distribution

$$\rho_0(x) = \theta(1-x^2)\frac{\Gamma\left(\nu+\frac{1}{2}\right)}{\sqrt{\pi}\,\Gamma(\nu)}(1-x^2)^{\nu-1}, \tag{2.20}$$

where $c = v/\kappa$, $\nu = \gamma/\kappa$, and $\Gamma$ denotes the Gamma function. The behaviour of $\rho(x)$ in correspondence of the edges is described by the exponent $\nu$: if we set $x_\epsilon \equiv c - \epsilon$, with small $\epsilon > 0$, then $\rho(\pm x_\epsilon) \sim \epsilon^{\nu-1}$. It follows that, by varying $\nu$, we can distinguish two main regimes, a *passive* and an *active* one.

The *passive* regime, corresponding to $\nu > 1$, is characterised by a bell-shaped $\rho(x)$ that vanishes at the edges $x \to \pm c$: for $\nu > 2$, the slope of $\rho(x)$ at $\pm c$ is finite, while it diverges for $1 < \nu < 2$; they correspond to the red and green curve in Fig. 2.3b, respectively. On the other hand, in the *active* regime, corresponding to $0 < \nu < 1$, particles tend to accumulate at the edges of the distribution: this results in a U-shaped $\rho(x)$ that diverges as $x \to \pm c$, see blue curve in Fig. 2.3b.

In general, one may consider the confining potential $V_q(x) \equiv \mu|x|^q$, with $q > 1$. Then, the corresponding stationary probability density $\rho_q(x)$ has a finite support $(-c_q, c_q)$, with $c_q \equiv [v/(\mu q)]^{1/(1-p)}$: the modulus of the velocity of the RTPs vanishes at $\pm c_q$ according to the zero velocity condition $V_q'(\pm c_q) = v\sigma(t)$. Moreover, the behaviour of $\rho_q(x)$, in correspondence of points at a distance $\epsilon > 0$ from the edges, is given by

$$\rho_q\left(x = \pm c_q \mp \epsilon\right) \sim \epsilon^{\nu(\mu,q)-1}, \tag{2.21}$$

where the exponent reads

$$\nu(\mu, q) = \left(\frac{\mu_c}{\mu}\right)^{1/(q-1)} \quad \text{with} \quad \mu_c = \left(\frac{v}{q}\right)^{2-q} \left[\frac{\gamma}{q(q-1)}\right]^{q-1}. \tag{2.22}$$

Also in this cases, the *passive* regime is realized for $\nu > 1$, corresponding to $\mu < \mu_c$, the *active* one otherwise.

## 2.3 Effect of the initial position distribution $\rho(x)$

In this Section we study the effect of the (random) initial position of the RTPs on its first-passage time statistics. In particular, we now consider RTPs with an absorbing target at position $L \geq 0$, and we let the initial position of the particle to be drawn from the distribution $\rho(x)$ in Eq. (2.19). Typical trajectories of this process are represented in Fig. 2.3c. It is then natural to investigate the statistics of first-passage time to the target in $x = L$. In particular, we study the properties of the probability density of the first-passage time $F(t)$ and the survival probability $S(t)$. From the previous Section, we know $F_0(t|d_L(x_0))$ and $S_0(t|d_L(x_0))$, respectively, the first-passage time distribution and the survival probability in the case where all particles are initialized at $x_0$, with a distance $d_L(x_0) = |x_0 - L|$ from the target. Then, we calculate the expressions of $F(t)$ and $S(t)$ by averaging $F_0(t|d_L(x_0))$ and $S_0(t|d_L(x_0))$ with respect to the initial position $x_0$: i.e.,

$$F(t) = \int_{-c}^{+c} \mathrm{d}x\, \rho(x) F_0(t|d_L(x)), \quad \text{and} \quad S(t) = \int_{-c}^{+c} \mathrm{d}x\, \rho(x) S_0(t|d_L(x)), \tag{2.23}$$

where we have used $\rho(x)$ in Eq. (2.19) has finite support $(-c, c)$.

In order to describe the properties of the probability density of the first-passage time $F(t)$, we introduce the set of dimensionless variables

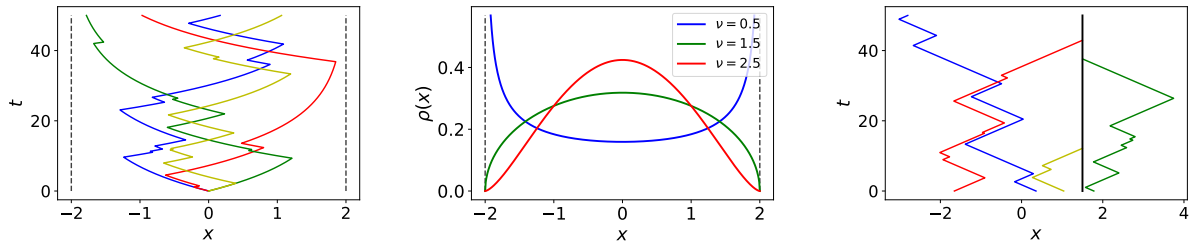
$$a \equiv \frac{L}{l_\gamma} \quad \text{and} \quad b \equiv \frac{L}{c}, \tag{2.24}$$

where $a$ is the ratio between the position $L$ of the target and the typical distance $l_\gamma$ travelled between two tumbles, while $b$ expresses how much the target is extended with respect to the size of the support of $\rho(x)$. The dimensionless first-passage probability $f(\tau)$ can be determined by averaging with respect to the the initial position:

$$f(\tau) = \int_{-1}^{+1} \mathrm{d}z\, \rho_0(z) f_0\left(\tau | \, a\, l(z)\right), \tag{2.25}$$

whose explicit expression is obtained by substituting $f_0(\tau|al(z))$ in Eq. (2.13) into the integral above, finding

$$f(\tau) = \frac{e^{-\tau}}{2} \left\{ \frac{b}{a} \left[\theta\left(1 - z_+\right) \rho_0\left(z_+\right) + \theta\left(1 - |z_-|\right) \rho_0\left(z_-\right)\right] + \int_{\max(-1,z_-)}^{\min(1,z_+)} \mathrm{d}z\, \rho_0(z) g_0\left(\tau | \, a\, l(z)\right) \right\}, \tag{2.26}$$




(a) (b) (c)

Figure 2.3: **RTPs with random initial position.** Panel **(a)** shows typical trajectories of RTPs in the harmonic potential in Eq. (2.17). The dashed grey vertical lines identifies the edges $x = \pm c$ of the dynamics. The value of the parameters are $\gamma = 0.15$, $v = 0.2$ and $\kappa = 0.1$. Panel **(b)** shows the probability distribution $\rho(x) = \rho_0(x/c)/c$ in Eq. (2.20) with $c = 2$ and different choices of $\nu$. *Passive* regime: the red and green line correspond , respectively, to $\nu = 2.5$, and $\nu = 1.5$. *Active* regime: the blue line corresponds to $\nu = 0.5$. Panel **(c)** shows typical trajectories of RTPs with initial position drawn from the probability density $\rho(x)$, corresponding to the green curve of (b). The black vertical line identifies the location of the target at $L = 1.5$. The other values of the parameters of the dynamics are $\gamma = 0.15$, and $v = 0.2$.

where we introduce the variables

$$l(z) \equiv \left|\frac{z}{b} - 1\right|, \quad \text{and} \quad z_\pm(\tau) \equiv b\left(1 \pm \frac{\tau}{a}\right). \tag{2.27}$$

The first two terms in the expression of $f(\tau)$ in Eq. (2.26) correspond to particles that have reached the target for the first time at the (scaled) time $\tau$ without experiencing a tumble, which occurs with a probability $\propto e^{-\tau}$. The first term $\propto \theta\left(1 - |z_+|\right) \rho\left(z_+\right)$ corresponds to particles having a velocity $-v$ (and they thus started from the initial position $L + v\,t$) while the second one $\propto \theta\left(1 - |z_-|\right) \rho\left(z_-\right)$ corresponds to particles having a velocity $+v$ (and they thus started from the initial position $L - v\,t$). The third and last term in Eq. (2.26) corresponds to particles that reached the target for the first time at $\tau$, having experienced at least one tumble. This last term controls the long-time asymptotic behaviour of $f(\tau)$ which reads, at the leading order for large $\tau$,

$$f(\tau) \simeq (2\pi\tau^3)^{-1/2} \left[1/2 + a \int_{-1}^{+1} \mathrm{d}z\, \rho_0(z)\, l(z)\right]; \tag{2.28}$$

for $\rho(x)$ in Eq. (3.18), one finds

$$\int_{-1}^{+1} \mathrm{d}z\, \rho(z)\, l(z) = \begin{cases} 1 & \text{for } b > 1, \\ \frac{\Gamma\left(\nu+\frac{1}{2}\right)}{\sqrt{\pi}\,\Gamma(\nu)} \left[2b\, {}_2F_1\left(\frac{1}{2}, 1-\nu, \frac{3}{2}, b^2\right) + \frac{(1-b^2)^\nu}{\nu b}\right] & \text{for } 0 < b < 1, \end{cases} \tag{2.29}$$

where ${}_2F_1$ denotes the hypergeometric function. The first-passage time probability density in Eq. (2.28) exhibits a standard $\tau^{-3/2}$ decay – as in the Brownian case in Eq. (1.20) – albeit with a different

amplitude that depends on the stationary distribution $\rho(x)$. In the opposite limit of shorter times, the average first-passage time $F(t)$ develops singularities which are due to the two first terms in Eq. (2.26). These singularities arise because of the theta-functions and they thus occur for $|z_\pm| = 1$. The nature of these singularities are different depending on the case where the target $L$ is inside the support $[-c, +c]$ of $\rho(x)$ (corresponding to $b < 1$) or outside of it (corresponding to $b > 1$). We thus discuss these two cases separately.

For $0 < b < 1$, the target is inside the support of $\rho(x)$, i.e., $0 \leq L < c$. Consequently, in this case, there are trajectories that hit the target exactly at time $t = 0$ (namely the trajectories that start from $x = L$). Hence the left edge of the support of $f(\tau)$ is $\tau_0 = 0$. The theta functions in Eq. (2.26) indicate that $f(\tau)$ is singular at $|z_\pm(\tau_\mp)| = 1$, i.e.,

$$\tau_\pm = a\left(\frac{1}{b} \pm 1\right) = \gamma \frac{c \pm L}{v} \ . \tag{2.30}$$

Clearly, $\tau_+$ (respectively $\tau_-$) is the time needed for a particle moving ballistically with velocity $+v$ (respectively $-v$) to reach the target located at $L$. The behaviour of $f(\tau)$ close to these singular points depends on the behaviour of $\rho(x)$ close to the edges at $x = \pm c$. One finds indeed, that for $\epsilon > 0$,

$$\begin{aligned} f(\tau_\pm - \epsilon) &= \frac{e^{-\tau_\pm}}{2} \frac{b}{a} \rho\left(1 - \epsilon \frac{b}{a}\right) + O(\epsilon^0) \\ &= \frac{e^{-\tau_\pm}}{4} \left(\frac{2b}{a}\right)^\nu N(\nu)\, \epsilon^{\nu-1} + O\left(\epsilon^0\right) \ . \end{aligned} \tag{2.31}$$

Hence, in the *active* regime $0 < \nu < 1$, $f(\tau)$ diverges to the left of $\tau_\pm$. This divergence comes from particles that are initially located near the edges, where $\rho(x)$ exhibits a divergence in this case (see Fig. 2.3), and reach the target from $\mp c$ at the time $\tau_\pm$ without tumbling. In the *passive* regime $\nu > 1$, $f(\tau)$ is continuous at $\tau_\pm$ but it still exhibits a singular behaviour close to these points $\tau_\pm$. For instance, for $1 < \nu < 2$ its first derivative diverges on the left of $\tau_\pm$. Note that the average first-passage time is always finite at $\tau_\pm + \epsilon$, i.e.,

$$\begin{aligned} f(\tau_+ + \epsilon) =& \frac{e^{-\tau_+}}{2} \int_{-1}^{+1} \mathrm{d}z\, \rho(z) g_0(\tau_+ | l(z)) + O(\epsilon), \\ f(\tau_- + \epsilon) =& \frac{e^{-\tau_-}}{2} \left[ \int_{2b-1}^{+1} \mathrm{d}z\, \rho(z) g_0(\tau_- | l(z)) + \rho(2b-1) + O(\epsilon) \right], \end{aligned} \tag{2.32}$$

in agreement with the fact that the particles reaching the target at $\tau_\pm + \epsilon$ have experienced at least one tumble. All these features are summarized in Fig. 2.4a, which shows the first-passage time probability density $F(t) = \gamma f(\tau = t\gamma)$ in the case where $0 < b < 1$ for various values of the exponent $\nu$.

For $b > 1$, the target is outside the support of $\rho(x)$, i.e., $L > c$. In this case, the minimal time to reach $L$, by $\tau_0 = |\tau_-| > 0$ (note that, correspondingly, $\tau_- = (c - L)/v < 0$). This simply corresponds to the time needed for the particles initially located at $+c$ and moving ballistically with velocity $+v$ (i.e., without tumbling) to reach the target located at $L > c$. In this case, as for $0 < b < 1$

discussed above, we find that the leading contribution to $f(|\tau_\mp| \pm \epsilon)$ is the same as in Eq. (2.31) with $|\tau_\pm|$ at replacing $\tau_\pm$. In the active regime, the divergence of $f(\tau)$ at $|\tau_\mp| \pm \epsilon$ corresponds to fronts of particles, initially at $\pm c$, that hit the target with constant velocity $\pm v$ without tumbling. As for the case $b < 1$, we have that $f(\tau_+ + \epsilon)$ is given by Eq. (2.32), while $f(|\tau_-| - \epsilon) = 0$ due to the fact that $|\tau_-| - \epsilon < \tau_0$ is outside of the support of $f(\tau)$. Figure 2.4c shows the behaviour of $F(t)$ for $b > 1$ for various values of $\nu$.

In general, the properties discussed above are found whenever the initial probability density $\rho(x)$ has similar qualitative features: a finite support, and a transition from *passive* to *active* regime. For example, the same considerations apply to $\rho_q(x)$ in Eq. (2.21). As in the case of the harmonic trap, the qualitative properties of the average first-passage time depend only on the behaviour of $\rho_q(x)$ near the edges of its support. Namely, except for the potential-dependent prefactor, $f(\tau)$ show the same scaling as in Eq. (2.31): for $0 < b < 1$, $f(\tau_\pm - \epsilon) \propto \epsilon^{\nu(\mu,q)-1}$, while for $b > 1$, one has $f(|\tau_\pm| \mp \epsilon) \propto \epsilon^{\nu(\mu,q)-1}$.

## 2.4 RTPs with stochastic resetting

In this Section, we study the dynamics of an RTP whose velocity and position are both reset at random times as follows. At the initial time, the position of the particle is randomly distributed according to the distribution $\rho(x)$ in Eq. (2.19) and it starts with a velocity $\pm v_0$ with equal probability. The particle then evolves according to Eq. (2.1) for a certain random time $\tau$, which is distributed according to an exponential distribution $P(\tau) = r\, e^{-r\tau}$, after which the velocity *and* the position of the particles are reset. The new velocity is set randomly to $\pm v_0$ with equal probability while the resetting position of the particle is again distributed according to the distribution $\rho(x)$. The resetting protocol is thus similar to the "fully-randomized" protocol introduced in Ref. [72] except that here the resetting position is chosen randomly from $\rho(x)$ at each resetting event.

Our main focus here is on the first-passage time to a target, modeled by an absorbing boundary, at $x = L$. We thus denote by $S_r(t)$ the survival probability of the particle up to time $t$, in the presence of resetting. Note that $S_r(t)$ is also averaged over the initial position. Following Refs. [72, 74], we can write a renewal equation for the survival probability $S_r(t)$ of the particle up to time $t$, in the presence of resetting. It reads [72, 74]:

$$S_r(t) = e^{-rt} S_0(t) + r \int_0^t \mathrm{d}\tau\, e^{-r\tau} S_0(\tau) S_r(t-\tau)\ , \tag{2.33}$$

where $S_0(t)$ is the survival probability of the RTP in the absence of resetting. This equation can be understood as follows. The first term accounts for trajectories that undergo no reset, while, the second, for trajectories that reset for the first time at $\tau$. Taking the Laplace transform with respect to $t$ of Eq. (2.33) allows us to convert the time convolution into a simple product, i.e.,

$$\tilde{S}_r(s) = [1 + r\tilde{S}_r(s)]\tilde{S}_0(s+r), \tag{2.34}$$

where $\tilde{S}_r(s) = \int_0^\infty \mathrm{d}t\, e^{-st} S_r(t)$. The Laplace transform of the survival probability is then given by

$$\tilde{S}_r(s) = \frac{\tilde{S}_0(s+r)}{1 - r\tilde{S}_0(s+r)}\ , \tag{2.35}$$

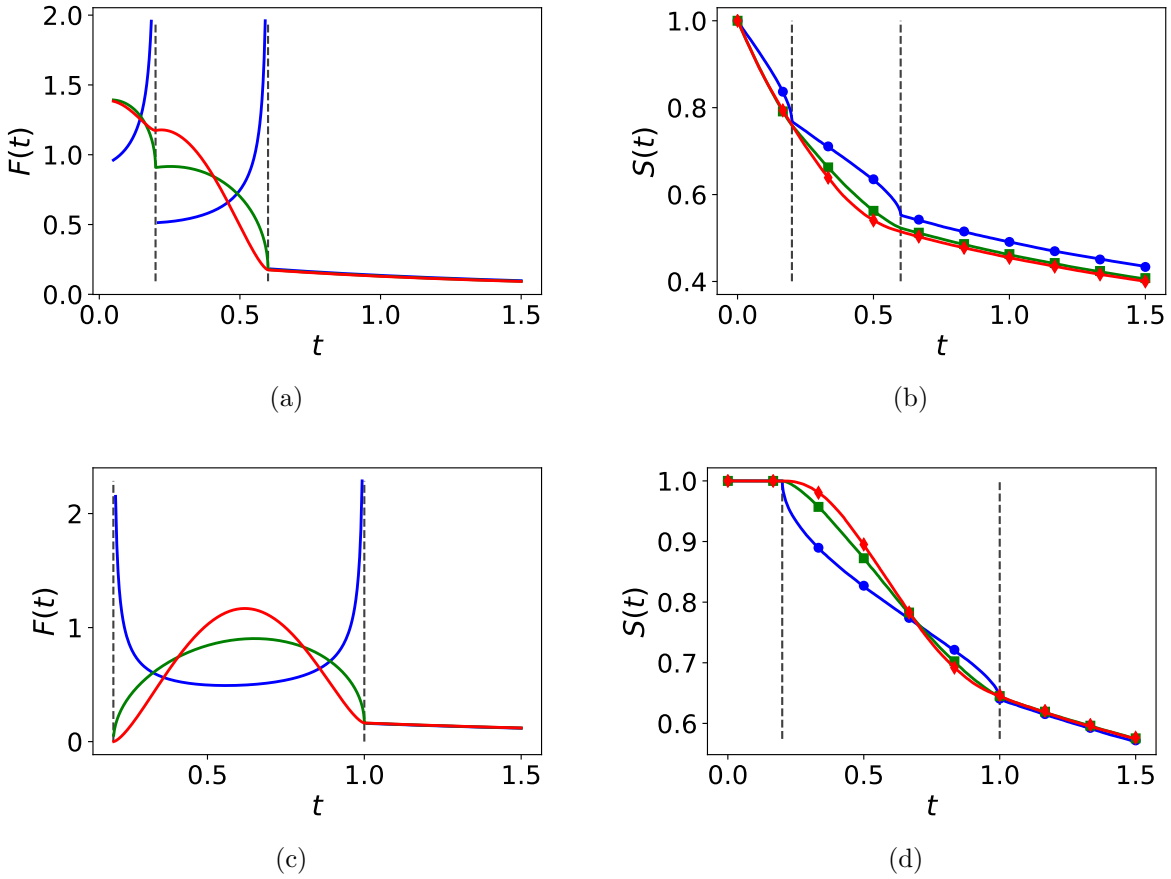



Figure 2.4: **First-passage time statistics.** In panel **(a)** and **(b)** we report, respectively, the first-passage time probability $F(t)$ density and the survival $S(t)$ probability in the case where the target is inside the support of the initial distribution $\rho(x)$ of the RTPs, i.e., $b < 1$. The parameters are: $L = 1$, $c = 2$, $\gamma = 1$, $v = 5$, and $\nu = 0.5$ (blue curve), $\nu = 1.5$ (green curve), $\nu = 2.5$ (red curve). Symbols in panel (b) represent the analytical expression in Eq. (2.26), while the solid line corresponds to numerical simulations. The dashed vertical lines indicate $t_\pm = \tau_\pm/\gamma$, the times at which particles starting at the edges $\pm c$ reach the target without tumbling. Analogously, in panels **(c)** and **(d)** we report $F(t)$ and $S(t)$ for $b > 1$, with $L = 3$. In this case the support of $F(t)$ is limited from below by $t_- = |\tau_-|/\gamma$, the time at which particles from $+c$ hit the target at $L > c$ without tumbling. The second vertical dashed line corresponds to $t_+ = \tau_+/\gamma$. Numerical predictions are computed by simulating $N = 10^5$ trajectories with a time step $\Delta t = 10^{-4}$. Error bars are not visible on the scale of the plot.

where $\tilde{S}_0(s)$ is given by Eq. (2.11). The first-passage time distribution $F_r(t)$ is obtained from $S_r(t)$ as $F_r(t) = -\dot{S}_r(t)$ the mean first-passage-time to the target is thus given by $\langle t_f \rangle = \tilde{S}_r(0)$, yielding,

from Eq. (2.35)

$$\langle t_f \rangle(r) = \frac{\tilde{S}_0(r)}{1 - r\tilde{S}_0(r)}. \tag{2.36}$$

In order to understand the behaviour of $\langle t_f \rangle$ as a function of $r$, we consider separately the two limits $r \to 0$ and $r \to \infty$. The small-$r$ limit of $\langle t_f \rangle$ is found by Taylor-expanding Eqs. (2.36) and (2.35) with respect to $r$, yielding

$$\langle t_f \rangle(r) = \frac{1}{\sqrt{2\gamma r}} \left( 1 + \frac{2\gamma}{v} \int_{-c}^{+c} \mathrm{d}x\, \rho(x) d_L(x) \right) + O(r^0), \tag{2.37}$$

where the convergence of the integral follows from the fact that $\rho(x)$ has finite first moment. As for the Brownian motion, Eq. (2.37) describes the divergence of the of mean first-passage time as $r^{-1/2}$ for $r \to 0$.

The large-$r$ limit is understood by analysing the behavior of the integral

$$\mathcal{I}(r) \equiv \int_{-c}^{+c} \mathrm{d}x\, \rho(x) \exp\left(-\lambda(r) d_L(x)\right), \tag{2.38}$$

keeping in mind that $\rho(x)$ has a finite support on the interval $(-c, c)$. We split the analysis by first considering the case where the target is inside the support of $\rho(x)$, i.e., $|L| < c$. We start by evaluating the asymptotic behavior of the integral $\mathcal{I}(r)$ in powers of $r^{-1}$ with $r \to \infty$:

$$\begin{aligned} \mathcal{I}(r) &= \frac{1}{\lambda(r)} \int_{-\lambda(r)(L+c)}^{\lambda(r)(c-L)} \mathrm{d}y\, p\left( \frac{y}{\lambda(r)} + L \right) e^{-|y|} \\ &= \frac{2v}{r} \rho(L) + O(r^{-2}); \end{aligned} \tag{2.39}$$

in the first line we make the change of variables $y = (x - L)\lambda(r)$, while in the second we expand $\rho(y/\lambda(r) + L)$ in power of $r^{-1}$ and we integrate over $y$. Note that the $\rho(x)$ expansion relies on the fact that the target in $L$ is in the support $(-c, c)$, and that $\rho(x)$ is sufficiently regular in it. By direct substitution of Eq. (2.39) in Eq. (2.36), we get

$$\langle t_f \rangle(r) = \frac{1}{v\, \rho(L)} + O(r^{-1}), \tag{2.40}$$

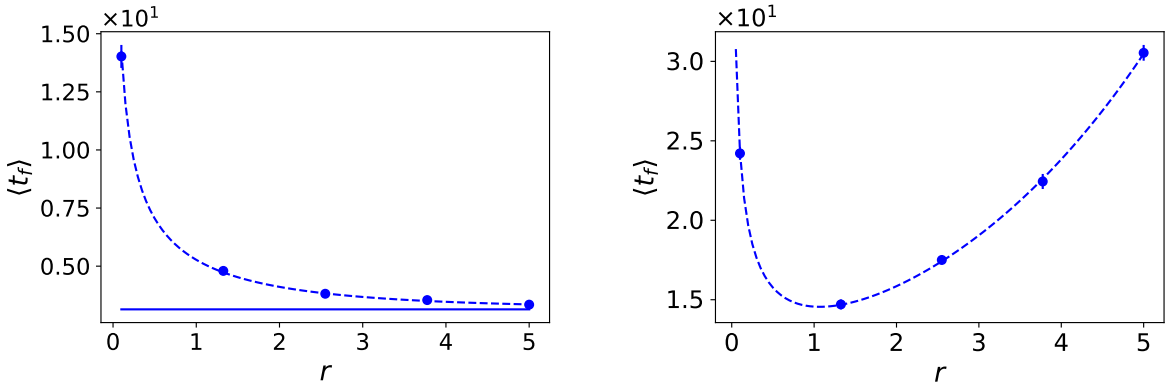
which tells us that $\langle t_f \rangle(r)$ tends to a constant in the large $r$ limit, see Fig. 2.5a. Equation (2.40) expresses the fact for very large rate $r$ the first-passage time depends on how probable is to reset close to the target and how fast particles move.

In the case with $L > c$, we can bound the integral in Eq. (2.38) according to

$$\mathcal{I}(r) = e^{-\lambda(r)L} \int_{-c}^{c} \mathrm{d}x\, \rho(x) e^{\lambda(r)x} \leq e^{-\lambda(r)(L-c)}, \tag{2.41}$$

where we have exploited the monotonicity of the exponential. Finally, by collecting the results above, we provide a lower bound for the first-passage time

$$\langle t_f \rangle(r) \geq \frac{1}{r} \left[ \frac{2\gamma e^{\lambda(r)(L-c)}}{r + 2\gamma - v\lambda(r)} - 1 \right], \tag{2.42}$$




(a) (b)

Figure 2.5: **RTPs with stochastic resetting.** Mean first-passage time $\langle t_f \rangle(r)$ in Eq. (2.36) as a function of the resetting rate $r$. Panel **(a)** displays $\langle t_f \rangle$ when target is inside the support of $\rho(x)$, i.e., $b < 1$ ($L = 2$), and the corresponding asymptotic value $(v\rho(L))^{-1}$ is denoted by the horizontal line. In panel **(b)**, the target is outside the support, i.e., $b > 1$ ($L = 3$). Parameters are $v = 1.5$, $\gamma = 2.5$, $c = 2.5$, and $\nu = 0.5$. In both figures, the dashed line represents the analytical expression in Eq. (2.36), while dots refer to numerical predictions, computed by simulating $N = 4 \times 10^4$ trajectories with time step $\Delta t = 10^{-3}$. Error bars, not always visible on the scale of the plot, are computed by standard deviation over the ensemble average.

which diverges exponentially as $r \to \infty$, reflecting the fact that the probability to hit the target outside of the support decreases exponentially at large-$r$. Accordingly, for $b > 1$ there always exists a minimum of the mean first-passage time as a function of $r$, see Fig. 2.5b.

Having understood the behaviour of $\langle t_f \rangle$ for rare and frequent resetting, we now address the problem of how to describe qualitatively the properties of the mean first-passage time at intermediate values of $r$. For this purpose, it is convenient to consider the dimensionless mean first-passage time $\langle \tau_f \rangle$, which is expressed in terms of the dimensionless variables

$$X \equiv L\lambda(r), \tag{2.43}$$

with $a$ and $b$ in Eq. (2.24), as

$$\langle \tau_f \rangle \equiv \frac{\langle t_f \rangle \gamma}{8a^2} = \frac{1}{4aX^2}\left[(2a + \sqrt{4a^2 + X^2})\left(\frac{1}{\rho_r(X,b)} - 1\right) + \frac{X}{\rho_r(X,b)}\right], \tag{2.44}$$

where we denote $\rho_r(X,b) \equiv \int_{-1}^{+1} \mathrm{d}z\, \rho_0(z)\, e^{-X\, l(z)}$. In this new set of dimensionless variables, the large $r$ limit of $\langle \tau_f \rangle$ in Eq. (2.44) for $b < 1$ corresponds to

$$\tau_\infty \equiv \lim_{X \to \infty} \langle \tau_f \rangle = \frac{1}{4ab\, \rho_0(b)}. \tag{2.45}$$

As we will see in next section, the behaviour of $\tau_\infty$ with respect to the parameters $a$ and $b < 1$ helps us to understand the one of $\langle \tau_f \rangle$ in the case of finite resetting, i.e., for $X = O(1)$.

### 2.4.1 Brownian motion

Despite the simplification due to the introduction of dimensionless quantities, the direct analysis of the behaviour of $\langle \tau_f \rangle$ depending on the full set of variables is far from being an easy task. For this reason, we start by considering its Brownian limit $\gamma \to \infty$, $v \to \infty$ with constant $D = v^2/(2\gamma)$: it corresponds to $a \to \infty$ (see Eq. (2.24)), and $X = L\sqrt{r/D}$ in Eq. (2.43). In this way, $b$ is the only relevant parameter of the system, while we treat $X$ as a variable. Once understood the behaviour of $\langle \tau_f \rangle$ in the Brownian limit, we can smoothly extend the analysis to RTPs, i.e., for finite $a$. Note, however, that the Brownian limit concerns only to the dynamics of the particle and not the probability density $\rho(x)$, which we assume to be still given by Eq. (3.18). Accordingly, $\langle \tau_f \rangle$ in Eq. (2.44) becomes

$$\langle \tau_f \rangle = \frac{1}{X^2} \left( \frac{1}{\rho_r(X, b)} - 1 \right), \tag{2.46}$$

which corresponds to Eq. (39) in Ref. [22].

The dimensionless variable $X$ in Eq. (2.43) is equal to the square root of the ratio of two time scales: $\tau_d = L^2/D$ the typical time associated to covering a distance $L$ by diffusion, and $\tau_r = 1/r$ the mean time between two successive resetting events, i.e., $X = \sqrt{\tau_d/\tau_r}$. For very rare resetting $X \ll 1$, that is $\tau_d \ll \tau_r$, the mean first-passage time diverges as $X^{-1}$, in agreement with Eq. (2.37).

In the limit of infinitely frequent resetting $X \to \infty$, the mean first-passage time $\langle \tau_f \rangle$ attains the value $\tau_\infty = 0$. Indeed, from Eq. (2.45) we can check that as we approach the Brownian limit, i.e., $a$ increases, the asymptotic value $\tau_\infty$ of $\langle \tau_f \rangle$ decreases until it vanishes. Actually, for $X \gg 1$, the main contribution to $\langle \tau_f \rangle$ comes from particles that reset in a neighborhood of the target at position $L$ of radius $\mathrm{d}l$, where $\mathrm{d}l$ is the typical infinitesimal displacement between two successive resets: $\mathrm{d}l_{\mathrm{BM}} = \sqrt{2D\,\mathrm{d}t}$ for the Brownian motion, and $\mathrm{d}l_{\mathrm{RT}} = v\,\mathrm{d}t$ for RTPs. The amount of particles that hit the target between two resetting events is then given by $\rho(L)\mathrm{d}l$. It follows that, being $\rho(L)$ the same for both dynamics, and $\mathrm{d}l_{\mathrm{BM}} > \mathrm{d}l_{\mathrm{RT}}$, for $X \gg 1$ (strong resetting), Brownian particles effectively reach the target faster than RTPs. This explains why the large $X$-limit $\tau_\infty$ of the mean first-passage time decreases upon increasing $a$.

The intermediate behaviour observed at $X = O(1)$ depends on the details of the resetting distribution and the location of the target. Qualitatively, if the peak of $\rho(x)$ is close to the target, $\langle \tau_f \rangle$ decreases monotonically upon increasing a $X$. In this case, the particles are concentrated around the target, and, the more they reset, the faster they get absorbed. Otherwise, if the distance of the maximum of $\rho(x)$ from $L$ is of order $c$, a local maximum $\tau_{\max}$ and a local minimum $\tau_{\min}$ appear in $\langle \tau_f \rangle$. A typical realization of this scenario is reported in Fig. 2.6a, where we plot $\langle \tau_f \rangle$ in Eq. (2.46) with $L \simeq c$ ($b = 0.95$). For small values of $\nu$, the distribution $\rho(x)$ is maximal at the edges $\pm c$, i.e., close to the target location. Accordingly, the larger $X$ is, the more particles are constrained close to the target, and the faster they reach it. Upon increasing $\nu$ there is a critical value $\nu_c(b)$ above which $\langle \tau_f \rangle$ displays a local minimum $\tau_{\min}$ at $X_{\min}$, see Fig. 2.6b and 2.6c. This minimum appears whenever the target location $L$ is sufficiently far from the region where particles accumulate most after a resetting event. Note that $\nu_c$ depends on the parameter $b$, hence is not universal. However, it is possible to estimate its value numerically from the expression of $\langle \tau_f \rangle$ by studying its first derivative. We encounter an analogous behavior for $L \simeq 0$: for large values of $\nu$, the maximum of $\rho(x)$ is close to the target and $\langle \tau_f \rangle$ decreases monotonically upon increasing $X$ (red curve in

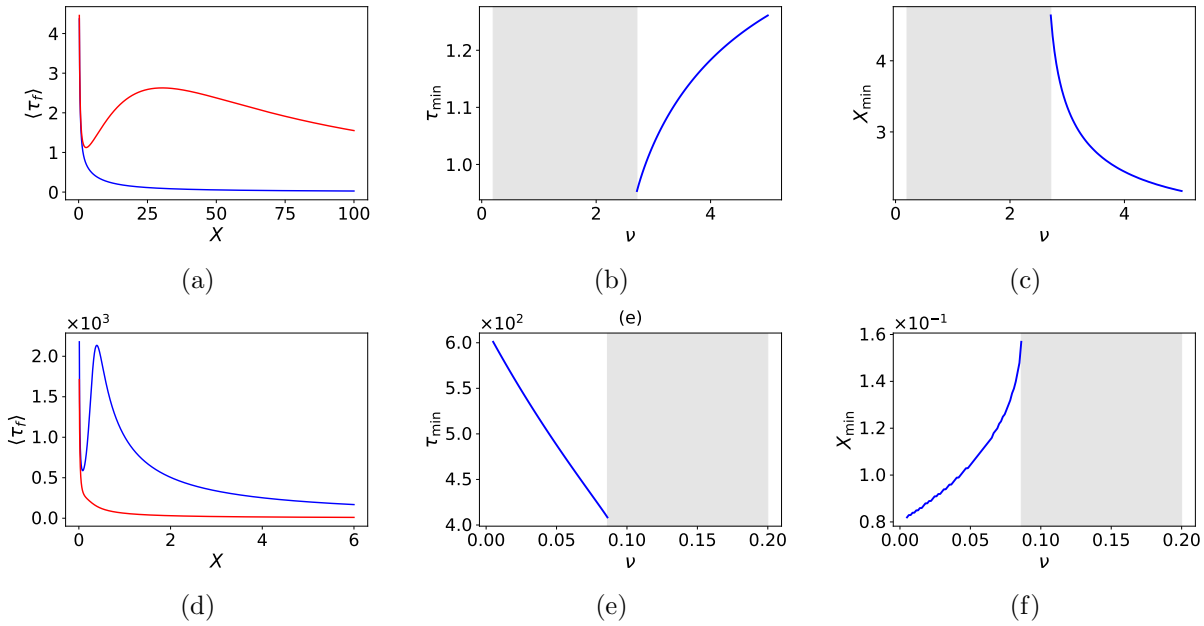
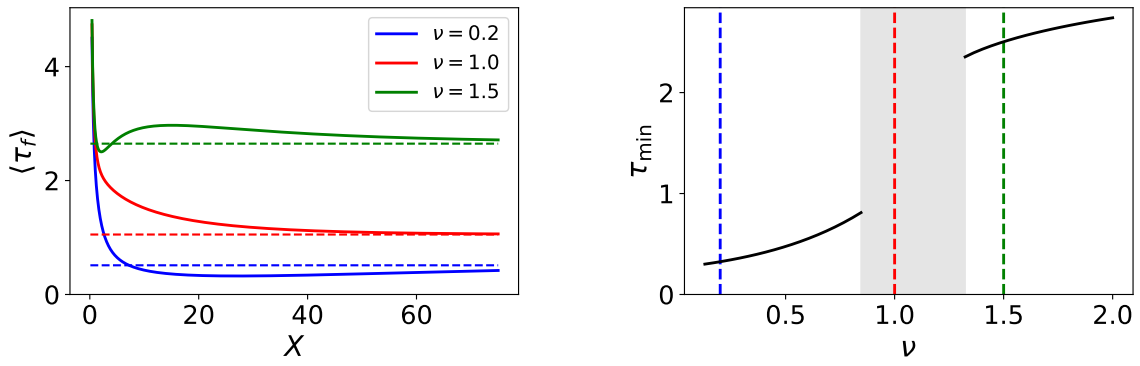



Figure 2.6: **Brownian motion.** Panel **(a)** displays two representative $\langle \tau_f \rangle$ as a function of $X$ according to Eq. (2.46): the blue curve corresponds to $\nu = 1.5$, while the red one to $\nu = 3.5$. In panel **(b)** and **(c)** we show how $\tau_{\min}$ and $X_{\min}$ vary depend on the exponent $\nu$ for $b = 0.95$ in Eq. (2.24). The gray area indicates the absence of a local minimum, meaning that for $\nu < \nu_c(b = 0.95) \simeq 2.7$, $\langle \tau_f \rangle$ is a monotonically decreasing function of $X$. For $\nu > \nu_c$, instead, we observe a minimum at $\tau_{\min}$. Analogously, in **(d)** we report $\langle \tau_f \rangle$ for $\nu = 0.01$ (blue curve), and $\nu = 0.2$ (red curve) for $b = 0.05$. Panel **(e)** and **(f)** display how $\tau_{\min}$ and $X_{\min}$ vary as function of the exponent $\nu$: for $\nu > \nu_c(b = 0.05) \simeq 0.087$, the mean first-passage time $\langle \tau_f \rangle$ is a monotonically decreasing function of $X$. In both cases, Eq. (2.46) implies that $\langle \tau_f \rangle(X_{\min}) \sim X_{\min}^{-2}$.

Fig. 2.6d); for small values of $\nu$ (blue curve in Fig. 2.6d), the maximal value of $\rho(x)$ is attained at the edges $\pm c$, at a distance $\simeq c$ from the target, inducing the presence of a minimum mean first-passage time $\tau_{\min}$ (Fig. 2.6e) at $X_{\min}$ (Fig. 2.6f). In all these cases, whenever $\langle \tau_f \rangle$ displays a minimum, Eq. (2.46) implies the scaling $\tau_{\min} \sim X_{\min}^{-2}$.

### 2.4.2 Run-and-tumble particles

For RTPs, i.e., with finite $a$ in Eq. (2.24), the mean first-passage time $\langle \tau_f \rangle$ in Eq. (2.44) displays a richer behaviour. In particular, we have seen that in the Brownian limit, when the target is close to point where $\rho(x)$ attains its maximum, the mean first-passage time $\langle \tau_f \rangle$ decreases monotonically upon increasing $X$. For RTPs, this scenario is strongly affected by the introduction of the time scale $\tau_\gamma$. Namely, the asymptotic limit $\tau_\infty$ is no longer vanishes, and it may induce the emergence of a local minimum. This phenomenon can be easily understood by comparing the blue curve in Fig. 2.6a and the blue curve in Fig. 2.7a. The former represents $\langle \tau_f \rangle$ for the Brownian particle ($a \to \infty$) with $b = 0.95$, and a small value of $\nu$, for which it is a monotonic decreasing function of




(a) (b)

Figure 2.7: **Run-and-tumble particles.** In panel **(a)**, the dimensionless mean first-passage time $\langle \tau_f \rangle$ in Eq. (2.44) is plotted as a function of $X$ for various values of the exponent $\nu$, with parameters $b = 0.95$, and $a = 0.5$. In panel **(b)**, the value $\tau_{\min}$ of the minimum as a function of the exponent $\nu$: the dashed vertical lines identify the values of $\nu$ used to plot with the same colors, the curves of $\langle \tau_f \rangle$ in (a), while the grey area marks the range of $\nu \in (\nu_c^{(1)}, \nu_c^{(2)})$ for which no minima appear in $\langle \tau_f \rangle$, with $\nu_c^{(1)} \simeq 0.89$, and $\nu_c^{(2)} \simeq 1.32$.

$X$. The latter shows the same quantity for the RTP ($a = 0.5$): the non-vanishing asymptotic limit $\tau_\infty$ forces $\langle \tau_f \rangle$ to have a local minimum. As shown in Fig 2.7b, for RTPs we have two critical values of $\nu$, i.e., $\nu_c^{(1)}(a, b)$ and $\nu_c^{(2)}(a, b)$, such that if $\nu \in (\nu_c^{(1)}, \nu_c^{(2)})$ the mean first-passage time $\langle \tau_f \rangle$ has no minima. The right branch ($\nu > \nu_c^{(2)}$) of Fig. 2.7b coincides with the curve appearing in Fig. 2.6b, whereas the left branch ($\nu < \nu_c^{(1)}$) is due to the fact that $\tau_\infty$ is strictly positive (finite $\tau_\gamma$). As for the Brownian particle, an analogous scenario is observed for $b \simeq 1$ ($L \simeq c$), sufficiently small values of $a$, and large values of $\nu$.

## 2.5 Periodic resetting and experimental protocol

Motivated by recent developments with Brownian particles [22], we are interested in designing a protocol that reproduces experimentally periodic resetting of RTPs. As anticipated, both instantaneous and point-wise resetting cannot be implemented in a actual physical systems. Inspired by Refs. [22], we consider the following *experimental* protocol. Initially, we let the dynamics of the RTP relax in a harmonic trap, with potential $V(x) = \kappa x^2/2$, for a time $T_{\rm eq}$. At the end of this *equilibration* phase, the particle position is distributed according to Eq. (3.18): this is true only if the typical relaxation time of the particle in the harmonic trap $\tau_{\rm rel} \equiv \kappa^{-1}$ is much smaller than $T_{\rm eq}$. The choice of this potential profile is not arbitrary, but it is motivated by the fact that it can be experimentally realized via optical tweezers. At the end of this *equilibration* phase, the confining potential is switched off and the particle resumes its free RT dynamics for a given period $T$. During this *search* phase, we keep track of the first-passage time to a target at position $L$. After a time $T$, the potential is switched on, a new equilibration phase starts, and measurements on the system

are suspended. The process goes on by alternating search and equilibration phases. Effectively, the motion of the RTP consists of a periodic resetting after a time $T$ to points drawn from the probability density $\rho(x)$. As for the case of Brownian particles [22], it can be shown that the mean first-passage time $\langle t_f \rangle$ is given by

$$\langle t_f \rangle = \frac{\int_0^T \mathrm{d}\tau \, S(\tau)}{1 - S(T)}, \tag{2.47}$$

where $S(t) = \int_{-\infty}^{+\infty} \mathrm{d}x \, \rho(x) S_0(t|x)$ is the survival probability of the same process without resetting, and initial position distribution $\rho(x)$. Qualitatively the properties of $\langle t_f \rangle$ are similar to those of stochastic resetting treated in the previous Section 2.4. For $T_{\mathrm{eq}} \gg \tau_{\mathrm{rel}}$, Eq. (2.47) predicts the mean first-passage time of the experimental protocol. On the other hand, as $T_{\mathrm{eq}}$ vanishes, the mean first-passage time reduces to the one of free RTPs, which is divergent. This two regimes are easily spotted in Fig. 2.8: at large $T_{\mathrm{eq}} \gtrsim 2\tau_{\mathrm{rel}}$ the mean first-passage time $\langle t_f \rangle$ is well approximated by (2.47), while as $T_{\mathrm{eq}}$ smaller, $\langle t_f \rangle$ increases until it diverges in the reset-free limit.

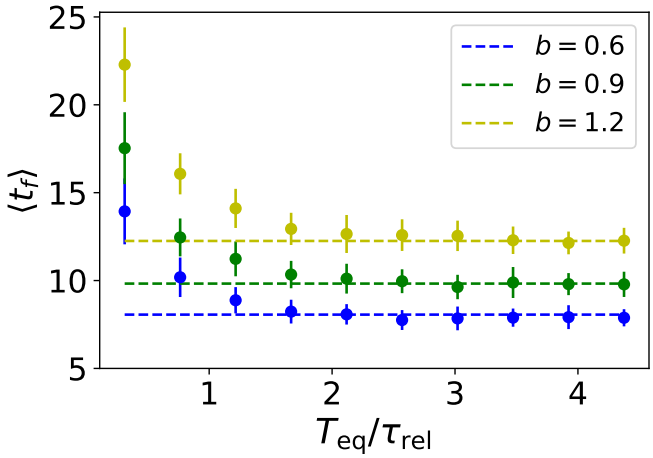



Figure 2.8: **Experimental protocol.** Each of the three dotted curves represents the mean first-passage time as a function of the equilibration time $T_{\mathrm{eq}}/\tau_{\mathrm{rel}}$, for various values of $b = L/c$. The dashed horizontal line corresponds to the prediction of Eq. (2.47), i.e., with full equilibration. The values of $\langle t_f \rangle$ have been computed numerically via $N = 2.5 \times 10^4$ realizations of the process $x(t)$ with time step $\Delta t = 0.005$, with parameters $\tau_{\mathrm{rel}} = 0.5$, $v = 5$, $\gamma = 2.5$, $c = v/\kappa = 2.5$, and $\nu = \gamma/\kappa = 1.25$. Error bars are given by standard deviation.

## 2.6 Conclusions

In this Chapter we have studied how the statistics of the first-passage time for RTPs to a target in $L$, reported in Section 2.2, is modified by the introduction of two additional ingredients in their dynamics. In Section 2.3, we let the initial position of the particles to be drawn from the probability density $\rho(x)$ and we have analysed how this affects the first-passage probability density. In particular, we choose $\rho(x)$ in Eq. (2.20) to be the stationary probability density of the position

of a RTP in a harmonic potential. One of the main features of this $\rho(x)$ is that it has a finite support $(-c, c)$. Moreover, by tuning the parameters of the system, the distribution $\rho(x)$ changes from the *passive* regime, with a bell-shaped and vanishing at the edges $\rho(\pm c) = 0$, to an *active* one, characterized by the accumulation of particles at the edges, i.e., $\lim_{x\to\pm c^{\mp}} \rho(x) = +\infty$. The two regimes affect differently the properties of the first-passage time probability density $F(t)$, and the survival probability $S(t)$: possible divergences in $\rho(x)$ are inherited by the first-passage statistics. In Section 2.4 we have introduced stochastic resetting into the dynamics analysed in Section 2.3: we let particles reset with constant rate $r$ to a point drawn from $\rho(x)$. As a consequence of the fact that $\rho(x)$ has a finite support, we can qualitatively distinguish two behaviours of the mean first-passage time $\langle t_f \rangle$. For frequent resetting, and the target inside the support of $\rho(x)$ (i.e., $L < c$), $\langle t_f \rangle$ attains the constant value $(v\rho(L))^{-1}$: only particles resetting close to the target contribute to $\langle t_f \rangle$. For $L > c$ and frequent resetting, particles are constrained far from $L$ and $\langle t_f \rangle$ diverges exponentially. Then, we qualitatively discuss how the position of the target and the shape of the distribution $\rho(x)$ are responsible for the emergence of an (optimal) minimal value of $\langle t_f \rangle$. In Section 2.5, we have considered RTPs resetting periodically over a period $T$ to the distribution $\rho(x)$. Finally, we show how the analytical expression of the mean first-passage time in Eq. (2.47) allows us to make contact with experimental setup designed in Ref. [22] in the case of RTPs. In this sense, it would be interesting to compare these results with actual experimental measurements. Moreover, from a theoretical point of view, it may be worth investigating the effect on the statistics of first-passage time of a distribution with finite support for the initial position of particles belonging to other classes of active processes.

# Chapter 3

# Modelling active non-Markovian oscillations

## 3.1 Introduction

As observed in several branches of natural sciences [15, 38, 53, 77, 102, 110, 169, 170, 215], most non-equilibrium systems *actively* sustain their dynamics by dissipating energy in their environment and by producing entropy. Important examples are *active oscillators*, the effective mesoscopic degrees of freedom if which are described by oscillating variables. In nature these oscillators drive climate changes, sustain heart beat, facilitate vocal and auditory systems, support neural signalling and circadian rhythms [5, 18, 24, 35, 44, 45, 76, 102, 110, 130, 132, 135, 137, 148, 153, 154, 176, 182, 212, 219, 220, 221, 225] etc. In this Chapter, we focus on those which are responsible for sound transduction in bullfrog's sacculus, for which experimental data are available [102, 132, 130].

Active oscillatory motion is often interpreted as relaxation oscillations or noisy bistable oscillations, which can be modelled by nonlinear stochastic Van der Pol and Duffing equations, two examples of noisy systems close to a Hopf bifurcation [5, 17, 18, 24, 35, 44, 45, 76, 102, 129, 130, 132, 135, 137, 148, 153, 154, 176, 182, 212, 219, 220, 221, 225], respectively. These two distinct dynamical regimes are not always easy to distinguish in experiments. For this reason, it has been proposed an alternative way to construct a system displaying bistable oscillations consists in letting one of its degrees of freedom to be a two-state stochastic process, e.g., telegraphic noise [4, 34, 94, 101, 112, 128, 144, 233, 234].

In this Chapter, we propose a stochastic linear model for self-sustained active bistable oscillations. The model generalizes the Ornstein-Uhlenbeck process by identifying the equilibrium position (i.e., the center of the harmonic potential) to be determined by a dichotomous process, which represents a non-Markovian generalization of the telegraphic noise. Notably, depending on the distributions of the time passed between two consecutive jumps of this two-state noise, the model reproduce a wide variety of bistable oscillations including Markovian and non-Markovian switching processes. In spite of the non-Markovianity of the system, we can obtain exact analytical expressions for several of dynamical and thermodynamic quantities characterizing its non-equilibrium nature. As a relevant application, we use our model to reproduce recordings of the spontaneous motion in bullfrog hair-cell bundles and estimate the dissipated power, which is yet experimentally inacces-

sible but crucial for interpreting the energetics of the system. In previous works, the dynamics of the microscopic degrees of freedom of the hair bundles is modelled by coupled stochastic differential equations with non-linear forces [130, 132]. On the other hand, our description is effective but linear, allowing us to provide theoretical predictions for the observables mentioned above. The content of this Chapter is organised in the following way. In Sec. 3.2, we present the model and we introduce its qualitative properties. In Sec. 3.3, we discuss the formal derivation of its statistics, enabling us to quantitatively discuss some of the main features of the system. In Sec. 3.4, we address the calculation of the power spectrum, which provides useful informations on the non-Markovian nature of the oscillator. Eventually, in Sec. 3.6, we apply our analytical results to make predictions on the energetics of hair-cell bundle spontaneous oscillations.

## 3.2 Active non-Markovian oscillator

In this Section, we introduce a minimal model describing a linear non-Markovian active oscillator. The building block for the system is a Brownian particle relaxing towards the minimum of a confining potential. If we let the center of this potential switch randomly between two different positions, the motion of the particle consists in an alternate relaxation in the direction of these two equilibrium points. Thus, the resulting dynamics is oscillatory, as long as the relaxation time in the traps are smaller than the permanence time in the corresponding potential.

To fix ideas, we consider the harmonic potential

$$V(x(t), c(t)) = \frac{\kappa}{2} \left[x(t) - c(t)\right]^2 , \tag{3.1}$$

with stiffness $\kappa$, and time-dependent center $c(t)$. Hence, the particle position $x(t)$ satisfies the Langevin equation of the Ornstein-Uhlenbeck process

$$\gamma \, \dot{x}(t) = -\kappa[x(t) - c(t)] + \xi(t), \tag{3.2}$$

with initial condition $x(0) = x_0$. Here $\gamma$ is the effective friction coefficient, while $\xi(t)$ is a Gaussian white noise with zero mean $\langle \xi(t) \rangle = 0$ and autocorrelation $\langle \xi(t_1)\xi(t_2) \rangle = 2\gamma D \delta(t_1 - t_2)$, see Appendix A.1. The effective diffusion coefficient $D = k_B T/\gamma$ is related to the temperature via Einstein relation. As anticipated, we choose the center $c(t)$ to be a dichotomous stochastic process taking the values $\pm c_0$, with $c_0 \geq 0$, and changing sign at stochastic times. At initial time the center of the potential is $c(0) = +c_0$ with probability $\lambda \in [0, 1]$, or $c(0) = -c_0$ with probability $1 - \lambda$. Then, the value of $c(t) = \pm c_0$ stays constant for a time $\tau$ drawn from the waiting time probability density $\psi_\pm(\tau)$. After a time $\tau$ the sign of $c(t)$ changes and the process goes on switching between the two states $\pm c_0$. Two instances of the process $c(t)$ are represented by the dashed trajectories in Figs. 3.1a and 3.1d for two different choices of the waiting-time distribution $\psi_\pm(\tau)$. As discussed in detail in Appendix C, we exploit this renewal structure of the process $c(t)$ to calculate its probability distribution, which turns out to be fundamental to understand the properties of $x(t)$. It is natural to identify two sets of relevant time scales of the dynamics: the average waiting times

$$\langle \tau \rangle_\pm \equiv \int_0^\infty \mathrm{d}\tau \, \tau \, \psi_\pm(\tau), \tag{3.3}$$

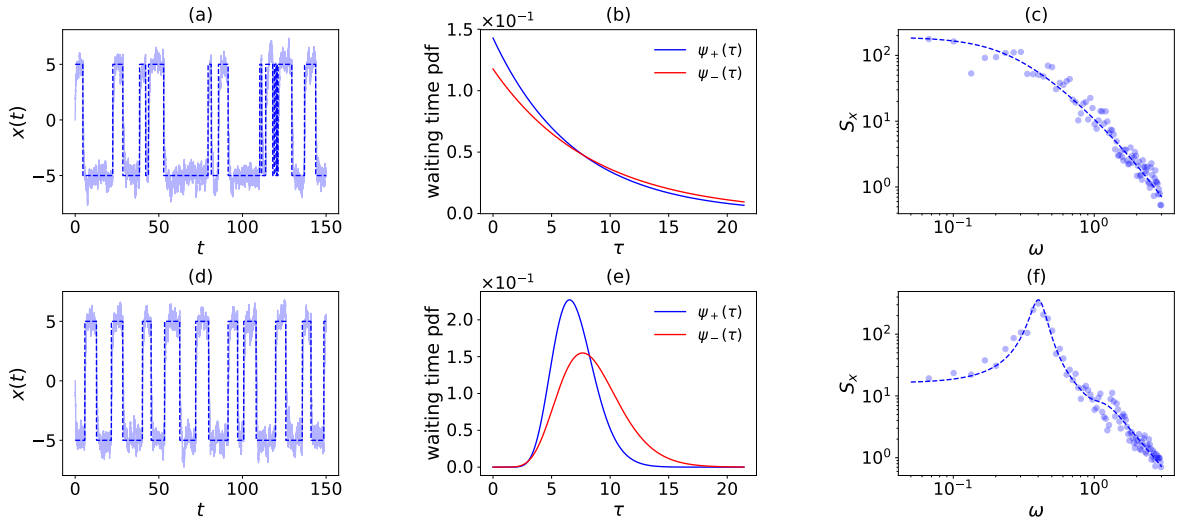



Figure 3.1: **Active oscillations.** First column: realisations of the stochastic driving $c(t)$ (dashed blue line) and of the process $x(t)$ (solid blue line) obtained from a numerical simulation of Eq. (3.2), for **(a)** the exponential and **(d)** the Gamma waiting-time distributions drawn, respectively, in panels **(b)** and **(e)** of the second column. In particular, the exponential distributions have rates $r_+ = 1/7$, and $r_- = 2/17$, while the Gamma distributions (see the main text) have shape parameters $k_+ = 15$, $k_- = 10$, and scale parameters $\theta_+ = 7/15$, $\theta_- = 17/20$. Third column: Power spectral density $S_x$ (symbols) of $x(t)$ in log-scale, obtained for two timeseries of total duration $t = 1.5 \times 10^3$ with the same parameters as those in panels **(a)** and **(d)**. The dashed lines are given by Eq. (3.47). The dynamics was simulations with $D = 1$, $c_0 = 5$, $\nu = 2.5$, and a time step $\Delta t = 10^{-3}$.

and the relaxation time $\tau_\nu = \nu^{-1}$ in the harmonic potential, where $\nu = \kappa/\gamma$. Then, the oscillatory regime of the system corresponds to the condition $\tau_\nu \ll \langle\tau\rangle_\pm$. Note that $c(t)$ is a non-Markovian process unless the two waiting time distributions are exponential

$$\psi_\pm(\tau) = r_\pm e^{-r_\pm \tau}, \tag{3.4}$$

where we set $r_\pm = (\langle\tau\rangle_\pm)^{-1}$. Indeed, for exponential distribution the center $c(t) = c_\pm$ the probability to switch is homogeneous in space and time, and it is given by $r_\pm dt$. In this case, $c(t)$ corresponds to the so-called (Markovian) telegraphic noise [107]. Note that for symmetric waiting-time distributions $r_\sigma = r$, Eq. (3.2) is equivalent to Eq. (2.16), up to the diffusive term. The dynamics of the model introduced in this Chapter is equivalent to the one of run-and-tumble particles in a harmonic trap [58] where the time between two tumbles $\tau$ is drawn from the distribution $\psi_\pm(\tau)$. Moreover, we point out that a very similar active system has been reproduced experimentally by means of optical tweezers, see Refs. [163, 61].

Figure 3.1 shows representative trajectories of the process $c(t)$ (dashed line) and $x(t)$ (continuous line) for various choices of the waiting time distributions $\psi_\pm(\tau)$. Panel (a) refers to the exponentially-distributed waiting times reported in panel (b), with the Lorentzian-like power spectrum (see further below) shown in panel (c). Panel (d), instead, shows a realization of the process $c(t)$ (dashed line) and $x(t)$ (continuous line) for the Gamma-distributed waiting times reported in panel (e), which is

characterized by fast jumps between the two (almost) equilibrium states. The power spectrum of the process, shown in panel (f), features a pronounced peak at the typical frequency of the coherent oscillations. As we will show below, the interplay between $\langle\tau\rangle_\pm$ and $\tau_\nu$ determines which type of stationary dynamics emerges from the fluctuations of the system, either monostable or bistable.

## 3.3 Dynamics

After having exposed the main qualitative features of the model, we now provide the exact derivation of its statistics. To do so, we encode the state of the system at time $t$ by the couple of stochastic variables $(x(t), \sigma(t))$, where $\sigma(t) = c(t)/c_0 = \pm 1$ is the sign of $c(t)$.

In order to describe the dynamics of the process $x(t)$, we introduce $G(x, \sigma, t|x_0, \sigma_0)$, the probability density of finding the system in the state $(x, \sigma)$ at time $t$ with initial configuration $(x_0, \sigma_0)$. We can express $G(x, \sigma, t|x_0, \sigma_0)$ by means of a renewal approach in terms of the probability density of the switch-free dynamics $G_\sigma^{(0)}(x, t|x_0)$, the waiting-time distribution $\psi_\sigma(t)$, and its cumulative $\Psi_\sigma(t)$, given by

$$\Psi_\sigma(t) \equiv \int_t^\infty \mathrm{d}\tau\, \psi_\sigma(\tau), \tag{3.5}$$

representing the probability that no switch has occurred in the time interval $[0, t]$. We recall that in the case of the Ornstein-Uhlenbeck process [84, 222] with center $c_\sigma \equiv \sigma c_0$, the particle position evolves according the Langevin equation

$$\gamma\, \dot{x}(t) = -\kappa[x(t) - c_\sigma] + \xi(t), \tag{3.6}$$

where we set the initial condition to be $x(0) = x_0$. Then, the probability density of the particle position $G_\sigma^{(0)}(x, t|x_0)$ reads

$$G_\sigma^{(0)}(x, t|x_0) \equiv \frac{1}{\sqrt{2\pi\Sigma^2(t)}} \exp\left\{-\frac{[x - \mu_\sigma(t|x_0)]^2}{2\Sigma^2(t)}\right\}, \tag{3.7}$$

i.e., a Gaussian distribution with time-dependent mean and variance respectively given by

$$\mu_\sigma(t|x_0) \equiv c_\sigma(1 - e^{-\nu t}) + x_0 e^{-\nu t}, \quad \text{and} \quad \Sigma^2(t) \equiv \frac{D}{\nu}(1 - e^{-2\nu t}). \tag{3.8}$$

In what follows, we show all the necessary steps to derive the probability density $G(x, \sigma, t|x_0, \sigma_0)$. We anticipate that the theoretical framework here developed is very general and holds for any process $x(t)$ subject to a force that switches between two values, parametrized by $c(t)$. We suggest to the reader to refer to Tab. 3.1 to keep track of all the probability (density) functions that we define in Subsecs. 3.3.1 and 3.3.2.

### 3.3.1 Switching probability density $G_S(x, \sigma, t|x_0, \sigma_0)$

Before proceeding to the calculation of $G(x, \sigma, t|x_0, \sigma_0)$, we introduce $G_S(x, \sigma, t|x_0, \sigma_0)$, the probability density associated with trajectories that start with configuration $(x_0, \sigma_0)$ and reach the state $(x, \sigma)$ at time $t + \mathrm{d}t$, conditioned on the fact that at least one switch occurs in the time interval

| $\psi_\sigma(\tau)$ | Waiting-time distribution |
|---|---|
| $\Psi_\sigma(t) \equiv \int_t^\infty \mathrm{d}\tau\, \psi_\sigma(\tau)$ | Cumulative waiting-time probability |
| $G_\sigma^{(0)}(x,t\|x_0)$ | Ornstein-Uhlenbeck p.d.f of $(x_0,\sigma,0) \to (x,\sigma,t)$ |
| $G_\sigma(x,t\|x_0) \equiv \psi_\sigma(t)\, G_\sigma^{(0)}(x,t\|x_0)$ | P.d.f of $(x_0,\sigma,0) \to (x,\sigma,t)$ with a first switch at $t+\mathrm{d}t$ |
| $G_S(x,\sigma,t\|x_0,\sigma_0)$ | P.d.f. of $(x_0,\sigma_0,0) \to (x,\sigma,t)$ conditioned on a switch at from $-\sigma$ to $\sigma$ at the final time $t$ |
| $G(x,\sigma,t\|x_0,\sigma_0)$ | P.d.f. of $(x_0,\sigma_0,0) \to (x,\sigma,t)$ |

Table 3.1: **Dictionary of probability (density) functions.** In this table we present the many probability densities functions (p.d.f.) appearing in Sec. 3.3. We denote with $(x_0,\sigma_0,0) \to (x,\sigma,t)$ the event of reaching the final state $(x,\sigma)$ at time $t$, given the initial configuration $(x_0,\sigma_0)$ at initial time $t_0 = 0$.

$(0,t)$ with the last one happening at time $t$. The expression of $G_S(x,\sigma,t|x_0,\sigma_0)$ depends on the initial and final configuration of $x(t)$, and we determine it using a renewal approach, by accounting for all the possible switches occurring in in the time interval $(0,t)$:

$$
\begin{aligned}
G_S(x,\sigma,t|x_0,\sigma) &= \sum_{n=1}^{\infty} \int_0^t \mathrm{d}\tau_1 \int_{-\infty}^{+\infty} \mathrm{d}z_1\, G_\sigma(z_1,\tau_1|x_0) \int_0^{t-\tau_1} \mathrm{d}\tau_2 \int_{-\infty}^{+\infty} \mathrm{d}z_2\, G_{-\sigma}(z_1,\tau_2|z_1) \\
&\quad \times \cdots \int_0^{t-\sum_{k=1}^{2n-2}\tau_k} \mathrm{d}\tau_{2n-1} \int_{-\infty}^{+\infty} \mathrm{d}z_{2n-1}\, G_\sigma(z_{2n-1},\tau_{2n-1}|z_{2n-2})\, G_{-\sigma}\left(x, t-\sum_{k=1}^{2n-1}\tau_k \middle| z_{2n-1}\right) \\
&= \int_{-\infty}^{+\infty} \mathrm{d}y \int_0^t \mathrm{d}\tau\, G_{-\sigma}(x,t-\tau|y) G_S(y,-\sigma,\tau|x_0,\sigma), \\
G_S(x,-\sigma,t|x_0,\sigma) &= G_\sigma(x,t|x_0) + \int_{-\infty}^{+\infty} \mathrm{d}y \int_0^t \mathrm{d}\tau\, G_\sigma(x,t-\tau|y) G_S(y,\sigma,\tau|x_0,\sigma),
\end{aligned}
\tag{3.9}
$$

where we define the "bare" probability density $G_\sigma(x,t|x_0) \equiv \psi_\sigma(t)\, G_\sigma^{(0)}(x,t|x_0)$, and we identify the initial state $(x_0,\sigma_0)$ as a switch state.

In the expression for $G_S(x,\sigma,t|x_0,\sigma)$, we sum with respect to the number of switches $n$ in $(0,t)$ with same initial and final state $\sigma$: this fixes an even number of switches, last one at $t$ included. Then, the evolution from the initial to final state results from the alternation of the bare probability densities $G_\sigma(x,t|x_0)$, describing the free dynamics between two switches. Similarly, the probability density $G_S(x,-\sigma,t|x_0,\sigma)$ is compatible with trajectories displaying an odd number of switches: the first contribution $G_\sigma(x,t|x_0)$ accounts for one single switch at $t$, the second with any odd number of switches larger than one. Given that the waiting-time distribution associated with the last switch is

not integrated over time, we can immediately deduce that $G_S(x,\sigma,t|x_0,\sigma_0)$ is a probability density also with respect to $t$. Indeed, we interpret $G_S(x,\sigma,t|x_0,\sigma_0)\mathrm{d}x\,\mathrm{d}t$ to be the probability to switch in $(t,t+\mathrm{d}t)$ to the state $\sigma$ at a position in the region $(x,x+\mathrm{d}x)$, given the initial state $(x_0,\sigma_0)$.

Integrating Eqs. (3.9) with respect to the final position $x$ we get

$$P_S(\sigma,t|\sigma_0) \equiv \int_{-\infty}^{+\infty} \mathrm{d}x\, G_S(x,\sigma,t|x_0,\sigma_0), \tag{3.10}$$

the probability density to be initially in the state $\sigma$ and to end up in $\pm\sigma$ after a switch at a time in $(t,t+\mathrm{d}t)$:

$$\begin{aligned} P_S(\sigma,t|\sigma) =& \sum_{n=1}^{\infty} \int_0^t \mathrm{d}\tau_1\, \psi_\sigma(\tau_1) \int_0^{t-\tau_1} \mathrm{d}\tau_2\, \psi_{-\sigma}(\tau_2) \\ & \times \cdots \int_0^{t-\sum_{k=1}^{2n-2}\tau_k} \mathrm{d}\tau_{2n-1}\, \psi_\sigma(\tau_{2n-1})\, \psi_{-\sigma}\left(t-\sum_{k=1}^{2n-1}\tau_k\right), \\ =& \int_0^t \mathrm{d}\tau\, \psi_{-\sigma}(t-\tau) P_S(-\sigma,\tau|\sigma), \\ P_S(-\sigma,t|\sigma) =& \psi_\sigma(t) + \int_0^t \mathrm{d}\tau\, \psi_\sigma(t-\tau) P_S(\sigma,\tau|\sigma), \end{aligned} \tag{3.11}$$

which both follow from the normalization of Eq. (3.7), $\int_{-\infty}^{+\infty} \mathrm{d}x\, G_\sigma^{(0)}(x,t|x_0) = 1$.

The expressions of $G_S(x,\sigma,t|x_0,\sigma_0)$ can be simplified by exploiting the properties of the Laplace transform. In particular, thanks to the convolution theorem we can trade the time integrals in Eq. (3.9) as a product of the Laplace transform of $G_\sigma(x,t|x_0)$, namely

$$\begin{aligned} \tilde{G}_S(x,\sigma,s|x_0,\sigma) =& \sum_{n=1}^{\infty} \int_{-\infty}^{+\infty} \left(\prod_{l=1}^{2n-1} \mathrm{d}z_l\right) \left(\prod_{k=1}^{n} \tilde{G}_\sigma(z_{2k-1},s|z_{2k-2})\, \tilde{G}_{-\sigma}(z_{2k},s|z_{2k-1})\right) \\ =& \int_{-\infty}^{+\infty} \mathrm{d}y\, \tilde{G}_{-\sigma}(x,s|y) \tilde{G}_S(y,-\sigma,s|x_0,\sigma), \\ \tilde{G}_S(x,-\sigma,s|x_0,\sigma) =& \tilde{G}_\sigma(x,s|x_0) + \int_{-\infty}^{+\infty} \mathrm{d}y\, \tilde{G}_\sigma(x,s|y) \tilde{G}_S(y,\sigma,s|x_0,\sigma), \end{aligned} \tag{3.12}$$

where we identify the initial and final position as $z_0 \equiv x_0$ and $z_{2n} \equiv x$.

Equation (3.12) allows us to calculate $\tilde{P}_S(\sigma,s|\sigma_0)$, the Laplace transform of $P_S(\sigma,t|\sigma_0)$, the probability to have a switch at time $t$ given the initial state $\sigma_0$, by applying repeatedly the convolution theorem of the Laplace transform to Eq. (3.11):

$$\begin{aligned} \tilde{P}_S(\sigma,s|\sigma) \equiv \int_{-\infty}^{+\infty} \mathrm{d}x\, \tilde{G}_S(x,\sigma,s|x_0,\sigma) &= \sum_{n=1}^{\infty} (\tilde{\psi}_+(s)\tilde{\psi}_-(s))^n = \frac{\tilde{\psi}_+(s)\tilde{\psi}_-(s)}{1-\tilde{\psi}_+(s)\tilde{\psi}_-(s)}, \\ \tilde{P}_S(-\sigma,s|\sigma) \equiv \int_{-\infty}^{+\infty} \mathrm{d}x\, \tilde{G}_S(x,-\sigma,s|x_0,\sigma) &= \tilde{\psi}_\sigma(s) \sum_{n=0}^{\infty} (\tilde{\psi}_+(s)\tilde{\psi}_-(s))^n = \frac{\tilde{\psi}_\sigma(s)}{1-\tilde{\psi}_+(s)\tilde{\psi}_-(s)}, \end{aligned} \tag{3.13}$$

where the convergence of the geometric series is ensured by $|\psi_\sigma(s)| < 1$ for $\mathrm{Re}(s) > 0$.

As we show below, the knowledge of $G_S(x, \sigma, t|x_0, \sigma_0)$ is fundamental to describe the properties of the process $x(t)$. Not only it represents the backbone to the calculation of the probability density $G(x, \sigma, t|x_0, \sigma_0)$, but it is necessary to characterize the energetics of the system. We anticipate that we can derive the first and second moment of the stochastic work associated to $x(t)$ by using as building blocks those of $G_S(x, \sigma, t|x_0, \sigma_0)$, which we calculate in Appendix C.1.

### 3.3.2 Probability density $G(x, \sigma, t|x_0, \sigma_0)$

We now proceed to build up the expression of the full probability density $G(x, \sigma, t|x_0, \sigma_0)$ in terms of the switching probability density $G_S(x, \sigma, t|x_0, \sigma_0)$ by conditioning on the last switching event:

$$\begin{aligned} G(x, \sigma, t|x_0, \sigma) =& \Psi_\sigma(t)\, G_\sigma^{(0)}(x, t|x_0) \\ &+ \int_0^t \mathrm{d}\tau \int_{-\infty}^{+\infty} \mathrm{d}y\, G_S(y, \sigma, \tau|x_0, \sigma)\, \Psi_\sigma(t-\tau) G_\sigma^{(0)}(x, t-\tau|y), \\ G(x, \sigma, t|x_0, -\sigma) =& \int_0^t \mathrm{d}\tau \int_{-\infty}^{+\infty} \mathrm{d}y\, G_S(y, \sigma, \tau|x_0, -\sigma)\, \Psi_\sigma(t-\tau) G_\sigma^{(0)}(x, t-\tau|y). \end{aligned} \tag{3.14}$$

The equation for $G(x, \sigma, t|x_0, \sigma)$ can be understood in the following way: the first contribution $\Psi_\sigma(t)\, G_\sigma^{(0)}(x, t|x_0)$ on the right hand side is due to trajectories with no switching event in the time interval $(0, t)$; whereas the second to trajectories that display a last switch at position $y$ at the intermediate time $\tau$, with a successive switch occurring after $t$. The expression for $G(x, \sigma, t|x_0, -\sigma)$ results from the same reasoning. It is immediate to check the initial condition $G(x, \sigma, 0|x_0, \sigma_0) = \delta_{\sigma\sigma_0}\delta(x - x_0)$, from the normalization of the waiting-time distribution $\Psi_\sigma(0) = 1$, and the initial condition of Eq. (3.7) $G_\sigma^{(0)}(x, 0|x_0) = \delta(x - x_0)$.

From the expression of $G(x, \sigma, t|x_0, \sigma_0)$, we can immediately calculate $P(\sigma, t|\sigma_0)$, the probability that $c(t)$ is in the state $\sigma$ at time $t$, given its initial configuration $\sigma_0$,

$$P(\sigma, t|\sigma_0) \equiv \int_{-\infty}^{+\infty} \mathrm{d}x\, G(x, \sigma, t|x_0, \sigma_0), \tag{3.15}$$

by integrating Eqs. (3.14) with respect to the final position $x$:

$$\begin{aligned} P(\sigma, t|\sigma) =& \ \Psi_\sigma(t) + \int_0^t \mathrm{d}\tau\, P_S(\sigma, \tau|\sigma)\Psi_\sigma(t-\tau) \\ P(\sigma, t|-\sigma) =& \int_0^t \mathrm{d}\tau\, P_S(\sigma, \tau|-\sigma)\Psi_\sigma(t-\tau). \end{aligned} \tag{3.16}$$

Moreover, we can relate $G(x, \sigma, t|x_0, \sigma_0)$ to $\rho_\sigma(x, t|x_0)$, the probability density to be in $(x, \sigma)$ at time $t$ given the initial position $x_0$, by marginalising with respect to the initial state $\sigma_0$:

$$\rho_\sigma(x, t|x_0) = \sum_{\sigma_0} \lambda_{\sigma_0}\, G(x, \sigma, t|x_0, \sigma_0), \tag{3.17}$$

where we adopt the compact notation $\lambda_{\sigma_0} \equiv [1-\sigma_0(1-2\lambda)]/2$ for the probability to be in the initial state $\sigma_0$. The corresponding initial condition translates into $\rho_\sigma(x,0|x_0) = \lambda_\sigma\,\delta(x-x_0)$. Then, the total density of particles $\rho(x,t|x_0)$ is simply given by

$$\rho(x,t|x_0) = \sum_\sigma \rho_\sigma(x,t|x_0), \tag{3.18}$$

with initial condition $\rho(x,0|x_0) = \delta(x-x_0)$. Note that $\rho(x,t|x_0)$ must satisfy the normalization condition $\int \mathrm{d}x\,\rho(x,t|x_0) = 1$, which, as shown below, we can easily check in the Laplace domain.

Similarly to what done for $G_S(x,\sigma,t|x_0,\sigma_0)$, Eq. (3.14) assumes a simpler form by considering its Laplace transform:

$$\begin{aligned}
\tilde{G}(x,\sigma,s|x_0,\sigma) =& \mathcal{L}\left\{\Psi_\sigma(t)\,G_\sigma^{(0)}(x,t|x_0)\right\}(s) \\
&+ \int_{-\infty}^{+\infty} \mathrm{d}y\,\tilde{G}_S(y,\sigma,s|x_0,\sigma)\,\mathcal{L}\left\{\Psi_\sigma(t)\,G_\sigma^{(0)}(x,t|y)\right\}(s), \\
\tilde{G}(x,\sigma,s|x_0,-\sigma) =& \int_{-\infty}^{+\infty} \mathrm{d}y\,\tilde{G}_S(y,\sigma,s|x_0,-\sigma)\,\mathcal{L}\left\{\Psi_\sigma(t)\,G_\sigma^{(0)}(x,t|y)\right\}(s).
\end{aligned} \tag{3.19}$$

Furthermore, by taking the Laplace transform of Eq. (3.16), we determine a closed relation for $\tilde{P}(\sigma,s|\sigma_0)$, the Laplace transform of $P(\sigma,t|\sigma_0)$, in terms of $\tilde{\psi}_\sigma(s)$:

$$\begin{aligned}
\tilde{P}(\sigma,s|\sigma) &\equiv \int_{-\infty}^{+\infty} \mathrm{d}x\,G(x,\sigma,t|x_0,\sigma) = \frac{\tilde{\Psi}_\sigma(s)}{1-\tilde{\psi}_+(s)\tilde{\psi}_-(s)}, \\
\tilde{P}(\sigma,s|-\sigma) &\equiv \int_{-\infty}^{+\infty} \mathrm{d}x\,G(x,\sigma,t|x_0,-\sigma) = \frac{\tilde{\Psi}_\sigma(s)\tilde{\psi}_{-\sigma}(s)}{1-\tilde{\psi}_+(s)\tilde{\psi}_-(s)}.
\end{aligned} \tag{3.20}$$

Last equation follows from applying the convolution theorem of the Laplace transform, and by substituting the expressions of $\tilde{P}_S(\sigma,s|\sigma_0)$ in Eqs. (3.13).

Finally, we find that $P(\sigma,t)$, the probability to find a particle in the state $\sigma$ at time $t$, has Laplace transform given by

$$\tilde{P}(\sigma,s) \equiv \int_{-\infty}^{+\infty} \mathrm{d}x\,\tilde{\rho}_\sigma(x,s|x_0) = \frac{\tilde{\Psi}_\sigma(s)}{1-\tilde{\psi}_+(s)\tilde{\psi}_-(s)}\left[\lambda_\sigma + \lambda_{-\sigma}\tilde{\psi}_{-\sigma}(s)\right], \tag{3.21}$$

yielding the correct normalisation in the Laplace transform

$$\int_{-\infty}^{+\infty} \mathrm{d}x\,\tilde{\rho}(x,s|x_0) = \tilde{P}(\sigma,s) + \tilde{P}(-\sigma,s) = \frac{1}{s}; \tag{3.22}$$

where we use the fact that

$$\tilde{\Psi}_\sigma(s) = \mathcal{L}\left\{1 - \int_0^t \mathrm{d}\tau\,\psi_\sigma(\tau)\right\} = \frac{1-\tilde{\psi}_\sigma(s)}{s}. \tag{3.23}$$

We conclude this Section by pointing out that the analysis carried out so far is general for any $G_\sigma^{(0)}(x,t|x_0)$, i.e., for any underlying process, and for any waiting time distribution $\psi_\sigma(\tau)$, as long

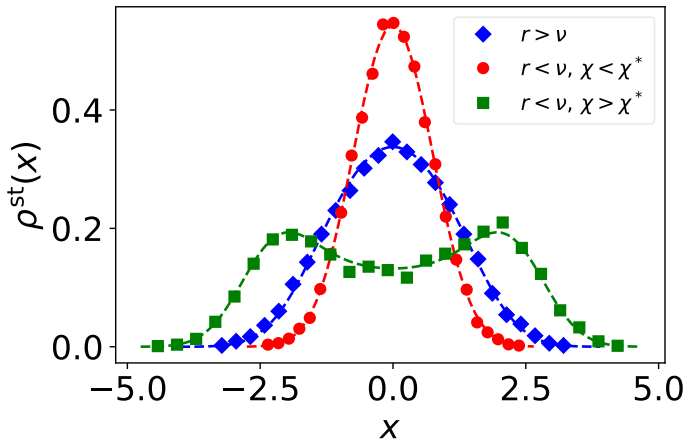



Figure 3.2: **Stationary probability** density $\rho^{\rm st}(x)$ for symmetric exponentially-distributed waiting times: numerical simulations (symbols) are compared with the analytical solution in Eq. (3.30) (dashed lines). The three cases correspond to fixed values of $D = 1$ and $\nu = 2.5$, but various values of $r$ and $c_0$: (blue) $c_0 = 2$ and $r = 5 > \nu$; (red) $c_0 = 0.5$ and $r = 1.25 < \nu$ for which $\chi \simeq 0.31$; (green) $c_0 = 2.5$ and $r = 1.25$, for which $\chi \simeq 7.8$. In the latter two cases $q = -0.5$ corresponding to the critical value $\chi^*(-0.5) \simeq 1.58$ (see main text). The numerical estimates of $\rho^{\rm st}(x)$ are obtained from $N = 10^4$ simulations of Eq. (3.2) using Euler's numerical integration method with time step $\Delta t = 5 \times 10^{-3}$.

they are suitably integrable. Moreover, all the quantities that we have computed do not rely on the symmetric nature of the process $c(t)$, but only on the fact that it is a two-state process. Indeed, one can use the same results for a generic process $c(t)$ taking any two values $c_+$ and $c_-$, by simply identifying the sign $\sigma(t)$ with the subscript of $c_\sigma$.

### 3.3.3 Fokker-Planck description

Besides to the integral representations of $G(x, \sigma, t|x_0, \sigma_0)$ in Eqs. (3.14), we show how to construct the Fokker-Planck description for the probability density $G(x, t, \sigma|x_0, \sigma_0)$. As discussed above, between two switches, the process $x(t)$ in Eq. (3.2) coincides with the Ornstein-Uhlenbeck process in Eq. (3.6) . Accordingly, the probability density $G^{(0)}_\sigma(x, t|x_0)$ satisfies the Fokker-Planck equation of the Ornstein-Uhlenbeck

$$\begin{aligned} \frac{\partial G^{(0)}_\sigma(x,t|x_0)}{\partial t} &= D\frac{\partial^2 G^{(0)}_\sigma(x,t|x_0)}{\partial x^2} + \nu\frac{\partial}{\partial x}\left[(x-c_\sigma)\, G^{(0)}_\sigma(x,t|x_0)\right] \\ &= \hat{O}_\sigma(x)\, G^{(0)}_\sigma(x,t|x_0), \end{aligned} \tag{3.24}$$

with initial condition $G^{(0)}_\sigma(x, 0|x_0) = \delta(x - x_0)$, and where one reads the expression of the Fokker-Planck differential operator $\hat{O}_\sigma(x)$. By differentiating $G(x, \sigma, t|x_0, \sigma)$ in Eq. (3.14) with respect to

the final time $t$, we get

$$\begin{aligned}\frac{\partial G(x,\sigma,t|x_0,\sigma)}{\partial t} =& -G_\sigma(x,t|x_0) + \hat{O}_\sigma(x)\,\Psi_\sigma(t) G_\sigma^{(0)}(x,t|x_0) \\ &+ \int_{-\infty}^{+\infty} \mathrm{d}y\, G_S(y,\sigma,t|x_0,\sigma)\Psi_\sigma(0) G_\sigma^{(0)}(x,0|y) \\ &+ \int_0^t \mathrm{d}\tau \int_{-\infty}^{+\infty} \mathrm{d}y\, G_S(y,\sigma,\tau|x_0,\sigma) \\ &\times \Big[-G_\sigma(x,t-\tau|y) + \Psi_\sigma(t-\tau)\hat{O}_\sigma(x)\, G_\sigma^{(0)}(x,t-\tau|y)\Big] \\ =& \hat{O}_\sigma(x)\, G(x,\sigma,t|x_0,\sigma) - G_S(x,-\sigma,t|x_0,\sigma) + G_S(x,\sigma,t|x_0,\sigma).\end{aligned} \tag{3.25}$$

In the first line of the equation above we have used the relation $\partial_t \Psi_\sigma(t) = -\psi_\sigma(t)$, and Eq. (3.24). In the second line, we substitute the normalization condition $\Psi(0) = 1$, and the initial condition $G_\sigma^{(0)}(x,0|y) = \delta(x-y)$.

Following the same steps for $G(x,\sigma,t|x_0,\sigma_0)$, it is possible to generalize Eq. (3.25) to any initial state $\sigma_0$:

$$\frac{\partial G(x,\sigma,t|x_0,\sigma_0)}{\partial t} = \hat{O}_\sigma(x)\, G(x,\sigma,t|x_0,\sigma_0) + G_S(x,\sigma,t|x_0,\sigma_0) - G_S(x,-\sigma,t|x_0,\sigma_0). \tag{3.26}$$

As expressed in Eq. (3.26), the time evolution of $G(x,\sigma,t|x_0,\sigma_0)$ is due to two type of mechanisms: the first term $\hat{O}_\sigma(x)\, G(x,\sigma,t|x_0,\sigma_0)$ reflects the evolution of particles in $(x,\sigma)$ at $t$ according the Ornstein-Uhlenbeck dynamics; the second quantifies the net flux of particles switching in or out from the state $(x,\sigma)$ at $t$ given the initial configuration $(x_0,\sigma_0)$, captured by the switching probability density $G_S(x,\sigma,t|x_0,\sigma_0)$.

Note that the Fokker-Planck description provided in this Section is independent of the fact that $G_\sigma^{(0)}(x,t|x_0)$ represents the probability density of a Ornstein-Uhlenbeck process. Indeed, it is sufficient that $G_\sigma^{(0)}(x,t|x_0)$ obeys Eq. (3.24), with $\hat{O}_\sigma(x)$ being the Fokker-Planck operator relative to the underlying stochastic processes.

**Markovian limit**

We now restrict the analysis to the statistical properties of the process $x(t)$ in its Markovian case, corresponding to exponentially distributed waiting times $\psi_\sigma(\tau) = r_\sigma\, e^{-r_\sigma \tau}$. Markovianity results from the fact that the center $c(t)$ switches to $c(t+\mathrm{d}t)$ with time-constant rate $r_\sigma$. Therefore, the probability density $G_S(x,\sigma,t|x_0,\sigma_0)$ is simply related to $G(x,\sigma,t|x_0,\sigma_0)$ as

$$G_S(x,\sigma,t|x_0,\sigma_0) = r_{-\sigma} G(x,-\sigma,t|x_0,\sigma_0), \tag{3.27}$$

as a consequence of the fact that switching at a given time $t$ depends only on the current state $\sigma(t)$. From a mathematical point of view Eq. (3.27) is a consequence of the identity $\psi_\sigma(\tau) = r_\sigma \Psi_\sigma(\tau)$.

By substituting Eq. (3.27) in Eq. (3.26), we get closed differential equations for the probability density $G(x,\sigma,t|x_0,\sigma_0)$, namely

$$\frac{\partial G(x,\sigma,t|x_0,\sigma_0)}{\partial t} = \hat{O}_\sigma(x)\, G(x,\sigma,t|x_0,\sigma_0) + r_{-\sigma}\, G(x,-\sigma,t|x_0,\sigma_0) - r_\sigma\, G(x,\sigma,t|x_0,\sigma_0). \quad (3.28)$$

Furthermore, the probability density $\rho_\sigma(x,t|x_0)$ in Eq. (3.17) also satisfies Eq. (3.28), due to the linearity of its definition. Accordingly, the stationary distribution $\rho^{\rm st}_\sigma(x)$ satisfies the equation

$$\hat{O}_\sigma(x)\, \rho^{\rm st}_\sigma(x) = r_\sigma\, \rho^{\rm st}_\sigma(x) - r_{-\sigma}\, \rho^{\rm st}_{-\sigma}(x), \quad (3.29)$$

whose solution is given by

$$\rho^{\rm st}_\sigma(x) = \frac{\mathcal{N}}{2} \int_{-1}^{+1} {\rm d}z\, \rho_{\rm G}(x - c_0 z)(1-\sigma z)^{r_\sigma/\nu - 1}(1+\sigma z)^{r_{-\sigma}/\nu}, \quad (3.30)$$

where we introduce the Gaussian distribution $\rho_{\rm G}(x) \equiv \exp[-x^2\nu/(2D)]/\sqrt{2\pi D/\nu}$. The constant $\mathcal{N}^{-1} \equiv \nu \sum_\sigma {}_2F_1(1, 1 - r_{-\sigma}/\nu, 1 + r_\sigma/\nu, -1)/r_\sigma$ enforces normalisation of $\rho^{\rm st}(x)$, where ${}_2F_1$ is the hypergeometric function. Similar results were recently reported in the context of run-and-tumble particles [83, 58].

**Unimodal to bimodal transition**

An intuitive way to characterize whether the process $x(t)$ displays oscillatory behaviour is to look at its total stationary density

$$\rho^{\rm st}(x) = \rho^{\rm st}_+(x) + \rho^{\rm st}_-(x). \quad (3.31)$$

Actually, whenever $\rho^{\rm st}(x)$ is unimodal typical trajectories are represented by noisy fluctuation around

$$\langle x \rangle^{\rm st} = c_0 \frac{\langle \tau \rangle_+ - \langle \tau \rangle_-}{\langle \tau \rangle_+ + \langle \tau \rangle_-}, \quad (3.32)$$

the stationary value of the average position, which is calculated in full details in Appendix C.2. On the other hand, if $\rho^{\rm st}(x)$ is bimodal, trajectories are properly oscillatory. These two regimes depend on the values of the parameters of the model, as shown in Fig. 3.2 numerically and analytically on the basis of Eq. (3.30). In particular, bistability emerges whenever the relaxation is fast enough with respect to the switching frequency, i.e., $\tau_\nu \ll \langle \tau \rangle_\pm$. To fix ideas, we consider the case of symmetric and exponential waiting-time distribution, for which we can characterize analytically the transition from the unimodal to the regime of bimodal stationary density $\rho^{\rm st}(x)$. This is done by studying whether the origin $x = 0$ is a point of maximum or minimum for $\rho^{\rm st}(x)$. In the former case, $\rho^{\rm st}(0)$ displays an unique global maximum and it is unimodal, see red and blue curve of Fig. 3.2. In the latter, $\rho^{\rm st}(0)$ is bimodal, and it shows a local minimum in the origin, and two symmetric maxima, see green curve of Fig. 3.2. The symmetric solution $\rho^{\rm st}(x)$ to Eq. (3.30) is given by:

$$\rho^{\rm st}(x) = \frac{1}{\sqrt{\pi}} \frac{\Gamma\left(\zeta + \frac{1}{2}\right)}{\Gamma\left(\zeta - \frac{1}{2}\right)} \int_{-1}^{+1} {\rm d}z\, \rho_{\rm G}(x - c_0 z)(1 - z^2)^{\zeta - 1}, \quad (3.33)$$

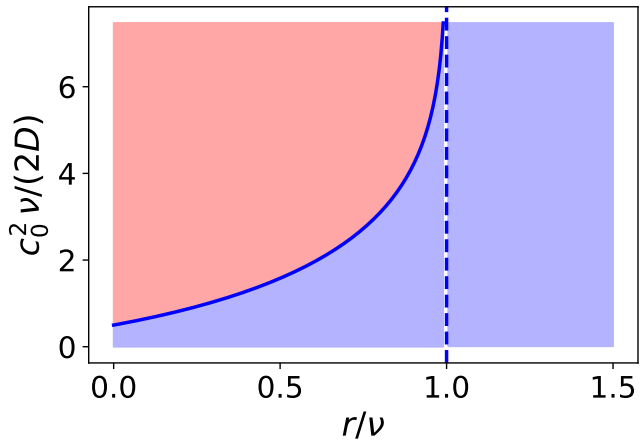



Figure 3.3: **Phase diagram.** The diagram shows the two parameter regions corresponding to an unimodal distribution $\rho^{\rm st}(x)$ (blue area), and bimodal (red area). The two regions are delimited by the critical line $\chi^*(\zeta)$ in Eq. (3.36) which is diverging at $r=\nu$ (dashed vertical line).

where $\Gamma$ denotes the Gamma function. First, we evaluate the derivative of $\rho^{\rm st}(x)$

$$\frac{\partial\rho^{\rm st}(x)}{\partial x}=\frac{\nu}{D\sqrt{\pi}}\frac{\Gamma\left(\zeta+\frac{1}{2}\right)}{\Gamma\left(\zeta-\frac{1}{2}\right)}\int_{-1}^{+1}\mathrm{d}z\,\rho_{\rm G}(x-c_0z)(1-z^2)^{\zeta-1}(c_0z-x), \tag{3.34}$$

which, as expected, vanishes at the origin, confirming that $x=0$ is always a point of maximum or minimum for $\rho^{\rm st}(x)$. In order to understand the nature of this stationary point we study the sign of the second derivative of $\rho^{\rm st}(x)$ at $x=0$:

$$\left.\frac{\partial^2\rho^{\rm st}}{\partial x^2}\right|_{x=0}=\frac{1}{\sqrt{2\pi(D/\nu)^3}}\left[\frac{\chi}{\zeta+1/2}\,{}_1F_1\left(\frac{3}{2},\zeta+\frac{3}{2},-\chi\right)-{}_1F_1\left(\frac{1}{2},\zeta+\frac{1}{2},-\chi\right)\right], \tag{3.35}$$

where we recall $\chi=c_0^2\nu/(2D)$, and ${}_1F_1$ denotes the confluent hypergeometric function. Hence, the transition occurs across the critical value $\chi^*$ found by imposing $\partial_x^2\rho^{\rm st}(0)=0$, i.e.,

$$\chi^*=\frac{(\zeta+1/2)\;{}_1F_1\left(1/2,\zeta+1/2,-\chi^*\right)}{{}_1F_1\left(3/2,\zeta+3/2,-\chi^*\right)}. \tag{3.36}$$

In general, if $\chi<\chi^*$ then $\partial_x^2\rho^{\rm st}(0)$ is negative and $\rho^{\rm st}(x)$ is unimodal, bimodal otherwise. More specifically, for $r\geq\nu$ ($\zeta\geq1$), the value of $\chi^*$ diverges and $\rho^{\rm st}(x)$ is always unimodal. For $r<\nu$ ($\zeta<1$), the critical $\chi^*$ is finite and grows monotonically with $\zeta$, see Fig. 3.3.

### Resetting limit

As we have seen, the model presented in Sec. 3.2 describes a wide class of systems, whose dynamics consists in the alternate evolution of processes associated to the probability density $G_\sigma(x,t|x_0)$.

Analogously, also the motion of a Brownian particle with stochastic resetting (see Sec. 1.2) is characterized by the repetition of two phases: a reset event followed by free diffusion. In this spirit, we show how the probability density of stochastic resetting can be retrieved from our model by looking at the total probability density $\rho(x,t)$ in Eq. (3.18). To fix ideas, we identify the $\sigma = +$ phase with Brownian diffusion, while the $\sigma = -$ phase with a resetting event.

Accordingly, the total density of particles is given by $\rho(x,t|x_0) = G(x,+,t|x_0,+)$, which reflects the fact no particle starts with a reset, i.e., $\lambda_+ = 1$, and $\lambda_- = 0$. For the diffusive phase, we impose that $G_+^{(0)}(x,t|x_0) = e^{-x^2/4Dt}/\sqrt{4\pi Dt}$ is the probability density of the Brownian motion, and that $\psi_+(\tau)$ identifies the waiting-time distribution between two resetting events. At a reset, particles are teleported to the resetting point $x_r$, and immediately leave the resetting phase: this translates in $G_-^{(0)}(x,t|x_0) = \delta(x - x_r)$, and $\psi_-(\tau) = \delta(\tau)$. Collecting all these considerations, the Laplace transform of the switching probability density $G_S(x,+,t|x_0,+)$ in Eqs. (3.12) reduces to

$$\tilde{G}_S(x,+,s|x_0,+) = \delta(x - x_r)\frac{\tilde{\psi}_+(s)}{1-\tilde{\psi}_+(s)}. \tag{3.37}$$

Finally, we substitute the expressions of Eq. (3.37) in Eq. (3.19) to calculate the probability density $\tilde{\rho}(x,s|x_0) = \tilde{G}(x,+,s|x_0,+)$, leading to

$$\tilde{\rho}(x,s|x_0) = \mathcal{L}\left\{\Psi_+(t)\,G_+^{(0)}(x,t|x_0)\right\}(s) + \frac{\tilde{\psi}_+(s)}{1-\tilde{\psi}_+(s)}\mathcal{L}\left\{\Psi_+(t)\,G_+^{(0)}(x,t|x_r)\right\}(s), \tag{3.38}$$

which is equivalent to $P(x,t|x_0)$ in Eq. (1.15) once one identifies $G_+^{(0)}(x,t|x_0) \equiv P_{\rm BM}(x,t|x_0)$, and $\psi_+(\tau) \equiv \psi(\tau)$.

### 3.4 Power spectrum

Because of its non-Markovianity properties of the process $x(t)$ are not entirely captured by the one-time statistics $G(x,\sigma,t|x_0,\sigma_0)$. In this spirit, we address the problem of evaluating the long-time two-point correlator

$$C_x(t) \equiv \lim_{\tau\to\infty}\langle x(t+\tau)x(\tau)\rangle. \tag{3.39}$$

As stated by the Wiener-Khinchin theorem [222], the Fourier transform of $C_x(t)$ is equal to the power spectral density $S_x(\omega) = \hat{C}_x(\omega) = \langle|\hat{x}(\omega)|^2\rangle$ of the process. Henceforth, we fix the convention $\hat{f}(\omega) \equiv \int_{-\infty}^{+\infty} {\rm d}\omega\, e^{-i\omega t} f(t)$ for the Fourier transform $\hat{f}(\omega)$ of a function $f(t)$. The independence of the two stochastic (noisy) terms $\xi(t)$ and $c(t)$ in Eq. (3.2) implies that they contribute separately to $S_x(t)$:

$$S_x(\omega) = \frac{2D + \nu^2 S_c(\omega)}{\nu^2+\omega^2}, \tag{3.40}$$

where the first term represents the contribution of the Ornstein-Uhlenbeck process ($c_0 = 0$), while $S_c(\omega) = \langle|\hat{c}(\omega)|^2\rangle$ is the power spectrum of $c(t)$.

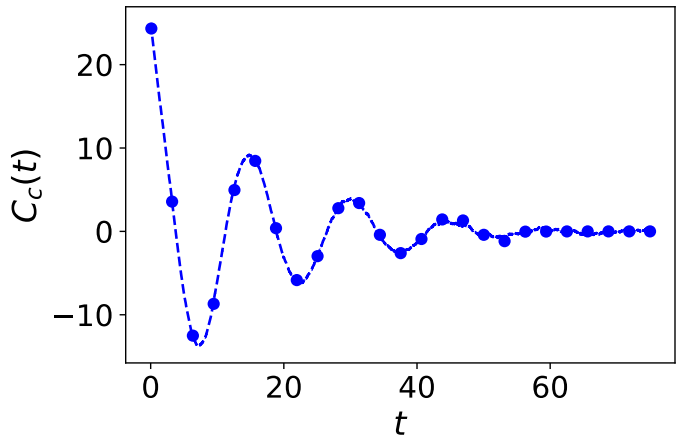



Figure 3.4: **Correlator $C_c(t)$.** The figure displays the time evolution of the correlator $C_c(t)$. Dashed line corresponds to simulations ($N = 10^4$ samples with $\Delta t = 0.005$) and dots by inverse Laplace transform of Eq. (3.43). The parameters of the model are: $D = 1$, $c_0 = 5$, $\nu = 2.5$, $k_+ = 15$, $\theta_+ = 0.5$, $k_- = 10$, $\theta_- = 0.75$, $x_0 = 0$ and $\lambda = 0.5$.

For generic non-Markovian $c(t)$, calculating $S_c(\omega)$ requires the knowledge of its stationary two-time statistics, which we derive in Appendix C. Specifically, the key quantity that allows us to determine $S_c(\omega)$ is $\tilde{C}_c(s)$, the Laplace transform of the long-time $c$-correlator

$$C_c(t) \equiv \lim_{\tau\to\infty} \langle c(t+\tau)c(\tau)\rangle. \tag{3.41}$$

We can determine $C_c(t)$ by providing an explicit representation of the expectation value $\langle\cdots\rangle$ with respect to the probability of the trajectories. In Appendix C, we derive $P_{\sigma_0}(\sigma_2, t+\tau|\sigma_1, \tau)$, the probability density that the process $c(t)$, initially at $\sigma_0$, reaches the state $\sigma_1$ at time $\tau$, and eventually the state $\sigma_2$ at $t+\tau$. Hence, we can make $C_c(t)$ explicit:

$$\begin{aligned} C_c(t) =& c_0^2 \lim_{\tau\to\infty} \sum_{\sigma_2,\sigma_1,\sigma_0} \lambda_{\sigma_0}\sigma_1\sigma_2\, P_{\sigma_0}(\sigma_2, t+\tau|\sigma_1,\tau) \\ =& c_0^2 \left[P_{\rm st}(+,t|+) + P_{\rm st}(-,t|-) - 2P_{\rm st}(-,t|+)\right]. \end{aligned} \tag{3.42}$$

In the second line of Eq. (3.42) follows from the independence of the stationary probability $P_{\rm st}(\sigma_2, t|\sigma_1) \equiv \lim_{\tau\to\infty} P_{\sigma_0}(\sigma_2, t+\tau|\sigma_1,\tau)$ on the probability of the initial state $\lambda_{\sigma_0}$, and from the equality $P_{\rm st}(+,t|-) = P_{\rm st}(-\sigma, t|+\sigma)$. We employ the expressions of $\tilde{P}_{\rm st}(\sigma, s|\sigma_0)$ in Eqs. (C.32) and (C.40) in Appendix C to compute the Laplace transform $\tilde{C}_c(s)$, yielding

$$\tilde{C}_c(s) = c_0^2 \left[\frac{1}{s} - \frac{2}{\langle\tau\rangle} \frac{\tilde{\Psi}_-(s)\tilde{\Psi}_+(s)}{1-\tilde{\psi}_-(s)\tilde{\psi}_+(s)}\right]. \tag{3.43}$$

We recall that $\tilde{\psi}_\sigma(s)$ and $\tilde{\Psi}_\sigma(s) = [1-\tilde{\psi}_\sigma(s)]/s$ are, respectively, the Laplace transform of the waiting-time distribution $\psi_\sigma(t)$ and of its cumulative $\Psi_\sigma(t)$, while

$$\langle\tau\rangle \equiv \frac{\langle\tau\rangle_+ + \langle\tau\rangle_-}{2}, \tag{3.44}$$

is the average half-period of the oscillations. In Fig. 3.4, we compare the inverse Laplace transform of $\tilde{C}_c(s)$ in Eq. (3.43) with its numerical estimate. The function $\tilde{C}_c(s)$ is analytic on the imaginary axis of the complex $s$-plane, entailing that the Fourier transform of $C_c(t)$ can be computed by analytically continuing $\tilde{C}_c(s)$ as

$$S_c(\omega) = \tilde{C}_c(i\omega) + \tilde{C}_c(-i\omega). \tag{3.45}$$

Notably, the equation for $S_c(\omega)$ holds for any waiting time distribution, as long as it is possible to calculate their Laplace transform. Finally, by substituting the expression of $S_c(\omega)$ in Eq. (3.45) into Eq. (3.40), one constructs $S_x(\omega)$, the power spectrum of the $x(t)$ process.

Recent works [217, 199] have revealed that, for a system effectively described as oscillations between two mesoscopic states, non-monotonic waiting-time distributions emerge if the underlying process is characterized by a non-equilibrium stationary state. These features may be described by Gamma-captured waiting times

$$\psi_\sigma(\tau) = \frac{\tau^{k_\sigma - 1}}{\theta_\sigma^{k_\sigma}\Gamma(k_\sigma)}\, e^{-\tau/\theta_\sigma}, \tag{3.46}$$

with the condition $k_\sigma > 1$, which ensures the existence of a maximum, that, similarly to the average $\langle\tau\rangle_\sigma = k_\sigma\theta_\sigma$, sets a time scale for the process. For this example, the power spectrum $S_c(\omega)$ reads

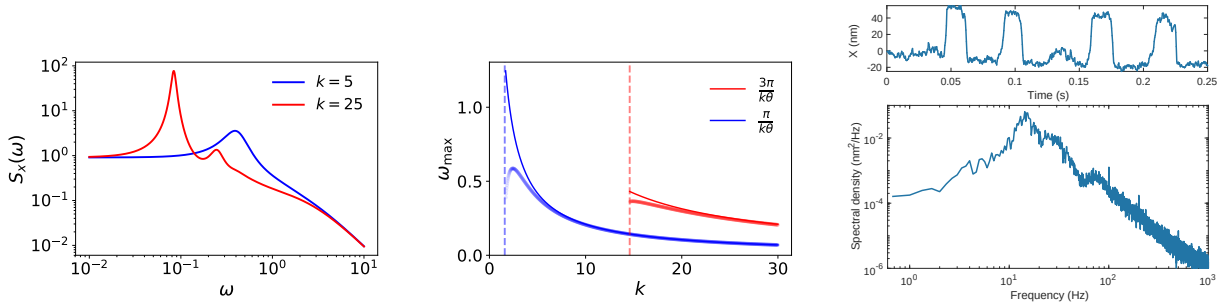
$$S_c(\omega) = \frac{4c_0^2}{\langle\tau\rangle\omega^2}\frac{(R_+R_-)^2 - 1 + (1-R_-^2)R_+\cos\phi_+ + (1-R_+^2)R_-\cos\phi_-}{(R_+R_-)^2 + 1 - 2R_+R_-\cos(\phi_+ + \phi_-)}, \tag{3.47}$$

where we define the auxiliary quantities

$$\phi_\sigma(\omega) \equiv k_\sigma \arctan(\omega\theta_\sigma), \quad \text{and} \quad R_\sigma(\omega) \equiv (1+\omega^2\theta_\sigma^2)^{k_\sigma/2}, \tag{3.48}$$

following from the expression of the Laplace transform $\tilde{\psi}_\sigma(s) = (1+s\theta_\sigma)^{-k_\sigma}$ of Eq. (3.46). Finally, by substituting Eq. (3.47) into Eq. (3.40) we find the expression of $S_x(\omega)$: it agrees with the numerical estimates of the power spectrum for both exponentially- and Gamma-distributed waiting times, as shown in panels (c) and (f), respectively, of Fig. 3.1. We find that the power spectrum $S_x(\omega)$ displays a peak at a frequency $\omega_{\max}$ for sufficiently large values of $k_\sigma$, which depend on the choice of parameters (blue curve of Fig. 3.5a). Moreover, for larger values of $k_\sigma$, the spectrum may present additional peaks close to the integer multiples of $\omega_{\max}$(red curve of Fig. 3.5a).

For symmetric Gamma-distributed waiting times, Fig. 3.5b shows the frequencies corresponding to the first two peaks of $S_x(\omega)$ as a function of the shape parameter $k$. We note that the second peak appears for $k \simeq 14.6$ at frequency $\simeq 3\,\omega_{\max}$, which results from the fact that, upon increasing $k$, $c(t)$ increasingly resembles a deterministic symmetric square wave whose Fourier spectrum has only odd harmonics. The appearance of peaks at these higher harmonics in the power spectrum is encountered in real active oscillators. For example, in Fig. 3.5c we report the experimental recording of the oscillating dynamics of the tip of the hair bundles in the bullfrog ear (see Section 3.6), and its power spectrum (curve in the bottom), which displays a second peak. This corroborates the fact that our model may be used to capture the mean features of active oscillating systems.




(a) (b) (c)

Figure 3.5: **Power spectrum.** Panel **(a)** shows the power spectrum $S_x(\omega)$ in Eq. (3.40) for two different values of $k$: for sufficiently small values of $k$ (blue curve) the power spectrum is qualitatively analogous to a Lorentzian; as $k$ increases new peaks appear in the power spectrum (red curve). Panel **(b)** displays the frequencies of the first (blue) and second (red) peak of the power spectrum $S_x(\omega)$. As $k$ increases above $\simeq 1.5$ (dashed blue vertical line) a first local maximum appears in $S_x(\omega)$ at a typical frequency (blue symbols), well approximated by the blue solid line. As $k$ increases above $\simeq 14.6$ (dashed red vertical line), a second peak arises at a typical frequency (red symbols), well approximated by the red solid line. The values of the parameters are $\theta = 1.5$, $D = 0.5$, $c_0 = 1$, and $\nu = 2.5$. On the top of panel **(c)**, we report the experimental recording of the oscillating tip of a hair bundle of the bullfrog inner ear, see Section 3.6. On the bottom, the corresponding power spectrum. These data are taken from Ref. [178] with authors' permission.

## 3.5 Energetics

In order to characterize the thermodynamics of the active mechanism driving the oscillations, in this Section we evaluate the statistics of the work done on the system. As reported in Appendix A.4, the stochastic work $\delta W(t)$ done on the system in the time interval $[t, t + \mathrm{d}t]$ is given by

$$\delta W(t) = \frac{\partial V}{\partial c} \circ \mathrm{d}c(t) = -\kappa\, x(t) \circ \mathrm{d}c(t), \tag{3.49}$$

where $\circ$ denotes the Stratonovich product [193], and the second equality follows from $c^2(t) = c_0^2$.

Note that $\delta W(t)$ is proportional to $\mathrm{d}c(t)$, which is non-zero only when a switch occurs at time $t$: energy is injected (extracted) into (from) the system, i.e., $\delta W(t) > 0$ ($\delta W(t) < 0$), when $x(t)\,\mathrm{d}c(t) < 0$ ($x(t)\mathrm{d}\,c(t) > 0$). Then, the stochastic work associated to a given trajectory of $x(t)$ reads

$$W(t) = \int_{\tau\in(0,t)} \delta W(\tau) = -\kappa \int_{\tau\in(0,t)} x(t) \circ \mathrm{d}c(t). \tag{3.50}$$

We now address the study of the statistics of the work $W(t)$ starting by the derivation of the probability density $P_{\delta W}(w|t)$ of the random process $\delta W(t)$:

$$
\begin{aligned}
P_{\delta W}(w|t) =& \delta(w)\left\{1-\mathrm{d}t\left[\lambda\left(P_S(-,t|+)+P_S(+,t|+)\right)+(1-\lambda)\left(P_S(-,t|-)+P_S(+,t|-)\right)\right]\right\} \\
&+\mathrm{d}t\int_{-\infty}^{+\infty}\mathrm{d}x\left\{\delta\left(w-2\kappa c_0\,x\right)\left[\lambda\,G_S(x,-,t|x_0,+)+(1-\lambda)G_S(x,-,t|x_0,-)\right]\right. \\
&\left.+\,\delta\left(w+2\kappa c_0\,x\right)\left[\lambda\,G_S(x,+,t|x_0,+)+(1-\lambda)G_S(x,+,t|x_0,-)\right]\right\}.
\end{aligned}
\tag{3.51}
$$

The first line in Eq. (3.51) accounts for trajectories that do not display a switch at time $t$, yielding $\delta W(t)=0$. The corresponding probability is the complementary of the probability of having a switch at $t$. The second and the third lines refer, respectively, to trajectories showing a switch from $\pm c_0$ to $\mp c_0$ at time $t$: hence, the work done in $[t,t+\mathrm{d}t]$ is given by $\delta W(t)=\pm 2\kappa c_0\,x$. As discussed in Subsec. 3.3.1, the presence of the $\mathrm{d}t$ factor results from the fact that $G_S(x,\sigma,t|x_0,\sigma_0)$ is a probability density also with respect to time. The knowledge of the explicit expression of $P_{\delta W}(w|t)$ in terms of $G_S(x,\sigma,t|x_0,\sigma_0)$ allows us to determine its moments:

$$
\langle(\delta W(t))^n\rangle=(2\kappa c_0)^n\mathrm{d}t\int_{-\infty}^{+\infty}\mathrm{d}x\,x^n\left[\rho_-^S(x,t|x_0)+(-1)^n\,\rho_+^S(x,t|x_0)\right],
\tag{3.52}
$$

holding for $n\geq 1$, whereas for $n=0$ one recovers normalization. In order to streamline Eq. (3.52), we have introduced the switching probability densities of particles:

$$
\rho_\sigma^S(x,t|x_0)\equiv\sum_{\sigma_0}\lambda_{\sigma_0}G_S(x,\sigma,t|x_0,\sigma_0),
\tag{3.53}
$$

Note that, independently of the moment degree $n$, $\langle(\delta W(t))^n\rangle$ is always proportional to $\mathrm{d}t$: it follows that their time integrals are not infinitesimal, and it is due that $\delta W(t)$ is compatible with only one switch at $t$.We now make use of the statistics of $\delta W(t)$ to build the first and second moment of $W(t)$.

### 3.5.1 First moment

The first moment of the stochastic work $W(t)$ in Eq. (3.50) can be expressed in terms of $\langle\delta W(t)\rangle$ in Eq. (3.52) as

$$
\langle W(t)\rangle=\int_{\tau\in(0,t)}\langle\delta W(\tau)\rangle=-2\kappa c_0\sum_{\sigma_0,\,\sigma}\lambda_{\sigma_0}\,\sigma\int_0^t\mathrm{d}\tau\,\langle x\rangle_{\sigma\sigma_0}^S(\tau|x_0).
\tag{3.54}
$$

In the last equality we have introduced $\langle x\rangle_{\sigma\sigma_0}^S(t|x_0)$, the first moment of the probability density $G_S(x,\sigma,t|x_0,\sigma_0)$. In Appendix C.1, we derive exact formulas for the Laplace transform of the moments $\langle x\rangle_{\sigma\sigma_0}^S(t|x_0)$, here denoted as $\langle\tilde{x}\rangle_{\sigma\sigma_0}^S(s|x_0)$. Similarly, the Laplace transform of Eq. (3.54) is given by:

$$
\langle\tilde{W}(s)\rangle=-\frac{2\kappa c_0}{s}\sum_{\sigma_0,\sigma}\lambda_{\sigma_0}\,\sigma\,\langle\tilde{x}\rangle_{\sigma\sigma_0}^S(s|x_0),
\tag{3.55}
$$

where the expressions of $\langle\tilde{x}\rangle^S$ and $\tilde{P}_S$ are reported in Eqs. (C.4), (C.5) and (3.13) of Appendix C.1. In Fig. 3.6a we numerically check Eq. (3.55). From Fig. 3.6a, it is apparent the linear long-time behaviour of $\langle W(t)\rangle$. By considering a small $s$ expansion of Eq. (3.55), we extract the linear coefficient of this line, representing the long-time average dissipated power $\langle\dot{W}\rangle = \lim_{t\to\infty}\langle\delta W(t)\rangle/\mathrm{d}t$:

$$\langle\dot{W}\rangle = \frac{2\kappa c_0^2}{\langle\tau\rangle}\frac{[1-\tilde{\psi}_+(\nu)][1-\tilde{\psi}_-(\nu)]}{1-\tilde{\psi}_+(\nu)\tilde{\psi}_-(\nu)}, \tag{3.56}$$

which holds for *arbitrary* waiting-time distributions $\psi_\sigma(\tau)$. The average stationary power is always positive in agreement with the second law, i.e., $\langle\dot{W}\rangle = T\langle\dot{\mathcal{S}}_{\rm tot}\rangle \geq 0$, where $\langle\dot{\mathcal{S}}_{\rm tot}\rangle$ is the rate of entropy production, see Appendix A.4. Moreover, Eq. (3.56) implies the upper bound $\langle\dot{W}\rangle \leq 2\kappa c_0^2/\langle\tau\rangle$, which is saturated in the limit of infinitely fast relaxation time ($\nu\to\infty$). The upper bound $2\kappa c_0^2/\langle\tau\rangle$ is the ratio between the characteristic energy $V_0 = \kappa(2c_0)^2/2$ that $x(t)$ fluctuating around the minimum of one potential acquires in the other potential immediately after the switch and the average time between two consecutive switches $\langle\tau\rangle$. For $\nu\to\infty$, this $V_0$ is indeed the energy injected in the system at a switch.

### 3.5.2 Second moment

By following similar steps as for the first moment, we calculate $\langle\tilde{W}^2(s)\rangle$, the Laplace transform of the second moment of the work $W(t)$. Accordingly, the second moment of the work $\langle W^2(t)\rangle$ is given by

$$\begin{aligned}
\langle W^2(t)\rangle =& \int_{t_1,t_2\in(0,t)}\langle\delta W(t_1)\delta W(t_2)\rangle \\
=& 2\int_{t_2\in(0,t)}\int_{t_1\in(0,t_2)}\langle\delta W(t_1)\delta W(t_2)\rangle + \int_{t_1\in(0,t)}\langle\delta W^2(t_1)\rangle \\
=& (2\kappa c_0)^2\left[2\sum_{\sigma_2,\sigma_1,\sigma_0}\sigma_1\sigma_2\int_0^t\mathrm{d}t_2\int_0^{t_2}\mathrm{d}t_1\int_{-\infty}^{+\infty}\mathrm{d}x_1\int_{-\infty}^{+\infty}\mathrm{d}x_2\; x_1\, x_2\,\rho^S_{\sigma_0}(x_1,t_1|x_0)\right. \\
&\left.\times\, G_S(x_2,\sigma_2,t_2-t_1|x_1,\sigma_1) + \int_0^t\mathrm{d}t_1\int_{-\infty}^{+\infty}\mathrm{d}x\; x^2\rho^S(x,t_1|x_0)\right].
\end{aligned} \tag{3.57}$$

The first equality follows from the definition of the second moment, while the second by splitting the domain of integration. As discussed above, $\delta W(t)$ is non-zero only if a switch occurs at $t$. Therefore, the first integral in the second equality has contributions only from trajectories displaying a switch both at $t_1$ and $t_2$. However, the second contribution to $\langle W^2(t)\rangle$ is the integral of $\langle(\delta W)^2\rangle$ in Eq. (3.52) for $n=2$, coinciding with a single switch at $t_1$. The first integral in the third equality of Eq. (3.57) expresses the explicit contributions of $\delta W(t_1)$ and $\delta W(t_2)$ in Eq. (3.50) to $\langle W^2(t)\rangle$, and the respective probability weight: the probability of the first switch at $t_1$ is denoted by the switching probability $\rho^S_\sigma(x_1,t_1)$, then particle reaches $x_2$ at the second switching time $t_2$, as represented by the probability weight $G_S(x_2,\pm\sigma,t_2-t_1|\sigma)$. The last line is a rephrasing of the integral of the second moment of Eq. (3.52). As for Eq. (3.54), the second moment depends on the first and second moment of $\rho^S_\sigma(x,t|x_0)$, or in general of $G_S(x,\sigma,t|x_0,\sigma_0)$.

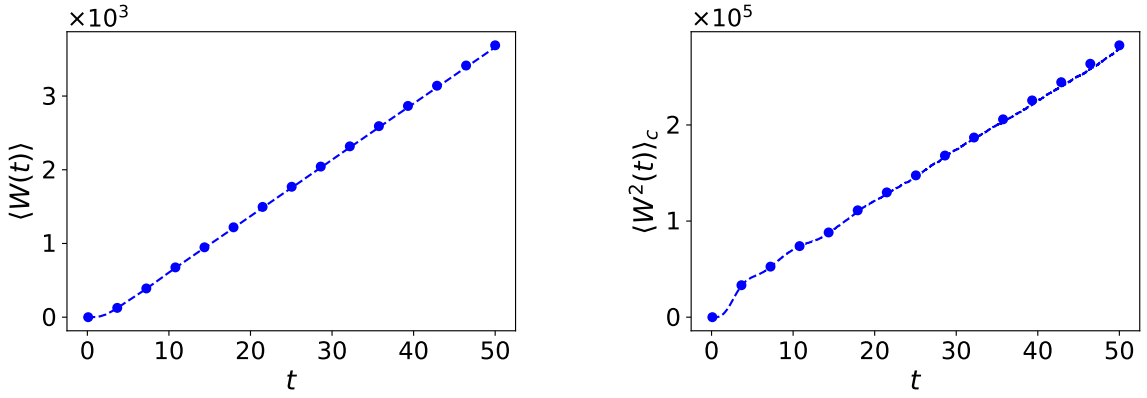



Figure 3.6: **Moments of the work.** Panel **(a)** and **(b)** represent, respectively, the time evolution of the average $\langle W(t)\rangle$, and the variance $\langle W^2(t)\rangle_c$ of the work. We compare the prediction coming from simulations of the system (dashed line), obtained via Euler method with $N = 5 \times 10^4$ trajectories and time step $\Delta t = 10^{-3}$, with the numerical inverse Laplace transform of Eq. (3.55) (symbols). The parameters of the plot are: $D = 5$, $c_0 = 5$, $\nu = 7.5$, $k_+ = 5$, $\theta_+ = 0.75$, $k_- = 7.5$, $\theta_- = 0.8$, $x_0 = 0$ and $\lambda = 0.5$.

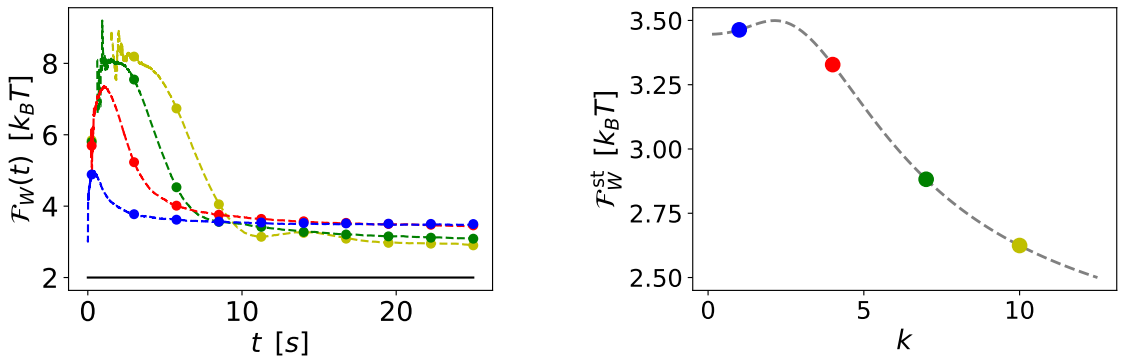
Once again, we get a closed expression of the Laplace transform of $\langle W^2(t)\rangle$ by substituting the moments $\langle \tilde{x}\rangle^S_{\sigma\sigma_0}(x_0|s)$ reported in Eqs. (C.4) and (C.5), and $\langle \tilde{x}^2\rangle^S_{\sigma\sigma_0}(x_0|s)$ in Eqs. (C.13) and (C.14), into the expression of $\langle W^2(t)\rangle$ in Eq. (3.57). Eventually, after some algebra, we get

$$\langle \tilde{W}^2(s)\rangle = \frac{(2\kappa c_0)^2}{s} \sum_\sigma \left[ (2E_\sigma(s) + 1)\, \langle \tilde{x}^2\rangle^S_\sigma(s|x_0) + 2\langle \tilde{x}\rangle^S_\sigma(s|x_0) F_\sigma(s) \right], \tag{3.58}$$

where $\langle \tilde{x}^2\rangle^S_\sigma(s|x_0)$, and $\langle \tilde{x}\rangle^S_\sigma(s|x_0)$, indicate respectively the Laplace transform of the first and second moment of $\rho^S(x,t|x_0)$, while we define the functions $E_\sigma(s)$ and $F_\sigma(s)$ via the relation $\langle \tilde{x}\rangle^S_{\sigma\sigma}(s|x_0) - \langle \tilde{x}\rangle^S_{-\sigma\sigma}(s|x_0) = x_0 E_\sigma(s) + F_\sigma(s)$; their cumbersome expressions are reported in Eq. (C.7) of Appendix C.1. A numerical check of Eq. (3.58) in shown in Fig. 3.6b, where we compare the numerical inverse Laplace transform of the variance $\langle W^2(t)\rangle_c = \langle W^2(t)\rangle - \langle W(t)\rangle^2$ (symbols) with predictions from simulations (dashed line). Notably, both the average and the variance of the work grow linearly at large times. This is due to the fact that work $W(t)$ in Eq. (3.50) satisfies the large deviation principle [216, 12].

### 3.5.3 Work Fano factor for symmetric waiting-time distributions

In the context of stochastic thermodynamics, it is interesting to characterize the trade-off between fluctuations and dissipation of time-integrated currents, such as the work in Eq. (3.50). This line of research has lead to the discovery of thermodynamic uncertainty relations [11, 91, 127, 99, 13, 36, 57, 52, 59, 223, 224, 166, 197]. In this optics, we consider the Fano factor of the work, defined as:




(a) (b)

Figure 3.7: **Work Fano factor.** The figure on the left shows the time-dependent Fano factor of the work $\mathcal{F}_W^{\rm st}(t)$ in the case of symmetric Gamma-distributed waiting times for different values of the $k$ parameter: we compare numerical prediction (continuous line), computed simulating with the Euler method $N = 10^5$ trajectories with time step $\Delta t = 5 \times 10^{-4}$, with the numerical inverse Laplace transform of Eqs. (3.55) and (3.58) (symbols). On the right, the stationary value of the Fano factor $\mathcal{F}_W^{\rm st}$ as a function of $k$: each curve in the left plot is in correspondence to the value of $k$ with the same color of the symbol in the figure on the right. The black horizontal line identifies the lower bound $2k_BT$. The values of the parameters are $D = 5$, $x_0 = 0$, $c_0 = 2.5$, $\nu = 2.5$, $\theta = 0.75$, $k = 1$ (blue), $k = 4$ (red), $k = 7$ (green), $k = 10$ (yellow).

$$\mathcal{F}_W(t) = \frac{\langle W^2(t)\rangle_c}{\langle W(t)\rangle}, \tag{3.59}$$

and its stationary limit $\mathcal{F}_W^{\rm st} \equiv \lim_{t\to\infty} \mathcal{F}_W(t)$. For Markovian systems, it can be proved that it satisfies the inequality [11, 91, 127, 99, 13, 36, 57, 52].

$$\frac{\mathcal{F}_W(t)}{\langle W(t)\rangle} \geq \frac{2k_B}{\langle \mathcal{S}_{\rm tot}(t)\rangle}, \tag{3.60}$$

that in the stationary limits translates to

$$\mathcal{F}_W^{\rm st} \geq 2k_BT, \tag{3.61}$$

where one has for isothermal systems the validity of the long-time relation $\langle \dot{\mathcal{S}}_{\rm tot}\rangle = T\langle \dot{W}\rangle$ for the total entropy production [192]. As already mentioned, these thermodynamic bounds do not hold only for the work, but for any time-integrated current satisfying the large deviation principle.

However, different types of thermodynamic uncertainty relations with respect to Eq. (3.59) hold for non-Markovian systems [59, 223, 224, 166, 197]. We show in Fig. 3.7a the Fano factor $\mathcal{F}_W(t)$, computed for symmetric Gamma-distributed waiting times for different values of the parameter $k$, which is proportional to the average half-period of oscillation $\langle \tau\rangle = k\theta$. In this case, $\mathcal{F}_W^{\rm st}$ seems to

satisfy the $2k_BT$ bound for Markovian systems. However, it is not clear whether this holds for any choice of $\psi_\sigma(t)$, and at all times.

As discussed in the previous Section, the average work $\langle W(t)\rangle$ in a given time interval depends on the number of switches that occur at that time. Therefore, at times smaller than $\langle\tau\rangle$, the average number of switches vanishes and $\mathcal{F}_W(t)$ is dominated by fluctuations: this phenomenon becomes more apparent as $\langle\tau\rangle$ increases. In the long-time limit, the Fano factor attains its stationary value $\mathcal{F}_W^{\rm st}$. In this case, as the value of $k$ grows, the effect of memory gets stronger and the oscillations of the process $x(t)$ more regular: this explains why $\mathcal{F}_W^{\rm st}$ decreases at large $k$. The dependence of $\mathcal{F}_W^{\rm st}$ on $k$ is shown in 3.7b.

We can determine the expression of $\mathcal{F}_W^{\rm st}$ by studying the long-time behaviour of the average $\langle W(t)\rangle$, and second moment $\langle W^2(t)\rangle$ of the work in the case of equally distributed waiting times $\psi_\sigma(\tau) = \psi(\tau)$. This asymptotic regime can be extracted from the expressions of $\langle\tilde{W}(s)\rangle$ and $\langle\tilde{W}^2(s)\rangle_c$ in Eqs. (3.55) and (3.58) by considering the leading terms in the $s\to 0$ Laurent series. In principle, this analysis holds also for asymmetric waiting-time distributions, but the corresponding expressions of $\langle W(t)\rangle$ and $\langle W^2(t)\rangle$ are too cumbersome and not more significant than their symmetric counterpart.

The long-time expansion for the average work yields

$$\langle W(t)\rangle = \frac{2\kappa c_0^2}{\langle\tau\rangle}\left[\frac{1-\tilde{\psi}(\nu)}{1+\tilde{\psi}(\nu)}t + Z(\nu) + O(t^{-1})\right], \tag{3.62}$$

where we have introduced the auxiliary function

$$Z(\nu) = \frac{1}{1+\tilde{\psi}(\nu)}\left[\frac{\langle\tau^2\rangle}{2\langle\tau\rangle}\left(1-\tilde{\psi}(\nu)\right) - \langle\tau\rangle - \frac{2\partial_\nu\tilde{\psi}(\nu)}{1+\tilde{\psi}(\nu)}\right], \tag{3.63}$$

with $\langle\tau^2\rangle \equiv \int_0^\infty {\rm d}\tau\,\tau^2\,\psi(\tau)$ denoting the second moment of the waiting-time distribution $\psi(\tau)$. Similarly, we carry out the asymptotic expansion for the second moment of the work $\langle W^2(t)\rangle$:

$$\langle W^2(t)\rangle = \frac{(2\kappa c_0)^2}{\langle\tau\rangle}\frac{1-\tilde{\psi}(\nu)}{1+\tilde{\psi}(\nu)}\left\{\frac{c_0^2}{\langle\tau\rangle}\frac{1-\tilde{\psi}(\nu)}{1+\tilde{\psi}(\nu)}t^2 + \left[\frac{D}{\nu} + c_0^2\left(\frac{4Z(\nu)}{\langle\tau\rangle} + H(\nu)\right)\right]t + O(t^0)\right\}, \tag{3.64}$$

where, to lighten the expression, we have introduced the function

$$H(\nu) = \frac{1}{1-\tilde{\psi}(2\nu)}\left[1 - 2\tilde{\psi}(\nu) + \tilde{\psi}(2\nu) - 2\left(\tilde{\psi}(\nu) - \tilde{\psi}(2\nu)\right)\frac{1-\tilde{\psi}(\nu)}{1+\tilde{\psi}(\nu)}\right]. \tag{3.65}$$

Finally, from the asymptotic expressions in Eqs. (3.62) and (3.64), we can construct the leading contributions to the expansion of the work variance $\langle W^2(t)\rangle_c$ at large times:

$$\langle W^2\rangle_c(t) = \frac{(2\kappa c_0)^2}{\langle\tau\rangle}\frac{1-\tilde{\psi}(\nu)}{1+\tilde{\psi}(\nu)}\left[\frac{D}{\nu} + c_0^2\left(\frac{2Z(\nu)}{\langle\tau\rangle} + H(\nu)\right)\right]t + O(t^0). \tag{3.66}$$

Equations (3.62) and (3.66) allow us to determine an exact expression the Fano factor of the work in the long-time limit:

$$\mathcal{F}_W^{\rm st} = 2k_BT + 2\kappa c_0^2\left(\frac{2Z(\nu)}{\langle\tau\rangle} + H(\nu)\right), \tag{3.67}$$

which follows from the relation $k_BT = \kappa D/\nu$. Note that, both the variance $\langle W^2(t)\rangle_c$ and the average $\langle W(t)\rangle_c$ are positive, and that the Fano factor is always larger than $2k_BT$, satisfying the bound in Eq. (3.61). Indeed, at large times, the system satisfies the large deviation principle, as a consequence of the fact that the memory time scale becomes negligible with the total duration of the dynamics, i.e., $t \gg \langle\tau\rangle$. In the particular case of exponentially-distributed waiting times in Eq. (3.4), we get $\mathcal{F}_W^{\rm st} = 2k_BT + 2\kappa[c_0\nu/(\nu+2r)]^2$. We point out that similar results have been measured experimentally for a system consisting of a colloidal particle in a dichotomously switching optical trap [61, 163] .

### 3.5.4 Energy and heat moments

We conclude this Section by mentioning how to extend the calculations done for the work, to other thermodynamic observables, such as energy and heat. For example, we can obtain the average of the energy $V\left(x(t), c(t)\right)$ according to

$$\begin{aligned}\langle V\left(x(t), c(t)\right)\rangle &= \frac{\kappa}{2}\left[\langle x^2(t)\rangle - 2\langle x(t)c(t)\rangle + \langle c^2(t)\rangle\right] \\ &= \frac{\kappa}{2}\left[\langle x^2(t)\rangle - 2\langle x(t)c(t)\rangle + c_0^2\right],\end{aligned} \tag{3.68}$$

where we use the symmetry property $c^2(t) = c_0^2$. The expression of $\langle x^2(t)\rangle$ is calculated in Appendix C in Eq. (C.21). Finally, the last contribution to $\langle V\left(x(t), c(t)\right)\rangle$ is represented by $\langle x(t)c(t)\rangle$, which we can cast as

$$\langle x(t)c(t)\rangle = c_0 \sum_\sigma \sigma\, P(\sigma, t)\langle x(t)\rangle_\sigma, \tag{3.69}$$

where we recall that $\langle x\rangle_\sigma$ is the first moment of $\rho_\sigma(x, t|x_0)$ in Eq. (3.17) and we derive its Laplace transform is in Eq. (C.17), while the Laplace transform of $P(\sigma, t)$ in Eq. (3.21) has been found in previous Section.

The stationary value of the average energy is then given by the constant

$$V_{\rm st} \equiv \lim_{t\to\infty}\langle V\left(x(t), c(t)\right)\rangle = \frac{\kappa}{2}\left\{\langle x^2\rangle^{\rm st} - c_0\left[\langle x\rangle_+^{\rm st} - \langle x\rangle_-^{\rm st}\right] + c_0^2\right\}, \tag{3.70}$$

where the stationary moments of the position $\langle x\rangle^{\rm st}$ and $\langle x^2\rangle^{\rm st}$ are determined in Eqs. (C.19) and (C.23) of Appendix C.

In general, all the moments of the energy reach a stationary value: this results from the fact that they can be expressed in terms of the moments of the process $x(t)$. Therefore, the statistics of the heat $Q$ can be derived from the first law of thermodynamics (see Appendix A)

$$\Delta V = W + Q. \tag{3.71}$$

In particular, it is easy to check that the long-time limit of the Fano factor of the heat reads $|\mathcal{F}_Q^{\rm st}| = \mathcal{F}_W^{\rm st}$.

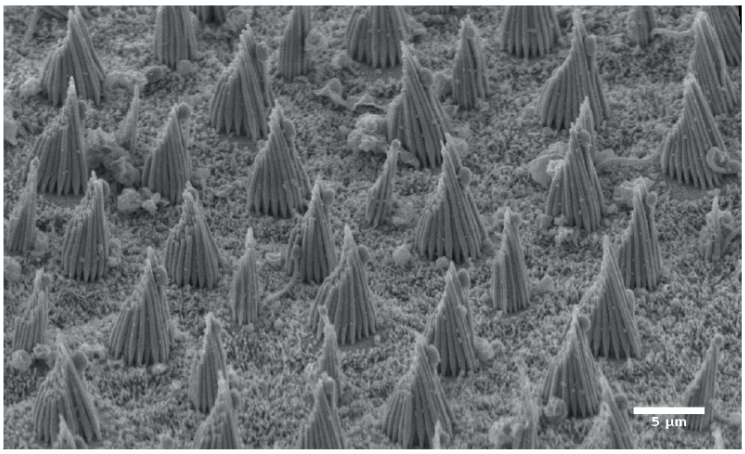



Figure 3.8: **Bullfrog hair bundles.** Electron micrograph showing hair bundles that protrude from the sensory epithelium of a bullfrog's sacculus. This organ from the frog's inner ear is dedicated to the detection of low frequency vibrations ($\sim$ 5–150 Hz). The height of the hair bundles is about $\sim 7$ $\mu$m. Picture taken from Ref. [178] with Authors' permission.

## 3.6 Experimental application: spontaneous oscillations of the bullfrog hair bundles

An example of a biological process displaying active oscillations is the spontaneous motion of hair-cell bundles from a bullfrog ear [102, 132, 130]. The hair bundle is an organelle formed by a cohesive tuft of cylindrical stereocillia, which protrude from the apical surface of the namesake hair cells, see Fig. 3.8. These receptor cells transduce a mechanical stimulus, such as a sound wave, into a neural signal and thus facilitate hearing and other sensory organs of vertebrates. The oscillatory motion of hair bundles is powered by an active process, which is essential for the organelle's sensory function, and result in the violation of the fluctuation-dissipation theorem [178].

Several stochastic models have been proposed for the time series of hair bundles [46, 130, 214, 173, 132, 226]. Most of these models, which can be reduced to the family of Duffing – Van der Pol oscillators [129, 17, 18, 132], rely on nonlinear equations of motion with hidden degrees of freedom of diverse origins. Under various conditions such a system can describe both bistable and limit-cycle regimes of oscillatory motion, which are often not easy to distinguish.

In typical experiments, the position of the hair-bundle's tip $x(t)$ is the only variable that can be tracked [131, 9, 8]. In particular, we aimed to apply our theoretical framework to symmetric bi-stable oscillations and therefore specifically selected appropriate traces from our experimental recordings[1]. These measurements were performed on a dissected mechanosensitive epithelium of a bullfrog's sacculus. The tissue is mounted in a two-chamber holder, such that the hair cells are exposed to two different ionic solutions from their apical and basal side [6, 9]. This setup mimics the physiological condition in the inner ear and evokes spontaneous oscillations of the hair bundles. To better resolve the movement of the hair bundle, a glass fiber has been attached to the bundle's

[1]Measurements have been performed by our collaborators, i.e., Prof. A. James Hudspeth and his laboratory.

| Case | $\langle \dot{W} \rangle$ ($k_B T$/cycle) | Error bar |
|---|---|---|
| 1 | 129.28 | 0.05 |
| 2 | 50.4 | 0.6 |
| 3 | 85.37 | 0.07 |

Table 3.2: **Power per cycle.** Estimate of the stationary average power per cycle $2\langle\tau\rangle\langle\dot{W}\rangle$ in units of $k_B T$ from Eq. (3.72) for the parameters corresponding to Figs. 3.9, 3.10, and 3.11.

tip and its shadow has been projected onto a photodiode [8]. The signal of the photodiode was calibrated by translating a image fo the bundle by a 50 $\mu$m step with a mirror mounted on a piezoelectric actuator. This calibrated signal reported the position of the oscillating bundle as a function of time.

As reported below, the linear model that we propose is also capable to account for the basic features of the hair-bundle motion, which are common to simple active oscillators Figs. 3.9, 3.10 and 3.11. Namely, we infer the parameters of the model by fitting the exact expression of the power spectrum $S_x(\omega)$ in Eq. (3.40) in the case of symmetric Gamma-distributed waiting times, i.e., $S_c(\omega)$ is given by Eq. (3.47) with $k_\sigma = k$ and $\theta_\sigma = \theta$. To make contact with the experimental data we apply a simulation-based inference approach [213, 159, 121, 213] (Appendix C.4) to determine the values of the unknown parameters in Eq. (3.2) for a selection of three experimental cases, in which we observed simple symmetric oscillations of $x(t)$. Our model reproduces well the pattern of the hair-bundle motion: this can be seen in Figs. 3.9a, 3.10a and 3.11a. Quantitatively the simulated time-series of $x(t)$ also match the probability density in Figs. 3.9.b, 3.10.b and 3.11.b. Using our analytical results for the average stationary power $\langle\dot{W}\rangle$ in Eq. (3.56) in the case of symmetric Gamma-distributed waiting times, i.e.,

$$\langle \dot{W} \rangle = \frac{2\kappa c_0^2}{\langle\tau\rangle} \frac{(1+\nu\theta)^k - 1}{(1+\nu\theta)^k + 1}, \tag{3.72}$$

we can estimate the average power per cycle $2\langle\tau\rangle\langle\dot{W}\rangle$ dissipated by the active process, which drives the hair-bundle oscillations in the bullfrog ear. Its value, reported in Table 3.2, $\langle\dot{W}\rangle \sim 10^2 k_{\mathrm{B}} T$/cycle, is of the same order of magnitude than the estimates of the heat dissipation rate in hair-bundle spontaneous fluctuations [178], and of the viscous energy dissipation under weak, external periodic stimulation [131]. Assuming that active oscillations result from ATP hydrolysis (with free energy change $\sim 10 k_{\mathrm{B}} T$) by Myosin motors [103], we predict that at least $\sim$ 10ATP molecules are required to fuel a single oscillation cycle of the hair-cell bundle. We conclude that the values of the average stationary power $\langle\dot{W}\rangle$ predicted by our model well reproduce the active nature of the hair bundle oscillations.

## 3.7 Conclusions

In Section 3.2 of this Chapter, we have introduced an minimal linear stochastic model describing the dynamics of non-Markovian active oscillators. This system displays key dynamical features of

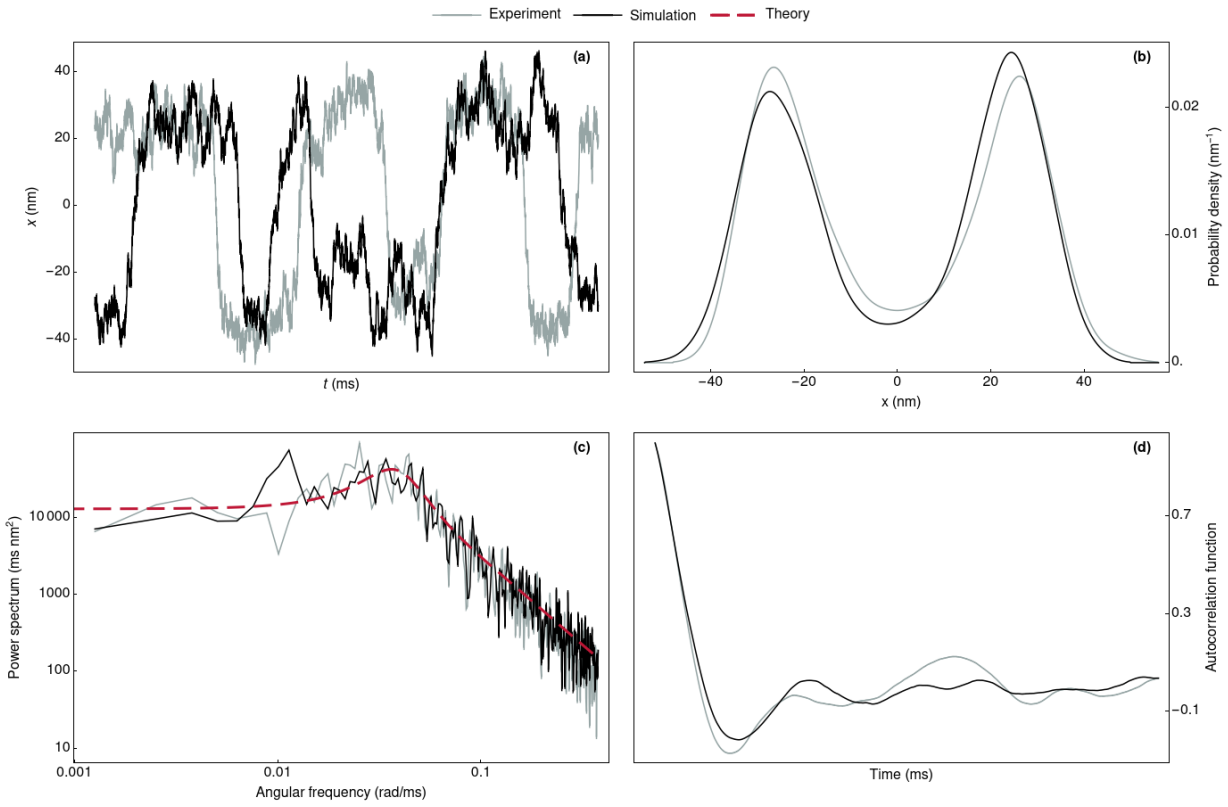



Figure 3.9: **Case 1.** Fitting experimental observations of the hair-bundle oscillations to our stochastic model. Panel **(a)**: fragments of the experimental and simulated time series. Panel **(b)**: probability distribution densities $\rho^{\mathrm{st}}(x)$ in the experiment and simulations. Panel **(c)**: power spectrum $S_x(\omega)$ of the experimental and simulated time series. Panel **(d)**: autocorrelation $C_x(t)$ function for the experimental and simulated time series. Model parameter values: $\nu = 0.172 \pm 0.002\,\mathrm{ms}^{-1}$, $D = 9.180 \pm 0.003\,\mathrm{nm}^2/\mathrm{ms}$, $c_0 = 25.991 \pm 0.002\,\mathrm{nm}$, $k = 4.267 \pm 0.006$, $\theta = 18.40 \pm 0.04\,\mathrm{ms}$.

active oscillators, e.g. transition from a monostable to bistable regime, sharp power spectra, and energy dissipation. In Sections 3.3 and 3.4, we have shown how to derive the most relevant dynamical observables of the system in a very general setting, accommodating asymmetric waiting-time distributions of the underlying noise, as observed in many biological processes [199]. In Section 3.5, we have analysed the the thermodynamic properties of the system, focusing on the work statistics. Moreover, we have checked the stationary Fano factor of the work satisfies the lower bound $2k_BT$, similarly to what predicted by thermodynamic uncertainty relation for Markovian processes. Accordingly, it would be interesting in the future to investigate whether similar bounds are satisfied at finite times for this or similar non-Markovian models. Eventually, in Section 3.6, we have also shown that our linear, non-Markovian model reproduces with high accuracy key statistics (probability density and power spectrum) of several experimental recordings from the tip of Bullfrog's sacculus hair-cell bundle. Fitting the data to the model, we have predicted that the power consumption by the hair-cell bundle during its spontaneous motion requires the consumption of at

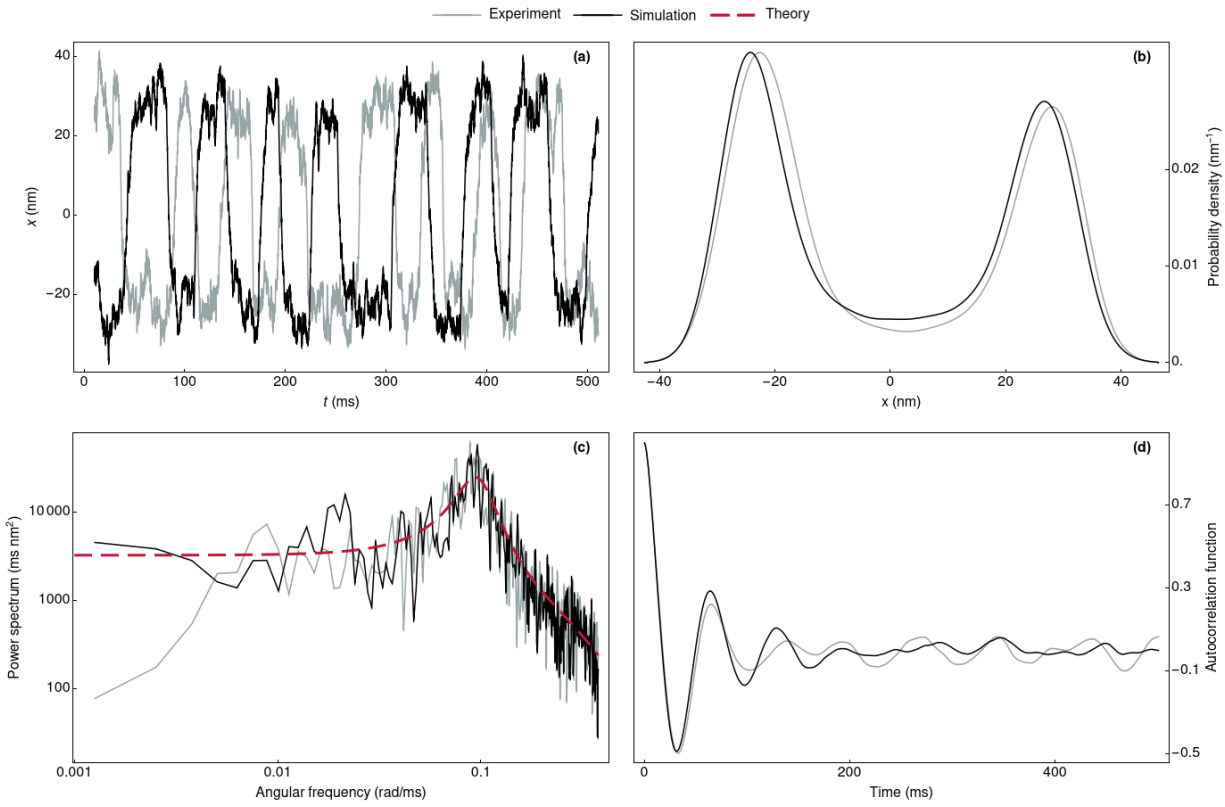



Figure 3.10: **Case 2.** Fitting experimental observations of the hair-bundle oscillations to our stochastic model. Panel **(a)**: fragments of the experimental and simulated time series. Panel **(b)**: probability distribution densities $\rho^{\mathrm{st}}(x)$ in the experiment and simulations. Panel **(c)**: power spectrum $S_x(\omega)$ of the experimental and simulated time series. Panel **(d)**: autocorrelation function $C_x(t)$ for the experimental and simulated time series. Model parameter values: $\nu = 0.260\,26 \pm 0.000\,02\,\mathrm{ms}^{-1}$, $D = 5.1752 \pm 0.0002\,\mathrm{nm}^2/\mathrm{ms}$, $c_0 = 26.2755 \pm 0.0008\,\mathrm{nm}$, $k = 7.133 \pm 0.002$, $\theta = 4.542 \pm 0.002\,\mathrm{ms}$.

least hundreds of ATP molecules per oscillation cycle. Given the minimal ingredients that characterize this model, we expect that our model could be applied to decipher the energetics of other relevant active oscillations observed in living systems, such as confined cell migration [32], neuronal networks [146], and actomyosin gels [164].

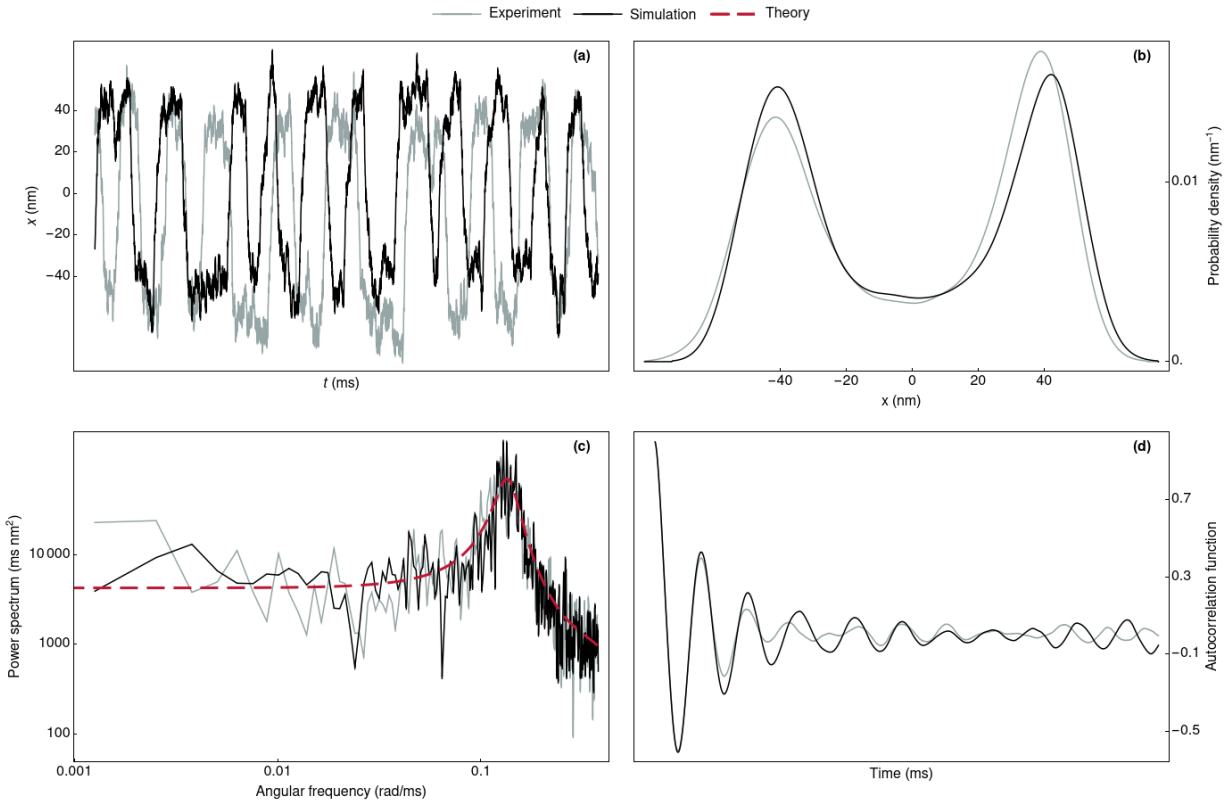



Figure 3.11: **Case 3.** Fitting experimental observations of the hair-bundle oscillations to our stochastic model. Panel **(a)**: fragments of the experimental and simulated time series. Panel **(b)**: probability distribution densities $\rho^{\mathrm{st}}(x)$ in the experiment and simulations. Panel **(c)**: power spectrum $S_x(\omega)$ of the experimental and simulated time series. Panel **(d)**: autocorrelation function $C_x(t)$ for the experimental and simulated time series. Model parameter values: $\nu = 0.281\,36 \pm 0.000\,02\,\mathrm{ms}^{-1}$, $D = 18.7724 \pm 0.0008\,\mathrm{nm}^2/\mathrm{ms}$, $c_0 = 43.850 \pm 0.001\,\mathrm{nm}$, $k = 11.591 \pm 0.003$, $\theta = 1.9979 \pm 0.0006\,\mathrm{ms}$.

# Chapter 4

# Stochastic representation of a quantum anharmonic oscillator

## 4.1 Introduction

In previous Chapters we have studied in details the statistical properties of several stochastic models with common features, such as the presence of the externally driven sudden events (e.g., resetting) and activity, and then we have seen how they can apply to describe the fluctuating behaviour of some biological systems. In this last Chapter we adopt a different point of view. Namely, we show how the dynamics of a prototypical quantum system can be re-parametrized in terms of the time evolution of classical stochastic differential equations, permitting us to translate quantum into stochastic fluctuations.

Recent advances in cold atom experiments have inspired great theoretical interest in the non-equilibrium dynamics of isolated many-body quantum systems [208, 231, 123, 227, 232, 26, 104, 209, 80, 10]. With the notable exception of integrable models [156], analytical insights into the time evolution of these systems are scarce. This motivates the search for novel numerical and analytical tools to analyse many-body quantum dynamics. A number of recent works [98, 81, 175, 184] considered an exact representation of the dynamics of many-body *spin* systems in terms of classical stochastic processes. This approach is based on a series of exact transformations, through which an interacting many-body quantum system can be exactly represented in terms of a non-interacting system under the action of a set of classical stochastic fields. In this stochastic approach, sometimes referred to as *disentanglement formalism*[1], physical observables can be expressed as averages of classical functions over realizations of suitably constructed stochastic processes. This not only breaks down the complexity of many-body quantum interactions to that of classical stochastic differential equations but also allows one to bridge the gap between the quantum realm and classical stochastic processes, for which powerful numerical tools have been developed [69]. Beside this numerical application, the formalism can also be used as a field-theoretical tool to develop analytic expansions for ob-

[1]This terminology originates from the fact that the approach described here "disentangles" the time-ordered exponential featured in the time-evolution operator into the product of ordinary exponentials, see ,e.g., Refs. [175, 43]. Hence, using this term does not necessarily point to a relation to quantum entanglement. Here we mostly stick with the terminology "stochastic approach".

servables [152]. The stochastic formalism has been mainly applied to many-body quantum systems composed by spins [98, 81, 175, 184, 185, 152, 190], where their natural interactions are mapped to classical stochastic fields. Here, we explore a generalization of the stochastic approach to systems of interacting bosons. In particular, we shall study the time-evolution of a zero-dimensional bosonic system with non-linear interaction potential. Such systems have attracted significant attention for their rich dynamical behaviour and relevant experimental applications [60, 86, 228, 124, 229, 181]. In particular, we shall consider the quartic quantum oscillator as paradigmatic, non-linear bosonic quantum system [198, 20, 189, 87, 7, 96, 19, 138]. While any system with harmonic interactions can be mapped to non-interacting bosons, this is no longer true for anharmonic potentials, whose simplest representative is the quartic one.

In spite of its apparent simplicity, the quartic quantum oscillator is notoriously hard to study and involves subtle conceptual mathematical issues, even in its equilibrium formulation: notably, the divergence of perturbation theory for the ground state in powers of the quartic coupling, and the fact that the energy levels are non-analytic in the quartic coupling complex plane. From a physical perspective, these singularities are caused by level crossings in the eigenenergies [198, 20], leading to a non-trivial perturbation theory of the energy spectrum [19, 95]. The quartic quantum oscillator is also of practical relevance, as it can be used to approximate the low-energy behaviour of more general quartic systems [195, 194, 145]. This system has been investigated by approximate techniques, such as the semiclassical evaluation of its propagator [189, 87, 7, 138, 116] and, more recently, by looking at the evolution of relevant time-dependent observables [30, 181]. Interestingly enough, the exact shape of the wave functions of the quartic oscillator has been reported only recently [62] but there is still no analytic expression for the quantized energy levels. Here, we show how the disentanglement approach can be used to represent the dynamics of a quartic quantum oscillator in terms of ensembles of stochastically evolving harmonic oscillators. The representation we introduce is formally exact and can be used to develop analytical approximations or to evaluate numerically expectation values, providing a different viewpoint as well as a practical alternative to existing techniques.

This Chapter is organized as follows. In Section 4.2 we derive a field-theoretical representation of the quantum quartic oscillator following earlier applications of the stochastic approach. This is done in two steps. First, the quartic part of the quantum quartic oscillator is decoupled with a Hubbard-Stratonovich transformation [206, 100], which casts the problem into that of the evolution of a quantum harmonic oscillator with time-dependent frequency. Second, a Lie-algebraic transformation is used to express the time evolution operator in terms of ordinary exponentials featuring time-dependent coefficients [230, 109, 43], which we refer to as *stochastic variables*. This yields a set of differential equations for the stochastic variables, which effectively describe the exact quantum dynamics of the quantum quartic oscillator. We also show that the formalism can be applied to quartic Hamiltonians with time-dependent coefficients. In Section 4.3 we explain how expectation values of operator are calculated within this formalism, providing a general recipe and exact equations for a range of observables and initial states. The classical formulas we obtain are then benchmarked by considering two exactly solvable limits: the quantum harmonic oscillator, and the inherently classical limit in which all operators in the Hamiltonian commute with each other, corresponding to the disappearance of the kinetic energy in the Hamiltonian. In Section 4.4, we elaborate on the stochastic interpretation of the present approach and discuss the conditions under which the field theory we obtain can be numerically simulated by means of stochastic processes.

Building on this discussion, we show that for the quantum quartic oscillator with generic parameters (i.e., away from the two exactly solvable limits) our method can be benchmarked by applying a numerical stochastic scheme to evaluate time-evolved observables. In Section 4.5 we adopt a field-theoretical viewpoint and develop a functional expansion of the time-evolution operator about the harmonic limit, which turns out to be equivalent to the perturbative Dyson series. In Section 4.6, we discuss how the semiclassical propagator and the partition function of the quantum quartic oscillator can be analytically recovered from the field-theoretical picture. We present our conclusions in Section 4.7, summarizing our results and outlining directions for further research. Appendix D cover mathematical details.

## 4.2 Stochastic representation of the quantum quartic oscillator

In this section we introduce the stochastic approach briefly described in the introduction alongside with its new application to bosonic system. In particular, we focus on the quantum quartic oscillator, which is described by the Hamiltonian

$$\hat{H} \equiv \frac{\hat{p}^2}{2m} + \frac{1}{2}m\omega^2\hat{x}^2 + \frac{\lambda}{4}\hat{x}^4 \,. \tag{4.1}$$

Here, the position operator $\hat{x}$ and the momentum operator $\hat{p}$ satisfy the canonical commutation relation $[\hat{x}, \hat{p}] = i\hbar$. The mass of the oscillator is denoted by $m$, the harmonic frequency by $\omega$ and the quartic potential is parametrized by the coupling constant $\lambda$. Since an exact solution is not available for $\lambda \neq 0$, different approaches have been used in order to obtain insights on the problem, e.g., perturbation theory [20, 198, 19] and semiclassical approximations [116, 87, 189].

Here, we develop a novel exact theoretical formulation of the quantum quartic oscillator, following the disentanglement approach recently applied to an ensemble of interacting quantum spin systems [98, 81, 175, 184]. This is done by employing a functional representation of the time-evolution operator

$$\hat{U}(t) \equiv \exp\left(-\frac{i}{\hbar}\hat{H}t\right). \tag{4.2}$$

First, we decouple the quartic term in the exponent of Eq. (4.2) via a Hubbard-Stratonovich transformation [100, 206] and trotterize [207, 196] the time evolution operator on the time interval $\tau_n \equiv t/n$, in the limit $n \to \infty$, i.e.,

$$\hat{U}(t) = \lim_{n\to\infty}\left(\exp\left[-\frac{i\tau_n}{\hbar}\frac{\hat{p}^2}{2m}\right]\exp\left[-\frac{i\tau_n}{\hbar}\left(\frac{m}{2}\omega^2\hat{x}^2 + \frac{\lambda}{4}\hat{x}^4\right)\right]\right)^n. \tag{4.3}$$

To each of the $n$ factor appearing in the formula above, we apply a Hubbard-Stratonovich transformation which allows us to replace the quartic interaction with a quadratic one by introducing a new integration variable $\phi$, i.e.,

$$\exp\left(-i\frac{\tau_n}{\hbar}\frac{\lambda}{4}\hat{x}^4\right) = \sqrt{\frac{\tau_n}{i\lambda\hbar\pi}}\int_{-\infty}^{\infty}\mathrm{d}\phi\,\exp\left[\frac{i\tau_n}{\hbar}\left(\frac{\phi^2}{\lambda} - \hat{x}^2\,\phi\right)\right], \tag{4.4}$$

where the choice of $\sqrt{i} = e^{i\pi/4}$ follows from the positivity of $\lambda$, and the scalar field $\phi$ is chosen to be real-valued. Equation (4.4) is derived in Appendix D.1. In the continuum limit $n \to \infty$, we can substitute the expression in Eq. (4.4) to each slice of the Suzuki-Trotter decomposition in Eq. (4.3), corresponding to the integration variable $\phi_k$ with $k \in \{1, \ldots, n\}$. By collecting all the integrals over $\phi_k$, we can express $\hat{U}(t)$ as a functional integral with respect to the Hubbard-Stratonovich field $\phi(t)$. The corresponding measure is given by $\mathcal{D}\phi(t) \equiv \prod_k \sqrt{\tau_n/(i\lambda\hbar\pi)}\mathrm{d}\phi_k$ in the limit $k \to \infty$, and we find

$$\hat{U}(t) = \int \mathcal{D}\phi \, e^{iS_0[\phi]} \, \mathbb{T} \exp\left[-\frac{i}{\hbar}\int_0^t \mathrm{d}\tau \left(\frac{\hat{p}^2}{2m} + \frac{m}{2}\Omega^2(\tau)\,\hat{x}^2\right)\right], \tag{4.5}$$

where $\mathbb{T}\exp(\cdot)$ denotes the time-ordered exponential. The quadratic coupling is absorbed into an effective time-dependent real frequency $\Omega^2(t)$, defined by

$$\Omega^2(t) \equiv \omega^2 + \frac{2\phi(t)}{m}, \tag{4.6}$$

and $S_0[\phi]$ denotes the Gaussian scalar action

$$S_0[\phi] = \frac{1}{\hbar\lambda}\int_0^t \mathrm{d}\tau \, \phi^2(\tau). \tag{4.7}$$

Equation (4.5) casts the time evolution operator of the quartic oscillator as an expectation value with respect to the Gaussian action $S_0[\phi]$ of the propagator of a harmonic oscillator with time-dependent frequency $\Omega(t)$. The associated effective Hamiltonian reads

$$\hat{H}_S(t) \equiv \frac{\hat{p}^2}{2m} + \frac{m}{2}\Omega^2(t)\hat{x}^2. \tag{4.8}$$

Despite the apparent simplification of dealing with the time evolution operator of a quadratic Hamiltonian, time-ordering prevents the direct evaluation of the action of the operator in Eq. (4.5). This difficulty can be circumvented by means of a Lie-algebraic disentanglement transformation [98, 81, 175]. We define a new set of operators, whose linear combination with suitable coefficients reproduces the Hamiltonian in Eq. (4.1), i.e.,

$$\hat{S}^+ \equiv \frac{\hat{x}^2}{2\hbar} \qquad \hat{S}^z \equiv i\frac{\{\hat{x},\hat{p}\}}{4\hbar}, \qquad \text{and} \qquad \hat{S}^- \equiv \frac{\hat{p}^2}{2\hbar}, \tag{4.9}$$

where $\{\hat{x},\hat{p}\} \equiv \hat{x}\hat{p} + \hat{p}\hat{x}$ denotes the anti-commutator of the two operators. These operators satisfy the commutation relations of the SU(2) algebra, viz.,

$$[\hat{S}^+, \hat{S}^-] = 2\hat{S}^z, \text{ and } [\hat{S}^z, \hat{S}^\pm] = \pm\hat{S}^\pm. \tag{4.10}$$

However, these operators differ from the conventional spin operators by the fact that $\hat{S}^+ = (\hat{S}^+)^\dagger$ and $\hat{S}^- = (\hat{S}^-)^\dagger$ are here Hermitian. The operators defined in Eq. (4.9) allow one to write the effective Hamiltonian as

$$\hat{H}_S(t) = \hbar\left[\frac{\hat{S}^-}{m} + m\Omega^2(t)\,\hat{S}^+\right]. \tag{4.11}$$

Following Refs. [230, 109, 43], we can express the time-ordered exponential in Eq. (4.5) as

$$\hat{U}_S \equiv \mathbb{T}\exp\left[-\frac{i}{\hbar}\int_0^t \mathrm{d}\tau\left(\frac{\hat{p}^2}{2m}+\frac{1}{2}m\Omega^2(\tau)\,\hat{x}^2\right)\right] = e^{\xi^+(t)\,\hat{S}^+}e^{\xi^z(t)\,\hat{S}^z}e^{\xi^-(t)\,\hat{S}^-}, \tag{4.12}$$

with the stochastic variables $\xi^+, \xi^z$ and $\xi^-$. In Section 4.4 we shall discuss the interpretation of these variables as stochastic processes, which motivates their naming.

The time evolution of $\xi^+, \xi^z$ and $\xi^-$ is obtained by imposing that the factorized expression on the right-hand side of Eq. (4.12) satisfies the same Heisenberg equation as $\hat{U}_S$ [43], leading to

$$i\frac{\mathrm{d}\xi^+}{\mathrm{d}t}+\frac{1}{m}(\xi^+)^2 = m\Omega^2(t), \qquad i\frac{\mathrm{d}\xi^z}{\mathrm{d}t}+\frac{2}{m}\xi^+ = 0, \qquad \text{and} \qquad i\frac{\mathrm{d}\xi^-}{\mathrm{d}t}-\frac{e^{\xi^z}}{m} = 0. \tag{4.13}$$

The initial condition $\hat{U}(0) = \mathbb{1}$ imposes $\xi^+(0) = \xi^z(0) = \xi^-(0) = 0$. Note that, for a real-valued field $\phi$, $\xi^+$ and $\xi^-$ are purely imaginary while $\xi^z$ is real, implying that the exponential operators in Eq. (4.12) are unitary. We shall see that the stochastic variables are generally complex and thus the product of exponential operators in Eq. (4.12) is not unitarity. The unitarity of the time-evolution operator is only recovered upon averaging, as described in Eq. (4.5). Substituting Eq. (4.12) into Eq. (4.5), allows one to express the time evolution operator as

$$\hat{U}(t) = \left\langle e^{\xi^+(t)\hat{S}^+}e^{\xi^z(t)\hat{S}^z}e^{\xi^-(t)\hat{S}^-}\right\rangle_\phi, \tag{4.14}$$

where $\langle\dots\rangle_\phi$ denotes the average with respect to the Gaussian field $\phi$, as defined in Eq. (4.5). The representation in Eq. (4.14) is exact and allows us to map the quantum dynamics on the time evolution of the stochastic parameters, see Eq. (4.13). Since the mapping is exact, the ensemble of trajectories $\{\xi(t)\}$ determined by the fields $\phi(t)$ encodes all the information about the underlying quantum problem. Moreover, Eq. (4.14) suggests that the time evolution is given by a weighted statistical average of successive actions of the exponential operators.

It is worth noting that the operators in Eq. (4.12) are the matrix elements of the covariance matrix

$$\begin{pmatrix} \hat{x}^2 & \frac{1}{2}\{\hat{x},\hat{p}\} \\ \frac{1}{2}\{\hat{x},\hat{p}\} & \hat{p}^2 \end{pmatrix}, \tag{4.15}$$

customarily used in the study of the dynamics of Gaussian wave packets under a quantum oscillator Hamiltonian [151, 75]. Indeed, the operators in Eq. (4.14) preserve the Gaussianity of a wave-packet and justifies why it is convenient to work within this setting.

We can physically understand the action of the individual exponential operators in Eq. (4.12), and hence of $\hat{U}_S$, by studying their effect on a Gaussian wave packet $|\psi\rangle$, generically given by

$$|\psi\rangle = \int_{-\infty}^{\infty}\frac{\mathrm{d}x}{(\pi\sigma^2)^{1/4}}\exp\left(-\frac{(x-a)^2}{2\sigma^2}+i(x-a)k\right)|x\rangle\,, \tag{4.16}$$

parametrized by its average position $\langle x\rangle \equiv \langle\psi|\,\hat{x}\,|\psi\rangle = a$, variance $\langle x^2\rangle_c \equiv \langle\psi|\,(\hat{x}-a)^2\,|\psi\rangle = \sigma^2/2$ (where $\langle\dots\rangle_c$ denotes the connected component of the expectation value), average momentum $\langle p\rangle \equiv \langle\psi|\,\hat{p}\,|\psi\rangle = k$ and its variance $\langle p^2\rangle_c \equiv \langle\psi|\,(\hat{p}-k)^2\,|\psi\rangle = (2\sigma^2)^{-1}$; here $|x\rangle$ denotes an eigenstate of the position operator and we set $\hbar = 1$. In order to visualize the action of these operators, it is convenient to see how the average and variance of the momentum and position operators transform. Namely, an operator of the type:

- $\exp(\xi^- \hat{S}^-)$ acts on a Gaussian wave packet $|\psi\rangle$ leaving unaltered the momentum cumulants $\langle p\rangle$ and $\langle p^2\rangle_c$, while shifting $\langle x\rangle = a - \mathrm{Im}(\xi^-)k$ and the variance $\langle x^2\rangle_c = \sigma^2/2 + (\mathrm{Im}(\xi^-)/\sigma)^2/2$ by terms that depend on the imaginary part of $\xi^-$;

- $\exp(\xi^z \hat{S}^z)$ rescales the $n-$th cumulant of position $\langle \hat{x}^n\rangle_c$ of the wave packet by an homogeneous constant $e^{-n\xi^z/2}$, while the $n-$th cumulant of the momentum $\langle \hat{p}^n\rangle_c$ by $e^{n\xi^z/2}$. For the first cumulants we have $\langle x\rangle = a\, e^{-\xi^z/2}$, $\langle x^2\rangle_c = \sigma^2 e^{-\xi^z}/2$, $\langle p\rangle = k e^{\xi^z/2}$ and $\langle p^2\rangle_c = e^{\xi^z}/(2\sigma^2)$. Thanks to the homogeneity of the transformation, the products $\langle x\rangle\langle p\rangle$ and $\langle x^2\rangle_c\langle p^2\rangle_c$ are preserved;

- $\exp(\xi^+ \hat{S}^+)$ leaves unaltered the position cumulants $\langle x\rangle$ and $\langle x^2\rangle_c$, while shifting $\langle p\rangle = k + \mathrm{Im}(\xi^+)a$ and the variance $\langle p^2\rangle_c = (2\sigma^2)^{-1} + (\mathrm{Im}(\xi^+)\sigma)^2/2$ by terms that depend on the imaginary part of $\xi^+$.

In order to further understand the physical significance of the action of the exponential operators on a Gaussian wave packet $|\psi\rangle$, it is useful to consider the exact phase space representation given by the Wigner function, defined as $W(x,p) \equiv \pi^{-1}\int \mathrm{d}y\, e^{-i2yp}\langle x+y|\psi\rangle\langle\psi|x-y\rangle$ [37, 122, 202]. The knowledge of $W(x,p)$ allows one to compute the expectation value of any operator $O(\hat{x},\hat{p})$, expressed as a function of $\hat{x}$ and $\hat{p}$, according to $\langle\psi|\, O(\hat{x},\hat{p})\,|\psi\rangle = \int \mathrm{d}x \int \mathrm{d}p\, W(x,p) O(x,p)$. This generalizes the results obtained above for the first cumulants of the wave packet, which are retrieved by identifying the operator $O(\hat{x},\hat{p})$ with $\hat{x}$, $\hat{p}$, $\hat{x}^2$, $\hat{p}^2$, and their connected expectation value. Figure 4.1 shows how the Wigner function $W(x,p) = \exp\left[-(x-a)^2/\sigma^2 - \sigma^2(p-k)^2\right]/\pi$ of a Gaussian wave packet is transformed upon the action of the three exponential operators in Eq. (4.12). In general, the exponential operators in Eq. (4.14) transform the parameters of the Gaussian wave packet by altering its original Heisenberg uncertainty relation $\langle\hat{x}^2\rangle_c\langle\hat{p}^2\rangle_c = 1/2$ [186], while they preserve the Gaussian structure of the relative Wigner function. For further details, see Appendix D.3.

## 4.3 Physical observables

In this Section, we illustrate how expectation values of observables can be expressed in the stochastic formalism by considering the position and momentum operator. In general, for a system prepared in a state $|\psi\rangle$, the expectation value of an observable $\hat{O}$ is given by $\langle\hat{O}\rangle \equiv \langle\psi|\,\hat{U}^\dagger(t)\,\hat{O}\,\hat{U}(t)\,|\psi\rangle$. In particular, we refer to $\langle\psi|\,\hat{O}^n\,|\psi\rangle$ as the $n$-th moment of the operator $\hat{O}$ with respect to the state $|\psi\rangle$. We can then express quantum expectation values as functional averages by replacing each time evolution operator by its exact representation given by Eq. (4.14). This requires introducing independent Hubbard-Stratonovich fields $\phi$ and $\bar{\phi}$ for the two time evolution operators. We refer to these fields as forward ($\phi$) and backward ($\bar{\phi}$) fields.

### 4.3.1 Dynamics of a Gaussian wave packet

The dynamics of a particle in the presence of a quartic potential can be studied via the time-dependent moments of its position and momentum. We model the particle as a Gaussian wave packet whose time evolution is governed by the time-evolution operator in Eq. (4.14). The evolved state is thus simply obtained by the subsequent action of the exponential operators in Eq. (4.14)

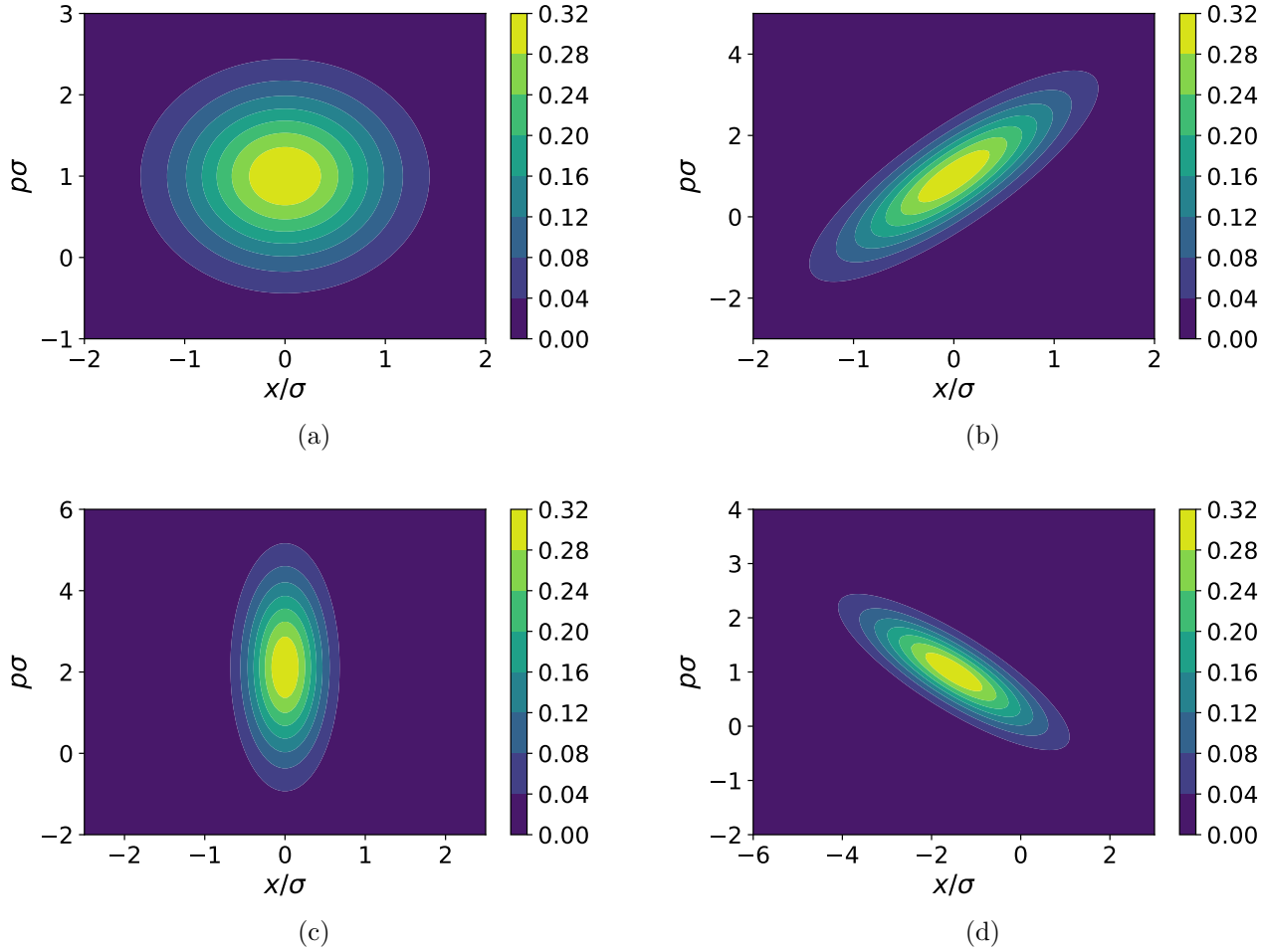



Figure 4.1: Panel **(a)** shows the contour plot of the Wigner function $W(x,p)$ for the wave function $|\psi\rangle$ in Eq. (4.16); its analytical expression is reported in Eq. (D.15) of Appendix D.3. In both $x$ and $p$ direction, $W(x,p)$ is a Gaussian centered in the phase space point $(a,k)$ and variance $\sigma^2/2$ and $(2\sigma^2)^{-1}$ respectively. The wave packet parameters are $a=0$, $k=1$, and $\sigma=1$. Panel **(b)** reports the contour plot of the Wigner function $W_+(x,p)$ for the wave function $|\psi_+\rangle \equiv \exp(\xi^+ \hat{S}^+)\,|\psi\rangle$ in Eq. (D.28). The effect of the transformation is to shift the $p$ variable by an $x$-dependent linear term, i.e., $p \to p - x\ \mathrm{Im}(\xi^+)$; here we choose the parameter $\xi^+ = 1.5i$. Panel **(c)** shows the contour plot of the Wigner function $W_z(x,p)$ for the wave function $|\psi\rangle \equiv \exp(\xi^z \hat{S}^z)\,|\psi\rangle$ in Eq. (D.23). The effect of the transformation is to rescale uniformly the variables $(x,p)$ to $(x\,e^{\xi^z/2}, p\,e^{-\xi^z/2})$, here shown for $\xi^z = 1.5$. Panel **(d)** shows the contour plot of the Wigner function $W_-(x,p)$ for the wave function $|\psi\rangle \equiv \exp(\xi^- \hat{S}^-)\,|\psi\rangle$ in Eq. (D.17). The effect of the transformation is to shift the $x$ variable by a $p$-dependent linear term according to $x \to x + p\ \mathrm{Im}(\xi^-)$, again shown here for $\xi^- = 1.5i$.

and we find

$$|\psi(t)\rangle = \hat{U}(t)\,|\psi\rangle = \left\langle \int \mathrm{d}y \frac{\sqrt{\beta(t)\sigma}}{\pi^{\frac{1}{4}}} \exp\left(-\frac{\sigma^2 k^2}{2} - \frac{y^2}{2}\gamma(t) + i\sigma^2\beta(t)\mu y + \frac{\sigma^4\mu^2}{2}\alpha(t)\right)|y\rangle \right\rangle_{\phi}. \tag{4.17}$$

Here, we have introduced the generalised initial momentum $\mu$ of the wave packet as $\mu \equiv k - ia\sigma^{-2}$ and the variables $\alpha(t), \beta(t)$ and $\gamma(t)$, which depend on the stochastic variables as

$$\alpha(t) \equiv \frac{1}{\sigma^2 - \xi^-(t)}, \qquad \beta(t) \equiv \frac{e^{\xi^z(t)/2}}{\sigma^2 - \xi^-(t)}, \qquad \gamma(t) \equiv \frac{e^{\xi^z(t)}}{\sigma^2 - \xi^-(t)} - \xi^+(t). \tag{4.18}$$

The time evolution of $\alpha, \beta$, and $\gamma$ is readily obtained from Eq. (4.13), i.e.,

$$i\frac{\mathrm{d}\gamma}{\mathrm{d}t} = \frac{\gamma^2}{m} - m\Omega^2, \qquad i\frac{\mathrm{d}\beta}{\mathrm{d}t} = \frac{\beta\gamma}{m}, \qquad i\frac{\mathrm{d}\alpha}{\mathrm{d}t} = \frac{\beta^2}{m}, \tag{4.19}$$

with initial conditions $\alpha(0) = \beta(0) = \gamma(0) = \sigma^{-2}$. As opposed to the stochastic variables, these parameters are no longer real or purely imaginary, but generically complex. Notably, the presence of $\sigma^2 > 0$ in Eq. (4.18) prevents divergences otherwise occurring for $\xi^-(t) = 0$, e.g., for $t = 0$.

The moments of the position operator on the Gaussian wave packet in Eq. (4.16) can be explicitly obtained by computing the expectation values $\langle\psi(t)|\,\hat{x}^n\,|\psi(t)\rangle$. To this end, we replace the time-evolved state $\hat{U}(t)\,|\psi\rangle$ by its representation involving the functional average $\langle\ldots\rangle_\phi$, derived in Eq. (4.14). A similar procedure is applied to $\hat{U}^\dagger(t)$, associated with the field $\bar{\phi}$ with action $-S_0[\bar{\phi}]$. We denote by $\alpha$, $\beta$ and $\gamma$ the solutions of Eqs. (4.19) that depend on the forward field $\phi$, and similarly we write $\bar{\alpha}$, $\bar{\beta}$, and $\bar{\gamma}$ for the solutions of the complex conjugates of Eqs. (4.19) associated with the backward field $\bar{\phi}$. The $n$-th moment of the position operator is finally found as

$$\langle\psi(t)|\,\hat{x}^n\,|\psi(t)\rangle = \left\langle 2\sigma(2\Gamma)^{-\frac{n+1}{2}} i^n \sqrt{\beta\bar{\beta}}\,\mathrm{H}_n\left(\frac{\sigma^2\Delta}{\sqrt{2\Gamma}}\right)\exp\left[-\sigma^2k^2 + \frac{\sigma^4}{2}\left(A - \frac{\Delta^2}{\Gamma}\right)\right]\right\rangle_{\phi,\bar{\phi}}, \tag{4.20}$$

where we defined the auxiliary variables $\Gamma \equiv \gamma + \bar{\gamma}$, $\Delta \equiv \mu\beta - \mu^*\bar{\beta}$, $A \equiv \mu^2\alpha + (\mu^*)^2\bar{\alpha}$, and $\mathrm{H}_n$ denotes the $n$-th degree Hermite polynomial and $\mu^*$ the complex conjugate. Similarly, the expression of the moments of the momentum operator are found to be

$$\begin{aligned}\langle\psi(t)|\,\hat{p}^n\,|\psi(t)\rangle = \Bigg\langle 2\sigma\left[2\left(\frac{1}{\gamma}+\frac{1}{\bar{\gamma}}\right)\right]^{-\frac{n+1}{2}} i^n\sqrt{\frac{\beta\bar{\beta}}{\gamma\bar{\gamma}}}\,\mathrm{H}_n\left(-i\frac{\sigma^2\left(\mu\frac{\beta}{\gamma}+\mu^*\frac{\bar{\beta}}{\bar{\gamma}}\right)}{\sqrt{2\left(\frac{1}{\gamma}+\frac{1}{\bar{\gamma}}\right)}}\right)\\ \times\exp\left\{-\sigma^2k^2 + \frac{\sigma^4}{2}\left[A + \mu^2\left(-\frac{\beta^2}{\gamma}\right) + (\mu^*)^2\left(-\frac{\bar{\beta}^2}{\bar{\gamma}}\right) + \frac{\left(\mu\frac{\beta}{\gamma}+\mu^*\frac{\bar{\beta}}{\bar{\gamma}}\right)^2}{\left(\frac{1}{\gamma}+\frac{1}{\bar{\gamma}}\right)}\right]\right\}\Bigg\rangle_{\phi,\bar{\phi}}.\end{aligned} \tag{4.21}$$

Note that these moments are formally retrieved from Eq. (4.20) by substituting $\gamma \to \gamma^{-1}$, $\beta \to -i\beta/\gamma$, and $\alpha \to \alpha - \beta^2/\gamma$. As in the case of the time evolution operator and the wave packet

evolution, it is possible to express the dynamics of an observable as the expectation value of functions of the auxiliary parameters $\alpha$, $\beta$ and $\gamma$, which depend on the field $\phi$. Below, we will see how we may use these expressions for numerical calculations. As a final remark, we note that the convergence of Eq. (4.17) requires that $\mathrm{Re}(\gamma) > 0$, which follows naturally from the unitarity of the exponential operators in Eq. (4.12), see Appendix D.4 for further details.

### 4.3.2 Exactly solvable cases

To the best of our knowledge, the non-linear evolution of the system of equations (4.13), in general, cannot be solved exactly. However, exact solutions can be found in two cases: the harmonic limit, in which Eqs. (4.13) become purely deterministic, and the *commuting limit*, in which the solutions of Eqs. (4.13) can be expressed in terms of the time-integral of the field $\phi$. We use these exactly solvable instances as benchmarks for the stochastic formalism as well as for a developing physical intuition.

#### Harmonic case

In the case $\lambda = 0$ of the harmonic oscillator, the absence of the quartic term implies that Eqs. (4.13) reduce to the system of ordinary differential equations

$$i\frac{\mathrm{d}\xi^+}{\mathrm{d}t} + \frac{1}{m}(\xi^+)^2 = m\omega^2, \qquad i\frac{\mathrm{d}\xi^z}{\mathrm{d}t} + \frac{2}{m}\xi^+ = 0, \qquad i\frac{\mathrm{d}\xi^-}{\mathrm{d}t} - \frac{e^{\xi^z}}{m} = 0, \tag{4.22}$$

which can be solved explicitly, i.e.,

$$\xi^+ = -im\omega\tan(\omega t), \qquad \xi^- = -\frac{i}{m\omega}\tan(\omega t), \qquad \xi^z = -\log\cos^2(\omega t). \tag{4.23}$$

This amounts to a known, exact parameterization of the quantum harmonic oscillator in terms of classical variables [43]. The time evolution of the stochastic variables $\xi^{+,-,z}$ for the harmonic oscillator shows periodic divergences at $t = \pi(1+2n)/(2\omega)$ with integer $n$, which, however, cancel out in the analytic computations of observables. This issue can be circumvented altogether by equivalently considering the time evolution of the variables $\alpha$, $\beta$, $\gamma$, introduced and discussed in Appendix D.4. The solutions (4.23) can be plugged in the expressions of the observables, obtained in Section 4.3, in order to compute exactly the corresponding dynamics. For instance, by inserting Eqs. (4.23) into Eq. (4.20), we retrieve the expressions of the moments of the position and momentum operator for the Gaussian wave packet:

$$\begin{aligned}
\langle\psi(t)|\,\hat{x}^n\,|\psi(t)\rangle &= \left(\frac{i}{2\sigma}\right)^n \left[\sigma^4\cos^2(\omega t) + x_0^4\sin^2(\omega t)\right]^{\frac{n}{2}} \mathrm{H}_n\left(-\frac{i\sigma[a\cos(\omega t) + kx_0^2\sin(\omega t)]}{\sqrt{\sigma^4\cos^2(\omega t) + x_0^4\sin^2(\omega t)}}\right), \\
\langle\psi(t)|\,\hat{p}^n\,|\psi(t)\rangle &= \left(\frac{i}{2x_0^2\sigma}\right)^n \left[x_0^4\cos^2(\omega t) + \sigma^4\sin^2(\omega t)\right]^{\frac{n}{2}} \mathrm{H}_n\left(-\frac{i\sigma[kx_0^2\cos(\omega t) - a\sin(\omega t)]}{\sqrt{x_0^4\cos^2(\omega t) + \sigma^4\sin^2(\omega t)}}\right),
\end{aligned} \tag{4.24}$$

where we introduced the typical harmonic oscillator length $x_0 \equiv (m\omega)^{-\frac{1}{2}}$.

**Commuting limit**

We study a particular case of the Hamiltonian in Eq. (4.1) in which the time evolution of the stochastic variables in Eq. (4.13) can be exactly solved. We consider the limit $m \to \infty$ with $m\omega^2$ is held constant in order to ensure a constant finite energy. In this limit, the kinetic part of the Hamiltonian is suppressed and it coincides with the quartic potential. Accordingly, the Hamiltonian is only a function of the position operator and does not contain the momentum operator. In this sense we refer to this as the *commuting limit*. Correspondingly, the non-linear terms in the differential equations (4.13) vanish, allowing us to express the explicit solution as

$$\xi^+ = -i\omega^2 m t - 2i \int_0^t \mathrm{d}\tau\, \phi(\tau), \qquad \xi^- = \xi^z = 0, \tag{4.25}$$

where $\xi^+$ depends on the variable $\mathcal{W} \equiv \int_0^t \mathrm{d}s\, \phi(s)$, and allows us to express the average $\langle \cdots \rangle_\phi$ in Eq. (4.14) as an average with respect to the Gaussian weight of $\mathcal{W}$, i.e.,

$$\hat{U}(t) = \int_{-\infty}^{+\infty} \mathrm{d}\mathcal{W}\, \frac{e^{i\mathcal{W}^2/(\lambda t)}}{\sqrt{i\pi\lambda t}} \exp\left[-i\left(2\mathcal{W} + m\omega^2 t\right)\hat{S}^+\right]. \tag{4.26}$$

From Eq. (4.26) it is apparent that the time evolution operator commutes with operators that depend only on the position operator $\hat{x}$. This implies the absence of dynamics for the particle position, compatibly with the vanishing kinetic energy. On the other hand, the moments of the momentum $\hat{p}$ grow in time, as a consequence of the Heisenberg uncertainty principle. We compute these moments by setting the auxiliary variables in Eq. (4.18) to $\alpha = \beta = \sigma^{-2}$ and $\gamma = \sigma^{-2} - i(2\mathcal{W} + \omega^2 m t)$ in Eq. (4.21) and by substituting the average $\langle \cdots \rangle$ with the integral $\int_{-\infty}^{+\infty} \mathrm{d}\mathcal{W}\, e^{i\mathcal{W}^2/(\lambda t)}/\sqrt{i\pi\lambda t}$ and similarly for the dual variables $\bar{\alpha}$, $\bar{\beta}$ and $\bar{\gamma}$. These expectation values can then be evaluated numerically, as we discuss in the next Section.

## 4.4 Stochastic interpretation and numerical benchmark

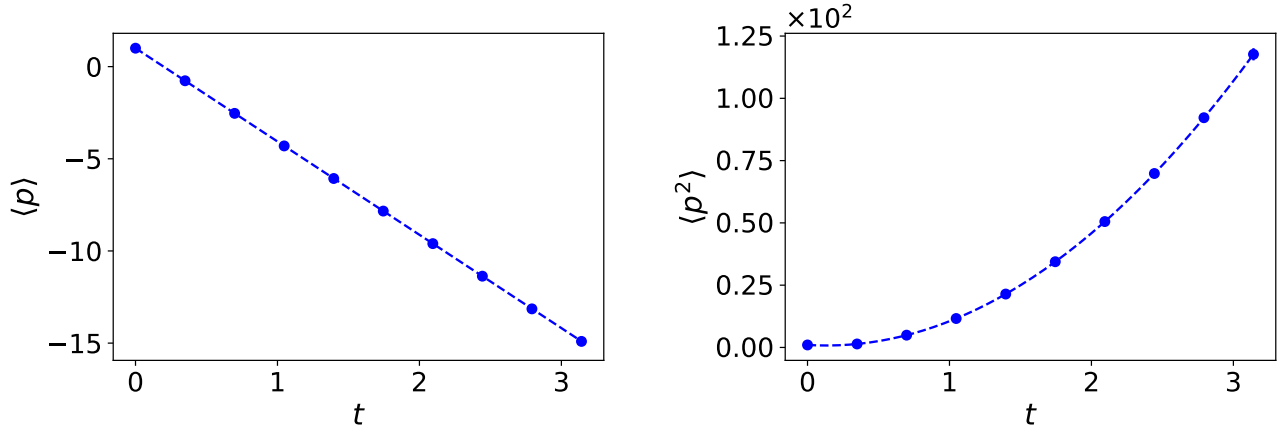
In this Section we show how the formalism presented above can be interpreted in terms of stochastic processes, which also allows us to benchmark our approach in cases where the model is not exactly solvable. In particular, by rotating the integration contour of the variable $\phi$ in the Hubbard-Stratonovich transformation for the case of time-dependent couplings in Eq. (D.12) in Appendix D, it is possible to show that

$$\exp\left(-i\frac{\tau_n}{\hbar}\frac{\lambda_n}{4}\hat{x}^4\right) = \sqrt{\frac{\tau_n}{\hbar\pi}} \int_{-\infty}^{\infty} \mathrm{d}\phi\, \exp\left[-\frac{\tau_n}{\hbar}\left(\phi^2 + i\sqrt{i\lambda_n}\,\hat{x}^2\,\phi\right)\right], \tag{4.27}$$

following from the change of variable $\phi/\sqrt{i} \to \phi$ in Eq. (D.12). Equation (4.27) allows one to represent $\hat{U}$ as

$$\hat{U}(t) = \int \mathcal{D}\phi\, e^{-S_0[\phi]}\, \hat{U}_S[\phi], \tag{4.28}$$

where $S_0$ is given by Eq. (4.7) and the time-evolution operator $\hat{U}_S$ in Eq. (4.12) displays the corresponding effective frequency $\Omega^2(t) \equiv \omega^2(t) + 2\sqrt{i\lambda(t)}\phi(t)/m$. The exponential of the action $S_0$ in




(a) (b)

Figure 4.2: Time evolution in units of $\omega^{-1}$ of the first and second moment of the $\hat{p}$-operator in units of their initial values $k$ and $(2\sigma^2)^{-1} + k^2$, respectively, for a Gaussian wave packet with $\sigma = 0.5$, $k = 1.0$, $a = 0.5$ and evolving according to Eq. (4.1) with $\lambda = 0.2$ in the commuting limit. The dashed line is computed by integrating numerically the Schrödinger equation with the Crank-Nicholson method (see Appendix D) with lattice spacing $\Delta x = 6 \times 10^{-4}$ and time step $\Delta t = \pi \times 10^{-4}$. Blue dots are computed with the stochastic method with $\Delta t = 10^{-4}$, and sampling by $N = 1.2 \times 10^6$ Gaussian random numbers. Error bars, corresponding to the statistical standard deviation over the sampling average, are not visible on the scale of the plot.

Eq. (4.7) can be identified as a Gaussian probability measure for the field $\phi(t)$, whose time integral can be interpreted as a Wiener process [69]. Accordingly, Eqs. (4.13) can be understood as complex stochastic differential equations with a Gaussian white noise $\phi$. In this reformulation, however, the stochastic variables are generically complex, and do not preserve the unitarity of $\hat{U}_S$, which is only retrieved upon averaging $\hat{U}$. As a consequence, the expression inside the average $\langle \cdots \rangle_\phi$ of the observable expressions in Eq. (4.17) does not have to be convergent at all times and for any value of the quartic coupling. More precisely, $\mathrm{Re}(\gamma)$ may attain a negative value after a certain time $t_\gamma > 0$, even though the initial value $\gamma(0) = \sigma^{-2} > 0$ is positive and real. One can numerically check that the average value of $t_\gamma$, interpreted as a random variable, decreases upon increasing the strength of the quartic coupling $\lambda$, see Fig. 4.3. Indeed, $t_\gamma$ is the first-passage time to the origin for the random variable $\mathrm{Re}(\gamma)$. This constitutes a limitation to the numerical application of the stochastic approach in the large-$\lambda$ regime. In this stochastic description, as reported in Appendix D.4, the divergences originate from the non-commutativity of the average $\langle \cdots \rangle_\phi$ over trajectories and the action of the operator $\hat{U}_S$ on a prescribed initial state $|\psi\rangle$: because of the non-unitarity of $\hat{U}_S$, the relation $\langle \hat{U}_S \rangle_\phi |\psi\rangle = \langle \hat{U}_S |\psi\rangle \rangle_\phi$ may not be satisfied. In the commuting limit, the above considerations translate in the simple change of variable $\mathcal{W}/\sqrt{i} \equiv \mathcal{W}'$ in Eq. (4.26), where this new $\mathcal{W}'$ can be interpreted a Gaussian random number with variance $\lambda t/2$. In spite of this limitation, the possibility to evaluate observables numerically by simulating classical stochastic dynamics allows us to further benchmark our approach. As a first check, we determine numerically the dynamics of the

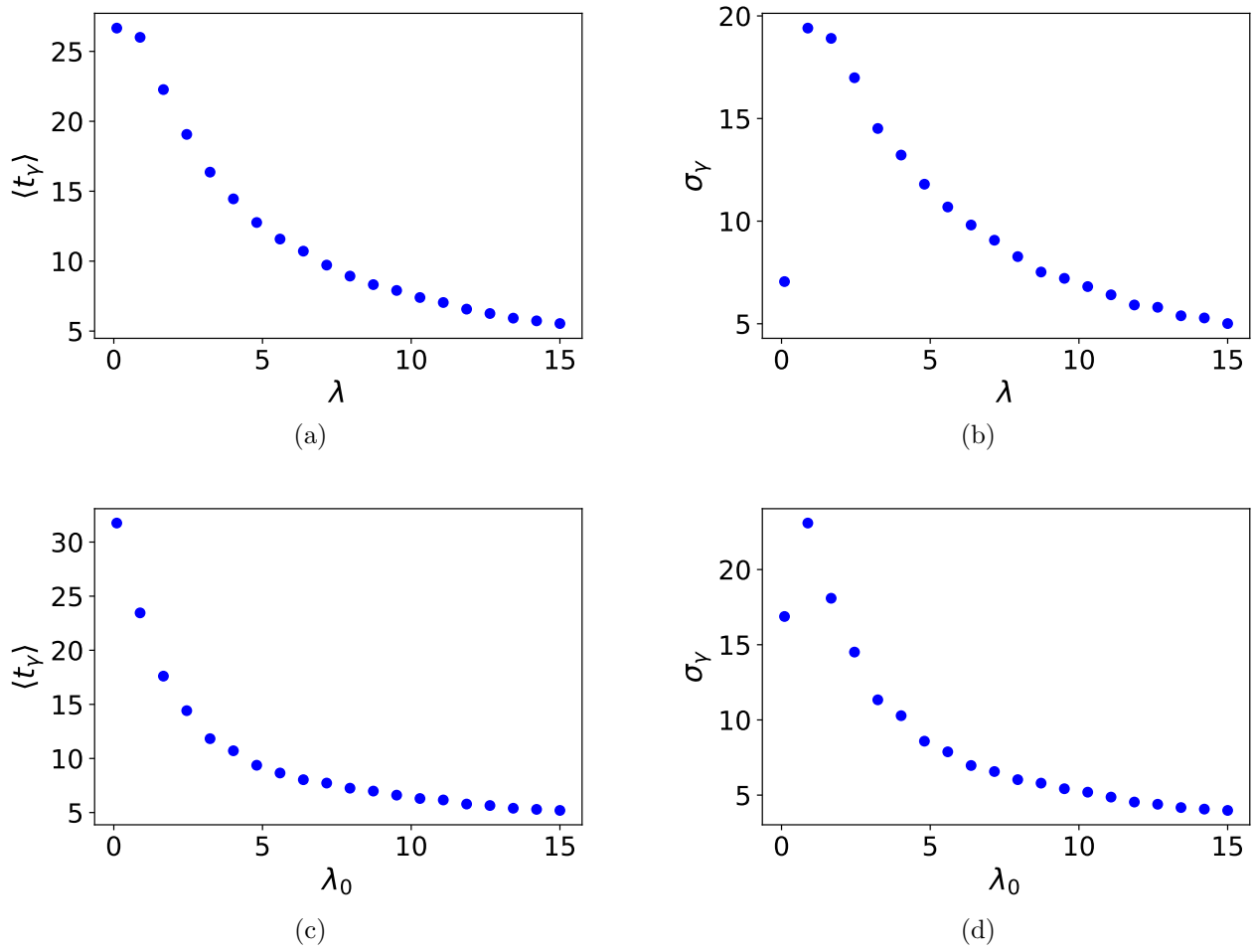



Figure 4.3: Panels **(a)** and **(b)** display a numerical estimate of the average value $\langle t_\gamma \rangle$ and the standard deviation $\sigma_\gamma \equiv \sqrt{\langle t_\gamma^2 \rangle - \langle t_\gamma \rangle^2}$ of the random variable $t_\gamma$, respectively, for the quartic oscillator, where $t_\gamma$ the time at which $\mathrm{Re}(\gamma(t_\gamma)) = 0$ for the first time. We have used the Euler scheme with time step $\Delta t = 2/\pi \times 10^{-3}$ to simulate the time evolution of $\gamma$ with physical parameters are $\omega = 1$, $m = 10$, and extracted the value of $t_\gamma$ for $N = 10^4$ trajectories. Panels **(c)** and **(d)** show the same quantities and parameters except for the presence of a time-dependent potential $\omega^2(t) = \sin^2(t)$ and $\lambda(t) = \lambda_0 \sin^2(t)$.

average momentum $\langle p \rangle$ for a Gaussian wave packet in the commuting limit. As we have shown, the stochastic differential equations are exactly solvable in this limit; it is thus possible to obtain directly the expressions for observables at a given time $t$ without having to integrate the time evolution numerically. These expressions are known functions of the time-integral $\xi^+ = -2\sqrt{i}\mathcal{W}' - i\omega^2 mt$, which can be numerically simulated by drawing Gaussian random numbers with zero mean and variance given by $\lambda t/2$. Figure 4.2 shows the comparison of the numerical prediction of the dynamics of the first two moments of the position of a wave packet between the Crank-Nicholson method (dashed line), see Appendix D, used to integrate the Schrödinger equation numerically, and the prediction based on the stochastic interpretation of Eq. (4.28) (dots), finding good agreement. As a further validation of the presented stochastic description, we evaluate the dynamics of the expectation values in Eq. (4.20) in a range of parameters where no exact solutions are available. We determine our numerical results up to a time $t < \langle t_\gamma \rangle$, where no divergences are actually detected. For this purpose, we use an Euler discretization scheme [69] with time step $\Delta\tau = 10^{-5}$ to solve the complex-valued stochastic differential equations (4.13) for a given realization of the Wiener process $\phi(t)$. Once a sufficiently large number of realizations for the stochastic variables $\xi^+$, $\xi^z$, and $\xi^-$ or $\alpha$, $\beta$, and $\gamma$ are known, by averaging with respect to them, it is possible to compute the expectation value of a desired observable, see e.g., Eq. (4.20) or (4.21). Figure 4.4 shows the time evolution of the first moments of the position operator for a Gaussian wave packet for various choices of the parameters. In particular, we compare the numerical prediction of the stochastic method (dots) with standard integration of the Schrödinger equation with the Cranck-Nicholson method (dashed line). Numerically, the proposed stochastic method has the advantage that the time-evolution of the many trajectories of the stochastic parameters, e.g., $\xi^{+,-,z}$, can be straightforwardly parallelized. On the other hand, an increasing large number of realizations is needed in order to have accurate predictions for observables at longer times or larger quartic coupling strength $\lambda$, since fluctuations due to the noise grow correspondingly. This is similar to the behaviour found for quantum spins systems [185].

In summary, we have demonstrated that our formalism allows to compute quantum observables for an interacting bosonic system from averaging classical stochastic processes, but we found that there are limitations to the applicability of this numerical technique. The mapping to stochastic processes also made it possible to further benchmark our approach in non-solvable cases. Since the stochastic description discussed in this Section is formally identical to the field theory introduced in Section 4.2, in the remainder of the manuscript we shall just refer to the present method as the "stochastic approach", although only its numerical application discussed here makes explicit use of stochastic processes.

## 4.5 Perturbative Expansion

In the stochastic approach, the time evolution operator $\hat{U}$ in Eq. (4.14) is represented as a functional average over classical fields $\phi$. In this Section, we show how this can be used to derive a perturbative expansion of $\hat{U}$ for the quartic oscillator in terms of the time evolution operator $\hat{U}_0(t)$ of the harmonic case obtained for $\lambda = 0$. We start by rescaling the Hubbard-Stratonovich field as $\phi = \sqrt{\lambda}\,\varphi$ in the

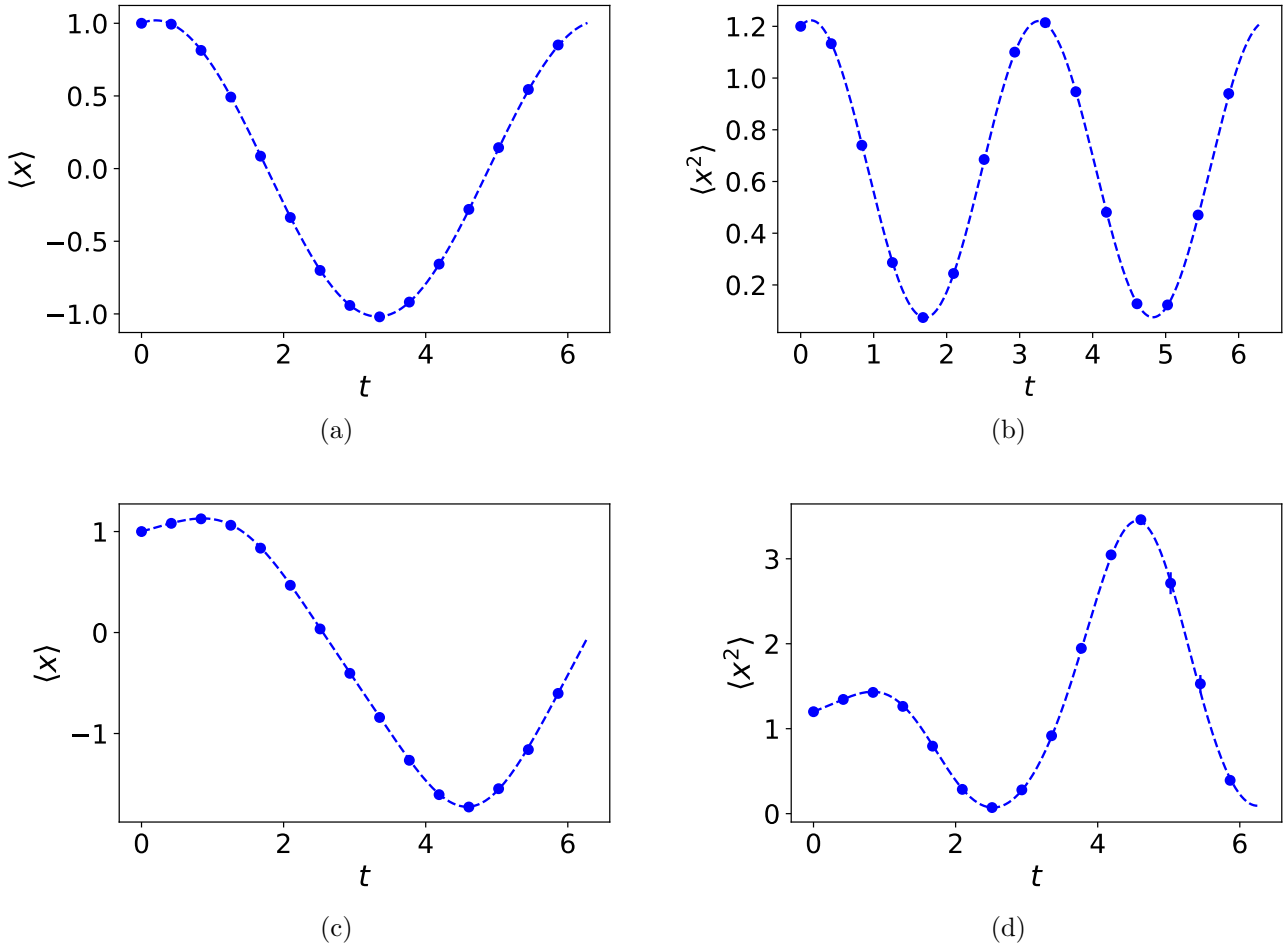



Figure 4.4: Panels **(a)** and **(b)** display the time evolution of the expected position $\langle\, x \,\rangle$ and squared position $\langle\, x^2 \,\rangle$, respectively, in units of their initial values $a$ and $a^2 + (\sigma/2)^2$, i.e., the first and second moment of a Gaussian wave packet with $\sigma = 0.5$, $k = 1.0$, $a = 0.5$ and evolving according to Eq. (4.1) with $m = 10$, $\omega = 1$, $\lambda = 0.2$, in time units of $\omega^{-1}$. The dashed line corresponds to the numerics performed with the Crank-Nicholson method with space bin $\Delta x = 10^{-5}$ and time step $\Delta t = 10^{-3}$, while the blue dots are computed with the stochastic method with $\Delta t = 10^{-4}$, and sampling $N = 1.2 \times 10^5$ trajectories. The time $t$ has been chosen such that $t < \langle t_\gamma \rangle$ with $\langle t_\gamma \rangle \simeq 27$, and $\sigma_\gamma \simeq 19$, see Fig. 4.3a-b . Similarly, panels **(c)** and **(d)** display the evolution of $\langle x \rangle$ and $\langle x^2 \rangle$, respectively, in the case of $\omega^2(t) = \omega_0^2 \sin^2(t)$ and $\lambda(t) = \lambda_0 \sin^2(t)$ with $\omega_0 = 1$, $\lambda_0 = 0.2$, and $\langle t_\gamma \rangle \simeq 31$, and $\sigma_\gamma \simeq 18$, see Fig. 4.3c-d . The dashed line corresponds to the numerics performed with the Crank-Nicholson method with space bin $\Delta x = 10^{-6}$ and time step $\Delta t = 10^{-3}$, while blue dots are computed with the stochastic method with $\Delta t = 10^{-4}$, and sampling $N = 1.2 \times 10^5$ trajectories. Error bars are given by statistical standard deviation over the trajectories average.

functional integral representation of $\hat{U}(t)$ in Eq. (4.5), yielding

$$\hat{U}(t) = \int \mathcal{D}\varphi \, e^{i\int_0^t \mathrm{d}s\, \varphi^2(s)}\, \hat{U}_S\left[\sqrt{\lambda}\varphi\right]. \tag{4.29}$$

Here, the functional $\hat{U}_S[\phi]$ (which is also a function of time) is identified with the time evolution operator of a harmonic oscillator with time-varying frequency, given by Eq. (4.12). By Taylor-expanding the functional $\hat{U}_S$ around $\phi = 0$, corresponding to the harmonic time evolution operator $\hat{U}_0$, we get an asymptotic series for the propagator

$$\hat{U}(t) = \sum_{n=0}^{\infty} \left(i\frac{\lambda}{4}\right)^n \int_0^t \left(\prod_{m=1}^{n} \mathrm{d}t_m\right) \left.\frac{\delta^{2n}\hat{U}_S[\phi]}{\delta\phi(s_1)\cdots\delta\phi(s_{2n})}\right|_{\substack{\phi=0 \\ s_{2n-1}=s_{2n}=t_n}}, \tag{4.30}$$

where, on the right-hand side, only even orders of functional derivatives appear as a consequence of Wick's theorem, leaving the functional derivative of $\hat{U}_S$ evaluated at $\phi = 0$ as the only unknown. The series in Eq. (4.30) can be shown to be equivalent term by term to the Dyson series, see Appendix D.5. The equivalence of the functional expansion about $\phi = 0$ with the Dyson series allows us to use this functional formulation to calculate perturbative approximations of observables by field-theoretical means: we express the time evolution operators in the stochastic formalism, such that all operators are replaced by classical functionals, and then functionally expand about the non-interacting case. As it is usually the case in perturbative calculations, the asymptotic series in Eq. (4.30) is expected to fail whenever we consider states for which the quartic term $\lambda\,\hat{x}^4/4$ is not negligible relative to the harmonic Hamiltonian. Indeed, it is a well-know fact that the Dyson series of the quartic oscillator has a vanishing radius of convergence [198, 20].

## 4.6 Semiclassical approximation

In this Section, we show how the semiclassical approximation for the propagator associated with $\hat{U}(t)$ in the representation of Eq. (4.14) and the partition function of the system in Eq. (4.1) can be expressed within the parametrization of the stochastic variables. Other than giving us an additional benchmark for the theory, we show how it is possible to find an alternative description of the stationary trajectories contributing to the semiclassical approximation for the quartic oscillator.

### 4.6.1 Propagator

The propagator $G(x_f, t|x_i, 0)$, which gives the probability amplitude for a particle located at $x_i$ at the initial time $t_i = 0$ to reach the position $x_f$ at time $t_f = t$, is defined by

$$G(x_f, t|x_i, 0) \equiv \langle x_f|\, \hat{U}(t)\, |x_i\rangle\,. \tag{4.31}$$

The semiclassical approximation of the propagator for the quantum quartic oscillator has been extensively studied in the literature, see, e.g., Ref. [189] for an overview. Here, we show how to express $G(x_f, t|x_i, 0)$ in terms of the stochastic variables. This expression can be derived by inserting

the representation of $\hat{U}$ in Eq. (4.14), by acting on an eigenstate of the position $|x_i\rangle$ according to Eq. (D.32) in Appendix D.4, and finally by projecting on $\langle x_f|$. This leads to

$$G(x_f, t|x_i, 0) = \left\langle \frac{1}{\sqrt{-2\pi\hbar\xi^-}} \exp\left[\frac{\xi^z}{4} + \frac{\xi^+ x_f^2}{2\hbar} + \frac{(x_f e^{\xi^z/2} - x_i)^2}{2\hbar\xi^-}\right] \right\rangle_\phi , \tag{4.32}$$

with the $\xi^{+,-,z}$ evaluated at time $t$. Note that the stochastic variables in the above expression are function of $\phi$ evaluated at the final time $t = t_f - t_i$, while the initial and final position $x_i$ and $x_f$ are fixed parameters.

In the harmonic case $\lambda = 0$, by explicit substitution of Eq. (4.23) into Eq. (4.32), we retrieve the known expression of the harmonic propagator $G_{\rm HO}$, i.e.,

$$G_{\rm HO}(x_f, t|x_i, 0) = \sqrt{\frac{m\omega}{2i\pi\hbar\sin(\omega t)}} \exp\left[\frac{im\omega}{2\hbar\sin(\omega t)}\left((x_f^2 + x_i^2)\cos(\omega t) - 2x_i\, x_f\right)\right]. \tag{4.33}$$

In the quartic case, inside the average in Eq. (4.32) we recognize a different way of representing the propagator of a harmonic oscillator with time-dependent frequency $\Omega^2(t)$. It well-known that in the case of quadratic interactions, even in the time-dependent case, the propagator can be expressed in a closed form through the contributions arising from classical paths, see, e.g., Ref. [189]. Accordingly, the propagator of a harmonic oscillator with generic time-dependent frequency can be reformulated as

$$G_{\rm HO}(x_f, t|x_i, 0) = G_{\rm HO}(0, t|0, 0) \exp\left[\frac{i}{\hbar} S_{\rm HO}(x_f, t|x_i, 0)\right]. \tag{4.34}$$

Here, the classical action $S_{\rm HO}$ of the harmonic oscillator is given by

$$S_{\rm HO}(x_f, t|x_i, 0) \equiv \frac{m}{2}\int_0^t \mathrm{d}\tau \left[\dot{x}^2(\tau) - \Omega^2(\tau)x^2(\tau)\right], \tag{4.35}$$

and is computed along the classical path $x(\tau)$ which satisfies the Euler-Lagrange equation

$$\ddot{x}(\tau) + \Omega^2(\tau)\, x(\tau) = 0, \tag{4.36}$$

with boundary conditions $x(0) = x_i$ and $x(t) = x_f$. The prefactor $G_{\rm HO}(0, t|0, 0)$ is given by

$$G_{\rm HO}(0, t|0, 0) = \sqrt{\frac{m}{2\pi i\hbar f(t)}}, \tag{4.37}$$

where the *density of paths* $f(t)$ is obtained, according to Gelfand-Yaglom formula [85], as a solution of the differential equation in Eq. (4.36) with $x \to f$, with initial conditions $f(0) = 0$ and $\dot{f}(0) = 1$. Note that, corresponding $G_{\rm HO}(0, t|0, 0)$ to the Feynman path integral with the quadratic action in Eq. (4.35), we deduce that the function $f$ is proportional to the determinant of the operator $d_t^2 + \Omega^2(t)$ expressed through Eq. (4.37); see Appendix D.6.

The solutions of Eq. (4.36) depend on the realization of the field $\phi$ which enters $\Omega$ according to Eq. (4.6). Alternatively, they can be expressed in terms of the stochastic variables according to

$$\begin{aligned} x(\tau|t) &= \frac{e^{-\xi^z(\tau)/2}}{\xi^-(t)}\left\{x_f\xi^-(\tau)e^{\xi^z(t)/2} + x_i\left[\xi^-(t) - \xi^-(\tau)\right]\right\}, \\ f(\tau) &= im\,\xi^-(\tau)\, e^{-\xi^z(\tau)/2}, \end{aligned} \tag{4.38}$$

where we emphasize that $t$, $x_i$, and $x_f$ are fixed parameters, and $\tau \in [0,t]$ as a variable. In turn, $\xi^{+,-,z}$ depend on $\phi$ via Eq. (4.13). In order to simplify the notation, the dependence of $x$ and $f$ on $x_i$ and $x_f$ and the functional dependence on $\phi$ are omitted.

Finally, by inserting Eq. (4.34) into (4.32), the propagator $G(x_f,t|x_i,0)$ for the quartic oscillator reads

$$\begin{aligned} G(x_f,t|x_i,0) &= \int \mathcal{D}\phi \, \sqrt{\frac{m}{2\pi i\hbar f(t)}} \exp\left[\frac{i}{\hbar\lambda}\int_0^t \phi^2(\tau)d\tau + \frac{i}{\hbar}S_{\rm HO}(x_f,t|x_i,0)\right] \\ &= \int \mathcal{D}\phi \, \exp\left[\frac{i}{\hbar\lambda}\int_0^t \phi^2(\tau)d\tau\right] G_{\rm HO}[\{\xi(t)\}]. \end{aligned} \tag{4.39}$$

As anticipated, Eq. (4.39) illustrates the fact that the propagator for the quartic oscillator is given by an infinite collection of classical path contributions of harmonic oscillators with different time dependent frequencies. Moreover, Eq. (4.39) provides the starting point to perform the semiclassical approximation, corresponding to the limit $\hbar\lambda \to 0$. We start by rescaling spatial coordinates as $y \equiv x\sqrt{\lambda}$, and we set $y_f \equiv \sqrt{\lambda}\, x_f$, $y_i \equiv \sqrt{\lambda}\, x_i$. Due to the homogeneity of $S_{\rm HO}$ with respect to $x_i$ and $x_f$, this rescaling allows us to cast the propagator $G$ as

$$G(x_f,t|x_i,0) = \int \mathcal{D}\phi \, \sqrt{\frac{m}{2\pi i\hbar f(t)}} \exp\left[\frac{i}{\hbar\lambda}\left(\int_0^t \phi^2(\tau)d\tau + \, S_{\rm HO}(y_f,t|y_i,0)\right)\right]. \tag{4.40}$$

In the limit $\hbar\lambda \to 0$, we can approximate the functional integral by applying the stationary phase method [235]. We obtain

$$\bar{\phi}(\tau) = -\frac{1}{2}\frac{\delta S_{\rm HO}(y_f,t;y_i,0)}{\delta\phi(\tau)}\Big|_{\bar{\phi}} = \frac{\bar{y}^2(\tau)}{2} = \lambda\frac{\bar{x}^2(\tau)}{2}. \tag{4.41}$$

By inserting Eq. (4.41) in Eq. (4.36) we retrieve the equation for the classical trajectories of the quartic oscillator

$$\ddot{\bar{x}}(\tau) + \omega^2\bar{x}(\tau) + \frac{\bar{x}^3(\tau)}{m} = 0, \tag{4.42}$$

with boundary conditions $\bar{x}(0) = x_i$ and $\bar{x}(t) = x_f$. The solution of Eq. (4.42) can be expressed in terms of Jacobi elliptic functions [116]. Note that, according to Eqs. (4.41) and (4.42), the stationary field $\bar{\phi}$ is continuous and twice differentiable, meaning that among all possible realizations of $\phi$ only a subset with sufficient regularity contributes in the semiclassical limit. As reported in Ref. [87], the associated stationary trajectories $\bar{x}$ can be classified in terms of the sign of the momentum $\hat{p}$ of the particles $\bar{p} = m\dot{\bar{x}}$ at the boundary points $x_i$ and $x_f$.

The semiclassical approximation is obtained by considering terms of the expansion in $\sqrt{\hbar\lambda}$ up to the second order around the stationary phase solution. In this spirit, we introduce the change of variable $\phi = \bar{\phi} + \sqrt{\hbar\lambda}\,\varphi$ and truncate the expansion around $\bar{\phi}$ at second order in $\varphi$, leading to

$$G(x_f,t|x_i,0) = \sum_k \sqrt{\frac{m}{2\pi i\hbar f_k(t)}}\; e^{\frac{i}{\hbar}S_k(x_f,t|x_i,0)} \int \mathcal{D}\varphi \exp\left[i\int_0^t \mathrm{d}t_1 \int_0^t \mathrm{d}t_2\, \varphi(t_1)H_k(t_1,t_2)\varphi(t_2)\right] \tag{4.43}$$

with $\mathcal{D}\varphi \equiv \prod_n \mathrm{d}\phi_n/\sqrt{i\pi}$, where the second functional derivative of the action computed at $\bar{\phi}$ corresponds to the operator

$$H_k(t_1,t_2) \equiv \delta(t_1-t_2) + \frac{1}{2}\frac{\delta^2 S_{\rm HO}(y_f,t|y_i,0)}{\delta\phi(t_1)\,\delta\phi(t_2)}\Big|_{\bar{\phi}_k}; \tag{4.44}$$

the zeroth order of the expansion renders the classical action $S_k(x_f,t|x_i,0)$ of the quartic oscillator

$$S_k(x_f,t|x_i,0)=\int_0^t \mathrm{d}\tau\left[\frac{m}{2}(\dot{x}_k)^2-\frac{1}{2}m\omega^2\,x_k^2-\frac{\lambda}{4}x_k^4\right], \tag{4.45}$$

evaluated on $x_k$, the $k$-th solution of Eq. (4.42) with $\phi_k\equiv\bar{\phi}[x_k]$, and $f_k\equiv f[\phi_k]$. In order to determine the functional Gaussian integral in Eq. (4.43) it is necessary to calculate the determinant of the operator $H_k$. As shown in Appendix D.7, this computation can be done explicitly, leading to the final expression of the semiclassical propagator as

$$G(x_f,t|x_i,0)=\sum_k\sqrt{\frac{m}{2\pi i\hbar\,F_k(t)}}\;e^{iS_k(x_f,t|x_i,0)/\hbar}, \tag{4.46}$$

where $F_k\equiv F[\phi_k]$, similarly to $f_k$, satisfies the differential equation

$$\ddot{F}_k(\tau)+\left[\omega^2+3\frac{\lambda}{m}x_k^2(\tau)\right]F_k(\tau)=0, \tag{4.47}$$

with $F_k(0)=0$ and $\dot{F}_k(0)=1$, being $F_k$ proportional to the determinant of the $H_k$ operator.

In the process of deriving Eq. (4.45) within the present approach we relate the operator $H_k(t_1,t_2)$ to the functional derivative of (4.36) according to Eq. (D.68) in Appendix D.7, leading to $\det(H_k)=\sqrt{f_k(t)/F_k(t)}$. In summary, we have derived an alternative representation of the propagator $G(x_f,t|x_i,0)$ of the quartic oscillator, expressed as a weighted collection of the propagators of effective harmonic oscillators $G_{\mathrm{HO}}(x_f,t|x_i,0)$. Moreover, we provided a parametrization of the time-evolution of these harmonic oscillators in terms of the stochastic variables. Finally, we have proven that the semiclassical approximation of $G(x_f,t|x_i,0)$ relies on the calculation of the determinant of the second variation of the effective action $S_{\mathrm{HO}}$, and how this determinant is linked to the *density of paths* along the classical trajectory $\bar{x}_k$ of the quartic oscillator.

### 4.6.2 Partition function

In this Section we show that our formulation is not only restricted to non-equilibrium problems, but it can be used to extract finite-temperature [98, 81] or ground state [152] properties by Wick-rotating to imaginary time. Taking a brief detour from dynamics, here we provide an additional confirmation of the validity of the stochastic representation of the quartic quantum oscillator by obtaining the semiclassical limit ($\hbar\to 0$) of its partition function $Z(\beta)$, where $\beta$ is the inverse temperature. The partition function $Z(\beta)$ is obtained from the propagator $G(x_f,t|x_i,0)$ in Eq. (4.32) according to [235]

$$Z(\beta)=\int_{-\infty}^{+\infty}\mathrm{d}x\,G(x,t=-i\hbar\beta|x,0)=\left\langle\frac{1}{\sqrt{-2\pi\hbar\xi^-}}\exp\left[\frac{\xi^z}{4}+\frac{x^2}{2\hbar}\left(\xi^+ +\frac{(e^{\xi^z/2}-1)^2}{\xi^-}\right)\right]\right\rangle_\phi . \tag{4.48}$$

The evolution of the stochastic variables as functions of $\beta$ is determined by the set of differential equations

$$\frac{1}{\hbar}\frac{\mathrm{d}\xi^+}{\mathrm{d}\beta}-\frac{(\xi^+)^2}{m}+m\omega^2+2\phi=0,\qquad \frac{1}{\hbar}\frac{\mathrm{d}\xi^z}{\mathrm{d}\beta}-\frac{2}{m}\xi^+=0,\qquad \frac{1}{\hbar}\frac{\mathrm{d}\xi^-}{\mathrm{d}\beta}+\frac{e^{\xi^z}}{m}=0, \tag{4.49}$$

with the usual initial conditions $\xi^{+,-,z}(0) = 0$. Equation (4.49) suggest that we may retrieve the semiclassical limit by retaining the leading-order contributions in a series expansion of $\xi^{+,-,z}$ in integer powers of $\hbar$, i.e.,

$$\xi^+(\beta) = \sum_{k=1}^{\infty} \hbar^k f_k(\beta), \qquad \xi^z(\beta) = \sum_{k=1}^{\infty} \hbar^k g_k(\beta), \qquad \xi^-(\beta) = \sum_{k=1}^{\infty} \hbar^k l_k(\beta). \tag{4.50}$$

By inserting these expansions in Eq. (4.49) and by retaining terms up to order $O(\hbar^3)$, we get closed-form expressions for the first coefficients, i.e.,

$$\begin{aligned}
&f_1 = -m\omega^2\beta - 2\int_0^\beta \mathrm{d}\tau\, \phi(\tau), \qquad && f_2 = 0, && f_3 = \frac{1}{m}\int_0^\beta \mathrm{d}\tau (f_1(\tau))^2, \\
&g_1 = 0, && g_2 = \frac{2}{m}\int_0^\beta \mathrm{d}\tau f_1(\tau), \qquad && g_3 = 0, \\
&l_1 = -\frac{\beta}{m}, && l_2 = 0, && l_3 = -\frac{2}{m^2}\int_0^\beta \mathrm{d}\tau \int_0^\tau \mathrm{d}s f_1(s).
\end{aligned} \tag{4.51}$$

It follows that all the coefficients in Eqs. (4.51) are expressed in terms of $f_1(\beta)$, so that all calculations reduce to the evaluation of moments of $f_1$. We now consider the leading contribution up to order $O(\hbar^2)$ of Eq. (4.48) by explicitly inserting the expansions in Eq. (4.50)

$$Z(\beta) = \int_{-\infty}^{+\infty} \mathrm{d}x \left\langle \frac{1}{\hbar}\sqrt{\frac{m}{2\pi\beta}} \exp\left(f_1 \frac{x^2}{2}\right) \left\{1 + \frac{\hbar^2}{2}\left[\frac{g_2}{2} - \frac{l_3}{l_1} + \frac{x^2}{2}\left(f_3 + \frac{g_2^2}{4l_1}\right)\right] + o(\hbar^2)\right\} \right\rangle_\phi . \tag{4.52}$$

The expectation value with respect the Gaussian field $\phi$ is then easily calculated and it is given by the sum of the following expressions

$$\begin{aligned}
&\left\langle \exp\left(f_1\frac{x^2}{2}\right)\frac{g_2}{2}\right\rangle_\phi = -e^{-\beta V(x)}\frac{\beta^2(m\omega^2+\lambda x^2)}{2m}, \\
&\left\langle \exp\left(f_1\frac{x^2}{2}\right)\frac{l_3}{l_1}\right\rangle_\phi = -e^{-\beta V(x)}\frac{\beta^2(m\omega^2+\lambda x^2)}{3m}, \\
&\left\langle \exp\left(f_1\frac{x^2}{2}\right) f_3\right\rangle_\phi = \beta^2\frac{e^{-\beta V(x)}}{m}\left[\frac{\beta(m\omega^2+\lambda x^2)^2}{3} - \lambda\right], \\
&\left\langle \exp\left(f_1\frac{x^2}{2}\right)\frac{g_2^2}{4l_1}\right\rangle_\phi = \beta^2\frac{e^{-\beta V(x)}}{m}\left[-\frac{\beta(m\omega^2+\lambda x^2)^2}{4} + \frac{2}{3}\lambda\right],
\end{aligned} \tag{4.53}$$

where $V(x) \equiv \frac{1}{2}m\omega^2x^2 + \frac{\lambda}{4}x^4$. Given that the average is computed with respect to a quadratic measure with zero average, the odd moments vanish and the contributions in Eq. (4.53) are real-valued. By collecting all of the above contributions, we finally obtain the semiclassical expansion of the partition function $Z(\beta)$:

$$\begin{aligned}
Z(\beta) &= \int_{-\infty}^{+\infty} \mathrm{d}x\, e^{-\beta V(x)} \left\{1 + \frac{\hbar^2\beta^2}{12m}\left[x^2\beta\frac{(m\omega^2+\lambda x^2)^2}{2} - (m\omega^2+3\lambda x^2)\right] + o(\hbar^2)\right\} \\
&= \int_{-\infty}^{+\infty} \mathrm{d}x\, e^{-\beta V(x)} \left\{1 + \frac{\hbar^2\beta^2}{12m}\left[\beta\frac{(V'(x))^2}{2} - V''(x)\right] + o(\hbar^2)\right\},
\end{aligned} \tag{4.54}$$

which matches the known expression, see ,e.g., Ref. [235]. Analogously to the calculation of the propagator $G(x_f, t|x_i, 0)$, we have shown how it is possible to represent the partition function $Z(\beta)$ of the quartic oscillator in terms of imaginary-time version of the stochastic variables.

## 4.7 Conclusions

In this Chapter we have generalized the stochastic formalism recently introduced for quantum spin systems [98, 81, 175, 184] to the case of non-linear bosonic systems, explicitly considering the quartic quantum oscillator. We derived the exact disentangled representation of the time-evolution operator of the quartic oscillator in Eq. (4.14) and provided exact formulas for the time evolution of Gaussian wave packets. In particular, we considered the time evolution of the expectation values of the position and of the momentum operator and their corresponding higher moments. We benchmarked our approach (i) in the harmonic and the commuting limit by comparison with the respective analytic solutions and (ii) for a quartic numerically using the stochastic interpretation of the formalism. We further use the stochastic formalism to derive a perturbative expansion of the time evolution operators in power of the quartic term. We recover the usual Dyson series for the quantum quartic oscillator which thus implies that our formalism is viable for evaluating perturbative expansions of observables. Finally, we provide a semiclassical expansion of the propagator and the partition function. Our results agree with known expressions, providing a non-trivial confirmation of this alternative formulation.

The stochastic approach presented in this work provides a novel theoretical formulation of the quartic quantum oscillator as a paradigm of non-linear bosonic systems. We described the quartic oscillator by an ensemble of harmonic oscillators under the influence of classical (stochastic) fields. This exact representation is a suitable starting point to develop a range of approximations, as we have illustrated in Sections 4.5 and 4.6. Furthermore, the realizations of the classical stochastic fields fully encodes the underlying quantum problem. Hence, their study should provide information about the dynamical properties of the corresponding quantum system, as recently found for spin systems [184]. Finally, the stochastic approach establishes a connection between bosonic quantum systems and the theory of classical stochastic processes. In particular, this connection allows us to evaluate the evolution of physical observables numerically in a novel fashion, e.g., our method does not require a truncation of the Hilbert space dimension. Despite this numerical strategy being quite intuitive and simple to implement, the non-unitarity of the effective time-evolution operator leads to artificial divergences such that the simulation breaks down after a finite time that depends on the strength of the quartic coupling.

Possible further directions worth investigating include the generalization of our approach to coupled oscillators [49] and bosonic lattice systems. This could be done by decoupling interactions between different sites by means of additional Hubbard-Stratonovich fields, as is done for quantum spin systems [98, 81, 175, 184]. The disentanglement approach could then provide a numerical technique to simulate bosonic dynamics as well as an analytical framework based on which further approximations can be developed.

# Appendix A

# Langevin equation and stochastic thermodynamics

## A.1 Wiener process

In this Appendix, we report a simple and heuristic way to build up the Wiener process [69, 84, 222, 177]. Let us consider the dynamics of a Brownian particle on a one-dimensional lattice evolving in continuous time according to

$$x(t+\Delta t) = x(t) + \epsilon(t)\Delta x, \tag{A.1}$$

where $\Delta t$ is the infinitesimal time increment, and $\Delta x$ the lattice spacing. The jump $\epsilon(t)$ is a stochastic process that takes value $\pm 1$ with probability $1/2$, with $\langle \epsilon(t)\epsilon(t')\rangle = 0$ for $t \neq t'$, and $\langle \epsilon^2(t)\rangle = 1$. We can construct a well defined continuous space limit for the process by considering $\Delta t \to 0$, $\Delta x \to 0$, and keeping constant $D = (\Delta x)^2/(2\Delta t)$. The resulting process is the Wiener process $W(t)$, and it possesses the following properties:

(i) $W(t)$ is Gaussian distributed with zero mean and variance $2Dt$, $W(t) \sim \mathcal{N}(0, 2Dt)$;

(ii) $W(t)$ is Markovian, i.e., $W(t)$ is independent of $W(t')$, for any $t' < t$;

(iii) The increment $W(t+\Delta t) - W(t)$ is independent of the value of $W(t)$.

From this last properties one has that

$$\langle (W(t+\Delta t) - W(t))\, W(t)\rangle = 0, \tag{A.2}$$

which implies that the two-point correlator of the Wiener process reads

$$\langle W(t+\Delta t)W(t)\rangle = \langle W^2(t)\rangle = 2Dt, \tag{A.3}$$

where we have substituted the explicit value of the variance from property (i). Therefore, given any $t$ and $t'$ one has

$$\langle W(t)W(t')\rangle = 2D\min(t,t'). \tag{A.4}$$

The Gaussian white noise is formally defined as the derivative of the Wiener process

$$\mathrm{d}W(t) = \xi(t)\mathrm{d}t, \tag{A.5}$$

which is commonly denoted as $\xi(t) = \mathrm{d}W(t)/\mathrm{d}t$. However, since $\xi(t)$ is obtained from a Gaussian process, $\xi(t)$ is also a Gaussian random variable. It immediately follows from $\langle W(t)\rangle = 0$ that $\langle \xi(t)\rangle = 0$. The correlation of the white noise is obtained from Eq. (A.4)

$$\langle \xi(t)\xi(t')\rangle = 2D\delta(t-t'). \tag{A.6}$$

All the properties listed above fully characterize the Gaussian white noise.

## A.2 Stochastic differential equations

Here, we report the most common convention for stochastic integration encountered in the thesis [69, 84, 222, 177]. Let us consider stochastic differential equations of the form

$$\frac{\mathrm{d}x(t)}{\mathrm{d}t} = f(x(t)) + g(x(t))\xi(t), \tag{A.7}$$

for any generic functions $f(t)$ and $g(t)$, and $\xi(t)$ being a Gaussian white noise, introduced in previous Section. The solution of these equations is given by

$$x(t) = x(0) + \int_0^t \mathrm{d}\tau\, f(x(t)) + \int_0^t \mathrm{d}W(\tau)\, g(x(\tau)). \tag{A.8}$$

The last integral in the above equation is calculated as

$$\int_0^t \mathrm{d}W(\tau)\, g(x(\tau)) = \lim_{\Delta\tau\to 0}\sum_i g(\tau_\alpha)[W(\tau_i+\Delta\tau) - W(\tau_i)], \tag{A.9}$$

where we define the intermediate time $\tau_\alpha \equiv \alpha\tau_i + (1-\alpha)\tau_{i+1}$, where $\alpha \in [0,1]$. There are two prescriptions commonly used to calculate this type of integrals introduced by Itô and Stratonovich:

(i) Itô: it corresponds to $\alpha = 1$ and $\tau_\alpha = \tau_i$;

(ii) Stratonovich: it corresponds to $\alpha = 1/2$ and $\tau_\alpha = (\tau_i + \tau_{i+1})/2$.

Therefore, the integrals of the type $\int \mathrm{d}W(\tau)\, g(x(\tau))$ can be calculated according to these two different conventions. In general, the following notation is used: for Itô calculus, Eq. (A.9) is evaluated using the following discretization scheme,

$$g(x(\tau))\,\mathrm{d}W(\tau) \to g(x(\tau))\,[W(\tau+\Delta\tau) - W(\tau)]\,, \tag{A.10}$$

whereas for Stratonovich calculus

$$g(x(\tau)) \circ \mathrm{d}W(\tau) \to \frac{g(x(\tau)) + g(x(\tau + \Delta\tau))}{2} \left[W(\tau + \Delta\tau) - W(\tau)\right]. \tag{A.11}$$

Depending on the prescription used, the values of integrals that involve stochastic terms may differ. In this case in which the noise is *additive*, that is when $g$ is constant, the two types of calculus yield the same result. In any other case, the two descriptions may lead to different values.

### A.2.1 Itô's Lemma

While Stratonovich calculus follows the same differential rules as standard calculus, this is not true for Itô's one. We now provide an heuristic derivation of Itô's Lemma, which allows one to correctly evaluate change of variables of $x(t)$ in Eq. (A.7) in the homonym convention [69, 84, 222, 177]. Let $F[(x(t))$ be a suitably differential function of $x(t)$, then we are interested in the estimate of its infinitesimal variation:

$$\begin{aligned} \mathrm{d}F(x(t)) &\equiv \frac{\mathrm{d}F(y)}{\mathrm{d}y}\Big|_{y=x(t)} \mathrm{d}x(t) + \frac{1}{2}\frac{\mathrm{d}^2F(y)}{\mathrm{d}y^2}\Big|_{y=x(t)} (\mathrm{d}x(t))^2 \\ &= \frac{\mathrm{d}F(y)}{\mathrm{d}y}\Big|_{y=x(t)} [f(x(t))\mathrm{d}t + g(x(t))\mathrm{d}W(t)] + \frac{\mathrm{d}^2F(y)}{\mathrm{d}y^2}\Big|_{y=x(t)} g^2(x(t))(\mathrm{d}W(t))^2, \end{aligned} \tag{A.12}$$

which follows from direct Taylor expansion around $x(t)$. By using the properties of the Wiener process presented in previous section, it can be proved that in Itô's convention one finds the formal identity $(\mathrm{d}W(t))^2 = 2D\mathrm{d}t$, see, e.g., Ref. [84]. Accordingly, one gets the well-known formula

$$\mathrm{d}F(x(t)) = \frac{\mathrm{d}F(y)}{\mathrm{d}y}\Big|_{y=x(t)} [f(x(t))\mathrm{d}t + g(x(t))\mathrm{d}W(t)] + D\,\frac{\mathrm{d}^2F(y)}{\mathrm{d}y^2}\Big|_{y=x(t)} g^2(x(t))\mathrm{d}t. \tag{A.13}$$

## A.3 Euler method

A simple and intuitive way to approximate Eq. (A.7) in Itô convention is the *Euler approximation* scheme [69]. The rigorous mathematical way of interpreting Eq. (A.7) is to consider its infinitesimal evolution

$$\mathrm{d}x(\tau) = f(x(\tau), \tau)\mathrm{d}t + g(x(\tau), \tau)\mathrm{d}W(\tau), \tag{A.14}$$

where we let the function $f$ and $g$ to explicitly depend on $\tau \in (0, t)$, and we fix the initial condition $x(0) = x_0$. Given the uniform time-partition $\tau_n \equiv n\Delta t$, with $n = 0, \ldots, N$ and $\tau_N = t$, we introduce the stochastic process $y(t)$ which approximates $x(t)$ by satisfying the iterative scheme

$$y_{n+1} = y_n + f(y_n, \tau_n)\Delta t + g(y_n, \tau_n)(W_{n+1} - W_n), \tag{A.15}$$

where we adopt the short-hand notation $y_n \equiv y(\tau_n)$ with $y_0 = x_0$, and $W_n \equiv W(\tau_n)$. The random variables $\Delta W_n \equiv W_{n+1} - W_n$, for $n = 0, \ldots, N-1$, are all independent due to property (iii) of Sec. A.1 and their distribution is a Gaussian with average $\langle \Delta W_n \rangle = 0$ and variance $\langle \Delta W_n^2 \rangle = 2D\Delta t$, see property (i). It follows that Eq. (A.15) can be numerically integrated by generating a sequence of independent and normally distributed random numbers $\{\Delta W_n\}_{n=0}^{N-1}$.

## A.4 Brownian motion and Langevin equation

The Brownian particle is the paradigmatic case study of stochastic thermodynamics. It is characterized by vanishing average position at any time $\langle x(t)\rangle = 0$, and average mean square displacement growing linearly in time according to $\langle x^2(t)\rangle = 2Dt$, where $D$ denotes the diffusion coefficient. Moreover, Einstein showed that the value of the diffusion coefficient in equilibrium is given by

$$D = \frac{k_B T}{\gamma}, \tag{A.16}$$

where $k_B$ is Boltzmann's constant, $T$ the temperature of the surrounding fluid and $\gamma$ the friction coefficient of the particle in the fluid.

The dynamics of the free Brownian particle of mass $m$ is characterized by its position $x(t)$ and momentum $p(t)$. The equations of motion for $(x(t), p(t))$ immediately follow by identifying the forces acting on the particle: a viscous force due to the fluid given by Stoke's law $F(t) = -\gamma v(t)$, and a stochastic contribution $\xi(t)$ representing the fluctuating force exerted by the molecules of the medium. By combining these two forces, the equations of motion read:

$$\begin{aligned} \frac{\mathrm{d}p}{\mathrm{d}t} &= -\gamma\frac{p}{m} + \xi, \\ \frac{\mathrm{d}x}{\mathrm{d}t} &= \frac{p}{m}, \end{aligned} \tag{A.17}$$

where $\xi(t)$ is a Gaussian white noise with zero mean $\langle \xi(t)\rangle = 0$, and delta correlated $\langle \xi(t)\xi(t')\rangle = 2D\delta(t-t')$. In the case where time resolution of measurements $\Delta t$ is much larger than the typical relaxation time of the velocity, i.e., $\Delta t \gg m/\gamma$, Eq. (A.17) reduces to its overdamped regime:

$$\gamma\,\frac{\mathrm{d}x}{\mathrm{d}t} = \xi. \tag{A.18}$$

Moreover, it is always possible to account for additional external forces applied to the Brownian particle in the Langevin equation. If this force is controlled by an external time-dependent parameter $c(t)$ via the potential $V(x(t), c(t))$, the underdamped Langevin equation is given by

$$\begin{aligned} \frac{\mathrm{d}p}{\mathrm{d}t} &= -\frac{\partial V(x,c)}{\partial x} - \gamma\frac{p}{m} + \xi, \\ \frac{\mathrm{d}x}{\mathrm{d}t} &= \frac{p}{m}. \end{aligned} \tag{A.19}$$

In general, the total external force applied on the particle $F(x, c)$ may be due to two contributions: a conservative one that come from a potential $-\partial_x V(x, c)$
$partialx$, and another that models the application of forces directly on the particle $f(x, c)$. Therefore, the total general force acting on the particle is given by

$$F(x,c) = -\frac{\partial V(x,c)}{\partial x} + f(x,c). \tag{A.20}$$

In the overdamped limit, Eq. (A.19) becomes

$$\gamma\frac{\mathrm{d}x}{\mathrm{d}t} = -\frac{\partial V(x,c)}{\partial x} + \xi. \tag{A.21}$$

## A.5 First law of thermodynamics at the mesoscopic scale

As explained in full details in Ref. [193], it is possible to extend thermodynamic notions as work and heat to the case of mesoscopic systems endowed with a Langevin description. Langevin equation expresses the balance of all forces acting on the particle, i.e.,

$$-\gamma\frac{\mathrm{d}x}{\mathrm{d}t}-\frac{\partial V(x,c)}{\partial x}+\xi=0, \tag{A.22}$$

in the overdamped case. In this force balance equation, there are two forces that are exerted by the environment on the particle, the friction force $-\gamma \mathrm{d}x/\mathrm{d}t$, and the force due to the environment $\xi(t)$. Therefore, $(-\gamma \mathrm{d}x/\mathrm{d}t+\xi)\circ \mathrm{d}x$ is the energy transfer from the environment to the particle, that is, the heat transferred to the particle; the $\circ$ represent Stratonovich product. Accordingly, one defines

$$\delta Q(t)\equiv\left[-\gamma\frac{\mathrm{d}x(t)}{\mathrm{d}t}+\xi(t)\right]\circ \mathrm{d}x(t), \tag{A.23}$$

as the heat transferred to an overdamped Brownian particle when it is displaced by the infinitesimal amount $\mathrm{d}x(t)$. In the underdamped limit, the above formula can be expressed as

$$\delta Q(t)=\left[-\gamma\frac{p(t)}{m}+\xi(t)\right]\circ \mathrm{d}x(t)=\left[\frac{\mathrm{d}p}{\mathrm{d}t}+\frac{\partial V(x,c)}{\partial x}\right]\circ \mathrm{d}x(t), \tag{A.24}$$

where the second equality follows from Eq. (A.19). The Stratonovich convention for stochastic calculus allows one to use standard differentiation rules, hence

$$\begin{aligned}\frac{\mathrm{d}p(t)}{\mathrm{d}t}\circ \mathrm{d}x(t)&=\frac{\mathrm{d}p(t)}{\mathrm{d}t}\circ\frac{p(t)}{m}\mathrm{d}t=\mathrm{d}\left(\frac{p^2(t)}{2m}\right),\\ \frac{\partial V(x,c)}{\partial x}\circ \mathrm{d}x(t)&=\mathrm{d}V(x,c)-\frac{\partial V(x,c)}{\partial c}\circ \mathrm{d}c(t).\end{aligned} \tag{A.25}$$

By summing these last two equations term by term one gets

$$\delta Q(t)=\mathrm{d}\left[\frac{p^2(t)}{2m}+V(x,c)\right]-\frac{\partial V(x,c)}{\partial c}\circ \mathrm{d}c(t). \tag{A.26}$$

The first term in Eq. (A.26) represents the internal energy of the particle (kinetic and potential)

$$U(x,p)=\frac{p^2}{2m}+V(x,c). \tag{A.27}$$

Therefore, if one identifies the second term on the right hand side of Eq. (A.26) as the work done by the external agent $c(t)$ on the particle when it displaces of a $\mathrm{d}x(t)$,

$$\delta W(t)\equiv\frac{\partial V(x,c)}{\partial c}\circ \mathrm{d}c(t), \tag{A.28}$$

one recovers the first law of thermodynamics at the mesoscopic scale, i.e.,

$$\mathrm{d}U=\delta Q+\delta W. \tag{A.29}$$

Note that the definitions of work and heat that have been introduced depend crucially on the trajectory of the particle. Hence, given a trajectory $x_t \equiv \{x(\tau)\}_{\tau=0}^{t}$, the total heat and work transferred in the time interval $(0,t)$ under the control of the external agent $c(t)$ are obtained by integrating over time as

$$Q[x_t] = \int_{x(0)}^{x(t)} \left.\frac{\partial V(x,c)}{\partial x}\right|_{(x(\tau),c(\tau))} \circ \mathrm{d}x(t), \quad \text{and} \quad W[x_t] = \int_{c(0)}^{c(t)} \left.\frac{\partial V(x,c)}{\partial c}\right|_{(x(\tau),c(\tau))} \circ \mathrm{d}c(t). \tag{A.30}$$

## A.6 Second law of Thermodynamics at the Mesoscopic scale

In the same spirit of previous Section, it is possible to generalize the second law of thermodynamics to the mesoscopic scale by extending the notion of entropy to systems where thermal fluctuations are relevant. By following Ref. [191], one considers a colloidal particle that moves in one dimension, subject to the external force $F(x,c)$. In the overdamped limit, the Langevin equation describing the motion of the particle reads

$$\gamma \frac{\mathrm{d}x}{\mathrm{d}t} = F(x,c) + \xi, \tag{A.31}$$

where $\langle \xi(t)\xi(t')\rangle = 2\gamma k_B T \delta(t-t')$, with mobility $\mu \equiv \gamma^{-1}$, and diffusion constant $D = k_B T \mu$. Then, the Fokker-Planck description [84] of the system is given by

$$\frac{\partial \rho(x,t)}{\partial t} = -\frac{\partial j(x,t)}{\partial x} = -\frac{\partial}{\partial x}\left[\left(\mu F(x,c) - D\frac{\partial}{\partial x}\right)\rho(x,t)\right], \tag{A.32}$$

where $\rho(x,t)$ is the probability density of the particle position at time $t$. The Shannon entropy [51] associated to the position of the particle at time $t$ can be interpreted as a non-equilibrium entropy:

$$\mathcal{S}(t) = -k_B \int \mathrm{d}x(t)\, \rho(x(t),t)\, \ln \rho(x(t),t), \tag{A.33}$$

which suggests the introduction of the following trajectory dependent entropy

$$\mathcal{S}[x(t)] = -k_B \ln \rho(x(t),t). \tag{A.34}$$

According to the above definition of entropy, the Shannon entropy at time $t$ is nothing but the ensemble average of $\mathcal{S}[x(t)]$, where the average is done over all trajectories with weight $\rho(x(t),t)$. Using the trajectory dependent entropy, one can recover a second law of thermodynamics in the mesoscopic scale. To do so, one considers the entropy production $\mathrm{d}\mathcal{S}[x(t)]/\mathrm{d}t$, which reads

$$\begin{aligned}
\frac{1}{k_B}\frac{\mathrm{d}\mathcal{S}[x(t)]}{\mathrm{d}t} &= -\frac{1}{\rho(x,t)}\left.\frac{\partial \rho(x,t)}{\partial t}\right|_{x(t)} - \frac{1}{\rho(x,t)}\left.\frac{\partial \rho(x,t)}{\partial x}\right|_{x(t)}\frac{\mathrm{d}x(t)}{\mathrm{d}t} \\
&= -\frac{1}{\rho(x,t)}\left.\frac{\partial \rho(x,t)}{\partial t}\right|_{x(t)} + \left.\frac{j(x,t)}{D\rho(x,t)}\right|_{x(t)}\frac{\mathrm{d}x(t)}{\mathrm{d}t} - \left.\frac{F(x,c)}{k_B T}\right|_{x(t)}\frac{\mathrm{d}x(t)}{\mathrm{d}t}
\end{aligned} \tag{A.35}$$

where we have used the definition of the current $j(x,t)$ in Eq. (A.32). The last term in the second line of Eq. (A.35) identifies the entropy change in the reservoir

$$\frac{\mathrm{d}\mathcal{S}_{\mathrm{res}}}{\mathrm{d}t} = -\frac{1}{T}\frac{\mathrm{d}Q}{\mathrm{d}t} = \left.\frac{F(x,c)}{k_B T}\right|_{x(t)} \frac{\mathrm{d}x}{\mathrm{d}t}, \tag{A.36}$$

where we have combined the expression of $Q$ in Eq. (A.23) with the Langevin equation in Eq. (A.31). The total entropy production is equal to

$$\frac{\mathrm{d}\mathcal{S}_{\mathrm{tot}}}{\mathrm{d}t} = \frac{\mathrm{d}\mathcal{S}}{\mathrm{d}t} + \frac{\mathrm{d}\mathcal{S}_{\mathrm{res}}}{\mathrm{d}t} = -\left.\frac{k_B}{\rho(x,t)}\frac{\partial\rho(x,t)}{\partial t}\right|_{x(t)} + \left.\frac{k_B\, j(x,t)}{D\rho(x,t)}\right|_{x(t)} \frac{\mathrm{d}x(t)}{\mathrm{d}t}. \tag{A.37}$$

Finally, by averaging over $\rho(x,t)$, one gets

$$\left\langle \frac{\mathrm{d}\mathcal{S}_{\mathrm{tot}}}{\mathrm{d}t} \right\rangle = k_B \int \mathrm{d}x\, \frac{j^2(x,t)}{D\rho(x,t)} \geq 0, \tag{A.38}$$

where the first term vanishes due to the boundary conditions of $\rho(x,t)$. Equation (A.38) expresses the fact that for a physical system evolving according to a Langevin dynamics, the entropy production is always positive on average at it is proportional to the square of the current $j(x,t)$. Indeed, it vanishes at equilibrium, compatibly with $j(x,t) = 0$.

# Appendix B

# Calculations of Chapter 1

## B.1 General expressions for $\tilde{P}_{\rm nc}(x,s|x_0)$ and $\tilde{P}(x,s|x_0)$

In this Appendix we report the solution for the Laplace transform of Eq. (1.33) for $P(x,t|x_0)$, the probability distribution of the Brownian particle position in one dimension, initially at $x_0$, resetting to $x_r$ according the space-dependent resetting rate $r_c(x) = r\,\theta(a-|x|)$, i.e., non vanishing within a segment of width $2a$ and constant rate $r$. More generally, we exert an external control on the system, parametrized by $\sigma_c$, corresponding to the identification of $r_c(x)$ as a resetting rate ($\sigma_c = 1$) or as an evaporation rate ($\sigma_c = 0$). In this picture, we denote by $P_{\rm nc}(x,t|x_0)$ the probability density of no-control, i.e., the probability that no reset/evaporation has occurred up to time $t$ in the space interval $[x, x+{\rm d}x]$ is given by $P_{\rm nc}(x,t|x_0){\rm d}x$.

We now outline the procedure used throughout the paper to compute $\tilde{P}(x,s|x_0)$:

(i) First, compute $\tilde{P}_{\rm nc}(x,s|x_0)$ from the Laplace transform of Eq.(1.33) with $\sigma_c = 0$, i.e.,

$$D\frac{\partial^2 \tilde{P}_{\rm nc}(x,s|x_0)}{\partial x^2} - (s + r_c(x))\,\tilde{P}_{\rm nc}(x,s|x_0) = -\delta(x-x_0) \tag{B.1}$$

with the proper boundary conditions.

(ii) Evaluate $\tilde{P}_{\rm res}(s|x_0)$ using Eq. (1.26).

(iii) Use Eq. (1.32) in order to compute $\tilde{P}(x,s|x_0,x_r)$.

As anticipated, we will compute explicitly $\tilde{P}(x,s|x_0,x_r)$ for $r_c(x) = r\,\theta(a-|x|)$, which requires a separate analysis of the two cases $|x_0| < a$ and $|x_0| > a$.

## B.2 Open boundary conditions

### B.2.1 Case with $x_0 < -a$

Due to the presence of a piece-wise resetting rate in Eq. (B.1), we have to consider separate contributions to $\tilde{P}_{\rm nc}(x,s|x_0)$ for any of the regions delimited by the boundary points $\{\pm a, x_0\}$:

$$\tilde{P}_{\rm nc}(x,s|x_0) = \begin{cases} A(s,x_0)\, e^{x\mu} & \text{for } x < x_0, \\ B_1(s,x_0)\, e^{x\mu} + B_2(s,x_0)\, e^{-x\mu} & \text{for } x \in (x_0,-a), \\ C_1(s,x_0)\, e^{x\nu} + C_2(s,x_0)\, e^{-x\nu} & \text{for } x \in (-a,a), \\ E(s,x_0)\, e^{-x\mu} & \text{for } x > a, \end{cases} \tag{B.2}$$

where we define

$$\mu(s) \equiv \sqrt{\frac{s}{D}} \qquad \nu(s) \equiv \sqrt{\frac{r+s}{D}}, \tag{B.3}$$

and the coefficients $A$, $B_{1,2}$, $C_{1,2}$, and $E$ are fixed as specified below. The non-divergence of the solution is ensured by requiring that the real part of $\mu$ is positive, $\mathrm{Re}(\mu) > 0$, this is equivalent to require that $\tilde{P}_{\rm nc}$ is defined on the entire complex $s$-plane except the negative real axis. We fix all the coefficients in Eq. (B.2) by imposing the continuity of $\tilde{P}_{\rm nc}$ at the boundary points and the generic continuity of the first derivative in all points, except for $x_0$. In fact, given the presence of a Dirac delta in Eq. (B.1), $\tilde{P}_{\rm nc}$ will present a discontinuity in the derivative according to

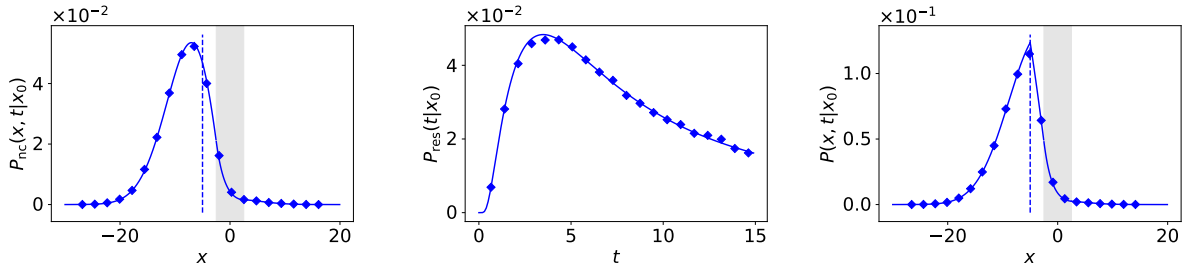
$$\partial_x \tilde{P}_{\rm nc}(x_0^+,s|x_0) - \partial_x \tilde{P}_{\rm nc}(x_0^-,s|x_0) = -\frac{1}{D}. \tag{B.4}$$

This results from integrating Eq. (B.1) around a small neighborhood of $x_0$ of radius $\epsilon > 0$, and then taking the limit $\epsilon \to 0$. Accordingly, the three conditions for the continuity of $\tilde{P}_{\rm nc}$ at the boundary points, the two conditions for the continuity of the first space derivative at $\pm a$ and Eq. (B.4) fix the constants in the solution (1.28). The final expressions for $\tilde{P}_{\rm nc}$ read

$$\tilde{P}_{\rm nc}(x,s|x_0) = \frac{1}{D}\left[(\mu^2+\nu^2)\sinh(2a\nu) + 2\mu\nu\cosh(2a\nu)\right]^{-1}$$

$$\begin{cases} e^{\mu(x-x_0)}\left[\mu\sinh(2a\nu) + \nu\cosh(2a\nu)\right] - \frac{r}{\mu D} e^{\mu(x+a)}\sinh(2a\nu)\sinh(\mu(a+x_0)) & \text{for } x \le x_0, \\ e^{-\mu(x-x_0)}\left[\mu\sinh(2a\nu) + \nu\cosh(2a\nu)\right] - \frac{r}{\mu D} e^{\mu(x_0+a)}\sinh(2a\nu)\sinh(\mu(a+x)) & \text{for } x \in (x_0,-a), \\ e^{\mu(x_0+a)}\left[\nu\cosh(\nu(x-a)) - \mu\sinh(\nu(x-a))\right] & \text{for } x \in [-a,a], \\ e^{\mu(2a+x_0-x)}\nu & \text{for } x > a; \end{cases} \tag{B.5}$$

Fig. B.1a shows a representative instance of $P_{\rm nc}(x,t|x_0)$. This probability distribution has no stationary distribution and "evaporation" prevents the conservation of probability. In the case of resetting, one may directly compute the Laplace transform of the probability distribution for the first reset time through Eqs. (1.26) and (B.5), finding




(a) (b) (c)

Figure B.1: **Statistics of the Brownian tunnelling:** (a) Probability density $P_{\rm nc}(x,t|x_0)$ at time $t = 15$ with $D = 1$, $r = 0.5$, $a = 2.5$, $x_0 = -5$. The solid line represents the inverse numerical Laplace transform of Eq. (B.5) while the symbols correspond to the result of numerical simulations. The grey shaded area highlights the interval within which resetting occurs. (b) Probability of first reset time $P_{\rm res}(t|x_0)$ up to time $t = 15$ with the same parameters as panel (a): comparison between inverse Laplace transform of Eq. (B.6) and numerical simulations. (c) Probability density $P(x,t|x_0)$ with $x_r = x_0$, indicated by the vertical dashed line. The solid line represents the inverse Laplace transform of Eq. (B.8) while symbols indicate the results of numerical simulations. All numerical simulations were done using the Euler numerical integration scheme with time step $\Delta t = 0.05$, and they were repeated $N = 10^5$ times.

$$\tilde{P}_{\rm res}(s|x_0) = \frac{r\, e^{\mu(a+x_0)}}{D\nu} \frac{\sinh(a\nu)}{\nu \sinh(a\nu) + \mu \cosh(a\nu)}, \tag{B.6}$$

the inverse transform of which is represented in Fig. B.1b. The long-time behavior of $P_{\rm res}$, see Ref. [172], can be extracted from the behavior for small $s$ of its Laplace transform,

$$\tilde{P}_{\rm res}(s|x_0) = 1 + \sqrt{s}\left(\frac{a+x_0}{\sqrt{D}} - \frac{\coth(a\sqrt{\frac{r}{D}})}{\sqrt{r}}\right) + O(s), \tag{B.7}$$

which, plugged in Eq. (1.32), implies the absence of a stationary distribution for the process, being $P_{\rm nc}(x,s|x_0) = O(1)$ as $s \to 0$, $P_{\rm st}(x|x_0) = \lim_{s\to 0} sP_{\rm nc}(x,s|x_0)/(1 - P_{\rm res}(s|x_0) = 0)$.

Moreover, apart for the zeroth-order term in Eq. (B.7) which corresponds to the normalization of the probability, the small $s$ expansion shows the presence of half-integer powers which reflects the fact that the integer moments of $\tilde{P}_{\rm res}(s|x_0)$ are infinite: e.g., the average time that a particle takes to reset is infinite because of the existence of infinite diffusive paths extending towards increasingly negative positions. The long-time behavior $P_{\rm res} \sim t^{-\frac{3}{2}}$ for $t \to \infty$ also follows from this expansion.

Finally, according to Eq. (1.32), using Eqs. (B.5) and (B.6), the Laplace transform of the

probability distribution $P(x,t|x_0)$ for $x_r = x_0$ reads

$$\tilde{P}(x,s|x_0) = \frac{\nu}{2D}\left\{[\mu\sinh(a\nu)+\nu\cosh(a\nu)]\left[\left(\nu^2-\frac{r}{D}e^{\mu(x_0+a)}\right)\sinh(a\nu)+\mu\nu\cosh(a\nu)\right]\right\}^{-1}$$

$$\begin{cases} e^{\mu(x-x_0)}\left[\mu\sinh(2a\nu)+\nu\cosh(2a\nu)\right]-\frac{r}{\mu D}e^{\mu(x+a)}\sinh(2a\nu)\sinh(\mu(a+x_0)) & \text{for } x\le x_0, \\ e^{-\mu(x-x_0)}\left[\mu\sinh(2a\nu)+\nu\cosh(2a\nu)\right]-\frac{r}{\mu D}e^{\mu(x_0+a)}\sinh(2a\nu)\sinh(\mu(a+x)) & \text{for } x\in(x_0,-a), \\ e^{\mu(x_0+a)}\left[\nu\cosh(\nu(x-a))-\mu\sinh(\nu(x-a))\right] & \text{for } x\in[-a,a], \\ e^{\mu(2a+x_0-x)}\nu & \text{for } x>a. \end{cases} \tag{B.8}$$

Note that, as expected, for $r = 0$ renders the Laplace transform of a Gaussian distribution with average $x_0$ and variance $2Dt$, i.e., $\tilde{P}(x,s|x_0) = e^{(-|x-x_0|\sqrt{s/D})}/(2\sqrt{s\,D})$. The cusp for $x_r = x_0$ is the distinctive feature of resetting being present at all times. Moreover, for short and long times, it can be easily checked that the tails of the distribution at large values of $x$ are Gaussian, signaling that diffusion is the main mechanism driving the system. These properties are clearly displayed in Fig. B.1c which reports a snapshot of the probability density $P(x,t|x_0)$ showing the cusp in correspondence of $x_r$ (vertical dashed line) and the exponential suppression of the probability upon advancing within the resetting area (grey region) due to particles that reset. As a final remark, we point out that the solution for $x_0 > a$ can be retrieved by that corresponding to $x_0 < -a$ upon exchanging $x_0 \to -x_0$ and $x \to -x$.

### B.2.2 Case with $|x_0| < a$

Following the same procedure as in Appendix B.2.1, for $|x_0| < a$ the Laplace transform of $P_{\rm nc}(x,t|x_0)$ can be computed, yielding

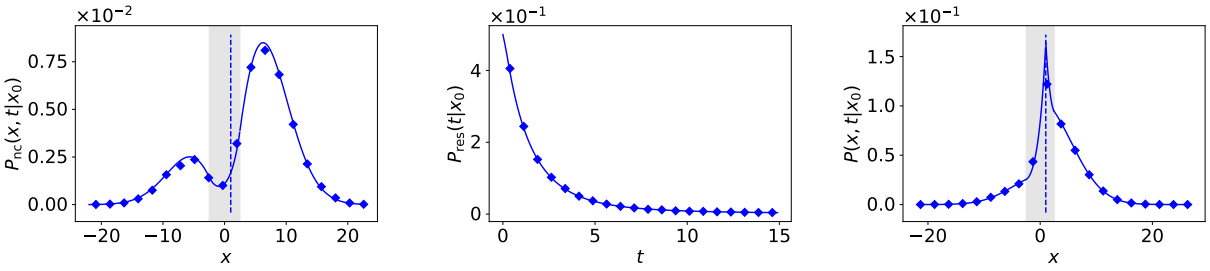
$$\tilde{P}_{\rm nc}(x,s|x_0) = \frac{1}{2D}\left\{[\mu\sinh(a\nu)+\nu\cosh(a\nu)]\,[\nu\sinh(a\nu)+\mu\cosh(a\nu)]\right\}^{-1}$$

$$\begin{cases} e^{\mu(x+a)}\left[\nu\cosh(\nu(a-x_0))+\mu\sinh(\nu(a-x_0))\right] & \text{for } x\le -a, \\ \mu\sinh(\nu(2a+x-x_0))+\frac{\mu^2+\nu^2}{2\nu}\cosh(\nu(2a+x-x_0))+\frac{r}{2\nu D}\cosh(\nu(x_0+x)) & \text{for } x\in(-a,x_0), \\ \mu\sinh(\nu(2a+x_0-x))+\frac{\mu^2+\nu^2}{2\nu}\cosh(\nu(2a+x_0-x))+\frac{r}{2\nu D}\cosh(\nu(x_0+x)) & \text{for } x\in[x_0,a], \\ e^{\mu(a-x)}\left[\nu\cosh(\nu(a+x_0))+\mu\sinh(\nu(a+x_0))\right] & \text{for } x>a; \end{cases} \tag{B.9}$$

Once again, as shown in Fig. B.2a, the resulting $P_{\rm nc}$ as a function of $x$ is exponentially suppressed within the resetting/evaporation area inducing an unbalance of the distribution and the presence of two peaks, whose relative intensity depends on the value of $x_0$.

The Laplace transform of the probability distribution of the first resetting time, combining Eq. (1.26) and Eq. (B.9), turns out to be

$$\tilde{P}_{\rm res}(s|x_0) = \frac{r}{D\nu^2}\left(1-\frac{\mu\cosh(x_0\nu)}{\mu\cosh(a\nu)+\nu\sinh(a\nu)}\right). \tag{B.10}$$




(a) (b) (c)

Figure B.2: **Statistics of the Brownian tunnelling. (a)** Probability density $P_{\rm nc}(x,t|x_0)$ at time $t=15$ with $D=1$, $r=0.5$, $a=2.5$, $x_0=1$. The solid line represents the inverse numerical Laplace transform of Eq. (B.9) while the symbols correspond to the result of numerical simulations. The grey shaded area highlights the interval within which resetting occurs. **(b)** Probability of first reset time $P_{\rm res}(t|x_0)$ up to time $t=15$ with the same parameters as panel (a): comparison between inverse Laplace transform of Eq. (B.10) and numerical simulations. **(c)** Probability density $P(x,t|x_0)$ with $x_r=x_0$, indicated by the vertical dashed line. The solid line represents the inverse Laplace transform of Eq. (B.11) while symbols indicate the results of numerical simulations. All numerical simulations were done using the Euler numerical integration scheme with time step $\Delta t=0.05$, and they were repeated $N=10^5$ times.

Fig. B.2b displays the probability $P_{\rm res}(t|x_0)$: being the initial position inside the resetting region, particles are more probable to reset for the first time at short times.

Finally, plugging Eq. (B.9) and Eq. (B.10) in Eq. (1.32), $\tilde{P}(x,s|x_0)$ reads

$$\tilde{P}(x,s|x_0)=\frac{\nu^2}{2D\mu}\left\{\left[\mu\sinh\left(a\nu\right)+\nu\cosh\left(a\nu\right)\right]\left[\mu\nu\sinh\left(a\nu\right)+\mu^2\cosh\left(a\nu\right)+\frac{r}{D}\cosh\left(x_0\nu\right)\right]\right\}^{-1}$$

$$\begin{cases} e^{\mu(x+a)}\left[\nu\cosh\left(\nu(a-x_0)\right)+\mu\sinh\left(\nu(a-x_0)\right)\right] & \text{for } x<-a, \\ \mu\sinh\left(\nu(2a+x-x_0)\right)+\frac{\mu^2+\nu^2}{2\nu}\cosh\left(\nu(2a+x-x_0)\right)+\frac{r}{2\nu D}\cosh\left(\nu(x_0+x)\right) & \text{for } x\in(-a,x_0), \\ \mu\sinh\left(\nu(2a+x_0-x)\right)+\frac{\mu^2+\nu^2}{2\nu}\cosh\left(\nu(2a+x_0-x)\right)+\frac{r}{2\nu D}\cosh\left(\nu(x_0+x)\right) & \text{for } x\in(x_0,a), \\ e^{\mu(a-x)}\left[\nu\cosh\left(\nu(a+x_0)\right)+\mu\sinh\left(\nu(a+x_0)\right)\right] & \text{for } x>a, \end{cases} \tag{B.11}$$

and its inverse Laplace transform is reported in Fig. B.2c. Since the resetting point (vertical dashed line) is inside the resetting region (grey area), particles tend to be more confined with respect to the case with $|x_0|>a$; however, this fact is not sufficient to ensure the existence of a stationary distribution for finite $a$.

## B.3 Periodic boundary conditions

Here we address the problem of a diffusing particle which possibly resets when located within a interval with the additional condition that its position is restricted to the segment $x\in(-L,L)$ with periodic boundary condition, i.e., the particle moves along a ring of length $2L$. As in the

case of simple diffusion with periodic boundary conditions and no resetting, the system will show the appearance of a stationary probability distribution [105]. The solution of this problem, as in the case with open boundary, generically depends on the position of the resetting point and of the initial point; for simplicity, in what follows, we set $x_0 = x_r$.

### B.3.1 Case with $-L < x_0 < -a$

The type of solution that we seek for Eq. (B.1) is of the form

$$\tilde{P}_{\rm nc}(x,s|x_0) = \begin{cases} A_1(s,x_0)\,e^{x\mu} + A_2(s,x_0)\,e^{-x\mu} & \text{for } x \in (-L,x_0), \\ B_1(s,x_0)\,e^{x\mu} + B_2(s,x_0)\,e^{-x\mu} & \text{for } x \in (x_0,a), \\ C_1(s,x_0)\,e^{x\nu} + C_2(s,x_0)\,e^{-x\nu} & \text{for } x \in (-a,a), \\ D_1(s,x_0)\,e^{x\mu} + D_2(s,x_0)\,e^{-x\mu} & \text{for } x \in (a,L), \end{cases} \tag{B.12}$$

with periodic boundary conditions, i.e., $\tilde{P}_{\rm nc}(-L,s|x_0) = \tilde{P}_{\rm nc}(L,s|x_0)$ and $\partial_x \tilde{P}_{\rm nc}(-L,s|x_0) = \partial_x \tilde{P}_{\rm nc}(L,s|x_0)$. These conditions ensure the continuity of the distribution and particle currents. We fix the eight constants in Eq. (B.12) by requiring the continuity of $\tilde{P}_{\rm nc}(-L,s|x_0)$ in $\{\pm a, x_0, \pm L\}$ (four conditions), the continuity of the first spatial derivative in $\pm a, \pm L$ (three conditions) and the condition (B.4) in $x_0$. The solution is given by

$$\tilde{P}_{\rm nc}(x,s|x_0) = \frac{\sinh(2a\nu)}{D}\left\{(\mu^2+\nu^2)\sinh(2a\nu)\sinh\left(2\mu\left(L-a\right)\right) + 2\mu\nu\left[\cosh(2a\nu)\cosh\left(2\mu\left(L-a\right)\right)-1\right]\right\}^{-1}$$

$$\begin{cases} \mu\cosh\left(\mu(a+x_0)\right)\cosh\left(\mu(2L-a+x)\right) - \frac{\nu^2}{\mu}\sinh\left(\mu(a+x_0)\right)\sinh\left(\mu(2L-a+x)\right) \\ +\nu\left[\cosh(2a\nu)\sinh\left(\mu\left(2L+x-x_0-2a\right)\right) - \sinh(\mu(x-x_0))\right]/\sinh(2a\nu) & \text{for } x \in [-L,x_0], \\ \mu\cosh\left(\mu(a+x)\right)\cosh\left(\mu(2L-a+x_0)\right) - \frac{\nu^2}{\mu}\sinh\left(\mu(a+x)\right)\sinh\left(\mu(2L-a+x_0)\right) \\ +\nu\left[\cosh(2a\nu)\sinh\left(\mu\left(2L+x_0-x-2a\right)\right) + \sinh(\mu(x-x_0))\right]/\sinh(2a\nu) & \text{for } x \in (x_0,-a), \\ \{\mu\left[\cosh\left(\mu(a+x_0)\right)\sinh\left(\nu(a+x)\right) + \cosh(\mu(2L+x_0-a))\sinh\left(\nu(a-x)\right)\right] \\ -\nu\left[\sinh\left(\mu(a+x_0)\right)\cosh\left(\nu(a+x)\right) - \sinh(\mu(2L+x_0-a))\cosh\left(\nu(a-x)\right)\right]\}/\sinh(2a\nu) & \text{for } x \in [-a,a], \\ \mu\cosh\left(\mu(a+x_0)\right)\cosh\left(\mu(x-a)\right) - \frac{\nu^2}{\mu}\sinh\left(\mu(a+x_0)\right)\sinh\left(\mu(x-a)\right) \\ +\nu\left[\sinh(\mu(2L+x_0-x)) - \cosh(2a\nu)\sinh\left(\mu\left(2a-x+x_0\right)\right)\right]/\sinh(2a\nu) & \text{for } x \in (a,L), \end{cases} \tag{B.13}$$

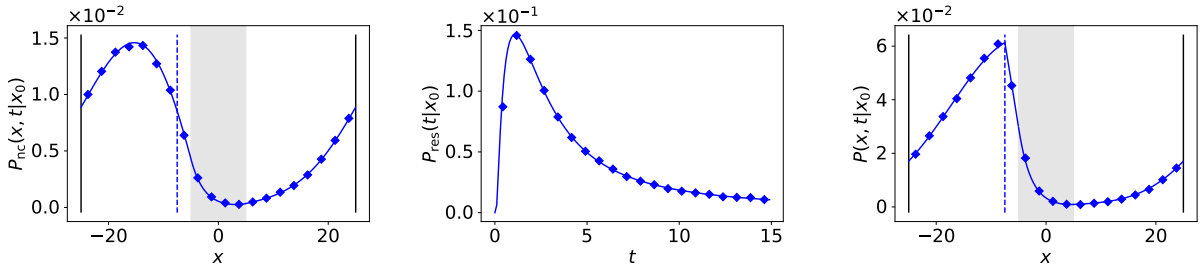
and it can be checked that in the limiting case, $r = 0$, of no resetting it reproduces the Laplace transform of the probability density of particles diffusing on the segment $(-L, L)$ with periodic boundary conditions, i.e.,

$$\tilde{P}(x,s|x_0) = \frac{\cosh\left(\mu(L-|x-x_0|)\right)}{2D\mu\sinh(\mu L)}, \tag{B.14}$$

whose inverse Laplace transform can be exactly computed as

$$P(x,t|x_0) = \frac{1}{2L}\left[1 + 2\sum_{n=1}^{\infty}(-1)^n e^{-\left(\frac{n\pi}{L}\right)^2 D\,t}\cos\left(n\pi\chi\right)\right], \tag{B.15}$$

with $\chi \equiv 1 - |x-x_0|/L$, see Ref. [188]; it is immediate to check that Eq. (B.15) has a uniform stationary distribution $P_{\rm st}$ given by $P_{\rm st}(x) = 1/2L$. Figure B.3a shows a snapshot of $P_{\rm nc}(x,t|x_0)$




(a) (b) (c)

Figure B.3: **Statistics of resetting with periodic boundary conditions.** **(a)** Probability density $P_{\rm nc}(x,t|x_0)$ at time $t = 15$ with $D = 5$, $r = 1$, $a = 5$, $x_0 = -7.5$. The solid line represents the inverse numerical Laplace transform of Eq. (B.13) while symbols correspond to simulations. The grey shaded area indicates the region within which resetting may occur. **(b)** Probability of first reset time $P_{\rm res}(t|x_0)$ as a function of $t$ with same parameters: comparison between inverse Laplace transform of Eq. (B.16) and simulations. **(c)** Probability density $P_{\rm nc}(x,t|x_0)$ as a function of position $x$ with $x_r = x_0$, indicated by the vertical dashed line. The solid line represents the inverse Laplace transform of Eq. (B.17) while diamonds simulations. Simulations were done using the Euler numerical integration scheme with time step $\Delta t = 0.05$, and they were repeated $N = 10^5$ times.

as a function of $x$: the solid line represents the inverse Laplace transform of Eq. (B.13) while the symbols correspond to the result of numerical simulations; in the resetting area (grey) $P(x,t|x_0)$ is exponentially suppressed compared to the values it has outside it as times goes by, due to resetting particles.

From $\tilde{P}_{\rm nc}(x,s|x_0)$ in Eq. (B.13) it is possible to obtain the Laplace transform $\tilde{P}_{\rm res}(s|x_0)$ of the probability $P_{\rm res}(t|x_0)$ that the particle resets for the first time at time $t$:

$$\tilde{P}_{\rm res}(s|x_0) = \frac{(r/\nu D)\sinh(a\nu)\cosh\left(\mu(L+x_0)\right)}{\nu\sinh(a\nu)\cosh\left(\mu(L-a)\right) + \mu\cosh(a\nu)\sinh\left(\mu(L-a)\right)}, \tag{B.16}$$

which is represented in Fig. B.3b.

Plugging Eqs. (B.13) and (B.16) into Eq. (1.32), we derive the Laplace transform for the probability distribution of $P(x,t|x_0)$:

$$\tilde{P}(x,s|x_0) = \frac{\nu}{4}\sinh(2a\nu)\left\{[\mu\sinh(a\nu)\cosh\left(\mu(L-a)\right)+\nu\cosh(a\nu)\sinh\left(\mu(L-a)\right)]\right.$$
$$\left.[\nu D(\nu\sinh(a\nu)\cosh\left(\mu(L-a)\right)+\mu\cosh(a\nu)\sinh\left(\mu(L-a)\right)) - r\sinh(a\nu)\cosh(\mu(L+x_0))]\right\}^{-1}$$

$$\begin{cases} \left[\mu\cosh\left(\mu(a+x_0)\right)\cosh\left(\mu(2L-a+x)\right) - \frac{\nu^2}{\mu}\sinh\left(\mu(a+x_0)\right)\sinh\left(\mu(2L-a+x)\right)\right] & \\ +\nu\left[\cosh\left(2a\nu\right)\sinh\left(\mu\left(2L+x-x_0-2a\right)\right) - \sinh(\mu(x-x_0))\right]/\sinh\left(2a\nu\right) & \text{for } x\in[-L,x_0], \\ \mu\cosh\left(\mu(a+x)\right)\cosh\left(\mu(2L-a+x_0)\right) - \frac{\nu^2}{\mu}\sinh\left(\mu(a+x)\right)\sinh\left(\mu(2L-a+x_0)\right) & \\ +\nu\left[\cosh\left(2a\nu\right)\sinh\left(\mu\left(2L+x_0-x-2a\right)\right) + \sinh(\mu(x-x_0))\right]/\sinh\left(2a\nu\right) & \text{for } x\in(x_0,-a), \\ \mu\left[\cosh\left(\mu(a+x_0)\right)\sinh\left(\nu(a+x)\right) + \cosh(\mu(2L+x_0-a))\sinh\left(\nu(a-x)\right)\right] & \\ -\nu\left[\sinh\left(\mu(a+x_0)\right)\cosh\left(\nu(a+x)\right) - \sinh(\mu(2L+x_0-a))\cosh\left(\nu(a-x)\right)\right]/\sinh\left(2a\nu\right) & \text{for } x\in[-a,a], \\ \mu\cosh\left(\mu(a+x_0)\right)\cosh\left(\mu(x-a)\right) - \frac{\nu^2}{\mu}\sinh\left(\mu(a+x_0)\right)\sinh\left(\mu(x-a)\right) & \\ +\nu\left[\sinh(\mu(2L+x_0-x)) - \cosh\left(2a\nu\right)\sinh\left(\mu\left(2a-x+x_0\right)\right)\right]/\sinh\left(2a\nu\right) & \text{for } x\in(a,L). \end{cases} \tag{B.17}$$

The probability density $P(x,t|x_0)$ is represented in Fig. B.3c: as a function of $x$ it features a cusp in correspondence of the resetting point $x = x_r = x_0$ (indicated by dashed vertical line) and a significant reduction of the probability within the resetting (grey) region.

Periodic boundary conditions, i.e., the geometry of a ring, allow the existence of a stationary distribution of Eq. (B.17), which is given by $P_{\rm st}(x|x_0) = \lim_{s\to 0} s\tilde{P}(x,s|x_0)$ and therefore by

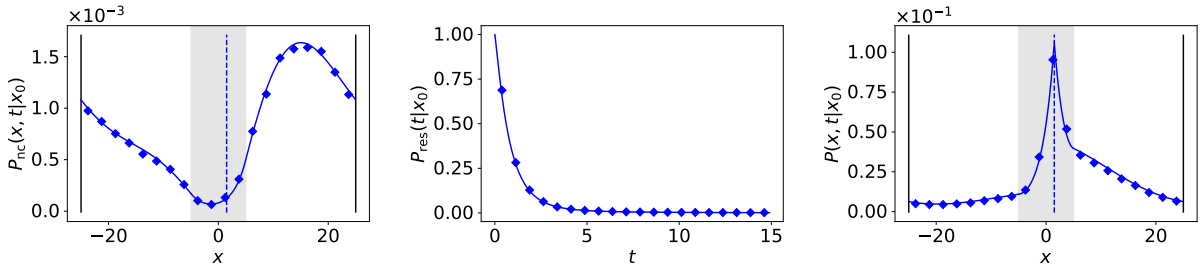
$$P_{\rm st}(a\,y|a\,y_0) = \frac{\rho}{a}\left\{\left[(\ell-1)\rho\cosh(\rho)+\sinh(\rho)\right]\left[2(\ell-1)\rho\cosh(\rho)+(2+\rho^2(1-2\ell-y_0)(1+y_0))\sinh(\rho)\right]\right\}^{-1}$$

$$\begin{cases} y\rho\sinh(\rho)\left[\sinh(\rho)-(1+y_0)\rho\cosh(\rho)\right] + \frac{\rho}{2}\left[y_0+(2\ell-2-y_0)\cosh(2\rho)\right] & \\ +\frac{1}{2}\left[1+\rho^2(1-2\ell)(1+y_0)\right]\sinh(2\rho) & \text{for } y\in[-\ell,y_0], \\ -y\rho\sinh(\rho)\left[\sinh(\rho)+(2\ell-1+y_0)\rho\cosh(\rho)\right] + \frac{\rho}{2}\left[(2\ell-2+y_0)\cosh(2\rho)-y_0\right] & \\ +\frac{1}{2}\left[1-\rho^2(2\ell+y_0-1)\sinh(2\rho)\right] & \text{for } y\in(y_0,-1), \\ \cosh(\rho)\left[\sinh(\rho)+(\ell-1)\rho\cosh(\rho)\right] - \rho(\ell+y_0)\sinh(\rho)\sinh(y\rho) & \text{for } y\in[-1,1], \\ y\rho\sinh(\rho)\left[\sinh(\rho)-(1+y_0)\rho\cosh(\rho)\right] + \frac{\rho}{2}\left[y_0+2\ell-(2+y_0)\cosh(2\rho)\right] & \\ +\frac{1}{2}\left[1+\rho^2(1+y_0)\right]\sinh(2\rho) & \text{for } y\in(1,\ell), \end{cases} \tag{B.18}$$

where we have introduced the dimensionless variables $\ell \equiv L/a$, $\rho \equiv a\sqrt{r/D}$, $y \equiv x/a$ and $y_0 \equiv x_0/a$.

### B.3.2 Case with $x_0 \in (-a,a)$

In this case the expression of $\tilde{P}_{\rm nc}(x,s|x_0)$ is given by




(a) (b) (c)

Figure B.4: **Statistics of resetting with periodic boundary conditions.** **(a)** Probability density $P_{\rm nc}(x,t|x_0)$ at time $t=15$ with $D=5$, $r=1$, $a=5$, $x_0=1.5$. The solid line represents the inverse numerical Laplace transform of Eq. (B.19) while symbols correspond to simulations. The grey shaded area indicates the region within which resetting may occur. **(b)** Probability of first reset time $P_{\rm res}(t|x_0)$ as a function of $t$ with same parameters: comparison between inverse Laplace transform of Eq. (B.20) and simulations. **(c)** Probability density $P(x,t|x_0)$ as a function of position $x$ with $x_r = x_0$, indicated by the vertical dashed line. The solid line represents the inverse Laplace transform of Eq. (B.21) while diamonds simulations. Simulations were done using the Euler numerical integration scheme with time step $\Delta t = 0.05$, and they were repeated $N = 10^5$ times.

$$\tilde{P}_{\rm nc}(x,s|x_0) = \frac{1}{D}\left\{(\mu^2+\nu^2)\sinh(2a\nu)\sinh(2\mu(L-a)) + 2\mu\nu\left[\cosh(2a\nu)\cosh(2\mu(L-a))-1\right]\right\}^{-1}$$

$$\begin{cases} \mu\left[\cosh(\mu(a+x))\sinh(\nu(a+x_0)) + \cosh(\mu(2L+x-a))\sinh(\nu(a-x_0))\right] & \\ -\nu\left[\sinh(\mu(a+x))\cosh(\nu(a+x_0)) - \sinh(\mu(2L+x-a))\cosh(\nu(a-x_0))\right] & \text{for } x\in[-L,-a], \\ \left\{\sinh(2\mu(L-a))\left[\mu^2\sinh(\nu(a+x))\sinh(\nu(a-x_0)) + \nu^2\cosh(\nu(a+x))\cosh(\nu(a-x_0))\right]\right. & \\ \left.+\mu\nu\left[\cosh(2\mu(L-a))\sinh(\nu(x+2a-x_0)) - \sinh(\nu(x-x_0))\right]\right\}/\nu & \text{for } x\in(-a,x_0), \\ \left\{\sinh(2\mu(L-a))\left[\mu^2\sinh(\nu(a+x_0))\sinh(\nu(a-x)) + \nu^2\cosh(\nu(a+x_0))\cosh(\nu(a-x))\right]\right. & \\ \left.+\mu\nu\left[\cosh(2\mu(L-a))\sinh(\nu(2a+x_0-x)) + \sinh(\nu(x-x_0))\right]\right\}/\nu & \text{for } x\in[x_0,a], \\ \mu\left[\cosh(\mu(x-a))\sinh(\nu(a-x_0)) + \cosh(\mu(2L-x-a))\sinh(\nu(a+x_0))\right] & \\ +\nu\left[\sinh(\mu(x-a))\cosh(\nu(a-x_0)) + \sinh(\mu(2L-x-a))\cosh(\nu(a+x_0))\right] & \text{for } x\in(a,L), \end{cases} \tag{B.19}$$

the inverse transform of which is reported in Fig. 10a as a function of the time $t$.

The Laplace transform of the probability $P_{\rm res}(t|x_0)$ that the particle resets for the first time at $t$, computed by plugging Eq. (B.9) in Eq. (1.26), is

$$\tilde{P}_{\rm res}(s|x_0) = \frac{r}{\nu^2 D}\left[1 - \frac{\mu\sinh(a\nu)\cosh(\mu(L+x_0))}{\nu\sinh(a\nu)\cosh(\mu(L-a)) + \mu\cosh(a\nu)\sinh(\mu(L-a))}\right], \tag{B.20}$$

and that probability, obtained from the inverse transform, is reported in Fig. B.4b as a function of time. From Eqs. (B.19) and (B.20) one can determine the Laplace transform $\tilde{P}(x,s|x_0)$ of the probability distribution $\tilde{P}(x,t|x_0)$ according to Eq. (1.32),

$$\tilde{P}(x,s|x_0) = \frac{\nu^2}{4}\left\{[\mu\sinh(a\nu)\cosh\left(\mu(L-a)\right) + \nu\cosh(a\nu)\sinh\left(\mu(L-a)\right)]\right.$$
$$\left.\left[\mu^2 D(\nu\sinh(a\nu)\cosh\left(\mu(L-a)\right) + \mu\cosh(a\nu)\sinh\left(\mu(L-a)\right)) - r\mu\cosh(x_0\nu)\sinh(\mu(L-a))\right]\right\}^{-1}\cdot$$

$$\begin{cases} \mu\left[\cosh\left(\mu(a+x)\right)\sinh\left(\nu(a+x_0)\right) + \cosh(\mu(2L+x-a))\sinh\left(\nu(a-x_0)\right)\right] & \\ -\nu\left[\sinh\left(\mu(a+x)\right)\cosh\left(\nu(a+x_0)\right) - \sinh(\mu(2L+x-a))\cosh\left(\nu(a-x_0)\right)\right] & \text{for } x\in[-L,-a], \\ \left\{\sinh\left(2\mu(L-a)\right)\left[\mu^2\sinh\left(\nu(a+x)\right)\sinh\left(\nu(a-x_0)\right) + \nu^2\cosh\left(\nu(a+x)\right)\cosh\left(\nu(a-x_0)\right)\right]\right. & \\ \left.+\mu\nu\left[\cosh\left(2\mu(L-a)\right)\sinh\left(\nu\left(x+2a-x_0\right)\right) - \sinh(\nu(x-x_0))\right]\right\}/\nu & \text{for } x\in(-a,x_0), \\ \left\{\sinh\left(2\mu(L-a)\right)\left[\mu^2\sinh\left(\nu(a+x_0)\right)\sinh\left(\nu(a-x)\right) + \nu^2\cosh\left(\nu(a+x_0)\right)\cosh\left(\nu(a-x)\right)\right]\right. & \\ \left.+\mu\nu\left[\cosh\left(2\mu(L-a)\right)\sinh\left(\nu\left(2a+x_0-x\right)\right) + \sinh(\nu(x-x_0))\right]\right\}/\nu & \text{for } x\in[x_0,a], \\ \mu\left[\cosh\left(\mu(x-a)\right)\sinh\left(\nu(a-x_0)\right) + \cosh(\mu(2L-x-a))\sinh\left(\nu(a+x_0)\right)\right] & \\ +\nu\left[\sinh\left(\mu(x-a)\right)\cosh\left(\nu(a-x_0)\right) + \sinh(\mu(2L-x-a))\cosh\left(\nu(a+x_0)\right)\right] & \text{for } x\in(a,L), \end{cases} \tag{B.21}$$

whose stationary distribution is given by $P_{\rm st}(x|x_0) = \lim_{s\to 0} s\tilde{P}(x,s|x_0)$, which yields

$$P_{\rm st}(a\,y|a\,x_0) = \frac{\rho}{2a}\left\{[(\ell-1)\rho\cosh(y_0\rho) + \sinh(\rho)]\,[(\ell-1)\rho\cosh(\rho) + \sinh(\rho)]\right\}^{-1}$$

$$\begin{cases} [\rho(\ell-1)\cosh(\rho)\cosh(y_0\rho) + \sinh(\rho)(\cosh(y_0\rho) - \rho(\ell+y)\sinh(y_0\rho))] & \text{for } y\in[-\ell,-1], \\ [\rho(\ell-1)\cosh((1+y)\rho)\cosh((1-y_0)\rho) + \sinh(\rho)\cosh((1+y-y_0)\rho)] & \text{for } y\in(-1,y_0), \\ [\rho(\ell-1)\cosh((1+y_0)\rho)\cosh((1-y)\rho) + \sinh(\rho)\cosh((1-y+y_0)\rho)] & \text{for } y\in[y_0,1], \\ [\rho(\ell-1)\cosh(\rho)\cosh(y_0\rho) + \sinh(\rho)(\cosh(y_0\rho) + \rho(\ell-y)\sinh(y_0\rho))] & \text{for } y\in(1,\ell). \end{cases} \tag{B.22}$$

At last we mention the particular case $a = L$ of the previous expression, corresponding to resetting in any position of the ring and leading to

$$\tilde{P}(x,s|x_0) = \frac{\nu}{2D\mu^2}\frac{\cosh(\nu(L-|x-x_0|))}{\sinh(L\nu)}, \tag{B.23}$$

which can be analytically inverted to obtain the expression in the time domain:

$$P(x,t|x_0) = \frac{1}{2}\sqrt{\frac{r}{D}}\frac{\cosh(\sqrt{\frac{r}{D}}(L-|x-x_0|))}{\sinh(L\sqrt{\frac{r}{D}})} + \sum_{n=1}^{\infty}(-1)^n\frac{n^2\pi^2}{L^3}\frac{e^{-Dr_n\,t}}{r_n}\cos\left(n\pi\chi\right), \tag{B.24}$$

where $r_n \equiv \frac{n^2\pi^2}{L^2} + \frac{r}{D}$, $\chi \equiv 1 - |x-x_0|/L$ and the first term corresponds to the stationary distribution.

# Appendix C

# Calculations of Chapter 3

## C.1 Moments of $G_S(x, \sigma, t|x_0, \sigma_0)$

In this Appendix, we derive the first and second moment of the probability density $G_S(x, \sigma, t|x_0, \sigma_0)$ in Eqs. (3.9). As we have shown in Chapter 3, their expression are crucial for the calculation of the relative moments of the work in Eqs. (3.54) and (3.57). For analytical convenience, we will compute these moments in the Laplace domain.

### C.1.1 First moment

In this spirit, we start by considering the Laplace transform of the first moment of $G_\sigma(x, t|x_0) = \psi_\sigma(\tau)G^{(0)}_\sigma(x, t|x_0)$, where we fix $G^{(0)}_\sigma(x, t|x_0)$ to be the probability density in Eq. (3.7) for the Ornstein-Uhlenbeck process in Eq. (3.6). It reads

$$\begin{aligned}\langle\tilde{x}\rangle_\sigma(s|x_0) \equiv \int_{-\infty}^{+\infty} \mathrm{d}x\, x\, \tilde{G}_\sigma(x, s|x_0) &= \mathcal{L}\left\{\psi_\sigma(t)\, \mu_\sigma(t|x_0)\right\} \\ &= \mathcal{L}\left\{\psi_\sigma(t)\left[x_0 e^{-\nu t} + c_\sigma(1 - e^{-\nu t})\right]\right\} \\ &= x_0\, \tilde{\psi}_\sigma(s + \nu) + c_\sigma\left[\tilde{\psi}_\sigma(s) - \tilde{\psi}_\sigma(s + \nu)\right] \\ &= x_0\, a^{(1)}_\sigma + b^{(1)}_\sigma,\end{aligned} \tag{C.1}$$

where we define the auxiliary quantities $a^{(n)}_\sigma \equiv \tilde{\psi}_\sigma(s + n\nu)$ and $b^{(1)}_\pm \equiv c_\sigma\left[\tilde{\psi}_\sigma(s) - \tilde{\psi}_\sigma(s + \nu)\right]$. The second line of Eq. (C.1) is found by direct substitution of $\mu_\sigma(t|x_0)$ in Eq. (3.8), while the third by applying the property of the Laplace transform $\mathcal{L}\left(e^{-\nu t} f(t)\right)(s) = \tilde{f}(s + \nu)$. We now have all the ingredients to calculate $\langle\tilde{x}\rangle_{\sigma\sigma}(s|x_0)$, the Laplace transform of the first moment of $G_S(x, t, \sigma|x_0, \sigma)$

in Eq. (3.12):

$$
\begin{aligned}
\langle \tilde{x} \rangle^S_{\sigma\sigma}(s|x_0) &= \int_{-\infty}^{+\infty} \mathrm{d}x\, x\, \tilde{G}_S(y,\sigma,s|x_0,\sigma) = \sum_{n=1}^{\infty} I^{(1)}_\sigma(n,s) \\
&= \sum_{n=1}^{\infty} \int_{-\infty}^{+\infty} \left( \prod_{k=1}^{2n-2} \mathrm{d}z_k \right) \left( \prod_{k=1}^{n-1} \tilde{G}_\sigma(z_{2k-1},s|z_{2k-2})\, \tilde{G}_{-\sigma}(z_{2k},s|z_{2k-1}) \right) \\
&\quad \times \int_{-\infty}^{+\infty} \mathrm{d}z_{2n-1} \int_{-\infty}^{+\infty} \mathrm{d}y\, y\, \tilde{G}_\sigma(z_{2n-1},s|z_{2n-2})\, \tilde{G}_{-\sigma}(y,s|z_{2n-1}) \\
&= \sum_{n=1}^{\infty} \int_{-\infty}^{+\infty} \left( \prod_{k=1}^{2n-2} \mathrm{d}z_k \right) \left( \prod_{k=1}^{n-1} \tilde{G}_\sigma(z_{2k-1},s|z_{2k-2})\, \tilde{G}_{-\sigma}(z_{2k},s|z_{2k-1}) \right) \left( z_{2n-1} A^{(1)} + B^{(1)}_\sigma \right) \\
&= \sum_{n=1}^{\infty} \left( I^{(1)}_\sigma(n-1,s) A^{(1)} + B^{(1)}_\sigma (A^{(0)})^{n-1} \right),
\end{aligned}
\tag{C.2}
$$

where we have defined the auxiliary functions $A^{(n)} \equiv a^{(n)}_+ a^{(n)}_-$, and $B^{(1)}_\sigma \equiv b^{(1)}_\sigma a^{(1)}_{-\sigma} + b^{(1)}_{-\sigma} \tilde{\psi}_\sigma(s)$. The definition of the integral $I^{(1)}_\sigma(n,s)$ is reported in the second and third line of Eq. (C.2), and results from the insertion of $G_S(x,\sigma,t|x_0,\sigma)$ expression in Eq. (3.9). The integral in the third line of Eq. (C.2), evaluated via Eq. (C.1), coincides with $I^{(1)}_\sigma(1,s) = x_0 A^{(1)} + B^{(1)}_\sigma$ in the case where the initial position coincides with the integration variable $z_{2n-1}$. In the last line we recognize the same type of integral $I^{(1)}_\sigma(n-1,s)$ as in the second and third line, plus the extra term $(A^{(0)})^{n-1} = (\tilde{\psi}_\sigma(s)\tilde{\psi}_{-\sigma}(s))^{n-1}$ which follows from $\int_{-\infty}^{+\infty} \mathrm{d}x\, \tilde{G}_\sigma(x,s|x_0) = \tilde{\psi}_\sigma(s)$.

It follows that the calculation of $\langle \tilde{x} \rangle^S_{\sigma\sigma}(s|x_0)$ reduced to the one of $I^{(1)}_\sigma(n-1,s)$, and its successive sum over $n$. We can evaluate the integral $I^{(1)}_\sigma(n,s)$ recursively substituting its lower $n$ expression, until we are left with the known $I^{(1)}_\sigma(1,s)$:

$$
\begin{aligned}
I^{(1)}_\sigma(n,s) &= I^{(1)}_\sigma(n-1,s) A^{(1)} + B^{(1)}_\sigma (A^{(0)})^{n-1} \\
&= \left( A^{(1)} \right)^k I^{(1)}_\sigma(n-k,s) + B^{(1)}_\sigma \sum_{l=0}^{k-1} \left( A^{(1)} \right)^l \left( A^{(0)} \right)^{n-1-l} \\
&= x_0 \left( A^{(1)} \right)^n + B^{(1)}_\sigma \sum_{l=0}^{n-1} \left( A^{(1)} \right)^l \left( A^{(0)} \right)^{n-1-l} \\
&= x_0 \left( A^{(1)} \right)^n + B^{(1)}_\sigma \frac{\left( A^{(0)} \right)^n - \left( A^{(1)} \right)^n}{A^{(0)} - A^{(1)}},
\end{aligned}
\tag{C.3}
$$

where in the last line we sum the truncated geometric series in $l$. Finally, we substitute the expression of $I^{(1)}_\sigma(n,s)$ Eq. (C.3) into Eq. (C.2), bringing the Laplace transform of first moment of the switching

probability density $G_S(x,\sigma,t|x_0,\sigma)$:

$$\begin{aligned}\langle\tilde{x}\rangle^S_{\sigma\sigma}(s|x_0) &= \sum_{n=1}^{\infty} I^{(1)}_\sigma(n,s)\\ &= \sum_{n=1}^{\infty}\left[x_0\,\left(A^{(1)}\right)^n + B^{(1)}_\sigma\frac{\left(A^{(0)}\right)^n-\left(A^{(1)}\right)^n}{A^{(0)}-A^{(1)}}\right]\\ &= x_0\frac{A^{(1)}}{1-A^{(1)}}+\frac{B^{(1)}_\sigma}{(1-A^{(0)})(1-A^{(1)})},\end{aligned} \tag{C.4}$$

where last equality follows by summing the geometric series, whose convergence is ensured by $|A^{(n)}|<1$ for $\mathrm{Re}(s)>0$. In general, it is easy to check that $A^{(n)}$ satisfies the inequality $|A^{(n)}|<|A^{(m)}|$ for $m<n$.

Analogously to what done for $\langle x\rangle^S_{\sigma\sigma}(s|x_0)$, we can compute $\langle\tilde{x}\rangle_{-\sigma\sigma}(s|x_0)$, the first moment of $\tilde{G}_S(x,-\sigma,s|x_0,\sigma)$ in Eq. (3.12), as

$$\begin{aligned}\langle\tilde{x}\rangle^S_{-\sigma\sigma}(s|x_0) &= \int_{-\infty}^{+\infty}\mathrm{d}x\,x\,\tilde{G}_S(x,-\sigma,s|x_0,\sigma)\\ &= \langle\tilde{x}\rangle_\sigma(s|x_0)+\int_{-\infty}^{+\infty}\mathrm{d}x\,\langle\tilde{x}\rangle_\sigma(s|x)\,\tilde{G}_S(x,\sigma,s|x_0,\sigma)\\ &= x_0\,a^{(1)}_\sigma+\,b^{(1)}_\sigma+\int_{-\infty}^{+\infty}\mathrm{d}x\,\left(x\,a^{(1)}_\sigma+\,b^{(1)}_\sigma\right)\tilde{G}_S(x,\sigma,s|x_0,\sigma)\\ &= x_0\,a^{(1)}_\sigma+\,b^{(1)}_\sigma+a^{(1)}_\sigma\left[x_0\frac{A^{(1)}}{1-A^{(1)}}+\frac{B^{(1)}_\sigma}{(1-A^{(0)})(1-A^{(1)})}\right]+b^{(1)}_\sigma\frac{A^{(0)}}{1-A^{(0)}}\\ &= \frac{a^{(1)}_\sigma}{1-A^{(1)}}\left[x_0+\frac{B^{(1)}_\sigma}{1-A^{(0)}}\right]+\frac{b^{(1)}_\sigma}{1-A^{(0)}}.\end{aligned} \tag{C.5}$$

For completeness, we evaluate the stationary value of $\langle\tilde{x}\rangle^S_{\sigma\sigma_0}(s|x_0)$ by using the final value theorem of the Laplace transform, that is

$$\begin{aligned}\langle x\rangle^S_\sigma &= \lim_{t\to\infty}\langle x\rangle^S_{\sigma\sigma_0}(t|x_0)=\lim_{s\to 0}s\,\langle\tilde{x}\rangle^S_{\sigma\sigma_0}(s|x_0)\\ &= \frac{c_\sigma\left(1-\tilde{\psi}_\sigma(\nu)\right)\tilde{\psi}_{-\sigma}(\nu)+c_{-\sigma}\left(1-\tilde{\psi}_{-\sigma}(\nu)\right)}{2\langle\tau\rangle\,\left(1-\tilde{\psi}_+(\nu)\tilde{\psi}_-(\nu)\right)},\end{aligned} \tag{C.6}$$

where with abuse of notation the stationary limit of $\langle\langle x\rangle^S_\sigma$ is denoted by simply dropping the time dependence.

The value $\langle x\rangle^S_\sigma$ depends only on the final state, on the Laplace transform of the waiting-time distribution $\tilde{\psi}_\sigma(\nu)$ computed at $\nu$, and on its average period $\langle\tau\rangle=(\langle\tau\rangle_+ + \langle\tau\rangle_-)/2$.

We conclude this part, by reporting the explicit expressions of $E_\sigma(s)$ and $F_\sigma(s)$ encountered in the second moment of the work in Eq. (3.58), defined as $\langle\tilde{x}\rangle^S_{\sigma\sigma}(s|x_0)-\langle\tilde{x}\rangle^S_{-\sigma\sigma}(s|x_0)=x_0E_\sigma(s)+$

$F_\sigma(s)$, and given by

$$E_\sigma(s) = \frac{A^{(1)} - a_\sigma^{(1)}}{1 - A^{(1)}}, \quad \text{and} \quad F_\sigma(s) = \frac{1}{1 - A^{(0)}} \left( B_\sigma^{(1)} \frac{1 - a_\sigma^{(1)}}{1 - A^{(1)}} - b_\sigma^{(1)} \right). \tag{C.7}$$

### C.1.2 Second moment

The Laplace transform of the second moments $\langle \tilde{x}^2 \rangle_{\sigma\sigma_0}(s|x_0)$ of $G_S(x, \sigma, t|x_0, \sigma_0)$ are computed following the same steps as $\langle \tilde{x}^2 \rangle_{\sigma\sigma_0}(s|x_0)$. First, we consider the second moment of the bare probability density $\tilde{G}_\sigma(x, s|x_0)$, which reads

$$\begin{aligned}
\langle \tilde{x}^2 \rangle_\sigma(s|x_0) \equiv & \int_{-\infty}^{+\infty} \mathrm{d}z \, z^2 \, \tilde{G}_\sigma(z, s|x_0) = \mathcal{L}\left\{ \psi_\sigma(t) \, \left[ \Sigma^2(t) + \mu_\sigma^2(t|x_0) \right] \right\} \\
= & \mathcal{L}\left\{ \psi_\sigma(t) \left[ x_0^2 e^{-2\nu t} + c_\sigma^2 (1 - 2e^{-\nu t} + e^{-2\nu t}) + 2x_0 \, c_\sigma \left( e^{-\nu t} - e^{-2\nu t} \right) + \frac{D}{\nu}(1 - e^{-2\nu t}) \right] \right\} \\
= & x_0^2 \, \tilde{\psi}_\sigma(s + 2\nu) + 2x_0 \, c_\sigma \left[ \tilde{\psi}_\sigma(s + \nu) - \tilde{\psi}_\sigma(s + 2\nu) \right] \\
& + c_\sigma^2 \left[ \tilde{\psi}_\sigma(s) - 2\tilde{\psi}_\sigma(s + \nu) + \tilde{\psi}_\sigma(s + 2\nu) \right] + \frac{D}{\nu} \left[ \tilde{\psi}_\sigma(s) - \tilde{\psi}_\sigma(s + 2\nu) \right] \\
= & x_0^2 \, a_\sigma^{(2)} + x_0 \, b_\sigma^{(2)} + c_\sigma^{(2)},
\end{aligned} \tag{C.8}$$

where we define the auxiliary variables

$$\begin{aligned}
b_\sigma^{(2)} &= 2 \, c_\sigma \left[ \tilde{\psi}_\sigma(s + \nu) - \tilde{\psi}_\sigma(s + 2\nu) \right], \\
c_\sigma^{(2)} &= c_\sigma^2 \left[ \tilde{\psi}_\sigma(s) - 2\tilde{\psi}_\sigma(s + \nu) + \tilde{\psi}_\sigma(s + 2\nu) \right] + \frac{D}{\nu} \left[ \tilde{\psi}_\sigma(s) - \tilde{\psi}_\sigma(s + 2\nu) \right].
\end{aligned} \tag{C.9}$$

In the second line of Eq. (C.8) we make explicit the expression of the second moment of the position of a Ornstein-Uhlenbeck process in Eq. (3.8), while in the third we evaluate its Laplace transform.

We now have all the ingredients to compute $\langle \tilde{x}^2 \rangle_{\sigma\sigma}^S(s|x_0)$:

$$\begin{aligned}
\langle \tilde{x}^2 \rangle_{\sigma\sigma}^S(s|x_0) = & \int_{-\infty}^{+\infty} \mathrm{d}x \, x^2 \, \tilde{G}_S(x, \sigma, s|x_0, \sigma) = \sum_{n=1}^{\infty} I_\sigma^{(2)}(n, s) \\
= & \sum_{n=1}^{\infty} \int_{-\infty}^{+\infty} \left( \prod_{k=1}^{2n-2} \mathrm{d}z_k \right) \left( \prod_{k=1}^{n-1} \tilde{G}_\sigma(z_{2k-1}, s|z_{2k-2}) \, \tilde{G}_{-\sigma}(z_{2k}, s|z_{2k-1}) \right) \\
& \times \int_{-\infty}^{+\infty} \mathrm{d}z_{2n-1} \int_{-\infty}^{+\infty} \mathrm{d}y \, y^2 \, \tilde{G}_\sigma(z_{2n-1}, s|z_{2n-2}) \, \tilde{G}_{-\sigma}(y, s|z_{2n-1}) \\
= & \sum_{n=1}^{\infty} \int_{-\infty}^{+\infty} \left( \prod_{k=1}^{2n-2} \mathrm{d}z_k \right) \left( \prod_{k=1}^{n-1} \tilde{G}_\sigma(z_{2k-1}, s|z_{2k-2}) \, \tilde{G}_{-\sigma}(z_{2k}, s|z_{2k-1}) \right) \\
& \times \left( z_{2n-1}^2 A^{(2)} + z_{2n-1} B_\sigma^{(2)} + C_\sigma^{(2)} \right) \\
= & \sum_{n=1}^{\infty} \left( I_\sigma^{(2)}(n-1, s) A^{(2)} + I_\sigma^{(1)}(n-1, s) B_\sigma^{(2)} + C_\sigma^{(2)} (A^{(0)})^{n-1} \right),
\end{aligned} \tag{C.10}$$

where the expression of $I_\sigma^{(2)}(n,s)$ coincides with second and third line, and we have introduced the auxiliary variables

$$\begin{aligned} B_\sigma^{(2)} &\equiv b_\sigma^{(2)} a_{-\sigma}^{(2)} + b_{-\sigma}^{(2)} a_\sigma^{(1)}, \\ C_\sigma^{(2)} &\equiv c_\sigma^{(2)} a_{-\sigma}^{(2)} + a_\sigma^{(0)} c_{-\sigma}^{(2)} + b_{-\sigma}^{(2)} b_\sigma^{(1)}. \end{aligned} \tag{C.11}$$

In the forth line we substitute the expression $I_\sigma^{(2)}(1,s) = x_0^2 A^{(2)} + x_0 B_\sigma^{(2)} + C_\sigma^{(2)}$, where the initial point coincides with the integration variable $z_{2n-1}$. In the last line, we recognize the appearance of integrals of the type $I_\sigma^{(2)}(n,s)$, and $I_\sigma^{(1)}(n,s)$ at lower order of $n$. Then, we evaluate the integral $I_\sigma^{(2)}(n,s)$ recursively as

$$\begin{aligned} I_\sigma^{(2)}(n,s) \equiv & \int_{-\infty}^{+\infty} \left( \prod_{l=1}^{2n} \mathrm{d}z_l \right) \left( \prod_{k=1}^{n} \tilde{G}_\sigma(z_{2k-1}, s | z_{2k-2}) \, \tilde{G}_{-\sigma}(z_{2k}, s | z_{2k-1}) \right) z_{2n}^2 \\ =& A^{(2)} I_\sigma^{(2)}(n-1,s) + B^{(2)} I_\sigma^{(1)}(n-1,s) + C_\sigma^{(2)} \left( A^{(0)} \right)^{n-1} \\ =& \left( A^{(2)} \right)^n x_0^2 + B_\sigma^{(2)} \left( A^{(2)} \right)^{n-1} x_0 + B_\sigma^{(2)} \sum_{j=0}^{n-2} \left( A^{(2)} \right)^j I_\sigma^{(1)}(n-1-j,s) \\ & + C_\sigma^{(2)} \sum_{j=0}^{n-1} \left( A^{(2)} \right)^j \left( A^{(0)} \right)^{n-1-j} \\ =& \left( A^{(2)} \right)^n x_0^2 + B_\sigma^{(2)} \left( A^{(2)} \right)^{n-1} x_0 \\ & + C_\sigma^{(2)} \frac{\left( A^{(0)} \right)^n - \left( A^{(2)} \right)^n}{A^{(0)} - A^{(2)}} + x_0 B_\sigma^{(0)} A^{(1)} \frac{\left( A^{(1)} \right)^{n-1} - \left( A^{(2)} \right)^{n-1}}{A^{(1)} - A^{(2)}} \\ & + \frac{B_\sigma^{(0)} B_\sigma^{(1)}}{A^{(0)} - A^{(1)}} \left[ A^{(0)} \frac{\left( A^{(0)} \right)^{n-1} - \left( A^{(2)} \right)^{n-1}}{A^{(0)} - A^{(2)}} - A^{(1)} \frac{\left( A^{(1)} \right)^{n-1} - \left( A^{(2)} \right)^{n-1}}{A^{(1)} - A^{(2)}} \right], \end{aligned} \tag{C.12}$$

which follows by summing the truncated geometric series in the third line. Finally, by substituting the integral $I_\sigma^{(2)}(n,s)$, and $I_\sigma^{(1)}(n,s)$ in Eq. (C.10), we get the second moment $\langle \tilde{x}^2 \rangle_{\sigma\sigma}^S(s|x_0)$:

$$\begin{aligned} \langle \tilde{x}^2 \rangle_{\sigma\sigma}^S(s|x_0) = \sum_{n=1}^{\infty} I_\sigma^{(2)}(n,s) =& x_0^2 \frac{A^{(2)}}{1 - A^{(2)}} + x_0 \frac{B_\sigma^{(2)}}{\left(1 - A^{(1)}\right)\left(1 - A^{(2)}\right)} \\ & + \frac{C_\sigma^{(2)}}{\left(1 - A^{(0)}\right)\left(1 - A^{(2)}\right)} + \frac{B_\sigma^{(2)} B_\sigma^{(1)}}{\left(1 - A^{(0)}\right)\left(1 - A^{(1)}\right)\left(1 - A^{(2)}\right)}. \end{aligned} \tag{C.13}$$

The same considerations are made for $\langle \tilde{x}^2 \rangle_{-\sigma\sigma}^S(s|x_0)$, whose calculation follows directly from the expression of $\tilde{G}_S(x, -\sigma, s | x_0, \sigma)$ in Eq. (3.12):

$$
\begin{aligned}
\langle\tilde{x}^2\rangle^S_{-\sigma\sigma}(s|x_0) &= \int_{-\infty}^{+\infty} \mathrm{d}x\, x^2\, \tilde{G}_S(x,-\sigma,s|x_0,\sigma) \\
&= \langle\tilde{x}^2\rangle_\sigma(s|x_0) + \int_{-\infty}^{+\infty} \mathrm{d}x\, \langle\tilde{x}^2\rangle_\sigma(s|x)\tilde{G}_S(x,\sigma,s|x_0,\sigma) \\
&= x_0^2\, a_\sigma^{(2)} + x_0\, b_\sigma^{(2)} + c_\sigma^{(2)} + \int_{-\infty}^{+\infty} \mathrm{d}x\, \left(x^2\, a_\sigma^{(2)} + x\, b_\sigma^{(2)} + c_\sigma^{(2)}\right) \tilde{G}_S(x,\sigma,s|x_0,\sigma) \\
&= x_0^2\, a_\sigma^{(2)} + x_0\, b_\sigma^{(2)} + \langle\tilde{x}^2\rangle^S_{\sigma\sigma}(s|x_0)\, a_\sigma^{(2)} + \langle\tilde{x}\rangle^S_{\sigma\sigma}(s|x_0)\, b_\sigma^{(2)} + \frac{c_\sigma^{(2)}}{1-A^{(0)}} \\
&= \frac{a_\sigma^{(2)}}{1-A^{(2)}}\left[x_0^2 + x_0\frac{B_\sigma^{(2)}}{1-A^{(1)}} + \frac{C_\sigma^{(2)}}{1-A^{(0)}} + \frac{B_\sigma^{(2)}B_\sigma^{(1)}}{\left(1-A^{(0)}\right)\left(1-A^{(1)}\right)}\right] \\
&+ \frac{c_\sigma^{(2)}}{1-A^{(0)}} + \frac{b_\sigma^{(2)}}{1-A^{(1)}}\left[x_0 + \frac{B_\sigma^{(1)}}{1-A^{(0)}}\right].
\end{aligned}
\tag{C.14}
$$

In the fifth line we substitute the expression of $\langle\tilde{x}^2\rangle^S_{\sigma\sigma}(s|x_0)$ in Eq. (C.13), and $\langle\tilde{x}\rangle^S_{\sigma\sigma}(s|x_0)$ in Eq. (C.4).

For later convenience, we conclude this Section by computing the stationary limit $\langle x^2\rangle^S_\sigma$ of $\langle\tilde{x}^2\rangle^S_{\sigma\sigma_0}(s|x_0)$. By applying the final value theorem of the Laplace transform to Eqs. (C.13) and (C.14), we get

$$
\langle x^2\rangle^S_\sigma = \frac{1}{2\langle\tau\rangle\left(1-\tilde{\psi}_+(2\nu)\tilde{\psi}_-(2\nu)\right)}\left(C_\sigma^{(2)}(0) + \frac{B_\sigma^{(1)}(0)B_\sigma^{(2)}(0)}{1-\tilde{\psi}_+(\nu)\tilde{\psi}_-(\nu)}\right), \tag{C.15}
$$

where with abuse of notation the stationary limit of $\langle\langle x^2\rangle^S_\sigma$ is denoted by simply dropping the time dependence.

In particular, we can give an explicit simple expression in the symmetric case $\psi = \psi_\sigma$, that is

$$
\langle x^2\rangle^S_\sigma = \frac{1}{2\langle\tau\rangle}\left\{\frac{D}{\nu} + \frac{c_0^2}{1-\tilde{\psi}(2\nu)}\left[1 - 2\tilde{\psi}(\nu) + \tilde{\psi}(2\nu) - 2\left(\tilde{\psi}(\nu) - \tilde{\psi}(2\nu)\right)\frac{1-\tilde{\psi}(\nu)}{1+\tilde{\psi}(\nu)}\right]\right\}, \tag{C.16}
$$

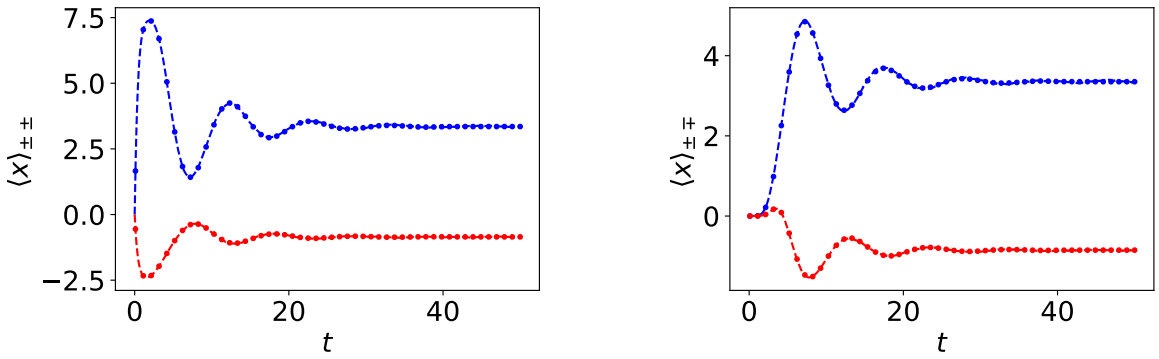
where $c_0 \equiv (c_\sigma - c_{-\sigma})/2$.

## C.2 Moments of $G(x,\sigma,t|x_0,\sigma_0)$

We now use the expressions of the first and second moments of the switching probability density $G_S(x,\sigma,t|x_0,\sigma_0)$ found in the previous Section to compute those of $G(x,\sigma,t|x_0,\sigma_0)$.

### C.2.1 First moment

As a first case, we consider the moment $\langle\tilde{x}\rangle_{\sigma\sigma_0} = \int_{-\infty}^{+\infty}\mathrm{d}x\, x\, \tilde{G}(x,\sigma,s|x_0,\sigma_0)$ , that we explicitly compute by substituting into Eq. (3.19) the definition of $\langle\tilde{x}\rangle_{\sigma\sigma_0}$. These moments are expressed in terms of the moments of the switching probability density $G_S(x,\sigma,t|x_0,\sigma_0)$ as




(a) (b)

Figure C.1: **First moments of $G(x, \sigma, t|x_0, \sigma_0)$.** The figure on the left displays the time evolution of the moment $\langle x \rangle_{++}$ (blue) and of $\langle x \rangle_{--}$ (red). The figure on the left displays the time evolution of the moment $\langle x \rangle_{+-}$ (blue) and of $\langle x \rangle_{-+}$ (red). In both pictures the dashed line correspond to simulations ($N = 10^6$ samples with $\Delta t = 0.005$) and dots by inverse Laplace transform of Eq. (C.17). The parameters of the model are: $D = 1$, $c_+ = 7.5$, $c_- = -2.5$, $\nu = 2.5$, $k_+ = 10$, $\theta_+ = 0.5$, $k_- = 5$, $\theta_- = 1$, $x_0 = 0$ and $\lambda = 0.5$.

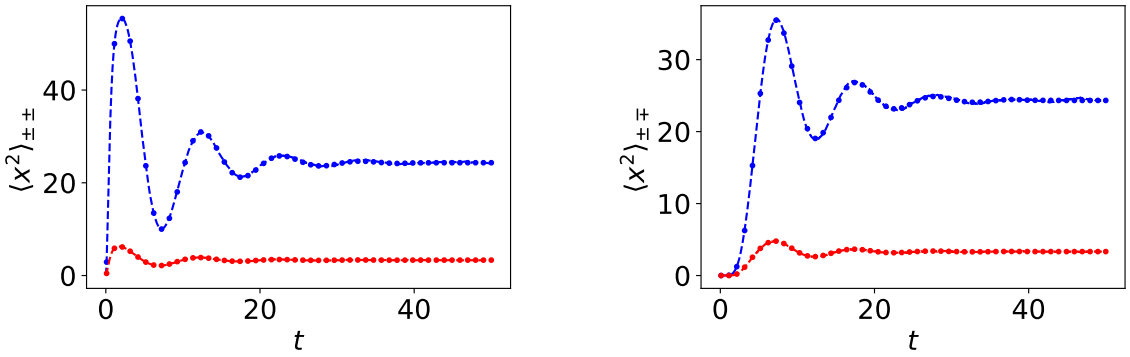
$$
\begin{aligned}
\langle \tilde{x} \rangle_{\sigma\sigma} &= \mathcal{L}\left\{\Psi_\sigma(t)\left[\Sigma^2(t) + \mu_\sigma^2(t|x_0)\right]\right\}(s) + \int_{-\infty}^{+\infty} \mathrm{d}x\, \tilde{G}_S(x, \sigma, s|x_0, \sigma)\mathcal{L}\left\{\Psi_\sigma(t)\left[\Sigma^2(t) + \mu_\sigma^2(t|y)\right]\right\}(s) \\
&= \tilde{\Psi}_\sigma(s+\nu)\langle \tilde{x} \rangle_{\sigma\sigma}^S(s|x_0) + c_\sigma \frac{\tilde{\Psi}_\sigma(s) - \tilde{\Psi}_\sigma(s+\nu)}{1 - \tilde{\psi}_+(s)\tilde{\psi}_-(s)} + x_0 \tilde{\Psi}_\sigma(s+\nu), \\
\langle \tilde{x} \rangle_{\sigma-\sigma} &= \int_{-\infty}^{+\infty} \mathrm{d}x\, \tilde{G}_S(x, \sigma, s|x_0, -\sigma)\mathcal{L}\left\{\Psi_\sigma(t)\left[\Sigma^2(t) + \mu_\sigma^2(t|y)\right]\right\}(s) \\
&= \tilde{\Psi}_\sigma(s+\nu)\langle \tilde{x} \rangle_{\sigma-\sigma}^S(s|x_0) + c_\sigma \tilde{\psi}_{-\sigma}(s) \frac{\tilde{\Psi}_\sigma(s) - \tilde{\Psi}_\sigma(s+\nu)}{1 - \tilde{\psi}_+(s)\tilde{\psi}_-(s)};
\end{aligned}
\tag{C.17}
$$

a graphic representation of such moments is displayed in Fig. C.1. Finally, one can reconstruct the average particle position by conditioning on the initial state as

$$
\langle \tilde{x} \rangle(s|x_0) = \sum_\sigma \langle \tilde{x} \rangle_\sigma(s|x_0), \quad \text{where} \quad \langle \tilde{x} \rangle_\sigma = \sum_{\sigma_0} \lambda_{\sigma_0} \langle \tilde{x} \rangle_{\sigma\sigma_0}(s|x_0), \tag{C.18}
$$

as it can be seen in the left panel of Fig. C.3.

The stationary value of these first moments is retrieved by applying the final value theorem of




(a) (b)

Figure C.2: **Second moments of $G(x, \sigma, t|x_0, \sigma_0)$.** The figure on the left displays the time evolution of the moment $\langle x^2 \rangle_{++}$ (blue) and of $\langle x^2 \rangle_{--}$ (red). The figure on the left displays the time evolution of the moment $\langle x^2 \rangle_{+-}$ (blue) and of $\langle x^2 \rangle_{-+}$ (red). In both pictures the dashed line correspond to simulations ($N = 10^6$ samples with $\Delta t = 0.005$) and dots by inverse Laplace transform of Eq. (C.21). The parameters of the model are: $D = 1$, $c_+ = 7.5$, $c_- = -2.5$, $\nu = 2.5$, $k_+ = 10$, $\theta_+ = 0.5$, $k_- = 5$, $\theta_- = 1$, $x_0 = 0$ and $\lambda = 0.5$.

the Laplace transform, that is

$$\begin{aligned} \langle x \rangle_\sigma^{\rm st} &= \lim_{t\to\infty} \langle x \rangle_{\sigma\sigma_0}(t|x_0) = \lim_{s\to 0} s\, \langle \tilde{x} \rangle_{\sigma\sigma_0}(s|x_0) \\ &= \tilde{\Psi}_\sigma(\nu) \langle x \rangle_\sigma^S + \frac{c_\sigma}{2\langle \tau \rangle} \Big( \langle \tau \rangle_\sigma - \tilde{\Psi}_\sigma(\nu) \Big) \\ &= \frac{\Big(1 - \tilde{\psi}_+(\nu)\Big)\Big(1 - \tilde{\psi}_-(\nu)\Big)}{2\nu \langle \tau \rangle} (c_{-\sigma} - c_\sigma) + \frac{c_\sigma \langle \tau \rangle_\sigma}{2\langle \tau \rangle}, \end{aligned} \tag{C.19}$$

that yields the stationary average position

$$\langle x \rangle^{\rm st} = \frac{c_+ \langle \tau \rangle_+ + c_- \langle \tau \rangle_-}{\langle \tau \rangle_+ + \langle \tau \rangle_-}, \tag{C.20}$$

which corresponds to the weighted average of the two centers $c_+$, and $c_-$ with respect to the corresponding average waiting time $\langle \tau \rangle_+$, and $\langle \tau \rangle_-$.

### Second moment

Analogously, we derive the second moments of the probability density $G(x, \sigma, t|x_0, \sigma_0)$ by multiplying by $x^2$ and integrating over $x$ Eq. (3.19):

$$
\begin{aligned}
\langle \tilde{x}^2 \rangle_{\sigma\sigma} &= \mathcal{L}\left\{\Psi_\sigma(t)\left[\Sigma^2(t)+\mu_\sigma^2(t|x_0)\right]\right\}(s) + \int_{-\infty}^{+\infty} \mathrm{d}x\, \tilde{G}_S(x,\sigma,s|x_0,\sigma)\mathcal{L}\left\{\Psi_\sigma(t)\left[\Sigma^2(t)+\mu_\sigma^2(t|y)\right]\right\}(s) \\
&= x_0^2\,\tilde{\Psi}_\sigma(s+2\nu) + 2x_0\,c_\sigma\left[\tilde{\Psi}_\sigma(s+\nu)-\tilde{\Psi}_\sigma(s+2\nu)\right] \\
&+ c_\sigma^2\left[\tilde{\Psi}_\sigma(s)-2\tilde{\Psi}_\sigma(s+\nu)+\tilde{\Psi}_\sigma(s+2\nu)\right] + \frac{D}{\nu}\left[\tilde{\Psi}_\sigma(s)-\tilde{\Psi}_\sigma(s+2\nu)\right] \\
&+ \langle \tilde{x}^2\rangle^S_{\sigma\sigma}(s|x_0)\,\tilde{\Psi}_\sigma(s+2\nu) + 2\langle \tilde{x}\rangle^S_{\sigma\sigma}(s|x_0)\,c_\sigma\left[\tilde{\Psi}_\sigma(s+\nu)-\tilde{\Psi}_\sigma(s+2\nu)\right] \\
&+ \frac{\tilde{\psi}_+(s)\tilde{\psi}_-(s)}{1-\tilde{\psi}_+(s)\tilde{\psi}_-(s)}\left\{c_\sigma^2\left[\tilde{\Psi}_\sigma(s)-2\tilde{\Psi}_\sigma(s+\nu)+\tilde{\Psi}_\sigma(s+2\nu)\right] + \frac{D}{\nu}\left[\tilde{\Psi}_\sigma(s)-\tilde{\Psi}_\sigma(s+2\nu)\right]\right\}, \\
\langle \tilde{x}^2 \rangle_{\sigma-\sigma} &= \int_{-\infty}^{+\infty} \mathrm{d}y\, \tilde{G}_S(x,\sigma,s|x_0,-\sigma)\,\mathcal{L}\left\{\Psi_\sigma(t)\left[\Sigma^2(t)+\mu_\sigma^2(t|y)\right]\right\}(s) \\
&= \tilde{\Psi}_\sigma(s+\nu)\langle \tilde{x}^2\rangle^S_{\sigma-\sigma}(s|x_0) + 2\,c_\sigma\,\langle \tilde{x}\rangle^S_{\sigma-\sigma}(s|x_0)\left[\tilde{\Psi}_\sigma(s+\nu)-\tilde{\Psi}_\sigma(s+2\nu)\right] \\
&+ \frac{\tilde{\psi}_{-\sigma}(s)}{1-\tilde{\psi}_+(s)\tilde{\psi}_-(s)}\left\{c_\sigma^2\left[\tilde{\Psi}_\sigma(s)-2\tilde{\Psi}_\sigma(s+\nu)+\tilde{\Psi}_\sigma(s+2\nu)\right] + \frac{D}{\nu}\left[\tilde{\Psi}_\sigma(s)-\tilde{\Psi}_\sigma(s+2\nu)\right]\right\},
\end{aligned}
\tag{C.21}
$$

whose graphical representation is reported in Fig. C.2. Finally, the second moment of the position reads

$$
\langle \tilde{x}^2\rangle(s|x_0) = \sum_\sigma \langle \tilde{x}^2\rangle_\sigma(s|x_0), \quad \text{where} \quad \langle \tilde{x}^2\rangle_\sigma = \sum_{\sigma_0}\lambda_{\sigma_0}\langle \tilde{x}^2\rangle_{\sigma\sigma_0}(s|x_0), \tag{C.22}
$$

whose time evolution is displayed in the right panel of Fig. C.3.

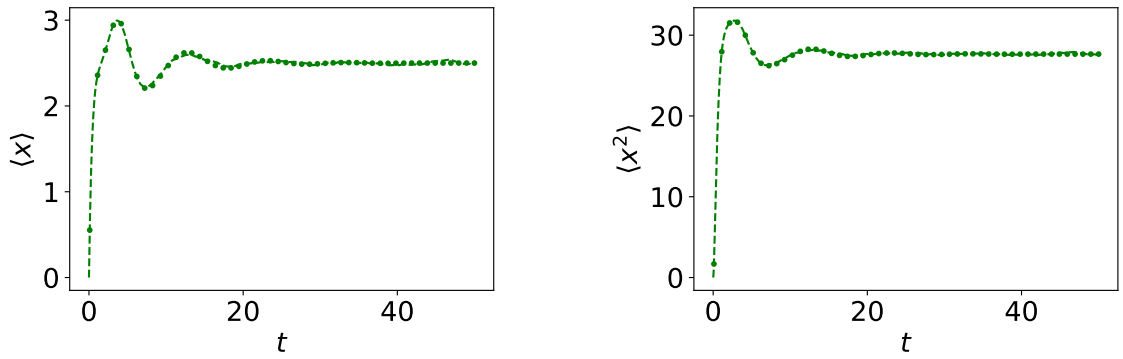
Always by direct application of the asymptotic theorem of the Laplace transform, we extract the stationary value of the second moment of the position conditioned on the final state $\sigma$, that is

$$
\begin{aligned}
\langle x^2\rangle^{\mathrm{st}}_\sigma =& \tilde{\Psi}_\sigma(2\nu)\langle x^2\rangle^S_\sigma + 2c_\sigma\left(\tilde{\Psi}_\sigma(\nu)-\tilde{\Psi}_\sigma(2\nu)\right)\langle x\rangle^S_\sigma \\
&+ \frac{1}{2\langle\tau\rangle}\left[c_\sigma^2\left(\langle\tau\rangle_\sigma - \tilde{\Psi}_\sigma(\nu)+\tilde{\Psi}_\sigma(2\nu)\right) + \frac{D}{\nu}\left(\langle\tau\rangle_\sigma - \tilde{\Psi}_\sigma(2\nu)\right)\right],
\end{aligned}
\tag{C.23}
$$

which immediately allows us to reconstruct the full second moment as $\langle x^2\rangle = \langle x^2\rangle_+ + \langle x^2\rangle_-$.

## C.3 Statistics of $c(t)$

In this Section we re-evaluate $P(\sigma,t)$ in Eq. (3.21), the probability that the process $c(t)$ takes the value $c_\sigma$ at time $t$, in a way that is more suitable to compute observables of interest. Moreover, this brief part allows the reader to get more familiar with renewal approaches. In order to access this probability distribution, it is useful to compute the conditional probability $P(\sigma_2,t_2|\sigma_1,t_1)$ of being in the state $\sigma_2$ at time $t_2$ given that the initial value $\sigma(t_1)=\sigma_1$ coincides with a switching event. It simply follows that $P(\sigma,t)=\sum_{\sigma_0}\lambda_{\sigma_0}P(\sigma,t|\sigma_0)$, where we omit the inital time whenever $t_1=0$. The computation of $P(\sigma_2,t_2|\sigma_1,t_1)$ can be tackled by means of a renewal approach. Let us start from the evaluation of $P(+,t_2|+,t_1)$, that can be expressed as




(a) (b)

Figure C.3: **Moments of $x(t)$.** The figure on the left display the time evolution of the moment $\langle x \rangle$. The figure on the left display the time evolution of the moment $\langle x^2 \rangle$ (blue). In both pictures the dashed line correspond to simulations ($N = 10^6$ samples with $\Delta t = 0.005$) and dots by inverse Laplace transform of Eq. (C.21). The parameters of the model are: $D = 1$, $c_+ = 7.5$, $c_- = -2.5$, $\nu = 2.5$, $k_+ = 10$, $\theta_+ = 0.5$, $k_- = 5$, $\theta_- = 1$, $x_0 = 0$ and $\lambda = 0.5$.

$$\begin{aligned} P(+,t_2|+,t_1) &= \Psi_+(t_2-t_1) + \int_{t_1}^{t_2} \mathrm{d}\tau\, \psi_+(\tau - t_1) P(+,t|-,\tau) \\ &= \Psi_+(t_2-t_1) + \int_0^{t_2-t_1} \mathrm{d}\tau'\, \psi_+(\tau') P(+,t-\tau'|-) \\ &= P(+,t_2-t_1|+). \end{aligned} \tag{C.24}$$

The first term $\Psi_+(t_2 - t_1)$ on the right hand side of Eq. (C.24) accounts for trajectories with no switches in the interval $(t_1, t_2)$. The second contribution is computed conditioning on the first switch at time $\tau$, after which the process starts from the state $\sigma(\tau) = -$ to reach the final state $\sigma(t) = +$. The second line in (C.24) simply follows from the change of variable $\tau' = t - \tau$, which makes apparent the time translation property $P(+, t_2|+, t_1) = P(+, t_2 - t_1|+)$. The time translation invariance property holds for all the $P(\sigma_2, t_2|\sigma_1, t_1)$, which allows us to simply consider $t_1 = 0$ in all the calculations. Similarly, the equations for the other possible configurations are given by

$$\begin{aligned} P(\sigma,t|\sigma) &= \Psi_\sigma(t) + \int_0^t \mathrm{d}\tau\, \psi_\sigma(\tau) P(\sigma,t-\tau|-\sigma), \\ P(\sigma,t|-\sigma) &= \int_0^t \mathrm{d}\tau\, \psi_\sigma(\tau) P(\sigma,t-\tau|\sigma). \end{aligned} \tag{C.25}$$

It is natural to solve Eq. (C.25) in the Laplace transform domain. By applying the LCT to Eqs. (C.25), we find a closed expression for the Laplace transform $\tilde{P}(\sigma, s| \pm \sigma)$:

$$\tilde{P}(\sigma,s|\sigma)=\frac{\tilde{\Psi}_\sigma(s)}{1-\tilde{\psi}_+(s)\tilde{\psi}_-(s)},$$
$$\tilde{P}(\sigma,s|-\sigma)=\frac{\tilde{\Psi}_\sigma(s)\tilde{\psi}_{-\sigma}(s)}{1-\tilde{\psi}_+(s)\tilde{\psi}_-(s)}, \tag{C.26}$$

where we recall Laplace transform of the cumulative waiting-time distribution $\tilde{\Psi}_\sigma(s)=(1-\tilde{\psi}_\sigma(s))/s$. Note that Eqs. (C.26) coincide exactly with Eqs. (3.20), and they satisfy the normalisation condition in the Laplace transform, e.g., $\tilde{P}(\sigma,s|\sigma_0)+\tilde{P}(-\sigma,s|\sigma_0)=1/s$ for any $\sigma_0$.

### C.3.1 General probability distribution with asymmetric waiting times

In this Section we generalize the expression of $P(\sigma,t|\sigma_0)$ by computing the probability to reach any state $\sigma_2$ at $t_2$ starting from any state $\sigma_1$ at a time $t_1$, not necessarily corresponding to an initial switching event. We denote this probability by $P_{\sigma_0}(\sigma_2,t_2|\sigma_1,t_1)$, with $\sigma_0$, $\sigma_1$, $\sigma_2\in\{-,+\}$, as the probability that the process reaches $\sigma(t_2)=\sigma_2$ from $\sigma(t_1)=\sigma_1$ given the initial condition $\sigma(0)=\sigma_0$.

**Conditional probability $P_+(+,t_2|+,t_1)$:** We start by deriving an integral equation for $P_+(+,t_2|+,t_1)$, that we can express, via renewal theory, as:

$$\begin{aligned}
P_+(+,t_2|+,t_1)=&\Psi_+(t_2)+\int_{t_1}^{t_2}\mathrm{d}\tau\,\psi_+(\tau)P(+,t_2-\tau|-)\\
&+\int_0^{t_1}\mathrm{d}\tau_1\int_{t_1}^{t_2}\mathrm{d}\tau_2\,\psi_+(\tau_2-\tau_1)P(+,t_2-\tau_2|-)P_S(+,\tau_1|+)\\
&+\int_0^{t_1}\mathrm{d}\tau_1\int_{t_2}^{\infty}\mathrm{d}\tau_2\,\psi_+(\tau_2-\tau_1)P_S(+,\tau_1|+)\\
=&\Psi_+(t_1+t)+\int_0^{t}\mathrm{d}\tau'\psi_+(t+t_1-\tau')P(+,\tau'|-)\\
&+\int_0^{t_1}\mathrm{d}\tau_1'\int_0^{t}\mathrm{d}\tau_2'\,\psi_+(t-\tau_2'+\tau_1')P(+,\tau_2'|-)P_S(+,t-\tau_1'|+)\\
&+\int_0^{t_1}\mathrm{d}\tau_1\int_0^{\infty}\mathrm{d}\tau_2'\,\psi_+(t+t_1+\tau_2'-\tau_1)P_S(+,t-\tau_1'|+).
\end{aligned} \tag{C.27}$$

The first contribution $\Psi_+(t_2)$ on the right hand side of Eq. (C.27) describes the case where $\sigma(t)=+$ for the whole time interval $(0,t_2)$, that is, no switching event occurs up to time $t_2$.The second contribution considers the case where the first switching event happens at a time $\tau\in(t_1,t_2)$, with probability $\psi_+(\tau)$; then the process reaches the state $+$ at time $t_2$ from the state $-$ at the switching time $\tau$, which comes with a probability weight $P(+,t_2-\tau|-)$. The second line corresponds to the scenario where a switch has occurred before $t_1$ and that, in the interval $(\tau_1,\tau_2)$ to which $t_1$ belongs, no switch occurs, so that the state is fixed to $+$, contributing with probability $\psi_+(\tau_2-\tau_1)$. In order to have a $+$ state in the interval $(\tau_1,\tau_2)$, being $\sigma(0)=+$, an even number of switches must take place in the interval $(0,\tau_1]$, whose probability is given by $P_S(+,\tau_1|+)$ in Eq. (3.11); finally,

the process attains the state $\sigma(t_2) = +$ from the state $\sigma(\tau_2) = -$ with probability $P(+, t_2 - \tau_2|-)$. The third line represents the case in which the last switch before $t_1$ happens at time $\tau_1$, and than no switching occurs in the interval $(\tau_1, t_2)$. The second inequality follows from the shift of the integration variables, such that it is apparent the dependence on the time $t_1$ and $t \equiv t_2 - t_1$. Indeed, our ultimate goal is to compute the stationary limit of Eq. (C.27), corresponding to $t_1 \to \infty$ and keeping $t$ fixed. In order to simplify the calculations, we compute the Laplace transform of Eq. (C.27) with respect to $t_1$, which reads

$$\begin{aligned}\tilde{P}_+(+,t|+,\eta) \equiv& \mathcal{L}_{t_1}\left\{P_+(+,t+t_1|+,t_1)\right\}(\eta) \\ =& \int_0^\infty \mathrm{d}t_1\, e^{-\eta t_1}\left[\int_{t_1+t}^\infty \mathrm{d}\tau\, \psi_+(\tau) + \int_0^t \mathrm{d}\tau\, \psi_+(t+t_1-\tau)P(+,\tau|-)\right] \\ &+ \tilde{P}_S(+,\eta|+)\int_0^t \mathrm{d}\tau\, P(+,\tau|-)\int_0^\infty \mathrm{d}y\, e^{-y\eta}\psi_+(t-\tau+y) \\ &+ \tilde{P}_S(+,\eta|+)\int_0^\infty \mathrm{d}\tau \int_0^\infty \mathrm{d}y\, e^{-y\eta}\psi_+(t+\tau+y),\end{aligned} \tag{C.28}$$

where the LCT allows us to factorize the contribution of $\tilde{P}_S(+,\eta|+)$ in the second and third line, whose expression is reported in Eq. (3.13). The convergence of $\tilde{P}_S(+,\eta|+)$ follows from the condition $|\psi(\eta)| < 1$ for $\mathrm{Re}(\eta) > 0$, while, as we will see, the final expression can be analytically extended to $\eta = 0$, consistently with the the final value theorem of the Laplace transform.

We can further simplify Eq. (C.28) by taking the Laplace transform with respect to $t$:

$$\tilde{P}_+(+,s|+,\eta) \equiv \mathcal{L}_t\left\{\tilde{P}_+(+,t|+,\eta)\right\}(s) = [1+\tilde{P}_S(+,\eta|+)]\left[\tilde{P}(+,s|-)\psi_d^+(\eta,s) + \Psi_d^+(\eta,s)\right]. \tag{C.29}$$

In the equation above, We have introduced the incremental ratios:

$$\psi_d^\sigma(\eta,s) \equiv \frac{\tilde{\psi}_\sigma(\eta) - \tilde{\psi}_\sigma(s)}{s-\eta}, \quad \Psi_d^\sigma(\eta,s) \equiv \frac{\tilde{\Psi}_\sigma(\eta) - \tilde{\Psi}_\sigma(s)}{s-\eta}, \tag{C.30}$$

corresponding to the joint Laplace transform of integrals of the type

$$f_d(\eta,s) \equiv \int_0^\infty \mathrm{d}\tau_1\, e^{-\eta\tau_1}\int_0^\infty \mathrm{d}\tau_2\, e^{-s\tau_2}\, f(\tau_1+\tau_2) = \frac{\tilde{f}(\eta) - \tilde{f}(s)}{s-\eta}, \tag{C.31}$$

where $f$ is any function for which its Laplace transform $\tilde{f}$ is well defined.

In order to compute the stationary limit of Eq. (C.29), we assume that $\psi(t)$ displays finite first moment $\langle\tau\rangle \equiv \int_0^\infty \mathrm{d}\tau\, \tau\psi(\tau)$. Hence, we can expand its Laplace transform $\tilde{\psi}_\sigma(\eta)$ around $\eta = 0$ as $\tilde{\psi}_\sigma(\eta) = 1 - \eta\langle\tau\rangle_\sigma + o(\eta)$. Accordingly, Eq. (C.29) allows us to compute the stationary limit $\tilde{P}_{\mathrm{st}}(+,s|+)$ of the distribution by means of the the final value theorem of the Laplace transform, that is

$$\tilde{P}_{\mathrm{st}}(+,s|+) = \lim_{\eta\to 0}\eta\tilde{P}_+(+,s|+,\eta) = \frac{1}{2\langle\tau\rangle}\left(\frac{\langle\tau\rangle_+}{s} - \frac{\tilde{\Psi}_+(s)\tilde{\Psi}_-(s)}{1-\tilde{\psi}_+(s)\tilde{\psi}_-(s)}\right), \tag{C.32}$$

that follows from the expressions

$$\lim_{\eta\to 0}\eta\left[1+\tilde{P}_S(+,s|+)\right]=\frac{1}{2\langle\tau\rangle}\quad\text{and}\quad\lim_{\eta\to 0}\tilde{\Psi}_\sigma(\eta)=\langle\tau\rangle_\sigma, \tag{C.33}$$

with $\langle\tau\rangle=(\langle\tau\rangle_+ + \langle\tau\rangle_-)/2$.

It can be easily checked that $P_-(-,t_2|-,t_1)$ satisfies the same equation (C.27) for $P_+(+,t_2|+,t_1)$ where all the + states are replaced by − ones and vice-versa. This reasoning generalises to all the configurations.

**Conditional probability $P_+(+,t_2|-,t_1)$:** Following the same steps as above, we can express the conditional probability $P_+(+,t_2|-,t_1)$ as

$$\begin{aligned}P_+(+,t_2|-,t_1)&=\int_0^{t_1}\mathrm{d}\tau_1\int_{t_1}^{t_2}\mathrm{d}\tau_2\,\psi_-(\tau_2-\tau_1)P(+,t_2-\tau_2|+)P_S(-,\tau_1|+)\\&=\int_0^{t_1}\mathrm{d}\tau_1'\int_0^{t}\mathrm{d}\tau_2'\,\psi_-(t-\tau_2'+\tau_1')P(+,\tau_2'|+)P_S(-,t_1-\tau_1'|+),\end{aligned} \tag{C.34}$$

where the right hand side of the equation accounts for trajectories that: have an odd number of switches in the interval $(0,\tau_1]$ before $t_1$, weighted by $P_S(-,\tau_1|+)$, have no switching in the interval $(\tau_1,\tau_2)$, with $\tau_2\in(t_1,t_2)$, with probability $\psi_-(\tau_2-\tau_1)$, and finally reach the state $\sigma(t_2)=+$ from $\sigma(\tau_2)=+$ according to $P(+,t_2-\tau_2|+)$. The second line of the equation follows from the change of variables $\tau_2'=t_2-\tau_2$, $\tau_1'=t_1-\tau_1$ and $t=t_2-t_1$, and allows us the immediate application of the LCT. The Laplace transform of Eq. (C.34) with respect to $t_1$, denoted by the $\eta$ dependence, is given by

$$\tilde{P}_+(+,t_2|-,\eta)\equiv\mathcal{L}_{t_1}\left\{P_+(+,t_2|-,t_1)\right\}(\eta)=\tilde{P}_S(-,\eta|+)\int_0^t\mathrm{d}\tau\,P(+,\tau|+)\int_0^\infty\mathrm{d}y\,e^{-\eta y}\psi_-(t-\tau+y), \tag{C.35}$$

where the Laplace of $P_S(-,t|+)$ is given by Eq. (3.13). Similarly to what done previously, we compute the Laplace transform $\tilde{P}_+(+,s|-,\eta)$ also with respect to $t$, that is

$$\tilde{P}_+(+,s|-,\eta)\equiv\mathcal{L}_t\left\{\tilde{P}_+(+,t|-,\eta)\right\}(s)=\tilde{P}_S(-,\eta|+)\tilde{P}(+,s|+)\psi_d^-(\eta,s). \tag{C.36}$$

The Laplace transform of stationary state probability $\tilde{P}(+,s|-)$ can be immediately computed from Eq. (C.36) by applying the the final value theorem of the Laplace transform,

$$\tilde{P}_{\mathrm{st}}(+,s|-)=\lim_{\eta\to 0}\eta\tilde{P}_+(+,s|-,\eta)=\frac{\tilde{P}(+,s|+)}{2\langle\tau\rangle}\tilde{\Psi}_-(s)=\frac{1}{2\langle\tau\rangle}\frac{\tilde{\Psi}_-(s)\tilde{\Psi}_+(s)}{1-\tilde{\psi}_-(s)\tilde{\psi}_+(s)}. \tag{C.37}$$

**Conditional probability $P_+(-,t_2|+,t_1)$:** The conditional probability $P_+(-,t_2|+,t_1)$ can be cast as the sum of two contributions:

$$\begin{aligned} P_+(-,t_2|+,t_1) &= \int_{t_1}^{t_2} \mathrm{d}\tau\, \psi_+(\tau) P(-,t_2-\tau|-) \\ &\quad + \int_0^{t_1} \mathrm{d}\tau_1 \int_{t_1}^{t_2} \mathrm{d}\tau_2\, \psi_+(\tau_2-\tau_1) P(-,t_2-\tau_2|-) P_S(+,\tau_1|+) \\ &= \int_0^{t} \mathrm{d}\tau'\, \psi_+(t+t_1-\tau') P(-,\tau'|-) \\ &\quad + \int_0^{t_1} \mathrm{d}\tau_1' \int_0^{t} \mathrm{d}\tau_2'\, \psi_+(t-\tau_2'+\tau_1') P(-,\tau_2'|-) P_S(+,t_1-\tau_1'|+) \end{aligned} \tag{C.38}$$

The first contribution comes from trajectories associated with a first switching at $\tau \in (t_1,t_2)$; the second, to trajectories that show up any even number of switches before $t_1$. The second equality comes from a simple change of variables. Following the same steps of previous Sections, we can express the Laplace transform of $P_+(-,t_2|+,t_1)$ with respect to $t_1$ and $t$, denoted by $\tilde{P}_+(-,s|+,\eta)$, as

$$\tilde{P}_+(-,s|+,\eta) = \left[1+\tilde{P}_S(+,\eta|+)\right] \tilde{P}(-,s|-)\psi_d^+(\eta,s). \tag{C.39}$$

The stationary limit of (C.38) gives the stationary probability $P_{\mathrm{st}}(-,t|+)$, whose Laplace transform is computed to be

$$\tilde{P}_{\mathrm{st}}(-,s|+) = \lim_{\eta\to 0} \eta \tilde{P}_+(-,s|+,\eta) = \frac{\tilde{P}(-,s|-)}{2\langle\tau\rangle}\tilde{\Psi}_+(s) = \frac{1}{2\langle\tau\rangle}\frac{\tilde{\Psi}_-(s)\tilde{\Psi}_+(s)}{1-\tilde{\psi}_-(s)\tilde{\psi}_+(s)}. \tag{C.40}$$

**Conditional probability $P_+(-,t_2|-,t_1)$** The conditional probability $P_+(-,t_2|-,t_1)$ also comes with two contributions:

$$\begin{aligned} P_+(-,t_2|-,t_1) &= \int_0^{t_1} \mathrm{d}\tau_1 \int_{t_1}^{t_2} \mathrm{d}\tau_2\, \psi_-(\tau_2-\tau_1) P(-,t_2-\tau_2|+) P_S(-,\tau_1|+) \\ &\quad + \int_0^{t_1} \mathrm{d}\tau_1 \int_{t_2}^{\infty} \mathrm{d}\tau_2\, \psi_-(\tau_2-\tau_1) P_S(-,\tau_1|+). \end{aligned} \tag{C.41}$$

The integrals account for trajectories with an odd number of switches before $t_1$ and at least one in $(t_1,t_2)$, first line, or none, second line. In this case we have

$$\tilde{P}_+(-,s|-,\eta) = \tilde{P}_S(-,\eta|+)\left(\tilde{P}(-,s|+)\psi_d(\eta,s) + \Psi_d^-(\eta,s)\right), \tag{C.42}$$

whose stationary limit is given by

$$\tilde{P}_{\mathrm{st}}(-,s|-) = \lim_{\eta\to 0} \eta \tilde{P}_+(-,s|-,\eta) = \frac{1}{2\langle\tau\rangle}\left(\frac{\langle\tau\rangle_-}{s} - \frac{\tilde{\Psi}_+(s)\tilde{\Psi}_-(s)}{1-\tilde{\psi}_+(s)\tilde{\psi}_-(s)}\right). \tag{C.43}$$

Finally, we check the Laplace transform normalization condition of $\tilde{P}_{\sigma_0}(\sigma_2, s|\sigma_1, \eta)$, which is equal

$$\sum_{\sigma_2,\sigma_1\in\{\pm\}} \tilde{P}_{\sigma_0}(\sigma_2, s|\sigma_1, \eta) = \frac{1}{s\eta}. \tag{C.44}$$

## C.4 Simulation-based inference

To fit values of the model parameters to experimental observations we employ a Simulation-Based Inference (SBI) toolkit implemented by [213]. Within the Bayesian framework, we define a uniform prior for the values of the parameters $\nu \in [0.1, 10]$ kHz, $D \in [0.5, 50]$ nm$^2$/ms, $c_0 \in [1.0, 50]$ nm, $k \in [1.0, 100]$, and the characteristic frequency $f_0 \in [10, 1000]$ kHz ($f_0 = 2k\theta$). The SBI toolkit simulates time-series of $x(t)$ for a large sample of parameter values and thereby extracts a sample of summary statistics $\boldsymbol{\chi}[x(t)]$. These summary statistics are then used to learn the posterior distribution $p(\nu, D, c_0, k, f_0|\boldsymbol{\chi})$ using the Sequential Neural Posterior Estimator [213].

After demeaning the experimental time series, the following quantities were used as the summary statistics:

1. The standard deviation $\sigma_x$ of $x(t)$;
2. The averages $\langle \phi_i(x/\sigma_x)/\sqrt{\sigma_x} \rangle$ of Hermite functions $\phi_i(x)$, defined below, for $i = 0, 2, 4$;
3. The average, the standard deviation, and the mode of the normalized power-spectrum of $x(t)$;
4. The Hermite-function modes $a_i$ of the autocorrelation function $\langle x(0)x(t) \rangle = \sum_i a_i \sqrt{f_i} \phi_i \left(\bar{f}t\right)$, in which $\bar{f}$ is the average of the normalized power-spectrum of $x(t)$, for $i = 0, 2, 4...12$.

Because the probability density and the autocorrelation function of our model are even in their arguments, in the above list we employed a subset of orthonormalized even Hermite functions

$$\phi_i(z) = \mathrm{e}^{-\frac{z^2}{2}} H_i(z) \left(2^i i! \sqrt{\pi}\right)^{-1/2},$$

in which $H_i$ is an $i^{\text{th}}$ Hermite polynomial.

Three inference rounds of $30 \times 10^3$ simulations were performed to learn the posterior distribution from summary statistics. We considered only 10-s-long time series sampled with a time step of 0.1 ms. By fixing the summary statistics to experimental observations, the posterior distribution was then sampled to obtain the model parameter values and their uncertainties. We applied this procedure to three experimental time series, in which we found symmetric oscillations of the hair-bundle tip (Figs. 3.9–3.11).

# Appendix D

# Calculations of Chapter 4

## D.1 Gaussian integral

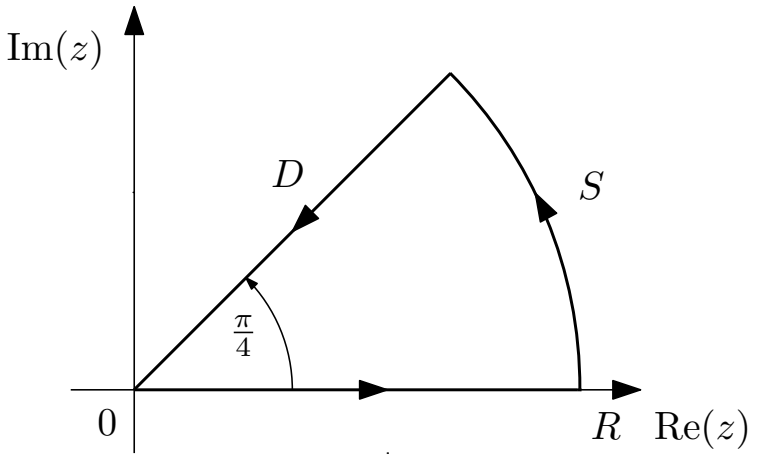



Figure D.1: Integration contour $C$ of Eq. (D.1): it consists of a circular section of angle $\pi/4$ and radius $R$, including the arc $S$ and the segment $D$, in addition to the segment $[0, R]$ on the real line.

In this Section, we derive Eq. (4.4), which is fundamental for the construction of the stochastic description of the quartic potential. First, we evaluate the integral

$$\oint_C \mathrm{d}z\, e^{iaz^2}, \tag{D.1}$$

where $a > 0$ and the contour $C$ is displayed in Fig. D.1. Because of the absence of singularities inside the contour $C$, the residue theorem immediately implies

$$\oint_C \mathrm{d}z\, e^{iaz^2} = 0, \tag{D.2}$$

which results from the sum of the following contributions:

$$\oint_C \mathrm{d}z\, e^{iaz^2} = \int_0^R \mathrm{d}x\, e^{iax^2} + \int_S \mathrm{d}z\, e^{iaz^2} + \int_D \mathrm{d}z\, e^{iaz^2} = 0, \tag{D.3}$$

where $S$ represents the circular arc of radius $R$, parametrized as $z = R\, e^{i\phi}$ with $\phi \in (0, \pi/4)$, and $D$ the radial contribution corresponding to $z = r\, e^{i\frac{\pi}{4}}$ with $r \in (0, R)$, in the direction shown in the picture. Finally, we are interested in the limit $R \to \infty$. The integral along $D$ can be expressed as

$$\int_D \mathrm{d}z\, e^{iaz^2} = e^{i\frac{\pi}{4}} \int_R^0 \mathrm{d}r\, \exp\left\{ia\left(r\, e^{i\frac{\pi}{4}}\right)^2\right\} = -\, e^{i\frac{\pi}{4}} \int_0^R \mathrm{d}r\, e^{-ar^2}, \tag{D.4}$$

coming from the change of variables $z = r\, e^{i\pi/4}$. Similarly, the integral along $S$ is given by

$$\int_S \mathrm{d}z\, e^{iaz^2} = iR \int_0^{\frac{\pi}{4}} \mathrm{d}\phi\, \exp\left\{iaR^2\left[\cos(2\phi) + i\sin(2\phi)\right]\right\}, \tag{D.5}$$

and it can be shown to vanish in the limit $R \to \infty$. In fact, we start from the inequality

$$\left| \int_S \mathrm{d}z\, e^{iaz^2} \right| \leq R \int_0^{\frac{\pi}{4}} \mathrm{d}\phi\, e^{-aR^2 \sin(2\phi)} = \frac{R}{2} \int_0^{\frac{\pi}{2}} \mathrm{d}\theta\, e^{-aR^2 \sin\theta}, \tag{D.6}$$

where last equality follows from introducing $\theta \equiv 2\phi$. Moreover, for $\theta \in (0, \pi/2)$, we have that $2\theta/\pi \leq \sin\theta \leq \theta$, yielding

$$\left| \int_S \mathrm{d}z\, e^{iaz^2} \right| \leq \frac{R}{2} \int_0^{\frac{\pi}{2}} \mathrm{d}\theta\, e^{-aR^2 \sin\theta} \leq \frac{R}{2} \int_0^{\frac{\pi}{2}} \mathrm{d}\theta\, e^{-\frac{2aR^2\theta}{\pi}} = \frac{\pi}{4aR}\left(1 - e^{-aR^2}\right), \tag{D.7}$$

which vanishes for $R \to \infty$. Finally, we get

$$\int_0^\infty \mathrm{d}x\, e^{iax^2} = e^{i\frac{\pi}{4}} \int_0^\infty \mathrm{d}r\, e^{-ar^2} = e^{i\frac{\pi}{4}} \sqrt{\frac{\pi}{4a}} = \sqrt{\frac{i\pi}{4a}}, \tag{D.8}$$

where we have fixed $\sqrt{i} = e^{i\frac{\pi}{4}}$. This last result can be generalised to

$$\int_{-\infty}^{+\infty} \mathrm{d}x\, e^{i(ax^2+bx)} = \sqrt{\frac{i\pi}{a}} e^{-ib^2/(4a)}. \tag{D.9}$$

## D.2 Time-dependent quartic Hamiltonian

In the framework discussed in Section 4.2, it is natural to generalise the expression of Eq. (4.14) to the case of the time-dependent Hamiltonian

$$\hat{H}(t) = \frac{\hat{p}^2}{2m} + \frac{1}{2} m\omega^2(t)\hat{x}^2 + \frac{\lambda(t)}{4}\hat{x}^4, \tag{D.10}$$

with a non-negative quartic coupling, $\lambda(t) \geq 0$. The procedure follows the same steps as in the time independent case, i.e.,

(i) we perform a Trotter-Suzuki splitting of the time evolution operator, yielding

$$\hat{U}(t) = \lim_{n\to\infty} \left\{ \exp\left[-\frac{i\tau_n}{\hbar}\frac{\hat{p}^2}{2m}\right] \exp\left[-\frac{i\tau_n}{\hbar}\left(\frac{m}{2}\omega_n^2\hat{x}^2 + \frac{\lambda_n}{4}\hat{x}^4\right)\right]\right\}^n, \tag{D.11}$$

with $\omega_n^2 \equiv \omega^2(n\tau_n)$ and $\lambda_n \equiv \lambda(n\tau_n)$;

(ii) this is followed by the Hubbard-Stratonovich transformation, performed through an integral of the type

$$\exp\left(-i\frac{\tau_n}{\hbar}\frac{\lambda_n}{4}\hat{x}^4\right) = \sqrt{\frac{\tau_n}{i\hbar\pi}}\int_{-\infty}^{\infty} \mathrm{d}\phi\, \exp\left[\frac{i\tau_n}{\hbar}\left(\phi^2 - \sqrt{\lambda_n}\,\hat{x}^2\,\phi\right)\right]; \tag{D.12}$$

(iii) Finally, combining all previous steps, we retrieve Eq. (4.14) with $\Omega^2(t) \equiv \omega^2(t) + 2\sqrt{\lambda(t)}\,\phi(t)/m$ and $S_0[\phi] = \hbar^{-1}\int_0^t \mathrm{d}\tau\, \phi^2(\tau)$.

Once again, this makes it possible to study the dynamics of a quantum problem by studying a set of classical differential equations.

## D.3 Action of $\exp(w\,\hat{S}^{\pm,z})$ on a Gaussian wave packet

We now investigate the action of the operators appearing in Eq. (4.12), i.e.,

$$\hat{U}^\alpha \equiv \exp(w\,\hat{S}^\alpha) \tag{D.13}$$

with complex $w$ and $\alpha \in \{+,-,z\}$, on the Gaussian wave packet $|\psi\rangle$, reported in Eq. (4.16). For a general complex-valued $w$, the exponential operators are not unitary and do not conserve the normalization of the state. For simplicity, we consider here values of $w$ for which the corresponding $\hat{U}^\alpha$ conserves the state normalization.

Note that the $\hat{S}^\alpha$ operators in Eqs. (4.9) are, at most, of quadratic order with respect to the operators $\hat{x}$ and $\hat{p}$. In what follows, we assume $\hbar = 1$ and a real-valued $w$.

In order to analyse the action of $\hat{U}^\alpha$ in Eq. (D.13), we introduce the Wigner function $W(x,p)$ for the generic state $|\phi\rangle$:

$$W(x,p) \equiv \frac{1}{\pi}\int \mathrm{d}y\, e^{-i2py}\langle x+y|\phi\rangle\langle\phi|x-y\rangle. \tag{D.14}$$

$W(x,p)$ provides a phase space description of the state, and allows us to compute expectation values of operators of the type $O(\hat{x},\hat{p})$ as $\int \mathrm{d}x \int \mathrm{d}p\, O(x,p)\, W(x,p)$ [37, 122, 202].

We start by evaluating the Wigner function for the Gaussian wave packet $|\psi\rangle$ in Eq. (4.16)

$$W(x,p) = \frac{1}{\pi}\exp\left[-\frac{(x-a)^2}{\sigma^2} - \sigma^2(p-k)^2\right], \tag{D.15}$$

obtained by substitution of Eq. (4.16) into (D.14) and integrating with respect to $y$.

To begin with, we consider the action of the operator $\hat{U}^+ = \exp(iw\hat{S}^+)$ on $|\psi\rangle$, that we denote as $|\psi_+\rangle \equiv U^+|\psi\rangle$. The state $|\psi_+\rangle$ is simply given by

$$|\psi_+\rangle = \int \frac{\mathrm{d}x}{\sqrt[4]{\pi\sigma^2}} \exp\left[-\frac{(x-a)^2}{2\sigma^2} + iw\frac{x^2}{2} + ik(x-a)\right]|x\rangle\,, \tag{D.16}$$

which follows from the fact that $\hat{S}^+$ acts trivially on its eigenstate $|x\rangle$.

By substituting Eq. (D.16) into (D.14) we get the Wigner function for $|\psi_+\rangle$:

$$W_+(x,p) = \frac{1}{\pi}\exp\left[-\frac{(x-a)^2}{\sigma^2} - \sigma^2(p-k-wx)^2\right], \tag{D.17}$$

which is equal to $W$ up to an $x-$dependent shift in the momentum. Accordingly, the expectation value of operators of the form $O(\hat{x})$ is unaffected by the $\hat{U}^+$ transformation, i.e., $\langle\psi|\,O(\hat{x})\,|\psi\rangle = \langle\psi_+|\,O(\hat{x})\,|\psi_+\rangle$. On the other hand, the expectation value of a momentum-dependent operator $O(\hat{p})$ can be expressed as

$$\begin{aligned}
\langle\psi_+|\,O(\hat{p})\,|\psi_+\rangle &= \int \mathrm{d}x \int \mathrm{d}p\, O(p)\, W_+(x,p) \\
&= \sqrt{\frac{\sigma^2}{\pi(1+\sigma^4w^2)}} \int \mathrm{d}p\, O(p) \exp\left[-\sigma^2\frac{(p-k-wa)^2}{1+\sigma^4w^2}\right] \\
&= \sqrt{\frac{\sigma^2}{\pi}} \int \mathrm{d}q\, O\left(\sqrt{1+\sigma^4w^2}\,(q-k) + wa + k\right) e^{-\sigma^2(q-k)^2} \\
&= \langle\psi|\,O\left(\sqrt{1+\sigma^4w^2}\,(\hat{p}-k) + wa + k\right)|\psi\rangle\,,
\end{aligned} \tag{D.18}$$

where the second line comes from direct substitution of Eq. (D.17) and the final result from the change of variable $p - wa - k = (q-k)\sqrt{1+\sigma^4w^2}$. Equation (D.18) tells us that expectation values with respect to the state $|\psi_+\rangle$ of operators depending only on $p$ is equivalent to the expectation value with respect to the Gaussian wave packet $|\psi\rangle$ with the rescaled and shifted momentum operator $\sqrt{1+\sigma^4w^2}\,(\hat{p}-k)+wa+k$. In particular, for the mean and the variance of the momentum operator we can immediately read off from Eq. (D.18) that

$$\begin{aligned}
&\langle p\rangle \equiv \langle\psi_+|\,\hat{p}\,|\psi_+\rangle = k + wa, \\
&\langle p^2\rangle_c \equiv \langle\psi_+|\,\hat{p}^2\,|\psi_+\rangle - \langle\psi_+|\,\hat{p}\,|\psi_+\rangle^2 = \frac{1+\sigma^4w^2}{2\sigma^2}.
\end{aligned} \tag{D.19}$$

These parameter, together with the unaltered cumulants of the position operator, allow us to fully characterize the state $|\psi_+\rangle$. As an explicit time-dependent example, we consider the evolution of the wave packet under the action of the harmonic oscillator Hamiltonian; referring to Eqs. (4.23), we find that

$$\begin{aligned}
&w(t) = -m\omega\tan(\omega t), \\
&\langle p(t)\rangle = k - am\omega\tan(\omega t), \\
&\langle p^2(t)\rangle_c = \frac{1+(m\omega\sigma^2)^2\tan^2(\omega t)}{2\sigma^2}.
\end{aligned} \tag{D.20}$$

Next, we consider the case of the operator $\hat{U}^z = \exp\left(iw\{\hat{x},\hat{p}\}/4\right)$ whose action on the Gaussian wave packet $|\psi\rangle$, which we denote by $|\psi_z\rangle \equiv \hat{U}^z\,|\psi\rangle$, reads

$$|\psi_z\rangle = \int \frac{\mathrm{d}x}{\sqrt[4]{\pi\sigma^2}} \exp\left[\frac{w}{4} - \frac{(x\,e^{w/2}-a)^2}{2\sigma^2} + ik(x\,e^{w/2}-a)\right]|x\rangle\,. \tag{D.21}$$

This is computed considering the direct action of $\hat{S}^z$ on $|x\rangle$ according the property of the dilation operator $e^{by\frac{d}{dy}}f(y) = f(e^b y)$, where $f$ is any sufficiently smooth function, similarly to what has been done for Eq. (D.32). The Wigner function $W_z(x,p)$ of the state $|\psi_z\rangle$ can be directly evaluated as

$$W_z(x,p) = \frac{1}{\pi}\exp\left[-\frac{(x\,e^{w/2}-a)^2}{\sigma^2} - \sigma^2(p\,e^{-w/2}-k)^2\right]. \tag{D.22}$$

Equation (D.21) shows that the action of $\hat{U}^z$ consists in a uniform rescaling all the $x$ variables by a factor $e^{w/2}$.

As for $|\psi_z\rangle$, the Wigner function $W_z$ is equivalent to $W$ up to a rescaling of the variables. It follows that the expectation value of an operator $O(\hat{x})$, depending only on $x$, is given by

$$\begin{aligned}\langle\psi_z|\,O(\hat{x})\,|\psi_z\rangle &= \int \mathrm{d}x \int \mathrm{d}p\, O(x) W_z(x,p) \\ &= \frac{e^{w/2}}{\sqrt{\pi\sigma^2}}\int \mathrm{d}x\, O(x)\exp\left[-\frac{(x\,e^{w/2}-a)^2}{\sigma^2}\right] \\ &= \langle\psi|\,O(\hat{x}\,e^{-w/2})\,|\psi\rangle\,,\end{aligned} \tag{D.23}$$

and, analogously, for a $p-$dependent operator $O(\hat{p})$, we get

$$\langle\psi_z|\,O(\hat{p})\,|\psi_z\rangle = \langle\psi|\,O(\hat{p}\,e^{\frac{w}{2}})\,|\psi\rangle\,, \tag{D.24}$$

which reflects the rescaling action of $\hat{U}^z$. It follows that the first connected moments of $\hat{x}$ and $\hat{p}$ on $|\psi_z\rangle$ are given by

$$\begin{aligned}&\langle x\rangle \equiv \langle\psi_z|\,\hat{x}\,|\psi_z\rangle = a\,e^{-w/2}, \\ &\langle x^2\rangle_c \equiv \langle\psi_z|\,\hat{x}^2\,|\psi_z\rangle - \langle\psi_z|\,\hat{x}\,|\psi_z\rangle^2 = \frac{\sigma^2}{2}\,e^{-w}, \\ &\langle p\rangle \equiv \langle\psi_z|\,\hat{p}\,|\psi_z\rangle = k\,e^{w/2}, \\ &\langle p^2\rangle_c \equiv \langle\psi_z|\,\hat{p}^2\,|\psi_z\rangle - \langle\psi_z|\,\hat{p}\,|\psi_z\rangle^2 = \frac{e^w}{2\sigma^2}.\end{aligned} \tag{D.25}$$

These quantities fully characterize the state $|\psi_z\rangle$. According to Eqs. (4.23), for a $|\psi\rangle$ evolving under the effect of an harmonic oscillator Hamiltonian, we have

$$\begin{aligned}&w(t) = -\log\cos^2(\omega t), \\ &\langle x(t)\rangle = a\cos(\omega t), \quad \langle p(t)\rangle = \frac{k}{\cos(\omega t)}, \\ &\langle x^2(t)\rangle_c = \frac{\sigma^2}{2}\,\cos^2(\omega t), \quad \langle p^2(t)\rangle_c = \frac{1}{2\sigma^2\cos^2(\omega t)}.\end{aligned} \tag{D.26}$$

Finally, we consider the action of the operator $\hat{U}^- = \exp\left(iw\hat{p}^2/2\right)$ on the wave packet $|\psi\rangle$; the resulting state $|\psi_-\rangle \equiv \hat{U}^- |\psi\rangle$ is found to be

$$|\psi_-\rangle = \sqrt{\frac{\sigma^2}{\sigma^2 - iw}} \int \frac{\mathrm{d}x}{(\pi\sigma^2)^{1/4}} \exp\left[-\frac{(x-a-ik\sigma^2)^2}{2(\sigma^2-iw)} - \frac{\sigma^2 k^2}{2}\right] |x\rangle \,. \tag{D.27}$$

The associated Wigner function $W_-(x,p)$ reads

$$W_-(x,p) = \frac{1}{\pi} \exp\left[-\sigma^2(p-k)^2 - \frac{(x-a+pw)^2}{\sigma^2}\right], \tag{D.28}$$

that is equivalent to $W$ up to a $p-$dependent rescaling of the $x$ variable. In this case expectation values of $p-$dependent operators are invariant under the action of $\hat{U}^-$, i.e., $\langle\psi_-| O(\hat{p}) |\psi_-\rangle = \langle\psi| O(\hat{p}) |\psi\rangle$, while the expectation value of an $x-$dependent operator $O(\hat{x})$ transforms as

$$\begin{aligned}
\langle\psi_-| O(\hat{x}) |\psi_-\rangle &= \int \mathrm{d}x \int \mathrm{d}p\, O(x)\, W_-(x,p) \\
&= \sqrt{\frac{\sigma^2}{\pi(\sigma^4+w^2)}} \int \mathrm{d}x\, O(x) \exp\left[-\sigma^2 \frac{(x-a+wk)^2}{\sigma^4+w^2}\right] \\
&= \frac{1}{\sqrt{\sigma^2\pi}} \int \mathrm{d}y\, O\left(\frac{y-a}{\sigma^2}\sqrt{\sigma^4+w^2} + a - wk\right) e^{-\frac{(y-a)^2}{\sigma^2}} \\
&= \langle\psi| O\left(\frac{\hat{x}-a}{\sigma^2}\sqrt{\sigma^4+w^2} + a - wk\right) |\psi\rangle \,,
\end{aligned} \tag{D.29}$$

where the second line is found by integrating $W_-(x,p)$ in Eq. (D.28) with respect to $p$, and the last two lines are obtained by performing the change of variable $x = (y-a)\sigma^{-2}\sqrt{\sigma^4+w^2} + a - wk$. We deduce that, in case of $x-$dependent operators, the expectation value with respect to $|\psi_-\rangle$ is equivalent to the expectation value with respect to $|\psi\rangle$ where the position operator has been rescaled and shifted according to the final line of Eq. (D.29). In particular, the first two cumulants of the position operator $\hat{x}$ read

$$\begin{aligned}
&\langle x\rangle \equiv \langle\psi_-| \hat{x} |\psi_-\rangle = a - wk, \\
&\langle x^2\rangle_c \equiv \langle\psi_-| \hat{x} |\psi_-\rangle - \langle\psi_-| \hat{x}^2 |\psi_-\rangle^2 = \frac{\sigma^4+w^2}{2\sigma^2}.
\end{aligned} \tag{D.30}$$

The evolution of the state $|\psi_-\rangle$ under the harmonic oscillator dynamics can be explicitly determined from Eq. (4.23):

$$\begin{aligned}
&w(t) = -\frac{\tan(\omega t)}{m\omega}, \\
&\langle x(t)\rangle = a + k\frac{\tan(\omega t)}{m\omega}, \\
&\langle x^2(t)\rangle_c = \frac{(m\omega\sigma^2)^2 + \tan^2(\omega t)}{2(m\omega\sigma)^2}.
\end{aligned} \tag{D.31}$$

As a last remark, we note that by combining the results in Eqs. (D.20), (D.26), and (D.31) into the factorised expression for the time evolution of the harmonic oscillator, Eq. (4.12), we can construct the time evolution of observable, e.g., the position and momentum moments in Eqs. (4.24).

### D.4 Time evolution of a Gaussian wave packet

Here we report the detailed calculations of the expectation values of the moments of the position and momentum operators on the Gaussian wave packet in Eq. (4.16). As a preliminary step to the calculation of Eq. (4.17), we consider the action of the operator $\hat{U}(t)$ on an eigenstate $|x\rangle$ of the position operator, given by

$$
\begin{aligned}
\hat{U}(t)\,|x\rangle &= \left\langle \int \frac{\mathrm{d}p}{\sqrt{2\pi}}\; e^{\xi^+(t)\frac{\hat{x}^2}{2}}\, e^{i\xi^z(t)\frac{\{\hat{x},\hat{p}\}}{4}}\, e^{\xi^-(t)\frac{p^2}{2}-ipx}\,|p\rangle \right\rangle_\phi \\
&= \left\langle e^{-\frac{\xi^z}{4}} \int \frac{\mathrm{d}p}{\sqrt{2\pi}}\; e^{\frac{\xi^+(t)}{2}\hat{x}^2}\, e^{-\frac{\xi^z(t)}{2}p\frac{\partial}{\partial p}}\, e^{\xi^-(t)\frac{p^2}{2}-ipx}\,|p\rangle \right\rangle_\phi \\
&= \left\langle e^{-\frac{\xi^z}{4}} \int \frac{\mathrm{d}p}{\sqrt{2\pi}}\; e^{\frac{\xi^+(t)}{2}\hat{x}^2}\, \exp\left[\xi^-(t)\frac{p^2}{2}e^{-\xi^z} - ipxe^{-\frac{\xi^z}{2}}\right]|p\rangle \right\rangle_\phi \\
&= \left\langle e^{-\frac{\xi^z}{4}} \int \frac{\mathrm{d}p}{\sqrt{2\pi}} \int \mathrm{d}y\; e^{\frac{\xi^+(t)}{2}y^2}\,|y\rangle\langle y|\exp\left[\xi^-(t)\frac{p^2}{2}e^{-\xi^z} - ipxe^{-\frac{\xi^z}{2}}\right]|p\rangle \right\rangle_\phi \\
&= \left\langle e^{-\frac{\xi^z}{4}} \int \frac{\mathrm{d}y}{\sqrt{2\pi}}\, e^{\frac{\xi^+(t)}{2}y^2} \int \frac{\mathrm{d}p}{\sqrt{2\pi}}\, \exp\left[\xi^-(t)\frac{p^2}{2}e^{-\xi^z} - ipxe^{-\frac{\xi^z}{2}} + ipy\right]|y\rangle \right\rangle_\phi \\
&= \left\langle \frac{e^{\frac{\xi^z}{4}+\frac{x^2}{2\xi^-}}}{\sqrt{-2\pi\xi^-}} \int \mathrm{d}y\; \exp\left[\frac{y^2}{2}\left(\frac{e^{\xi^z}}{\xi^-}+\xi^+(t)\right) - y\frac{xe^{\frac{\xi^z}{2}}}{\xi^-}\right]|y\rangle \right\rangle_\phi
\end{aligned}
\tag{D.32}
$$

where $\langle\dots\rangle_\phi$ denotes the expectation value with respect to the Gaussian action $S_0$.

In the first line a completeness relation for the momentum basis, $\int dp\,|p\rangle\langle p| = \mathbb{I}$, was inserted between the last exponential operator and the position eigenket, leading to the appearance of the plane wave $\langle p|x\rangle = e^{-ipx}/\sqrt{2\pi}$, where $\hbar = 1$. In the second line, we substituted $\hat{x}\,|p\rangle = i\frac{\partial}{\partial p}\,|p\rangle$ and the consequent action of the dilation operator was written explicitly, i.e., $e^{by\frac{d}{dy}}f(y) = f(e^b y)$. Finally, a further position completeness relation insertion and a Gaussian integration was performed. The convergence of the Gaussian integral is ensured by the fact that the argument of the exponential is purely imaginary. Analogously, the corresponding dual vector evolves according to

$$
\langle x|\,U^\dagger(t) = \left\langle \frac{e^{\frac{\bar{\xi}^z}{4}+\frac{x^2}{2\bar{\xi}^-}}}{\sqrt{-2\pi\bar{\xi}^-}} \int \mathrm{d}z\; \exp\left[\frac{z^2}{2}\left(\frac{e^{\bar{\xi}^z}}{\bar{\xi}^-}+\bar{\xi}^+(t)\right) - z\frac{xe^{\frac{\bar{\xi}^z}{2}}}{\bar{\xi}^-}\right]\langle z|\right\rangle_{\bar{\phi}}, \tag{D.33}
$$

with $\langle\dots\rangle_{\bar{\phi}}$ denoting the expectation value with respect to the Gaussian action $S_0[\bar{\phi}]$, and $\bar{\xi} \equiv [\xi(\bar{\phi}(t))]^*$ the complex conjugate of $\xi^{+,-,z}$. Finally, Eq. (4.17) follows by plugging Eq. (D.32) into

Eq. (4.16) and integrating the Gaussian integral with respect to $x$.

Finally, the evolution of the wave packet, reported in Eq. (4.17), is eventually computed by integrating the expression of $\hat{U}(t)\,|x\rangle$ over the variable $x$ with respect to the Gaussian measure $e^{-(x-a)^2/(2\sigma^2)+i(x-a)k}(\pi\sigma^2)^{-1/4}$. The convergence is ensured by requiring that $\mathrm{Re}(\gamma) > 0$. In our description we have $\xi^{\pm} \in i\mathbb{R}$ and real $\xi^z$, so that it is useful to define $\xi^{\pm} \equiv i\xi_i^{\pm}$ with $\xi_i^{\pm} \in \mathbb{R}$, which, together with Eq. (4.18), leads to

$$\mathrm{Re}(\gamma) = \frac{\sigma^2 e^{\xi^z}}{\sigma^4 + (\xi_i^-)^2} \geq 0. \tag{D.34}$$

A better understanding of the behaviour of $\mathrm{Re}(\gamma)$ can be achieved by considering the following real-valued auxiliary variables:

$$\begin{aligned} X &\equiv \xi_i^- e^{-\xi^z/2}, \\ Y &\equiv e^{-\xi^z/2}. \end{aligned} \tag{D.35}$$

These variables evolve according to the harmonic equations with time-dependent frequency given in Eq. (4.6),

$$\begin{aligned} \ddot{X}(t) + \Omega^2(t)X(t) &= 0, \\ \ddot{Y}(t) + \Omega^2(t)Y(t) &= 0, \end{aligned} \tag{D.36}$$

with initial conditions $X(0) = 0$, $\dot{X}(0) = -m^{-1}$, $Y(0) = 1$ and $\dot{Y}(0) = 0$. These new variables allow one to write $\mathrm{Re}(\gamma) = \sigma^2(\sigma^4 Y^2 + X^2)^{-1}$, making it apparent that $\mathrm{Re}(\gamma(t)) = 0$ if $X(t)$ or $Y(t)$ are infinite. In either case, $\beta(t) = [\sigma^2 Y(t) - iX(t)]^{-1}$ which multiplies Eq. (4.17), vanishes, i.e., $|\psi(t)\rangle = 0$. Accordingly, the convergence of the Gaussian integral in Eq. (4.17) is guaranteed by the fact that $\mathrm{Re}(\gamma) \geq 0$ and that whenever $\mathrm{Re}(\gamma) = 0$ the whole $|\psi\rangle$ vanishes.

As a last remark, we point out that the introduction of the variables $X$ and $Y$ in Eq. (D.35) explains why in the case of the harmonic oscillator, in which the $\xi^{+,-,z}$ are found to be periodically divergent according to the Eqs. (4.23), there are no divergences in the expectation values of Eqs. (4.24): in fact, these values depend on a well-behaved combination of the $\xi^{+,-,z}$, satisfying an harmonic equation with constant frequency but different initial conditions.

## D.5 Derivations of the Dyson series

In order to prove the equivalence of the Dyson series for the quantum quartic oscillator and the asymptotic expansion of $\hat{U}(t)$ around the harmonic case according to Eq. (4.30), we begin by calculating the second variation of the time-evolution operator of the harmonic oscillator, which will be useful to determine the first-order correction according to Eq. (4.30), namely:

$$\hat{U}^{(1)}(t) \equiv i\frac{\lambda}{4}\int_0^t \mathrm{d}s \left.\frac{\delta^2 \hat{U}_S[\phi]}{\delta\phi(s_1)\delta\phi(s_2)}\right|_{\substack{\phi=0 \\ s_1=s_2=s}}. \tag{D.37}$$

This expression involves the first functional derivative of $\hat{U}_S$, given by

$$\frac{\delta \hat{U}_S[\phi]}{\delta \phi(s)} \equiv G^{(1)}(s|t)\hat{U}_S[\phi], \tag{D.38}$$

where $G^{(1)}$ is explicitly computed by exploiting the $SU(2)$ commutation relations (4.10) of the $S$ operators and $\hat{U}_S$, leading to

$$G^{(1)}(s) \equiv \left[\frac{\delta \xi^+}{\delta \phi} - \xi^+ \frac{\delta \xi^z}{\delta \phi} - (\xi^+)^2 e^{-\xi^z}\frac{\delta \xi^-}{\delta \phi}\right]\hat{S}^+ + \left(\frac{\delta \xi^z}{\delta \phi} + 2\xi^+ e^{-\xi^z}\frac{\delta \xi^-}{\delta \phi}\right)\hat{S}^z + \frac{\delta \xi^-}{\delta \phi}e^{-\xi^z}\hat{S}^-, \tag{D.39}$$

where the parametric dependence on the final time $t$ is understood.

Similarly, the second order functional derivative $\frac{\delta^2 \hat{U}_S[\phi]}{\delta\phi(s_1)\delta\phi(s_2)}$, required to be symmetric under the exchange $s_1 \leftrightarrow s_2$, can be expressed as

$$\frac{\delta^2 \hat{U}_S[\phi]}{\delta\phi(s_1)\delta\phi(s_2)} = \left[G^{(1)}(s_1)G^{(1)}(s_2) + G^{(2)}(s_1,s_2)\right]\hat{U}_S[\phi], \tag{D.40}$$

where $G^{(2)}(s_1,s_2)$ is found to be

$$\begin{aligned} G^{(2)} \equiv & \left\{\xi^+_{1,2} - \xi^+\xi^z_{1,2} - \frac{1}{2}\left(\xi^z_1\xi^+_2 + \xi^z_2\xi^+_1\right) - \xi^+ e^{-\xi^z}\left[\xi^-_1\xi^+_2 + \xi^-_2\xi^+_1 - \frac{\xi^+}{2}\left(\xi^z_1\xi^-_2 + \xi^z_2\xi^-_1\right) + \xi^+\xi^-_{1,2}\right]\right\}\hat{S}^+ + \\ & + e^{-\xi^z}\left[\xi^-_{1,2} - \frac{1}{2}\left(\xi^z_1\xi^-_2 + \xi^z_2\xi^-_1\right)\right]\hat{S}^- + \\ & + \left\{\xi^z_{1,2} + e^{-\xi^z}\left[\xi^-_1\xi^+_2 + \xi^-_2\xi^+_1 - \xi^+\left(\xi^z_1\xi^-_2 + \xi^z_2\xi^-_1\right) + 2\xi^+\xi^-_{1,2}\right]\right\}\hat{S}^z; \end{aligned} \tag{D.41}$$

in order to streamline the formulas, the subscripts $\{1,2\}$ above are used to denote the functional differentiation with respect to $\phi(s_1)$ and $\phi(s_2)$, i.e., $\frac{\delta\xi(t)}{\delta\phi(s_1)} \equiv \xi(s_1|t) = \xi_1$. By taking the functional derivative of Eqs. (4.13) we obtain a system of differential equations for the first functional derivatives $\xi_{1,2}$, namely

$$\begin{aligned} & i\frac{\mathrm{d}}{\mathrm{d}t}\xi^+(s|t) + 2\frac{\xi^+}{m}\xi^+(s|t) = 2\delta(t-s), \\ & i\frac{\mathrm{d}}{\mathrm{d}t}\xi^z(s|t) + \frac{2}{m}\xi^+(s|t) = 0, \\ & i\frac{\mathrm{d}}{\mathrm{d}t}\xi^-(s|t) - \frac{e^{\xi^z}}{m}\xi^z(s|t) = 0, \end{aligned} \tag{D.42}$$

with initial conditions $\xi(s|s) = 0$ for $t \leq s$, reflecting the fact that we assume an Itô-like discretization in deriving Eqs. (4.13)[69]. The solution to these equations reads

$$\begin{aligned} & \xi^+(s|t) = -\theta(t-s)\,2i\,\exp\left\{\frac{2i}{m}\int_s^t \mathrm{d}\tau\,\xi^+(\tau)\right\}, \\ & \xi^z(s|t) = \theta(t-s)\frac{2i}{m}\int_s^t \mathrm{d}\tau\,\xi^+(s|\tau), \\ & \xi^-(s|t) = -\theta(t-s)\frac{i}{m}\int_s^t \mathrm{d}\tau\,\xi^z(s|\tau)\,e^{\xi^z(\tau)}. \end{aligned} \tag{D.43}$$

For $\phi = 0$ they reduce to

$$\begin{aligned}
\left.\frac{\delta\xi^+(t)}{\delta\phi(s)}\right|_{\phi=0} &= -i\theta(t-s)\,2\frac{\cos^2(\omega s)}{\cos^2(\omega t)},\\
\left.\frac{\delta\xi^z(t)}{\delta\phi(s)}\right|_{\phi=0} &= \theta(t-s)\frac{4}{m\omega}\cos^2(\omega s)\left[\tan(\omega t)-\tan(\omega s)\right],\\
\left.\frac{\delta\xi^-(t)}{\delta\phi(s)}\right|_{\phi=0} &= -i\theta(t-s)\frac{2}{m^2\omega^2}\cos^2(\omega s)\left[\tan(\omega t)-\tan(\omega s)\right]^2.
\end{aligned} \tag{D.44}$$

As expected, the functional derivative $\xi^+(s|t)$ vanishes for $t < s$, as a consequence of the fact that the differential equation at time $t$ does not depend on the realizations of $\phi$ at later times, reflecting the causality of the problem. Following the same line of reasoning as before, the second functional derivatives can be computed directly from their differential equations and can be expressed in terms of first functional derivative according to

$$\begin{aligned}
\xi^+_{1,2} &= \frac{\xi^z_1\xi^+_2 + \xi^z_2\xi^+_1}{2},\\
\xi^z_{1,2} &= -e^{-\xi^z(t)}\left(\xi^-_1\xi^+_2 + \xi^-_2\xi^+_1\right),\\
\xi^-_{1,2} &= \frac{\xi^z_1\xi^-_2 + \xi^z_2\xi^-_1}{2},
\end{aligned} \tag{D.45}$$

and they are non-zero only if $t > \max(s_1, s_2)$. Moreover, by plugging Eqs. (D.45) into Eq. (D.41), we get $G^{(2)}(s_1, s_2) = 0$, such that the only contributing term in the functional derivative in Eq. (D.40) is

$$G^{(1)}(s)|_{\phi=0} = -i\theta(t-s)\,x_0^2\left[\cos(\omega(t-s))\frac{\hat{x}}{x_0} - \sin(\omega(t-s))x_0\,\hat{p}\right]^2, \tag{D.46}$$

which finally yields

$$\begin{aligned}
\left.\frac{\delta^2\hat{U}_S[\phi]}{\delta\phi(s_1)\delta\phi(s_2)}\right|_{s_1=s_2=s,\phi=0} &= -\theta(t-s)\,x_0^4\left[\cos(\omega(t-s))\frac{\hat{x}}{x_0} - \sin(\omega(t-s))x_0\,\hat{p}\right]^4\hat{U}_0(t)\\
&= -\theta(t-s)\hat{U}_0(t-s)\,\hat{x}^4\,\hat{U}_0(s),
\end{aligned} \tag{D.47}$$

where the time ordering $t > s$ arises naturally from the fact that the equation for $\xi^+$ depends linearly on $\phi$. Collecting the above results of Eqs. (D.37) and (D.47), the first-order correction to $\hat{U}(t)$ reads

$$\hat{U}^{(1)} = -i\frac{\lambda}{4}\,\hat{U}_0(t)\int_0^t \mathrm{d}s\,\hat{U}_0^\dagger(s)\,\hat{x}^4\,\hat{U}_0(s), \tag{D.48}$$

which is nothing but the first order term in the Dyson series [186]. This can be seen noticing that the time evolution operator in the Schrödinger picture $\hat{U}(t)$ can be written in terms of the interaction time evolution operator in the interaction picture $\hat{U}_I$ as

$$\hat{U}_I(t) \equiv \hat{U}_0^\dagger(t)\,\hat{U}(t)\,\hat{U}_0(0), \tag{D.49}$$

so that, since $\hat{U}_0(0) = \mathbb{I}$,

$$\hat{U}(t) = \hat{U}_0(t)\,\hat{U}_I(t). \tag{D.50}$$

The fact that $G^{(2)} = 0$ makes all functional derivatives of order larger than one to depend only on $G^{(1)}$; this allows one to easily generalize the result above to an arbitrary order $n$, leading to

$$\left.\frac{\delta^{2n}\hat{U}_S[\phi]}{\delta\phi(s_1)\cdots\delta\phi(s_{2n})}\right|_{\substack{\phi=0\\ s_1=s_2=t_1\\ \cdots\\ s_{2n-1}=s_{2n}=t_n}} = [G^{(1)}(t_1)]^2[G^{(1)}(t_2)]^2\cdots[G^{(1)}(t_n)]^2\hat{U}_0(t), \tag{D.51}$$

with $t > t_n > t_{n-1} > \cdots > 0$. Using the expression for $G^{(n)}$, this readily yields

$$\hat{U}^{(n)}(t) = \left(-i\frac{\lambda}{4}\right)^n \hat{U}_0(t)\int_0^t \mathrm{d}t_n \int_0^{t_n} \mathrm{d}t_{n-1}\cdots\int_0^{t_2} \mathrm{d}t_1\,\hat{x}^4(t_n)\cdots\hat{x}^4(t_1), \tag{D.52}$$

where $\hat{x}^4(t) = \hat{U}_0^\dagger(t)\,\hat{x}^4\,\hat{U}_0(t)$. Equation (D.52) is precisely the $n$-th order contribution to the Dyson series in the Schrödinger picture.

## D.6 Evaluation of $G_{\mathrm{HO}}(0,t|0,0)$

We now report from Ref. [189] the calculation of the propagator $G_{\mathrm{HO}}(0,t|0,0)$ appearing in Sec. 4.6.1. It can be expressed as the according to Feynman path integral as

$$\begin{aligned} G_{\mathrm{HO}}(0,t|0,0) &= \int_{x(0)=0}^{x(t)=0} \mathcal{D}x(\tau)\,\exp\left\{\frac{i}{\hbar}\frac{m}{2}\int_0^t \mathrm{d}\tau\left[(\dot{x}(\tau))^2 - \Omega^2(\tau)x^2(\tau)\right]\right\} \\ &= \lim_{N\to\infty}\int \mathrm{d}x_1\cdots\mathrm{d}x_N\left(\frac{m}{2\pi i\hbar\Delta t}\right)^{(N+1)/2} \\ &\quad\times\exp\left\{\frac{i}{\hbar}\sum_{j=0}^{N}\left[\frac{m}{2\Delta t}(x_{j+1}-x_j)^2 - \frac{1}{2}\Delta t\,c_j x_j^2\right]\right\}, \end{aligned} \tag{D.53}$$

where $c_j = m\Omega^2(t_j)$, with $t_j = j\Delta t$ and $j = 1,\ldots,N$. In order to calculate the path integral in Eq. (D.53) we introduce the column vector

$$\zeta^T \equiv (x_1\cdots x_N), \tag{D.54}$$

where $T$ identifies matrix transposition. Accordingly, the exponent in Eq. (D.53) can be written as

$$-\,\zeta^T\,Q\,\zeta, \tag{D.55}$$

where we define the matrix

$$Q \equiv \frac{m}{2\hbar i\Delta t}\begin{pmatrix} 2 & -1 & & 0 \\ -1 & \ddots & \ddots & \\ & \ddots & \ddots & -1 \\ 0 & & -1 & 2 \end{pmatrix} + \frac{i\Delta t}{2\hbar}\begin{pmatrix} c_1 & & 0 \\ & \ddots & \\ 0 & & c_N \end{pmatrix}, \tag{D.56}$$

allowing one to recast Eq. (D.53) as

$$G(0,t|0,0) = \lim_{N\to\infty} \left(\frac{m}{2\pi i\hbar\Delta t}\right)^{(N+1)/2} \int \mathrm{d}^N\zeta \, \exp\left(-\zeta^T \, Q \, \zeta\right). \tag{D.57}$$

Given that the matrix $Q$ is of the form $Q = i\tilde{Q}$ with $\tilde{Q}$ real and symmetric, it is possible to diagonalize $Q$ by the real orthogonal matrix $V$:

$$Q = V^T \, D \, V, \tag{D.58}$$

where $D$ is the diagonal matrix of eigenvalues of $Q$, which we denote by $q_j$. Therefore, we have that the Gaussian integral in Eq. (D.57) is given by

$$\int \mathrm{d}^N\zeta \, \exp\left(-\zeta^T \, Q \, \zeta\right) = \prod_{j=1}^{N} \sqrt{\frac{\pi}{q_j}} = \frac{\pi^{N/2}}{\sqrt{\mathrm{det}Q}}, \tag{D.59}$$

provided that there are no zero eigenvalues. By substituting Eq. (D.59) in Eq. (D.57) we get

$$G_{\mathrm{HO}}(0,t|0,0) = \lim_{N\to\infty} \left[\frac{m}{2\pi i\hbar\Delta t}\frac{1}{\mathrm{det}Q'}\right]^{1/2}, \tag{D.60}$$

where one defines the auxiliary matrix $Q' \equiv (2i\hbar\Delta t/m)Q$, and its determinant $p_N \equiv \mathrm{det}Q'$. It can be shown that $p_N$ satisfies the recursion formula

$$p_{j+1} = \left[2 - \frac{(\Delta t)^2}{m} c_{j+1}\right] p_j - p_{j-1}, \quad j = 1, \ldots, N \tag{D.61}$$

where $p_1 = 2 - (\Delta t)^2 c_1/m$ and $p_0 = 1$. It is convenient to write Eq. (D.61) in the form

$$\frac{p_{j+1} - 2p_j + p_{j-1}}{(\Delta t)^2} = -\frac{c_{j+1}p_j}{m}, \tag{D.62}$$

which makes clear the emergence of the discrete second time derivative. Then, by defining $f(t) = \Delta p_j$, in the limit $\Delta \to 0$, one gets the differential equation

$$\frac{\mathrm{d}^2 f(t)}{\mathrm{d}t^2} = -\Omega^2(t) f(t), \tag{D.63}$$

with initial conditions

$$\begin{aligned} &f(0) = \lim_{\Delta\to 0} \Delta t \, p_0 = 0, \\ &\left.\frac{\mathrm{d}f(t)}{\mathrm{d}t}\right|_{t=0} = \lim_{\Delta\to 0} \Delta t \left(\frac{p_1 - p_0}{\Delta t}\right) = 2 - \frac{(\Delta t)^2}{m} c_1 - 1 = 1. \end{aligned} \tag{D.64}$$

Finally, by collecting Eq. (D.57) and the definition of $f(t)$ we find the closed expression

$$G_{\mathrm{HO}}(0,t|0,0) = \sqrt{\frac{m}{2\pi i\hbar f(t)}}. \tag{D.65}$$

We conclude that the determinant of the operator $d_t^2 + \Omega^2(t)$ appearing in the Gaussian action of Eq. (D.6) is proportional to the function $f(t)$, satisfying Eq. (D.63) with initial conditions given by Eq. (D.64).

## D.7 Semiclassical limit

In this Section we provide details of the computation of the semiclassical approximation for the propagator. The stationary path in Eq. (4.41) is computed considering the first functional derivative of Eq. (4.34), namely

$$\begin{aligned}\frac{\delta S_{\rm HO}(y_f,t|y_i,0)}{\delta\phi(\tau)} &= \frac{\delta}{\delta\phi(\tau)}\frac{m}{2}\int_0^t \mathrm{d}s\,\left[\dot y^2(s)-\Omega^2(s)y^2(s)\right]\\ &= -y^2(\tau)+m\int_0^t \mathrm{d}s\,\left[\dot y(s)\dot y_1(\tau|s)-\Omega^2(s)y(s)y_1(\tau|s)\right]\\ &= -y^2(\tau)+m\left[\dot y(t)y_1(\tau|t)-\dot y(0)y_1(\tau|0)\right]-m\int_0^t \mathrm{d}s\,y_1(\tau|s)\left[\ddot y(s)+\Omega^2(s)y(s)\right]\\ &= -y^2(\tau),\end{aligned} \tag{D.66}$$

where $y_1(\tau|s)\equiv\delta y(t)/\delta\phi(\tau)$, $y_f=\sqrt{\lambda}\,x_f$, $y_i=\sqrt{\lambda}\,x_i$, and the $t$ dependence is understood; in the third line we integrated by parts the right-hand side and finally we exploited Eq. (4.36) and the explicit expression of $y_1(\tau|s)$

$$\begin{aligned}y_1(\tau|s) =& -\left[\frac{\xi_1^-(\tau|t)}{\xi^-(t)}+\frac{\xi_1^z(\tau|s)}{2}\right]y(\tau|t)\\ &+\frac{e^{-\xi^z(s)/2}}{\xi^-(t)}\left[y_f\,e^{-\xi^z(t)/2}\left(\frac{\xi^-(\tau)}{2}\xi_1^z(\tau|t)+\xi_1^-(\tau|s)\right)+y_i\,\left(\xi_1^-(\tau|t)-\xi_1^-(\tau|s)\right)\right],\end{aligned} \tag{D.67}$$

where $\xi_1(t_1|t_2)$ is null if $t_1\geq t_2$, so that $y_1(\tau|t)=y_1(\tau|0)=0$. Note that by taking the functional derivative of Eq. (4.36) computed along the stationary solution $\bar\phi$ in Eq. (4.41) one has

$$\ddot{\bar y}_1(t_2|t_1)+\left[\omega^2+\frac{\bar y^2(t_1)}{m}\right]\bar y_1(t_2|t_1)+\frac{2}{m}\bar y(t_1)\delta(t_1-t_2)=0, \tag{D.68}$$

with boundary conditions $\bar y_1(t_2|0)=\bar y_1(t_2|0)=0$. The path integral in the second line of Eq. (4.43) can be expressed in terms of the determinant of the operator $H(t_1,t_2)$ , defined in Eq. (4.44) as

$$\begin{aligned}H(t_1,t_2)&\equiv\delta(t_1-t_2)+\frac{1}{2}\frac{\delta^2 S_{\rm HO}(y_f,t|y_i,0)}{\delta\phi(t_1)\delta\phi(t_2)}\Big|_{\bar\phi_k}\\ &=\delta(t_1-t_2)-\bar y(t_1)\bar y_1(t_2|t_1),\end{aligned} \tag{D.69}$$

where last equality follows from direct functional derivation of Eq. (D.66).The determinant of $H$ can be evaluated by relying on the fact that this operator can be recast as the product of two operators whose determinant can be computed exactly. We start by defining the operators

$$O_1(t_1,t_2)\equiv\delta(t_1-t_2)\frac{1}{\bar y(t_1)}\left[\frac{d^2}{dt_1^2}+\omega^2+\frac{\bar y^2(t_1)}{m}\right], \tag{D.70}$$

$$
\begin{aligned}
O_2(t_1,t_2) &\equiv \delta(t_1-t_2)\frac{1}{\bar{y}(t_1)}\left[\frac{d^2}{dt_1^2}+\omega^2+3\frac{\bar{y}^2(t_1)}{m}\right] \\
&= O_1(t_1,t_2)+2\,\delta(t_1-t_2)\frac{\bar{y}(t_1)}{m}.
\end{aligned}
\tag{D.71}
$$

It follows that, given Eqs. (D.70) and (D.71) one can recast $H(t_1,t_2)$ in Eq. (D.69) as

$$
\begin{aligned}
H(t_1,t_2) &= \int_0^t \mathrm{d}\tau\, O_2(t_1,\tau)O_1^{-1}(\tau,t_2) \\
&= \delta(t_1-t_2)+2\frac{\bar{y}(t_1)}{m}O_1^{-1}(t_1,t_2),
\end{aligned}
\tag{D.72}
$$

where the inverse operator satisfies the following relation

$$
\int_0^t \mathrm{d}\tau\, O_1(t_1,\tau)\, O_1^{-1}(\tau,t_2)=\delta(t_1-t_2). \tag{D.73}
$$

By plugging Eq. (D.68) in the inverse operator definition in Eq. (D.73) we identify $O_1^{-1}(t_1,t_2)$ as

$$
O_1^{-1}(t_1,t_2)=-\frac{m}{2}\bar{y}_1(t_2|t_1). \tag{D.74}
$$

Hence, we have proved Eq. (D.69) to be true. It then follows that the path integral evaluates to

$$
\begin{aligned}
&\int \mathcal{D}\varphi \exp\left\{-\int_0^t \mathrm{d}t_1\int_0^t \mathrm{d}t_2\,\varphi(t_1)H(t_1,t_2)\varphi(t_2)\right\} \\
&= \left[\det\left(O_2\,O_1^{-1}\right)\right]^{-\frac{1}{2}} = \sqrt{\frac{\det O_1}{\det O_2}} = \sqrt{\frac{f(t)}{F(t)}},
\end{aligned}
\tag{D.75}
$$

where in the last relation we exploited the fact that $f$ and $F$ are respectively proportional to the determinant of $O_1$ and $O_2$ with the same proportionality constant, according to Eq. (4.37) and the fact that the determinant of a product of operators is given by the product of the determinants of the individual operators.

## D.8 Crank-Nicholson algorithm

Here, we report from Refs. [141, 168] the Cranck-Nicholson algorithm, which allows one to numerically compute the time-dependent solution of the one-dimensional Schrödinger equation, with initial wave function $\psi(x,0)$. In units of $\hbar=1$, the time evolution operator of the system is give by $\exp(-i\hat{H}t)$, where $\hat{H}=-\partial_x^2+V(x)$ is the time-independent Hamiltonian in the position representation. Accordingly, the wave function evolves according the relation $\psi(x,t+\Delta)=\exp(-i\hat{H}\Delta)\psi(x,t)$, which is the one that is discretized in the algorithm.

The Cranck-Nicholson method is based on the discretized form of the time evolution operator

$$
\exp(-i\hat{H}\Delta)=\frac{1-i\hat{H}\Delta/2}{1+i\hat{H}\Delta/2}+O(\Delta^3), \tag{D.76}
$$

which is accurate to second order in the time step $\Delta$. Notably, as the time evolution operator, Eq. (D.76) is unitary, and preserves the norm of the wave function. The evolution equation is then given by

$$[1 + i\hat{H}\Delta t/2]\psi(x, t + \Delta) \simeq [1 - i\hat{H}\Delta t/2]\psi(x, t). \tag{D.77}$$

If one considers the auxiliary function $y(x, t) \equiv \psi(x, t + \Delta) + \psi(x, t)$, and the definition of $\hat{H}$, one finds

$$\frac{\partial^2 y(x,t)}{\partial x^2} - \left[V(x) - i\frac{2}{\Delta}\right] y(x, t) = i\frac{4}{\Delta}\psi(x, t), \tag{D.78}$$

where $\psi(x, t)$ is known from the previous time step. The numerical procedure relies on the discretization of the second derivative in space as

$$h^2\frac{\partial^2 y}{\partial x^2} \simeq y(x + h) + y(x - h) - 2y(x), \tag{D.79}$$

which allows one to solve numerically Eq. (D.78) with an accuracy to third order in the space increment $h$.

### D.8.1 Space discretization: Numerov approximation

Equation (D.78) is of the form

$$\frac{\partial^2 y(x)}{\partial x^2} = f(x)y(x) + g(x), \tag{D.80}$$

which leads to the implementation of the Numerov method. Briefly, the idea is to use this equation to evaluate the next order term in a discrete approximation to the second derivative. To do so, we introduce the short-hand notation $y_j \equiv y(x_j = x_0 + hj)$, and similarly for $f_j$ and $g(x_j)$. Then, by Taylor-expanding with respect to $x_j$ Eq. (D.79) one gets

$$y_{j+1} + y_{j-1} - 2y_j = y^{(2)}(x_j)\, h^2 + \frac{1}{12}y^{(4)}(x_j)\, h^4 + O(h^6), \tag{D.81}$$

where $y^{(n)}$ represents the $n$-th derivative with respect to $x$. The fourth derivative $y^{(4)}$ can be deduced from Eq. (D.80) to be $(fy + g)^{(2)}(x_j)$ , yielding

$$y^{(4)}(x_j)h^2 = f_{j+1}y_{j+1} + g_{j+1} + f_{j-1}y_{j-1} + g_{j-1} - 2f_jy_j - 2g_j + O(h^4). \tag{D.82}$$

Then, one substitutes this result into Eq. (D.81) to find a refined estimate of $y^{(2)}(x_j)$.

One can now approximate the original equation $y^{(2)}(x_j) = f_jy_j + g_j$, to a finite difference relation that differs from the original by terms that are of order $O(h^6)$. The resulting equation becomes very compact thanks to the introduction of the auxiliary variables $d_j \equiv 1 - h^2f_j/12$ and $w_j \equiv d_jy_j - h^2g_j/12$, i.e.,

$$w_{j+1} + w_{j-1} = \left[2 + h^2\frac{f_j}{d_j}\right] w_j + h^2\frac{g_j}{d_j}. \tag{D.83}$$

The quantities $w_j$, $y_j$, and $f_j$ also depend on $t$, which is discretized as $t_n = n\Delta$, which now appears in the Eq. (D.83) $w_j \to w_j^n \equiv d_j y_j^n - h^2 f_j^n/12$. The Cranck-Nicholson procedure in Eq. (D.79) coincides with $y_j^n = \psi_j^{n+1} + \psi_j^n$, $f_j = V_j - 2i/\Delta$, and $f_j^n = 4i\psi_j^n/\Delta$.

Equation (D.83) represents a three-term recursion expression for the unknown $w_j$. The numerical solution is computed once the initial condition $w_0^n$ and $w_1^n$ are known. For our purposes, we assume the solution to vanish at the end points of a sufficiently large interval, corresponding to $w_0^n = w_J^n = 0$ for some $J > 0$ and all $n$. As shown in Ref. [89], this is done by reducing the original three-term recursion relation to a couple of two-term recursions for two new functions $e_j$ and $q_j^n$ by requiring that $w_{j+1}^n = e_j w_j^n + q_j^n$ for all $j = 1, 2, \ldots, J-1$. If one substitutes these expressions in Eq. (D.83), one finds

$$\begin{aligned} e_j + \frac{1}{e_{j-1}} &= 2 + h^2 \frac{f_j}{d_j}, \\ q_j^n &= \frac{q_{j-1}^n}{e_{j-1}} + h^2 \frac{g_j^n}{d_j}. \end{aligned} \tag{D.84}$$

According to this equation, $e$ and $q_j^n$ are generated from the initial condition $e_0$ and $q_0^n$. In the case of $w_0^n = 0$ boundary condition, one lets $e_0 \to \infty$, thus permitting to easily compute $e_j$ and $q_j^n$ from Eq. (D.84). Then, starting with $w_J^n = 0$, one can construct $w_{j-1}^n = (w_j^n - q_{j-1}^n)/e_{j-1}$.

# Bibliography


[1] Abdolvahab, R. H., Ejtehadi, M. R., and Metzler, R. Sequence dependence of the binding energy in chaperone-driven polymer translocation through a nanopore. *Phys. Rev. E 83*, 1 (2011), 011902.

[2] Abdolvahab, R. H., Metzler, R., and Ejtehadi, M. R. First passage time distribution of chaperone driven polymer translocation through a nanopore: Homopolymer and heteropolymer cases. *J. Chem. Phys. 135*, 24 (2011), 12B619.

[3] Abramowitz, M., Stegun, I. A., and Romer, R. H. *Handbook of mathematical functions with formulas, graphs, and mathematical tables*. American Association of Physics Teachers, 1988.

[4] Aharony, A., Entin-Wohlman, O., Chowdhury, D., and Dattagupta, S. Is telegraph noise a good model for the environment of mesoscopic systems? *J. Stat. Phys 175*, 3, 704.

[5] Alonso, R., Goller, F., and Mindlin, G. B. Motor control of sound frequency in birdsong involves the interaction between air sac pressure and labial tension. *Phys. Rev. E 89*, 3 (2014), 032706.

[6] Alonso, R., Tobin, M., Martin, P., and Hudspeth, A. Fast recovery of disrupted tip links induced by mechanical displacement of hair bundles. *PNAS 117*, 48, 30722.

[7] Auberson, G., and Peyranère, M. Quantum anharmonic oscillator in the Heisenberg picture and multiple scale techniques. *Phys. Rev. A 65*, 3 (2002), 032120.

[8] Azimzadeh, J. B., Fabella, B. A., Kastan, N. R., and Hudspeth, A. Thermal excitation of the mechanotransduction apparatus of hair cells. *Neuron 97*, 3, 586.

[9] Azimzadeh, J. B., and Salvi, J. D. Physiological preparation of hair cells from the sacculus of the american bullfrog (Rana catesbeiana). *J. Vis. Exp.*, 121 (2017), e55380.

[10] Bakr, W. S., Peng, A., Tai, M. E., Ma, R., Simon, J., Gillen, J. I., Foelling, S., Pollet, L., and Greiner, M. Probing the superfluid–to–Mott insulator transition at the single-atom level. *Science 329*, 5991, 547.

[11] Barato, A., Chetrite, R., Faggionato, A., and Gabrielli, D. A unifying picture of generalized thermodynamic uncertainty relations. *J. Stat. Mech.: Theory Exp.*, 8 (2019), 084017.

[12] Barato, A. C., and Chetrite, R. A formal view on level 2.5 large deviations and fluctuation relations. *J. Stat. Phys. 160*, 5, 1154.

[13] Barato, A. C., and Seifert, U. Thermodynamic uncertainty relation for biomolecular processes. *Phys. Rev. Lett. 114*, 15 (2015), 158101.

[14] Basu, U., Kundu, A., and Pal, A. Symmetric exclusion process under stochastic resetting. *Phys. Rev. E 100* (2019), 032136.

[15] Bechinger, C., Di Leonardo, R., Löwen, H., Reichhardt, C., Volpe, G., and Volpe, G. Active particles in complex and crowded environments. *Rev. Mod. Phys. 88*, 4 (2016), 045006.

[16] Belan, S. Restart could optimize the probability of success in a Bernoulli trial. *Phys. Rev. Lett. 120*, 8 (2018), 080601.

[17] Belousov, R., Berger, F., and Hudspeth, A. Volterra-series approach to stochastic nonlinear dynamics: The Duffing oscillator driven by white noise. *Phys. Rev. E 99*, 4 (2019), 042204.

[18] Belousov, R., Berger, F., and Hudspeth, A. Volterra-series approach to stochastic nonlinear dynamics: Linear response of the Van der Pol oscillator driven by white noise. *Phys. Rev. E 102*, 3 (2020), 032209.

[19] Bender, C., and Wu, T. Anharmonic oscillator. II. A study of perturbation theory in large order. *Phys. Rev. D 7*, 6 (1973), 1620.

[20] Bender, C. M., and Wu, T. T. Anharmonic oscillator. *Phys. Rev. 184*, 5 (1969), 1231.

[21] Berg, H. C. *E. Coli in Motion*. Springer Science & Business Media, 2008.

[22] Besga, B., Bovon, A., Petrosyan, A., Majumdar, S. N., and Ciliberto, S. Optimal mean first-passage time for a Brownian searcher subjected to resetting: experimental and theoretical results. *Phys. Rev. Research 2*, 3 (2020), 032029.

[23] Besga, B., Faisant, F., Petrosyan, A., Ciliberto, S., and Majumdar, S. N. Dynamical phase transition in the first-passage probability of a Brownian motion. *Phys. Rev. E 104* (2021), L012102.

[24] Beta, C., and Kruse, K. Intracellular oscillations and waves. *Annu. Rev. Condens. Matter Phys. 8*, 239.

[25] Bhat, U., De Bacco, C., and Redner, S. Stochastic search with Poisson and deterministic resetting. *J. Stat. Mech.: Theory Exp.*, 8 (2016), 083401.

[26] Blatt, R., and Roos, C. Quantum simulations with trapped ions. *Nat. Phys. 8*, 4, 277.

[27] Boyer, D., and Solis-Salas, C. Random walks with preferential relocations to places visited in the past and their application to biology. *Phys. Rev. Lett. 112*, 24 (2014), 240601.

[28] Bray, A. J., Majumdar, S. N., and Schehr, G. Persistence and first-passage properties in nonequilibrium systems. *Adv. Phys. 62*, 3, 225.

[29] Bressloff, P. C. Directed intermittent search with stochastic resetting. *J. Phys. A: Math. Theor. 53*, 10 (2020), 105001.

[30] Brizuela, D. Classical and quantum behavior of the harmonic and the quartic oscillators. *Phys. Rev. D 90*, 12 (2014), 125018.

[31] Brown, R. XXVII. A brief account of microscopical observations made in the months of June, July and August 1827, on the particles contained in the pollen of plants; and on the general existence of active molecules in organic and inorganic bodies. *Philos. Mag. 4*, 21 (1828), 161.

[32] Brückner, D. B., Arlt, N., Fink, A., Ronceray, P., Rädler, J. O., and Broedersz, C. P. Learning the dynamics of cell–cell interactions in confined cell migration. *PNAS 118*, 7, 1.

[33] Brugués, J., Nuzzo, V., Mazur, E., and Needleman, D. J. Nucleation and transport organize microtubules in metaphase spindles. *Cell 149*, 3, 554.

[34] Buceta, J., Lindenberg, K., and Parrondo, J. M. Stationary and oscillatory spatial patterns induced by global periodic switching. *Phys. Rev. Lett. 88*, 2 (2001), 024103.

[35] Buzsáki, G., and Draguhn, A. Neuronal oscillations in cortical networks. *Science 304*, 5679, 1926.

[36] Carollo, F., Jack, R. L., and Garrahan, J. P. Unraveling the large deviation statistics of Markovian open quantum systems. *Phys. Rev. Lett. 122*, 13 (2019), 130605.

[37] Case, W. Wigner functions and Weyl transforms for pedestrians. *Am. J. Phys. 76*, 10, 937.

[38] Cates, M. E., and Tailleur, J. Motility-induced phase separation. *Annu. Rev. Condens. Matter Phys. 6*, 1, 219.

[39] Cates, M. E., and Tailleur, J. When are active Brownian particles and run-and-tumble particles equivalent? Consequences for motility-induced phase separation. *EPL 101*, 2 (2013), 20010.

[40] Chatterjee, A., Christou, C., and Schadschneider, A. Diffusion with resetting inside a circle. *Phys. Rev. E 97* (2018), 062106.

[41] Chechkin, A., and Sokolov, I. Random search with resetting: a unified renewal approach. *Phys. Rev. Lett. 121*, 5 (2018), 050601.

[42] Chechkin, A. V., Seno, F., Metzler, R., and Sokolov, I. M. Brownian yet non-Gaussian diffusion: From superstatistics to subordination of diffusing diffusivities. *Phys. Rev. X 7* (2017), 021002.

[43] Cheng, C., and Fung, P. The evolution operator technique in solving the Schrödinger equation, and its application to disentangling exponential operators and solving the problem of a mass-varying harmonic oscillator. *J. Phys. A: Math. Gen. 21*, 22 (1988), 4115.

[44] Cherevko, A., Bord, E., Khe, A., Panarin, V., and Orlov, K. The analysis of solutions behaviour of Van der Pol Duffing equation describing local brain hemodynamics. *J. Phys. Conf. Ser. 894*, 1 (2017), 012012.

[45] Cherevko, A., Mikhaylova, A., Chupakhin, A., Ufimtseva, I., Krivoshapkin, A., and Orlov, K. Y. Relaxation oscillation model of hemodynamic parameters in the cerebral vessels. *J. Phys. Conf. Ser. 722*, 1 (2016), 012045.

[46] Choe, Y., Magnasco, M. O., and Hudspeth, A. A model for amplification of hair-bundle motion by cyclical binding of Ca2+ to mechanoelectrical-transduction channels. *PNAS 95*, 26, 15321.

[47] Christou, C., and Schadschneider, A. Diffusion with resetting in bounded domains. *J. Phys. A: Math. Theor. 48*, 28 (2015), 285003.

[48] Chubynsky, M. V., and Slater, G. W. Diffusing diffusivity: a model for anomalous, yet Brownian, diffusion. *Phys. Rev. Lett. 113*, 9 (2014), 098302.

[49] C.M. Bender, A. Felski, N. H. S. K., and Beygi, A. Analytic structure of eigenvalues of coupled quantum systems. *Phys. Scr. 92*, 1 (2016), 015201.

[50] Coghi, F., and Harris, R. J. A large deviation perspective on ratio observables in reset processes: Robustness of rate functions. *J. Stat. Phys. 179*, 1 (2020).

[51] Cover, T. M. *Elements of information theory.* John Wiley & Sons, 1999.

[52] Dabelow, L., Bo, S., and Eichhorn, R. Irreversibility in active matter systems: Fluctuation theorem and mutual information. *Phys. Rev. X 9*, 2 (2019), 021009.

[53] Das, M., Schmidt, C. F., and Murrell, M. Introduction to active matter. *Soft Matter 16*, 31, 7185.

[54] De Bruyne, B., Randon-Furling, J., and Redner, S. Optimization in first-passage resetting. *Phys. Rev. Lett. 125*, 5 (2020), 050602.

[55] De Bruyne, B., Randon-Furling, J., and Redner, S. Optimization and growth in first-passage resetting. *J. Stat. Mech.: Theory Exp.*, 1 (2021), 013203.

[56] De Magistris, G., and Marenduzzo, D. An introduction to the physics of active matter. *Phys. A: Stat. Mech. Appl. 418*, 65.

[57] Dechant, A., and Sasa, S.-i. Continuous time reversal and equality in the thermodynamic uncertainty relation. *Phys. Rev. Research 3*, 4 (2021), L042012.

[58] Dhar, A., Kundu, A., Majumdar, S. N., Sabhapandit, S., and Schehr, G. Run-and-tumble particle in one-dimensional confining potentials: Steady-state, relaxation, and first-passage properties. *Phys. Rev. E 99*, 3 (2019), 032132.

[59] Di Terlizzi, I., and Baiesi, M. A thermodynamic uncertainty relation for a system with memory. *J. Phys. A Math. Theor. 53*, 47 (2020), 474002.

[60] Dicke, R. H. Coherence in spontaneous radiation processes. *Phys. Rev. 93*, 99.

[61] Dieterich, E., Camunas-Soler, J., Ribezzi-Crivellari, M., Seifert, U., and Ritort, F. Single-molecule measurement of the effective temperature in non-equilibrium steady states. *Nat. Phys. 11*, 11, 971.

[62] Dong, Q., Sun, G.-H., Aoki, M. A., Chen, C.-Y., and Dong, S.-H. Exact solutions of a quartic potential. *Mod. Phys. Lett. A 34*, 26 (2019), 1950208.

[63] Durang, X., Henkel, M., and Park, H. The statistical mechanics of the coagulation–diffusion process with a stochastic reset. *J. Phys. A: Math. Theor. 47*, 4 (2014), 045002.

[64] Einstein, A. On the theory of the Brownian movement. *Ann. Phys 19*, 4 (1906), 371.

[65] Einstein, A. Über die von der molekularkinetischen Theorie der Wärme geforderte Bewegung von in ruhenden Flüssigkeiten suspendierten Teilchen [AdP 17, 549 (1905)]. *Ann. der Phys. (Berl.) 14*, S1 1 (2005), 182.

[66] Elgeti, J., and Gompper, G. Run-and-tumble dynamics of self-propelled particles in confinement. *EPL 109*, 5 (2015), 58003.

[67] Eliazar, I., Koren, T., and Klafter, J. Searching circular DNA strands. *J. Phys. Condens. Matter 19*, 6 (2007), 065140.

[68] Engel, C., Sainsbury, S., Cheung, A. C., Kostrewa, D., and Cramer, P. RNA polymerase I structure and transcription regulation. *Nature 502*, 7473, 650.

[69] E.P. Kloeden, E. P., and Schurz, H. *Numerical solution of SDE through computer experiments*. Springer Science & Business Media, 2012.

[70] Evans, M. R., and Majumdar, S. N. Diffusion with stochastic resetting. *Phys. Rev. Lett. 106*, 16 (2011), 160601.

[71] Evans, M. R., and Majumdar, S. N. Diffusion with resetting in arbitrary spatial dimension. *J. Phys. A: Math. Theor. 47*, 28 (2014), 285001.

[72] Evans, M. R., and Majumdar, S. N. Run-and-tumble particle under resetting: a renewal approach. *J. Phys. A: Math. Theor. 51*, 47 (2018), 475003.

[73] Evans, M. R., Majumdar, S. N., and Mallick, K. Optimal diffusive search: nonequilibrium resetting versus equilibrium dynamics. *J. Phys. A: Math. Theor. 46*, 18 (2013), 185001.

[74] Evans, M. R., Majumdar, S. N., and Schehr, G. Stochastic resetting and applications. *J. Phys. A: Math. Theor. 53*, 19 (2020), 193001.

[75] F. Nicacio, A. Ferraro, A. I. M. P., and Semião, F. Thermal transport in out-of-equilibrium quantum harmonic chains. *Phys. Rev. E 91*, 4 (2015), 042116.

[76] FitzHugh, R. Impulses and physiological states in theoretical models of nerve membrane. *Biophys. J. 1*, 6, 445.

[77] Fodor, É., and Marchetti, M. C. The statistical physics of active matter: From self-catalytic colloids to living cells. *Phys. A: Stat. Mech. Appl. 504*, 106.

[78] Fokker, A. D. Die mittlere Energie rotierender elektrischer Dipole im Strahlungsfeld. *Ann. Phys. (Berl.) 348*, 5, 810.

[79] Fuchs, J., Goldt, S., and Seifert, U. Stochastic thermodynamics of resetting. *EPL 113*, 6 (2016), 60009.

[80] G. Lamporesi, S. Donadello, S. S. F. D., and Ferrari, G. Spontaneous creation of Kibble–Zurek solitons in a Bose–Einstein condensate. *Nat. Phys. 9*, 10, 656.

[81] Galitski, V. Quantum-to-classical correspondence and Hubbard-Stratonovich dynamical systems: A Lie-algebraic approach. *Phys. Rev. A 84*, 1 (2011), 012118.

[82] García-García, R., Genthon, A., and Lacoste, D. Linking lineage and population observables in biological branching processes. *Phys. Rev. E 99* (2019), 042413.

[83] Garcia-Millan, R., and Pruessner, G. Run-and-tumble motion in a harmonic potential: field theory and entropy production. *J. Stat. Mech.: Theory Exp.*, 6 (2021), 063203.

[84] Gardiner, C. *Handbook of stochastic methods*, vol. 3. springer Berlin, 1985.

[85] Gel'fand, I., and Yaglom, A. Integration in functional spaces and its applications in quantum physics. *J. Math. Phys. 1*, 1, 48.

[86] Giovannetti, V., Lloyd, S., and Maccone, L. Capacity of nonlinear bosonic systems. *Phys. Rev. A 70* (2004), 012307.

[87] Girard, M. On the semiclassical propagator for the anharmonic oscillator. *J. Phys. A: Math. Gen. 25*, 15 (1992), 4199.

[88] Giuggioli, L., Gupta, S., and Chase, M. Comparison of two models of tethered motion. *J. Phys. A: Math. Theor. 52*, 7 (2019), 075001.

[89] Goldberg, A., Schey, H. M., and Schwartz, J. L. Computer-generated motion pictures of one-dimensional quantum-mechanical transmission and reflection phenomena. *Am. J. Phys. 35*, 3, 177.

[90] Guillet, A., Roldán, E., and Jülicher, F. Extreme-value statistics of stochastic transport processes. *New J. Phys. 22*, 12 (2020), 123038.

[91] Gupta, D., and Maritan, A. Thermodynamic uncertainty relations in a linear system. *Eur. Phys. J. B 93*, 2, 1.

[92] Gupta, S., Majumdar, S. N., and Schehr, G. Fluctuating interfaces subject to stochastic resetting. *Phys. Rev. Lett. 112*, 22 (2014), 220601.

[93] Gupta, S., and Nagar, A. Resetting of fluctuating interfaces at power-law times. *J. Phys. A: Math. Theor. 49*, 44 (2016), 445001.

[94] Gurvitz, S., Aharony, A., and Entin-Wohlman, O. Temporal evolution of resonant transmission under telegraph noise. *Phys. Rev. B 94*, 7 (2016), 075437.

[95] Halliday, I., and Suranyi, P. Anharmonic oscillator: A new approach. *Phys. Rev. D 21*, 6 (1980), 1529.

[96] Halpern, F. Quantum mechanics of the anharmonic oscillator. *J. Math. Phys. 14*, 2, 219.

[97] Harris, R. J., and Touchette, H. Phase transitions in large deviations of reset processes. *J. Phys. A: Math. Theor. 50*, 10 (2017), 10LT01.

[98] Hogan, P., and Chalker, J. Path integrals, diffusion on su (2) and the fully frustrated antiferromagnetic spin cluster. *J. Phys. A: Math. Gen. 37*, 49 (2004), 11751.

[99] Horowitz, J. M., and Gingrich, T. R. Proof of the finite-time thermodynamic uncertainty relation for steady-state currents. *Phys. Rev. E 96*, 2 (2017), 020103.

[100] Hubbard, J. Calculation of partition functions. *Phys. Rev. Lett. 3*, 2 (1959), 77.

[101] Huber, D., and Tsimring, L. Dynamics of an ensemble of noisy bistable elements with global time delayed coupling. *Phys. Rev. Lett. 91*, 26 (2003), 260601.

[102] Hudspeth, A. Integrating the active process of hair cells with cochlear function. *Nat. Rev. Neurosci. 15*, 9, 600.

[103] Hudspeth, A., and Gillespie, P. G. Pulling springs to tune transduction: adaptation by hair cells. *Neuron 12*, 1, 1.

[104] I. Bloch, J. D., and Zwerger, W. Many-body physics with ultracold gases. *Rev. Mod. Phys. 80*, 3 (2008), 885.

[105] Jacobs, K. *Stochastic Processes for Physicists: Understanding Noisy Systems*. Cambridge University Press, 2010.

[106] Jülicher, F., Ajdari, A., and Prost, J. Modeling molecular motors. *Rev. Mod. Phys. 69*, 4 (1997), 1269.

[107] Kac, M. A stochastic model related to the telegrapher's equation. *Rocky Mt. J. Math. 4*, 3, 497.

[108] Keller, D., and Bustamante, C. The mechanochemistry of molecular motors. *Biophys. J. 78*, 2, 541.

[109] Kolokolov, I. Functional representation for the partition function of the quantum Heidenberg ferromagnet. *Phys. Lett. A 114*, 2, 99.

[110] Kruse, K., and Jülicher, F. Oscillations in cell biology. *Curr. Op. Cell. Biol. 17*, 1, 20.

[111] Kuhn, C.-D., Geiger, S. R., Baumli, S., Gartmann, M., Gerber, J., Jennebach, S., Mielke, T., Tschochner, H., Beckmann, R., and Cramer, P. Functional architecture of RNA polymerase I. *Cell 131*, 7, 1260.

[112] Kurzyński, M. Statistical properties of the dichotomous noise generated in biochemical processes. *Cell. Mol. Biol. Lett. 13*, 4, 502.

[113] Kuśmierz, Ł., and Gudowska-Nowak, E. Optimal first-arrival times in Lévy flights with resetting. *Phys. Rev. E 92*, 5 (2015), 052127.

[114] Kusmierz, L., Majumdar, S. N., Sabhapandit, S., and Schehr, G. First order transition for the optimal search time of Lévy flights with resetting. *Phys. Rev. Lett. 113*, 22 (2014), 220602.

[115] Kuśmierz, Ł., and Toyoizumi, T. Robust random search with scale-free stochastic resetting. *Phys. Rev. E 100*, 3 (2019), 032110.

[116] Lam, C. Stationary phase approximation of Feynman path integrals. *Il Nuovo Cimento A 47*, 3, 451.

[117] Langevin, P. Sur la théorie du mouvement brownien. *Compt. Rendus 146*, 530.

[118] Lisica, A., Engel, C., Jahnel, M., Roldán, É., Galburt, E. A., Cramer, P., and Grill, S. W. Mechanisms of backtrack recovery by RNA polymerases I and II. *PNAS 113*, 11, 2946.

[119] Lodish, H., Berk, A., Kaiser, C. A., Kaiser, C., Krieger, M., Scott, M. P., Bretscher, A., Ploegh, H., Matsudaira, P., et al. *Molecular cell biology*. Macmillan, 2008.

[120] Luby, M., Sinclair, A., and Zuckerman, D. Optimal speedup of Las Vegas algorithms. *Inf. Process. Lett. 47*, 4, 173.

[121] Lueckmann, J., Gonçalves, P. J., Bassetto, G., Oecal, K., Nonnenmacher, M., and Macke, J. H. Flexible statistical inference for mechanistic models of neural dynamics. In *Neural Information Processing Systems (NIPS 2017)* (2018).

[122] M. Belloni, M. D., and Robinett, R. Wigner quasi-probability distribution for the infinite square well: Energy eigenstates and time-dependent wave packets. *Am. J. Phys. 72*, 9, 1183.

[123] M. Johanning, A. V., and Wunderlich, C. Quantum simulations with cold trapped ions. *J. Phys. B 42*, 15 (2009), 154009.

[124] M.A. Timpanaro, S. Wald, F. S., and Landi, G. Dynamical chaotic phases and constrained quantum dynamics. *Phys. Rev. A 100*, 1 (2019), 012117.

[125] Maes, C., and Thiery, T. The induced motion of a probe coupled to a bath with random resettings. *J. Phys. A: Math. Theor. 50*, 41 (2017), 415001.

[126] Malakar, K., Jemseena, V., Kundu, A., Kumar, K. V., Sabhapandit, S., Majumdar, S. N., Redner, S., and Dhar, A. Steady state, relaxation and first-passage properties of a run-and-tumble particle in one-dimension. *J. Stat. Mech.: Theory Exp.*, 4 (2018), 043215.

[127] Manikandan, S. K., and Krishnamurthy, S. Exact results for the finite time thermodynamic uncertainty relation. *J. Phys. A Math. Theor. 51*, 11 (2018), 11LT01.

[128] Mankin, R., Laas, T., Soika, E., and Ainsaar, A. Noise-controlled slow–fast oscillations in predator–prey models with the Beddington functional response. *Eur. Phys. J. B 59*, 2, 259.

[129] Maoiléidigh, D. Ó., Nicola, E. M., and Hudspeth, A. The diverse effects of mechanical loading on active hair bundles. *PNAS 109*, 6, 1943.

[130] Martin, P., Bozovic, D., Choe, Y., and Hudspeth, A. Spontaneous oscillation by hair bundles of the bullfrog's sacculus. *J. Neurosci. 23*, 11, 4533.

[131] Martin, P., and Hudspeth, A. Active hair-bundle movements can amplify a hair cell's response to oscillatory mechanical stimuli. *Proceedings of the National Academy of Sciences 96*, 25, 14306.

[132] Martin, P., and Hudspeth, A. Mechanical frequency funing by sensory hair cells, the receptors and amplifiers of the inner ear. *Annu. Rev. Condens. Matter Phys. 12*, 1, 29.

[133] Masoliver, J. Telegraphic processes with stochastic resetting. *Phys. Rev. E 99*, 1 (2019), 012121.

[134] Méndez, V., and Campos, D. Characterization of stationary states in random walks with stochastic resetting. *Phys. Rev. E 93* (2016), 022106.

[135] Mindlin, G. B. Nonlinear dynamics in the study of birdsong. *Chaos 27*, 9 (2017), 092101.

[136] Miotto, J. M., Pigolotti, S., Chechkin, A. V., and Roldán-Vargas, S. Length scales in Brownian yet non-Gaussian dynamics. *Phys. Rev. X 11*, 3 (2021), 031002.

[137] Mirollo, R. E., and Strogatz, S. H. Synchronization of pulse-coupled biological oscillators. *SIAM J. Appl. Math. 50*, 6, 1645.

[138] Mizrahi, M. The semiclassical expansion of the anharmonic-oscillator propagator. *J. Math. Phys. 20*, 5, 844.

[139] Montanari, A., and Zecchina, R. Optimizing searches via rare events. *Phys. Rev. Lett. 88*, 17 (2002), 178701.

[140] Mora, T. Physical limit to concentration sensing amid spurious ligands. *Phys. Rev. Lett. 115*, 3 (2015), 038102.

[141] Moyer, C. Numerov extension of transparent boundary conditions for the Schrödinger equation in one dimension. *Am. J. Phys. 72*, 3, 351.

[142] Mukherjee, B., Maiti, P. K., Dasgupta, C., and Sood, A. Single-file diffusion of water inside narrow carbon nanorings. *ACS Nano 4*, 2, 985.

[143] Mukherjee, B., Sengupta, K., and Majumdar, S. N. Quantum dynamics with stochastic reset. *Phys. Rev. B 98* (2018), 104309.

[144] Müller-Hansen, F., Droste, F., and Lindner, B. Statistics of a neuron model driven by asymmetric colored noise. *Phys. Rev. E 91*, 2 (2015), 022718.

[145] Murch, K., Vijay, R., Barth, I., Naaman, O., Aumentado, J., Friedland, L., and Siddiqi, I. Quantum fluctuations in the chirped pendulum. *Nat. Phys. 7*, 2, 105.

[146] Nadkarni, S., and Jung, P. Spontaneous oscillations of dressed neurons: a new mechanism for epilepsy? *Phys. Rev. Lett. 91*, 26 (2003), 268101.

[147] Nagar, A., and Gupta, S. Diffusion with stochastic resetting at power-law times. *Phys. Rev. E 93* (2016), 060102.

[148] Nagumo, J., Arimoto, S., and Yoshizawa, S. An active pulse transmission line simulating nerve axon. *Proc. IEEE 50*, 10, 2061.

[149] Nash, R., Adhikari, R., Tailleur, J., and Cates, M. Run-and-tumble particles with hydrodynamics: Sedimentation, trapping, and upstream swimming. *Phys. Rev. Lett. 104*, 25 (2010), 258101.

[150] Nayak, I., Das, D., and Nandi, A. Comparison of mechanisms of kinetochore capture with varying number of spindle microtubules. *Phys. Rev. Research 2*, 1 (2020), 013114.

[151] Nicacio, F., and Semião, F. Coupled harmonic systems as quantum buses in thermal environments. *J. Phys. A: Math. Gen. 49*, 37 (2016), 375303.

[152] Nicola, S. D. Disentanglement approach to quantum spin ground states: field theory and stochastic simulation. *J. Stat. Mech.: Theory Exp. 2021*, 1 (2021), 013101.

[153] Nomura, T., Sato, S., Doi, S., Segundo, J. P., and Stiber, M. D. A Bonhoeffer-van der Pol oscillator model of locked and non-locked behaviors of living pacemaker neurons. *Biol. Cybern. 69*, 5, 429.

[154] Oates, A. C., Morelli, L. G., and Ares, S. Patterning embryos with oscillations: structure, function and dynamics of the vertebrate segmentation clock. *Development 139*, 4, 625.

[155] Odde, D. J., Cassimeris, L., and Buettner, H. M. Kinetics of microtubule catastrophe assessed by probabilistic analysis. *Biophys. J. 69*, 3, 796.

[156] P. Calabrese, F. E., and Mussardo, G. Introduction to 'quantum integrability in out of equilibrium systems'. *J. Stat. Mech.: Theory Exp. 2016*, 6 (2016), 064001.

[157] Pal, A., Kuśmierz, Ł., and Reuveni, S. Search with home returns provides advantage under high uncertainty. *Phys. Rev. Research 2*, 4 (2020), 043174.

[158] Pal, A., and Reuveni, S. First passage under restart. *Phys. Rev. Lett. 118* (2017), 030603.

[159] Papamakarios, G., and Murray, I. Fast $\varepsilon$-free inference of simulation models with bayesian conditional density estimation. In *Adv. Neural Inf. Process Syst.*, p. 1028.

[160] Pavin, N., and Tolić-Nørrelykke, I. M. Swinging a sword: how microtubules search for their targets. *Syst. Synth. Biol. 8*, 3, 179.

[161] Perrin, J. Mouvement brownien et réalité moléculaire. *J. Phys. Theor. Appl. 9*, 1, 5.

[162] Pietzonka, P., Barato, A. C., and Seifert, U. Universal bound on the efficiency of molecular motors. *J. Stat. Mech. 2016*, 12 (2016), 124004.

[163] Pietzonka, P., Ritort, F., and Seifert, U. Finite-time generalization of the thermodynamic uncertainty relation. *Phys. Rev. E 96*, 1 (2017), 012101.

[164] Plaçais, P.-Y., Balland, M., Guérin, T., Joanny, J.-F., and Martin, P. Spontaneous oscillations of a minimal actomyosin system under elastic loading. *Phys. Rev. Lett. 103*, 15 (2009), 158102.

[165] Planck, M. Über einen satz der statistischen dynamik und seine erweiterung in der quantentheorie sitz. *Preußischen Akad. Wissen 24* (1917), 324.

[166] Potts, P. P., and Samuelsson, P. Thermodynamic uncertainty relations including measurement and feedback. *Phys. Rev. E 100*, 5 (2019), 052137.

[167] Prelogović, M., Winters, L., Milas, A., Tolić, I. M., and Pavin, N. Pivot-and-bond model explains microtubule bundle formation. *Phys. Rev. E 100*, 1 (2019), 012403.

[168] Press, W. H., Flannery, B. P., Teukolsky, S. A., Vetterling, W. T., et al. *Numerical recipes*. Cambridge University Press, 1989.

[169] Prost, J., Jülicher, F., and Joanny, J.-F. Active gel physics. *Nature Phys. 11*, 2, 111.

[170] Ramaswamy, S. The mechanics and statistics of active matter. *Annu. Rev. Condens. Matter Phys. 1*, 1, 323.

[171] Ray, S., Mondal, D., and Reuveni, S. Péclet number governs transition to acceleratory restart in drift-diffusion. *J. Phys. A: Math. Theor. 52*, 25 (2019), 255002.

[172] Redner, S. *A Guide to First-Passage Processes*. Cambridge University Press, 2001.

[173] Reichenbach, T., and Hudspeth, A. The physics of hearing: fluid mechanics and the active process of the inner ear. *Rep. Prog. Phys. 77*, 7 (2014), 076601.

[174] Reimann, P., Van den Broeck, C., H., L., Hänggi, P., Rubi, J., and Pérez-Madrid, A. Giant acceleration of free diffusion by use of tilted periodic potentials. *Phys. Rev. Lett. 87*, 1 (2001), 010602.

[175] Ringel, M., and Gritsev, V. Dynamical symmetry approach to path integrals of quantum spin systems. *Phys. Rev. A 88*, 6 (2013), 062105.

[176] Roenneberg, T., Chua, E. J., Bernardo, R., and Mendoza, E. Modelling biological rhythms. *Curr. Biol. 18*, 17, R826.

[177] Roldán, É. *Irreversibility and dissipation in microscopic systems.* Springer, 2014.

[178] Roldán, É., Barral, J., Martin, P., Parrondo, J. M., and Jülicher, F. Quantifying entropy production in active fluctuations of the hair-cell bundle from time irreversibility and uncertainty relations. *New J. Phys. 23*, 8 (2021), 083013.

[179] Roldán, E., and Gupta, S. Path-integral formalism for stochastic resetting: Exactly solved examples and shortcuts to confinement. *Phys. Rev. E 96* (2017), 022130.

[180] Roldán, É., Lisica, A., Sánchez-Taltavull, D., and Grill, S. W. Stochastic resetting in backtrack recovery by RNA polymerases. *Phys. Rev. E 93*, 6 (2016), 062411.

[181] Romatschke, P. Quantum mechanical out-of-time-ordered-correlators for the anharmonic (quartic) oscillator. *J. High Energy Phys. 2021*, 1 (2021), 30.

[182] Rompala, K., Rand, R., and Howland, H. Dynamics of three coupled Van der Pol oscillators with application to circadian rhythms. *Commun. Nonlinear. Sci. Numer. Simul. 12*, 5, 794.

[183] Rotbart, T., Reuveni, S., and Urbakh, M. Michaelis-Menten reaction scheme as a unified approach towards the optimal restart problem. *Phys. Rev. E 92*, 6 (2015), 060101.

[184] S. De Nicola, B. D., and Bhaseen, M. Stochastic approach to non-equilibrium quantum spin systems. *J. Phys. A: Math. Theor. 52*, 5 (2019), 05LT02.

[185] S. De Nicola, B. D., and Bhaseen, M. Non-equilibrium quantum spin dynamics from classical stochastic processes. *J. Stat. Mech.: Theory Exp. 2020*, 1 (2020), 013106.

[186] Sakurai, J., and Napolitano, J. *Modern Quantum Mechanics. 2-nd edition.* Person New International edition, 2014.

[187] Santra, I., Basu, U., and Sabhapandit, S. Run-and-tumble particles in two dimensions under stochastic resetting conditions. *J. Stat. Mech.: Theory Exp. 2020*, 11 (2020), 113206.

[188] Schiff, J. *The Laplace Transform: Theory and Applications.* Springer-Verlag New York, 1999.

[189] Schulman, L. *Techniques and applications of path integration*. Courier Corporation, 2012.

[190] S.E. Begg, A. G., and Bhaseen, M. Fluctuations and non-Hermiticity in the stochastic approach to quantum spins. *J. Phys. A 53*, 50 (2020), 50LT02.

[191] Seifert, U. Stochastic thermodynamics: From principles to the cost of precision. *Phys. A: Stat. Mech. Appl. 504*, 176.

[192] Sekimoto, K. Langevin equation and thermodynamics. *Prog. Theor. Exp. Phys. 130*, 17.

[193] Sekimoto, K. *Stochastic energetics*, vol. 799. Springer, 2010.

[194] Shalibo, Y., Resh, R., Fogel, O., Shwa, D., Bialczak, R., Martinis, J. M., and Katz, N. Direct Wigner tomography of a superconducting anharmonic oscillator. *Phys. Rev. Lett. 110*, 10 (2013), 100404.

[195] Shalibo, Y., Rofe, Y., Barth, I., Friedland, L., Bialczack, R., Martinis, J. M., and Katz, N. Quantum and classical chirps in an anharmonic oscillator. *Phys. Rev. Lett. 108*, 3 (2012), 037701.

[196] Shankar, R. *Principles of quantum mechanics*. Springer Science & Business Media, 2012.

[197] Shreshtha, M., and Harris, R. J. Thermodynamic uncertainty for run-and-tumble–type processes. *EPL 126*, 4 (2019), 40007.

[198] Simon, B., and Dicke, A. Coupling constant analyticity for the anharmonic oscillator. *Ann. Phys. 58*, 1, 76.

[199] Skinner, D. J., and Dunkel, J. Estimating entropy production from waiting time distributions. *Phys. Rev. Lett. 127* (2021), 198101.

[200] Smoluchowski, M. Sur le chemin moyen parcouru par les molécules d'un gaz et sur son rapport avec la théorie de la diffusion. *Pisma Mariana Smoluchowskiego 1*, 1, 479.

[201] Smoluchowski, M. *Essai d'une théorie cinétique du mouvement Brownien et des milieux troublés*. Acad. Litterarum Cracoviensis, 1906.

[202] Snygg, J. Use of operator wave functions to construct a refined correspondence principle via the quantum mechanics of Wigner and Moyal. *Am. J. Phys. 48*, 11, 964.

[203] Solon, A. P., Cates, M. E., and Tailleur, J. Active brownian particles and run-and-tumble particles: A comparative study. *Eur. Phys. J. Spec. Top. 224*, 7, 1231.

[204] Sposini, V., Chechkin, A. V., Seno, F., Pagnini, G., and Metzler, R. Random diffusivity from stochastic equations: comparison of two models for Brownian yet non-Gaussian diffusion. *New J. Phys. 20*, 4 (2018), 043044.

[205] Steiger, D. S., Rønnow, T. F., and Troyer, M. Heavy tails in the distribution of time to solution for classical and quantum annealing. *Phys. Rev. Lett. 115*, 23 (2015), 230501.

[206] Stratonovich, R. On a method of calculating quantum distribution functions. 416.

[207] Suzuki, M. Improved Trotter-like formula. *Phys. Lett. A 180*, 3, 232.

[208] T. Kinoshita, T., and Weiss, D. A quantum Newton's cradle. *Nature 440*, 7086, 900.

[209] T. Langen, R. G., and Schmiedmayer, J. Ultracold atoms out of equilibrium. *Annu. Rev. Condens. Matter Phys. 6*, 1, 201.

[210] Tailleur, J., and Cates, M. Statistical mechanics of interacting run-and-tumble bacteria. *Phys. Rev. Lett. 100*, 21 (2008), 218103.

[211] Tal-Friedman, O., Pal, A., Sekhon, A., Reuveni, S., and Roichman, Y. Experimental realization of diffusion with stochastic resetting. *J. Phys. Chem. Lett. 11*, 17, 7350.

[212] Tang, E., Agudo-Canalejo, J., and Golestanian, R. Topology protects chiral edge currents in stochastic systems. *Phys. Rev. X 11*, 3 (2021), 031015.

[213] Tejero-Cantero, A., Boelts, J., Deistler, M., Lueckmann, J.-M., Durkan, C., Gonçalves, P. J., Greenberg, D. S., and Macke, J. H. Sbi–a toolkit for simulation-based inference. *arXiv preprint arXiv:2007.09114* (2020).

[214] Tinevez, J.-Y., Jülicher, F., and Martin, P. Unifying the various incarnations of active hair-bundle motility by the vertebrate hair cell. *Biophys. J. 93*, 11, 4053.

[215] Toner, J., Tu, Y., and Ramaswamy, S. Hydrodynamics and phases of flocks. *Ann. Phys. 318*, 1, 170.

[216] Touchette, H. The large deviation approach to statistical mechanics. *Phys. Rep. 478*, 1-3, 1.

[217] Tu, Y. The nonequilibrium mechanism for ultrasensitivity in a biological switch: Sensing by Maxwell's demons. *PNAS 105*, 33, 11737.

[218] Van den Broeck, C. Taylor dispersion revisited. *Physica A 168*, 2, 677.

[219] Van Der Pol, B. Biological rhythms considered as relaxation oscillations. *Acta Med. Scand. 103*, S108, 76.

[220] Van Der Pol, B., and Van Der Mark, J. LXXII. The heartbeat considered as a relaxation oscillation, and an electrical model of the heart. *Lond. Edinb. Dublin Philos. Mag. J. Sci. 6*, 38, 763.

[221] van Dijk, P., and Wit, H. P. Amplitude and frequency fluctuations of spontaneous otoacoustic emissions. *J. Acoust. Soc. Am. 88*, 4, 1779.

[222] Van Kampen, N. G. *Stochastic processes in physics and chemistry*, vol. 1. Elsevier, 1992.

[223] Van Vu, T., and Hasegawa, Y. Uncertainty relations for time-delayed Langevin systems. *Phys. Rev. E 100*, 1 (2019), 012134.

[224] Van Vu, T., and Hasegawa, Y. Uncertainty relation under information measurement and feedback control. *J. Phys. A Math. Theor. 53*, 7 (2020), 075001.

[225] Vettoretti, G., and Peltier, W. R. Fast physics and slow physics in the nonlinear Dansgaard–Oeschger relaxation oscillation. *J. Clim. 31*, 9, 3423.

[226] Vilfan, A., and Duke, T. Two adaptation processes in auditory hair cells together can provide an active amplifier. *Biophys. J. 85*, 1, 191.

[227] W. Bakr, J. Gillen, A. P. S. F., and Greiner, M. A quantum gas microscope for detecting single atoms in a Hubbard-regime optical lattice. *Nature 462*, 7269, 74.

[228] Wald, S., and Henkel, M. Lindblad dynamics of a quantum spherical spin. *J. Phys. A: Math. Theor. 49*, 12 (2016), 125001.

[229] Wald, S., Moreira, S. V., and Semião, F. L. In- and out-of-equilibrium quantum metrology with mean-field quantum criticality. *Phys. Rev. E 101* (2020), 052107.

[230] Wei, J., and Norman, E. Lie algebraic solution of linear differential equations. *J. Math. Phys. 4*, 4, 575.

[231] Weiler, C. N., Neely, T. W., Scherer, D. R., Bradley, A. S., Davis, M. J., and Anderson, B. P. Spontaneous vortices in the formation of Bose–Einstein condensates. *Nature 455*, 7215, 948.

[232] Weitenberg, C., Endres, M., Sherson, J. F., Cheneau, M., Schauss, P., Fukuhara, T., Bloch, I., and Kuhr, S. Single-spin addressing in an atomic Mott insulator. *Nature 471*, 7338, 319.

[233] Wittrock, S., Talatchian, P., Romera, M., Garcia, M. J., Cyrille, M.-C., Ferreira, R., Lebrun, R., Bortolotti, P., Ebels, U., Grollier, J., et al. Flicker and random telegraph noise between gyrotropic and dynamic C-state of a vortex based spin torque nano oscillator. *AIP Adv. 11*, 3 (2021), 035042.

[234] Yuzhelevski, Y., Yuzhelevski, M., and Jung, G. Random telegraph noise analysis in time domain. *Rev. Sci. Instrum 71*, 4, 1681.

[235] Zinn-Justin, J. *Quantum field theory and critical phenomena*, vol. 171. Oxford University Press, 2021.